Integer Ambiguity Resolution for Multi-GNSS and Multi-Signal Raw Phase Observations

Heft 58
Schriftenreihe der Fachrichtung Geodäsie
Fachbereich Bau- und Umweltingenieurwissenschaften
Technische Universität Darmstadt
ISBN 978-3-935631-47-1

Darmstadt, März 2020

TECHNISCHE
UNIVERSITÄT
DARMSTADT

Heft 58

Darmstadt, März 2020

Florian Reckeweg

Integer Ambiguity Resolution for Multi-GNSS and Multi-Signal Raw Phase Observations

Schriftenreihe
Fachrichtung Geodäsie
Fachbereich Bau- und Umweltingenieurwissenschaften
Technische Universität Darmstadt

ISBN 978-3-935631-47-1

Schriftenreihe Fachrichtung Geodäsie der Technischen Universität Darmstadt

Online unter: *https://tuprints.ulb.tu-darmstadt.de/id/eprint/11483*

Diese Arbeit ist gleichzeitig veröffentlicht in der Reihe C der
Deutschen Geodätischen Kommission, München 2020.

Verantwortlich für die Herausgabe der Schriftenreihe:

Der Sprecher der Fachrichtung Geodäsie
im Fachbereich Bau- und Umweltingenieurwissenschaften
der Technischen Universität Darmstadt

Bezugsnachweis:

Technische Universität Darmstadt
Institut für Geodäsie
Franziska-Braun-Str. 7
64287 Darmstadt

ISBN: 978-3-935631-47-1

Integer Ambiguity Resolution for Multi-GNSS and Multi-Signal Raw Phase Observations

Vom Fachbereich Bau- und Umweltingenieurwissenschaften
der Technischen Universität Darmstadt
zur Erlangung des akademischen Grades eines
Doktor-Ingenieurs (Dr.-Ing.) genehmigte

Dissertation

vorgelegt von

Florian Reckeweg, M.Sc.
geboren in Heppenheim

Referent:	Prof. Dr.-Ing. Matthias Becker
Korreferent:	Prof. Dr.-Ing. Werner Enderle
Korreferent:	Prof. Dr.-Ing. Andreas Eichhorn

Tag der Einreichung:	14. Oktober 2019
Tag der mündlichen Prüfung:	05. Dezember 2019

Darmstadt, März 2020
D17

"**Integers are the fountainhead of all mathematics**"

Hermann Minkowski
Diophantine Approximations (1907)

Preface

This dissertation has been written during my time as research associate at the chair of Physical Geodesy and Satellite Geodesy at the Technische Universität Darmstadt, Germany. During that time I had the great opportunity to work as a full team member in the Navigation Support Office at the European Space Operations Centre (ESOC) in Darmstadt, Germany. The research presented in this work would not have been able to conduct without the excellent collaboration between these two institutes. I am grateful to my supervisors for giving me the chance to work in this exciting field of research and contribute to the cooperation between academia and space industry.
In particular I would like to thank my supervisor Prof. Dr.-Ing. Matthias Becker from Technische Universität Darmstadt for his support and advice during the past five years. His encouragement and positive attitude always motivated me and gave me the confidence to perform this research.
I would like to thank my supervisor Prof. Dr.-Ing. Werner Enderle, Head of the Navigation Support Office at ESOC, for his guidance and the confidence in my work. His suggestions and continuous support helped me to define the direction of this thesis and gave me the freedom to realise own ideas.
I also wish to thank Prof. Dr.-Ing. Andreas Eichhorn for his willingness to appraise this dissertation.

Special thanks go to my colleagues at Technische Universität Darmstadt for many fruitful discussions and debates about work-related and other topics. In particular I would like to thank Dr. Stefan Leinen, who has always been available and willing to answer my questions related to parameter estimation and other fundamental topics. I am thankful to Björn Reuper for the great time we shared working on our theses and many fruitful and interesting discussions about work and life. I also wish to thank Angelika Klinkrad for her support throughout the years.

Special thanks also go to my colleagues at ESOC for always being supportive, for the great team spirit and the interesting debates at work and after work. In particular I would like to thank Dr. Erik Schönemann and Dr. Tim Springer for many fundamental scientific discussions. Without their support it would not have been possible to conduct this research.

My parents deserve a particular note of thanks: Without your guidance and advice I would not have achieved any of this. And to the most important person in my life: Annabel, thank you so much for always supporting me all these years, in good times and difficult times. Your patience and ever forthright and refreshing comments gave me the freedom and necessary feedback to conclude this thesis. Thank you for everything!

Florian Reckeweg
Bensheim, October 2019

Abstract

The continuous modernisation of existing Global Navigation Satellite Systems (GNSS) and the development of new systems with a multitude of different carrier frequencies and a variety of signal modulations creates a true multi-GNSS and multi-signal environment available today.

Still most precise GNSS processing strategies rely on dual-frequency measurements only by applying the Ionosphere-Free (IF) Linear Combination (LC) of GNSS observables and therefore do not benefit from the available multi-signal environment. While in this processing approach the first order effect of the ionospheric delay can be eliminated almost completely, the formation of linear combinations of GNSS observables leads to a noise increase for the resulting observations and a loss of some of the physical characteristics of the original signals, like the integer nature of the carrier phase ambiguity.

In order to benefit from the multi-GNSS and multi-signal environment available today, the scientific analyses and precise applications presented in this work are based on the raw observation processing approach, which makes use of the original (raw) observations without forming any linear combinations or differences of GNSS observables. This processing strategy provides the flexibility to make use of all or a selection of available multi-GNSS and multi-signal raw observations, which are jointly processed in a single adjustment as there is no inherent limitation on the number of usable signals. The renunciation of linear combinations and observation differences preserves the physical characteristics of individual signals and implies that multi-signal biases and ionospheric delays need to be properly determined or corrected in the parameter estimation process.

The raw observation processing approach is used in this work to jointly process measurements from up to three different GNSS, including eleven signals tracked on up to eight different carrier frequencies in one single adjustment.

The bias handling for multi-GNSS and multi-signal applications is analysed with a focus on physically meaningful parameter estimates to demonstrate the benefits of handling clock offset parameters, multi-signal code biases and ionospheric delay estimates in a physically meaningful and consistent way. In this context, receiver-specific multi-GNSS and multi-signal biases are analysed and calibrated by the use of a GNSS signal simulator. The disadvantages of eliminating physical characteristics due to the formation of linear combinations of observations or commonly used parameter estimation strategies are demonstrated and discussed.

The carrier phase Integer Ambiguity Resolution (IAR) approach developed and implemented in the course of this work is based on the joint processing of multi-GNSS and multi-signal raw observations without forming any linear combinations or observation differences. Details of the implemented IAR approach are described and the performance is analysed for available carrier signal frequencies of different GNSS. Achieved results are compared to the conventional IAR approach based on IF linear combinations and the so called Widelane (WL) and Narrowlane (NL) ambiguities. In addition, the resolution of inter-system integer ambiguities is analysed for common GNSS signal frequencies.

The performance of the implemented IAR approach is demonstrated and analysed by the joint Precise Orbit Determination (POD) of multi-GNSS satellites based on fixed multi-frequency carrier phase ambiguities. The improvement of the satellite orbit and clock quality by fixing raw observation ambiguities confirms the successful implementation of the IAR approach based on raw observation processing. Multi-GNSS satellite orbits and clock offsets determined with this approach are compared to results generated with the conventional IF linear combination processing approach and independent external products. This comparison demonstrates an at least equivalent performance of the implemented IAR approach based on raw observation processing. In addition, the fixed raw observation ambiguities are used to investigate and discuss characteristics of multi-GNSS and multi-frequency phase biases.

Zusammenfassung (in German)

Die kontinuierliche Modernisierung existierender Globaler Navigationssatellitensysteme (GNSS) und die Entwicklung neuer Systeme mit einer Vielzahl verschiedener Trägerfrequenzen und Signalmodulationen führt zu einem wahren Multi-GNSS- und Multi-Signal-Umfeld, das heutzutage zur Verfügung steht.
Dennoch beruhen die meisten präzisen GNSS-Prozessierungsstrategien nur auf Zweifrequenz-Messungen durch die Verwendung der ionosphären-freien (IF) Linearkombination (LC) von GNSS-Beobachtungen und profitieren daher nicht von der verfügbaren Multi-Signal-Umgebung. Während bei diesem Prozessierungsansatz ionosphärische Laufzeitverzögerungen erster Ordnung fast vollständig eliminiert werden können, führt die Linearkombinationsbildung von GNSS-Beobachtungen zu einem Anstieg des entsprechenden Beobachtungsrauschens und dem Verlust gewisser physikalischer Eigenschaften der Originalsignale, wie dem ganzzahligen Charakter der Trägerphasen-Mehrdeutigkeit.
Um von dem Multi-GNSS- und Multi-Signal-Umfeld, das heutzutage zur Verfügung steht, zu profitieren, basieren die wissenschaftlichen Analysen und präzisen Anwendungen, die in dieser Arbeit präsentiert werden, auf dem Prozessierungsansatz für Rohbeobachtungen. Dieser Ansatz verwendet die originalen (Roh-)Beobachtungen, ohne jegliche Linearkombinations- oder Differenzbildung von GNSS-Beobachtungen. Diese Prozessierungsstrategie bietet die Flexibilität alle verfügbaren oder eine Auswahl an Multi-GNSS- und Multi-Signal-Rohbeobachtungen gemeinsam in einer Ausgleichsrechnung zu verarbeiten, da keine inhärente Limitierung der Anzahl an benutzbaren Signalen existiert. Der Verzicht jeglicher Linearkombinations- und Beobachtungsdifferenzbildung bewahrt die physikalischen Eigenschaften der einzelnen Signale und bedeutet, dass systematische Multi-Signal-Messabweichungen und ionosphärische Laufzeitverzögerungen in dem verwendeten Parameterschätzverfahren korrekt bestimmt oder korrigiert werden müssen.
Der Prozessierungsansatz für Rohbeobachtungen wird in dieser Arbeit verwendet, um Messungen von bis zu drei verschiedenen GNSS und elf Signalen auf bis zu acht verschiedenen Trägerfrequenzen gemeinsam in einer Ausgleichsrechnung zu verarbeiten.
Die Handhabung von systematischen Messabweichungen für Multi-GNSS- und Multi-Signal-Anwendungen wird analysiert mit Fokus auf die Bestimmung physikalisch sinnvoller Parameterwerte. Die Vorteile eines physikalisch sinnvollen und konsistenten Umgangs mit Uhrenfehlern, systematischen Multi-Signal-Codeabweichungen und ionosphärischen Laufzeitverzögerungen werden demonstriert. In diesem Zusammenhang werden empfängerspezifische systematische Multi-Signal-Messabweichungen analysiert und mit Hilfe eines GNSS-Signalsimulators kalibriert. Die Nachteile der Eliminierung physikalischer Eigenschaften durch die Linearkombinationsbildung von GNSS-Beobachtungen oder häufig verwendete Parameterschätzverfahren werden demonstriert und diskutiert.
Der im Rahmen dieser Arbeit entwickelte und implementierte Ansatz zur Bestimmung ganzzahliger Trägerphasen-Mehrdeutigkeiten (IAR) basiert auf der gemeinsamen Verarbeitung von Multi-GNSS- und Multi-Signal-Rohbeobachtungen ohne die Bildung jeglicher Linearkombinationen und Beobachtungsdifferenzen. Details des implementierten IAR-Ansatzes werden beschrieben und die Leistungsfähigkeit für verfügbare Trägerfrequenzen verschiedener GNSS analysiert. Erzielte Ergebnisse werden mit dem konventionellen IAR-Ansatz verglichen, der auf der Verwendung ionosphären-freier Linearkombinationen und so genannter Widelane (WL) und Narrowlane (NL) Mehrdeutigkeiten beruht. Darüber hinaus wird die Bestimmung ganzzahliger Trägerphasen-Mehrdeutigkeiten zwischen zwei Systemen für gemeinsame Signalfrequenzen analysiert.
Die Leistungsfähigkeit des implementierten IAR-Ansatzes wird anhand der gemeinsamen präzisen Orbitbestimmung (POD) von Multi-GNSS-Satelliten, die auf fixierten Mehrfrequenz-Trägerphasen-Mehrdeutigkeiten basiert, demonstriert und analysiert. Die Verbesserung der Orbit- und Uhrenqualität von Satelliten durch die Fixierung von Mehrdeutigkeiten für Rohphasen-Beobachtungen bestätigt die erfolgreiche Implementierung des IAR-Ansatzes unter der Verwendung von Rohbeobachtungen. Die mit diesem Ansatz bestimmten Multi-GNSS-Satellitenorbits und -uhrenfehler werden mit Ergebnissen basierend auf der konventionellen Verarbeitung von ionosphären-freien Linearkombinationen und unabhängigen externen Produkten verglichen. Dies demonstriert eine mindestens äquivalente Leistungsfähigkeit des implementierten IAR-Ansatzes basierend auf der Verarbeitung von Rohbeobachtungen. Darüber hinaus werden fixierte Trägerphasen-Mehrdeutigkeiten von Rohbeobachtungen benutzt, um Eigenschaften von systematischen Multi-GNSS-Mehrfrequenz-Phasenabweichungen zu untersuchen und zu diskutieren.

Contents

Page

Preface i

Abstract iii

Zusammenfassung (in German) v

Contents vii

1 Introduction 1
- 1.1 Background and Motivation . . . 1
- 1.2 Objectives of this work . . . 2
- 1.3 Outline . . . 2

2 Global Navigation Satellite Systems 3
- 2.1 Operational Principles . . . 3
  - 2.1.1 GNSS Architecture . . . 3
- 2.2 Overview of Existing GNSS . . . 3
  - 2.2.1 GPS . . . 3
  - 2.2.2 Galileo . . . 3
  - 2.2.3 Beidou . . . 4
  - 2.2.4 GLONASS . . . 4
- 2.3 GNSS Signals . . . 4
  - 2.3.1 Signal Structure and Modulation . . . 5
- 2.4 GNSS Receiver . . . 5
  - 2.4.1 Receiver System Components . . . 6
  - 2.4.2 GNSS Measurements . . . 6

3 Reference Systems 7
- 3.1 Coordinate Systems . . . 7
  - 3.1.1 International Terrestrial Reference System . . . 7
  - 3.1.2 Celestial Reference Systems . . . 8
  - 3.1.3 Earth Orientation Parameters . . . 8
- 3.2 Time Scales . . . 8
  - 3.2.1 International Atomic Time . . . 8
  - 3.2.2 Universal Time . . . 8
  - 3.2.3 Coordinated Universal Time . . . 9
  - 3.2.4 GNSS System Time . . . 9
  - 3.2.5 Clock Offsets, Epochs and Points in Time . . . 10

4 GNSS Observation Model 11
- 4.1 GNSS Raw Observables . . . 11
  - 4.1.1 Pseudorange Observation Equation . . . 11
  - 4.1.2 Carrier Phase Observation Equation . . . 14
  - 4.1.3 GNSS Signal Delays . . . 16
  - 4.1.4 Correction and Error Modelling . . . 16
  - 4.1.5 Reduced Raw Observation Equations . . . 25
- 4.2 Linear Combinations of GNSS Observables . . . 25
  - 4.2.1 Geometry-Free . . . 26
  - 4.2.2 Ionosphere-Free . . . 26
  - 4.2.3 Melbourne-Wuebbena . . . 27
- 4.3 Summary of Different Observation Models . . . 28

5 GNSS Observation Processing 29
- 5.1 Conventional GNSS Observation Processing . . . 29
  - 5.1.1 Code Bias Handling . . . 29

5.1.2 Observation Differences . . . 30
5.1.3 Carrier Phase Integer Ambiguity Resolution . . . 31
5.1.4 Phase Bias Handling and PPP-RTK . . . 33
5.2 Multi-GNSS Multi-Signal Raw Observation Processing . . . 33
5.2.1 Benefits and Challenges . . . 34
5.2.2 Handling of Raw Observation Biases . . . 34
5.2.3 Handling of Ionospheric Delay . . . 36
5.2.4 Raw Observation Processing with Ionosphere-Free Products . . . 36
5.3 Parameter Estimation Applied in Raw Method . . . 37
5.3.1 Linearisation of the Functional Model . . . 38
5.3.2 Solution of the Weighted Linearised System . . . 38
5.3.3 Sequential Batch Least Squares . . . 39
5.3.4 Solution of the Linearised Iterative Weighted Batch Least Squares Problem . . . 39
5.3.5 Constrained Least Squares Adjustment . . . 40
5.3.6 Stochastic Model . . . 41
5.4 Satellite Orbit Determination . . . 42

6 Carrier Phase Integer Ambiguity Resolution with Raw Observations 44
6.1 Concept of Raw Observation Ambiguity Resolution . . . 44
6.2 Multi-Frequency Double Difference Integer Ambiguity Resolution . . . 45
6.2.1 Forming Double Difference Ambiguities . . . 46
6.2.2 Histogram of Double Difference Ambiguity Fractionals . . . 46
6.2.3 Fixing Double Difference Integer Ambiguities . . . 47
6.2.4 Inter-Frequency Consistency Check . . . 48
6.2.5 Inter-System Integer Ambiguity Resolution . . . 49
6.3 Undifferenced Raw Integer Ambiguities and Phase Biases . . . 50

7 Analyses, Results and Applications 52
7.1 Multi-GNSS Multi-Signal Raw Observation Code Biases . . . 52
7.1.1 Receiver System Code Biases . . . 52
7.1.2 GNSS Satellite Code Biases . . . 58
7.2 Ionospheric Delay Estimation . . . 64
7.3 GNSS Time Offset Analysis . . . 65
7.3.1 System Time Offset to UTC . . . 65
7.3.2 Inter-System Time Offset . . . 67
7.4 Multi-GNSS Precise Orbit Determination with Fixed Raw Carrier Phase Ambiguities . . . 69
7.4.1 Global Network Adjustment . . . 69
7.4.2 Multi-GNSS Multi-Signal Integer Ambiguity Resolution . . . 71
7.4.3 Multi-GNSS Satellite Orbit Quality . . . 79
7.4.4 Multi-GNSS Satellite Clock Quality . . . 83
7.5 Multi-GNSS Multi-Signal Raw Observation Phase Biases . . . 84
7.5.1 Receiver Phase Bias Analysis based on Simulated Observations . . . 84
7.5.2 Satellite Phase Bias Analysis with Real Observations . . . 86
7.5.3 Aspects for PPP-IAR with Determined Satellite SD Phase Biases . . . 89

8 Conclusion 90
8.1 Signal Bias Handling in Multi-GNSS and Multi-Signal Raw Observation Processing . . . 90
8.2 Integer Ambiguity Resolution Based on Multi-GNSS and Multi-Signal Raw Observations . . . 90
8.3 Multi-GNSS Precise Orbit Determination Based on Fixed Raw Observation Ambiguities . . . 91

9 Outlook 92

10 Appendix 93
A Notation and Symbols . . . 93
B Constants . . . 95
C Definitions . . . 95
D Acronyms . . . 95
E List of Figures . . . 99
F List of Tables . . . 103
G Additional Results . . . 104

G.1 Satellite Differential Code Bias Estimation 104
G.2 Signal-Specific DD Ambiguity Fractional Histograms 106
G.3 Satellite SD Phase Biases 110

Bibliography **112**

1 Introduction

Global Navigation Satellite Systems (GNSS) have become an essential part of modern society. Services, including those directly provided by the multiple GNSS available today and those based on the existence of GNSS, are used on every continent by a vast number of people. Classically, GNSS services consist of the determination of position, velocity and time at any point on Earth, including at sea and in the air. In the last decade, the application of GNSS services for satellites orbiting the Earth in a Low Earth Orbit (LEO) has gained considerable interest and in recent years there has been extensive research and development in the field of using GNSS services to support satellite missions above the GNSS satellite altitude, an application referred to in the literature as the Space Service Volume (SSV).
The enhancements of the U.S. Global Positioning System (GPS) and the Russian GNSS (GLONASS), as well as the development of the European GNSS (Galileo) and the Chinese GNSS (BeiDou) have established a proper multi-GNSS and multi-signal environment available today. In addition, Regional Navigation Satellite Systems (RNSS) like the Japanese Quasi-Zenith Satellite System (QZSS) and the Indian Regional Navigation Satellite System (IRNSS) provide supplementary position, navigation and timing services in their respective regions.
The required accuracies for applications based on GNSS signals range from tens of nanoseconds for timing applications and a few metres for standard position and navigation solutions to centimetre- and millimetre-level accuracy in precise positioning applications.

1.1 Background and Motivation

In the last decade, the satellite navigation system environment has changed from GPS-only dual-frequency to multi-GNSS multi-frequency and multi-signal, enabled by the satellite navigation systems existing today and their use of different carrier signal frequencies with a variety of signal modulations.
Despite this environmental change, most of the operational and precise GNSS processing strategies rely only on dual-frequency measurements and therefore do not benefit from the available multi-signal environment. When dealing with only dual-frequency GNSS observables, signal hardware delays play a subordinate role and are usually not considered since estimated and applied clock offsets are specific to the commonly-used dual-frequency ionosphere-free (IF) linear combination (LC) as described in section 5.1. While the first order effect of the ionospheric delay can almost entirely be eliminated, the formation of IF linear combinations amplifies the noise of the resulting observations and leads to a loss of some of the physical characteristics of the original signals, like the integer nature of the carrier phase ambiguity. The conventional dual-frequency IF LC processing approach does not provide the flexibility to make use of multiple signals as the number of usable signals is limited by definition.
In order to benefit from the multi-GNSS and multi-signal environment, the raw observation processing approach (Schönemann et al., 2011; Schönemann, 2014), also referred to as Raw Method (RAW), is applied in this work. This processing strategy, described in section 5.2, makes use of the original (raw) observations without forming any linear combinations or differences of GNSS observables and provides the flexibility to process all or a selection of available multi-GNSS and multi-signal raw observations. The renunciation of linear combinations and observation differences implies that signal biases and ionospheric delays remain in the observation equation and need to be properly handled. In the raw observation processing approach there is no inherent limitation on the number of usable signals and the use of the original (raw) observations preserves the physical signal characteristics and allows to analyse them. As the original noise characteristics of the individual signals are maintained, this approach allows to benefit from the low code noise of modern GNSS signals.
The focus of the work presented in this thesis are scientific analyses and precise applications based on the joint processing of multi-GNSS and multi-signal raw observations. The GNSS raw observation equations have been refined to describe a rigorous handling of all involved points in time and define all components of the observation equation with proper time arguments, which is often missing in the literature.
Whereas previous works performed in the field of GNSS raw observation processing (Schönemann, 2014; Strasser et al., 2018) were limited in the number of available GNSS or signals, or did not make use of all available signals, the raw observation processing approach described in this work is used to jointly process measurements from up to three different GNSS, including eleven signals tracked on up to eight different carrier frequencies, in one single adjustment.
In the context of multi-GNSS and multi-signal bias handling, a rigorous analysis of what is referred to as physically meaningful code biases is performed to demonstrate the benefits of handling clock offset parameters, signal code biases and ionospheric delay estimates in a physically meaningful and consistent way. The negative impact of removing correct physical characteristics from signal code biases, as it is commonly done in the generation of conventional code bias products, is demonstrated and discussed. In addition, the conventional handling of so called Inter-System Bias (ISB) is described and issues with this approach are presented and discussed.
While most commonly used carrier phase IAR approaches, as described in section 5.1.3, are based on the formation of dual-frequency IF and Melbourne-Wuebbena (MW) linear combinations as well as GNSS observation differences

(Hofmann-Wellenhof et al., 1992; Wübbena, 1989), the IAR approach developed and implemented in the course of this work is based on the joint processing of multi-GNSS and multi-signal raw observations without forming any linear combinations or observation differences.
In order to demonstrate the performance of the implemented IAR approach based on raw observations, the approach has been applied to the joint determination of precise satellite orbits for up to 72 satellites from three GNSS for a variety of different scenarios. In addition, the results of these analyses have been used to investigate characteristics of multi-frequency phase biases based on raw observation ambiguity estimates for signals of different GNSS.

1.2 Objectives of this work

The aim of this work is to apply and further develop the raw observation processing approach by analysing several fundamental issues in the context of multi-GNSS and multi-signal processing. A refined and detailed description of the GNSS code and phase raw observation equations has been developed to describe a rigorous handling of all involved points in time. The handling of signal biases for multi-GNSS and multi-signal raw observation processing is analysed to motivate the use of physically meaningful signal code biases for different applications. A carrier phase integer ambiguity resolution approach based on raw observation processing has been developed and implemented, making use of all available multi-GNSS and multi-signal raw observations in a single global network adjustment without forming any linear combinations or observation differences. The successful implementation of the integer ambiguity resolution approach is demonstrated by its application to the problem of multi-GNSS satellite precise orbit determination.

The main objectives of this work can be summarised as follows:

- Analyses of signal bias handling in multi-GNSS and multi-signal raw observation processing
- Development and implementation of a carrier phase integer ambiguity resolution approach based on multi-GNSS and multi-signal raw observation processing
- Demonstration of successful integer ambiguity resolution by the precise orbit determination of multi-GNSS satellites

1.3 Outline

Section 2 gives a short overview of available GNSS, their signal structure and the fundamental GNSS receiver measurements. Important coordinate and time reference systems are summarised in section 3.
The GNSS raw observation models introduced in section 4 have been refined to describe a rigorous handling of all involved points in time and define all components of the observation equation with proper time arguments, which is often missing in the literature. The handling of GNSS signal delays is described and applied corrections are specified. In addition, a summary of linear combinations of GNSS observables describes the commonly applied observation models used in conventional state-of-the-art GNSS processing and carrier phase integer ambiguity resolution approaches.
The description of conventional GNSS processing methods in section 5 is followed by the introduction of the multi-GNSS and multi-signal raw observation processing approach applied in this work. The section is closed out by a description of the fundamentals of the applied linearised iterative weighted batch least squares adjustment with soft constraints.
Section 6 describes the developed and implemented carrier phase integer ambiguity resolution approach based on multi-GNSS and multi-signal raw observations in detail.
Analyses performed in the course of this work related to a physically meaningful handling of multi-GNSS and multi-signal raw observation code biases, code bias calibrations, single receiver absolute ionospheric delay estimation and inter-system time offset determination are shown in section 7. In addition, the carrier phase integer ambiguity resolution approach based on multi-GNSS and multi-signal raw observations is applied to the problem of multi-GNSS satellite precise orbit determination and raw observation phase biases are analysed.
The achieved results are summarised and concluded in section 8 and a description of remaining issues with respect to the analysed field of research and an outlook on future work is given in section 9.

2 Global Navigation Satellite Systems

2.1 Operational Principles

The basic principle of positioning with GNSS is based on the concept of trilateration. The location of a user is determined by the measurement of distances to multiple GNSS satellites in combination with the known positions of these satellites. The basic distance measurement is the time required for a signal to propagate from a GNSS satellite to the user receiver. Section 2.4.2 describes the fundamentals of different distance measurements performed by a GNSS receiver and specifies how the signal propagation time of different measurements can be modelled.
Before describing the details of GNSS receiver measurements, an overview of the general GNSS architecture and different existing systems is given, followed by a description of the GNSS signal structure.

2.1.1 GNSS Architecture

All GNSS consist of three different segments, namely the ground segment, space segment and user segment. While the user segment is mostly shared among different GNSS, each system has its own dedicated ground and space segment.

The **ground or control segment** usually consists of two (master and backup) control centres, a network of globally distributed Telemetry, Tracking and Command (TT&C) stations for spacecraft and payload control and monitoring, globally distributed sensor stations to monitor the navigation signals sent by the GNSS satellites and globally distributed uplink stations to distribute navigation information to the GNSS satellites. The ground segment also defines the GNSS system time scale, computes the navigation information prior to uplink and prepares official notifications about the system status.

The **space segment** consists of the GNSS satellites orbiting the Earth. The satellites transmit electromagnetic waves modulated with navigation information on different carrier frequencies, called GNSS signals to the users. The number of satellites and their orbital parameters differ for each GNSS, as described in section 2.2.

The **user segment** consists of all receivers which measure the GNSS signals and use them for Positioning Navigation Timing (PNT) applications. There is a wide range of supported timing and positioning applications for different types of dynamics like cars, ships, trains and aircrafts, as well as orbit determination of LEO and beyond LEO satellites in the so called SSV.

2.2 Overview of Existing GNSS

As the satellite types and orbital parameters differ for each GNSS, this section provides a short overview of the space segments of the four existing GNSS. Throughout this work the symbol Σ is used to refer to a generic GNSS, whereas the following uppercase letter are used to refer to a specific system: G for GPS, E for Galileo, C for BeiDou and R for GLONASS.

2.2.1 GPS

The GPS space segment nominally consists of 24 (usually around 30) Medium Earth Orbit (MEO) satellites, orbiting the Earth with an orbital period of 11 hours 58 minutes and 42 seconds (half a sidereal day) at a nominal altitude of 20200 km (U.S. Government, 2019). The satellites are arranged in six equally spaced orbital planes around the Earth with an inclination of 55 deg. The current GPS space segment consists of 31 operational satellites from four different generations (1 Block IIA, 11 Block IIR, 7 Block IIR-M and 12 Block IIF) (U.S. Government, 2019).

GPS employs Code Division Multiple Access (CDMA) to distinguish between satellites and therefore navigation signals are sent on the identical three nominal carrier frequencies: L1 (1575.42 MHz), L2 (1227.6 MHz) and L5 (1176.45 Mhz).

2.2.2 Galileo

The nominal Galileo space segment consists of 30 MEO satellites (including 6 spares) orbiting the Earth with an orbital period of 14 hours 4 minutes and 41 seconds at a nominal altitude of 23222 km (GSA, European GNSS Agency, 2019b). The satellites are arranged in three equally spaced orbital planes around the Earth with an inclination of 56 deg in a so called Walker 24/3/1 constellation. The current Galileo space segment consists of 22 operational satellites from two different satellite types (3 In-Orbit Validation (IOV) satellites and 19 Full Operational Capability (FOC) satellites (GSA,

European GNSS Agency, 2019b).

Galileo employs CDMA and satellites transmit navigation signals on the identical four nominal carrier frequencies: E1 (1575.42 MHz), E5a (1176.45 MHz), E5b (1207.14 MHz) and E6 (1278.75 MHz). The signals on frequencies E5a and E5b are combined by the so called Alternative Binary Offset Carrier (BOC) (AltBOC) modulation, generating a wideband signal with the effective carrier frequency: E5 (1191.795 MHz)

2.2.3 Beidou

The BeiDou space segment nominally consists of 27 MEO, 3 Inclined GeoSynchronous Orbit (IGSO) and 5 Geostationary Orbit (GEO) satellites. The MEO satellites are arranged in three equally spaced orbital planes around the Earth with an inclination of 55 deg and orbit the Earth with an orbital period of 12 hours 53 minutes and 14 seconds at a nominal altitude of 21528 km (Roskosmos, 2019b). The GEO satellites at an altitude of 35786 km are positioned at longitudes in the range between 58 deg and 160 deg East. The IGSO satellites orbit the Earth at an altitude of 35786 km and an inclination of 55 deg.
The current BeiDou space segment consists of 33 operational satellites from two different satellite types (15 BeiDou-2 and 18 BeiDou-3) in three different orbits (5 GEO, 7 IGSO and 21 MEO) (Roskosmos, 2019a). It should be noted that for the analyses shown in this work BeiDou GEO satellites were not used.

BeiDou employs CDMA and satellites transmit navigation signals on the identical three nominal carrier frequencies: B1I (1561.098 MHz), B2I (1207.14 MHz) and B3I (1268.52 Mhz). To support interoperability with other GNSS, the BeiDou-3 MEO and IGSO satellites also transmit the B1C signal on carrier frequency 1575.42 MHz (BeiDou OS B1C SIS ICD, 2017) and the B2a signal on carrier frequency 1176.45 MHz (BeiDou OS B2a SIS ICD, 2017).

2.2.4 GLONASS

The nominal GLONASS space segment consists of 24 MEO satellites orbiting the Earth with an orbital period of 11 hours 14 minutes and 32 seconds at a nominal altitude of 19100 km (Roskosmos, 2019d). The satellites are arranged in three equally spaced orbital planes around the Earth with an inclination of 64.8 deg. The current GLONASS space segment consists of 22 operational satellites (Roskosmos, 2019c).

GLONASS mainly employs Frequency Division Multiple Access (FDMA) to distinguish between satellites and therefore each satellite transmits navigation signals on a slightly different frequency. The two nominal carrier centre frequencies for the FDMA signals are: L1 (1602.00 MHz) and L2 (1246.00 MHz). The carrier frequency for the CDMA signal, transmitted by the newer GLONASS satellites is: L3 (1202 Mhz) (Roskosmos, 2019d).

An overview of the GNSS signal frequencies used in this work is given in Figure 2.1.

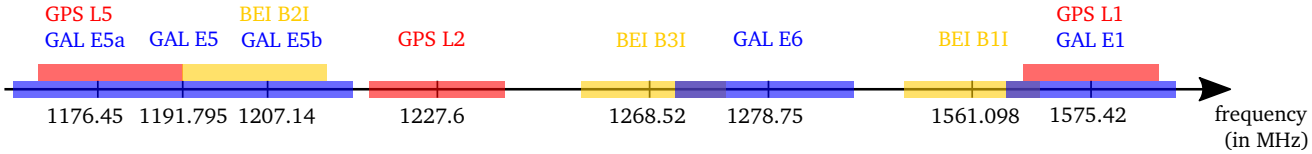

Figure 2.1: Overview of GNSS signal frequencies used in this work with schematically indicated signal bandwidths.

2.3 GNSS Signals

GNSS signals are generated on-board the GNSS satellites and are based on the frequency output and time signal of the on-board atomic clock, inherent to every GNSS satellite. The time signal usually is referred to as satellite time scale or satellite clock. The atomic clock provides the nominal frequency used to generate the different carrier frequencies of the GNSS signals and the satellite time signal used to modulate the carrier wave to enable measurements of the satellite time at the receiver and to transmit information to the user.

Signals sent by the GNSS satellites therefore not only differ in carrier frequency, but also in how the navigation information is modulated onto the carrier wave and which information is provided to the user. In order to identify GNSS signals, a three character ID is used throughout this work, indicating the corresponding GNSS (Σ), the carrier frequency index (i) and the signal identifier (a). The frequency index and signal identifier used in this work are in line with the definition

in the Receiver Independent Exchange (RINEX) format. A generic GNSS satellite signal is written Σia, with the example of a GPS C/A signal on carrier frequency L1 (G1C) or a Galileo signal on carrier frequency E5a without navigation data (E5Q). Table 2.1 describes the mapping of the Galileo, GPS and BeiDou satellite signals introduced in section 2.2 to the three character ID of the GNSS observations used in this work.

Table 2.1: Mapping of Galileo, GPS and BeiDou satellite signals to the three-character ID used in this work.

GNSS	Frequency (in MHz)		Signal Component	3-char. ID
Galileo	E1	1575.42	no data	E1C
	E5a	1176.45	no data	E5Q
	E5b	1207.14	no data	E7Q
	E5	1191.795	Q	E8Q
	E6	1278.75	no data	E6C
GPS	L1	1575.42	C/A	G1C
	L2	1227.6	P(Y)	G2W
	L5	1176.45	Q	G5Q
BeiDou	B1I	1561.098	I	C2I
	B2I	1207.14	I	C7I
	B3I	1268.52	I	C6I

2.3.1 Signal Structure and Modulation

In order to enable the basic distance measurement required for positioning with GNSS, the carrier wave of a GNSS signal is modulated with a so called Pseudo Random Noise (PRN) code. This characteristic sequence of zeros and ones facilitates the measurement of the signal generation time on-board the GNSS satellite, as described in detail in section 2.4.2.

The navigation information contained in the so called navigation message are modulated onto the GNSS signal carrier wave in addition to the PRN code, as illustrated in Figure 2.2. The navigation message mainly contains information about the position and time of the GNSS satellites, required for positioning based on the concept of trilateration.

Various signal modulation schemes are applied by the different GNSS and they have become more complex for newer generation of GNSS satellites and signals in the last decade. GNSS signal modulation schemes are ranging from simple Binary Phase Shift Keying (BPSK) modulation used in the GPS L1 C/A signal via different versions of BOC modulations like Composite BOC (CBOC) and Multiplexed BOC (MBOC) to advanced wideband signal modulations like AltBOC, used for the generation of the Galileo E5 signal.

Detailed information on the different GNSS signal structures and modulation schemes can be found at (European Space Agency, 2019).

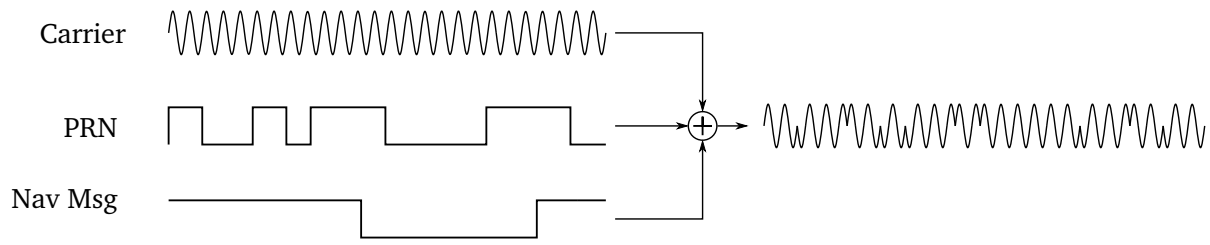

Figure 2.2: Signal structure of a GNSS signal carrier wave modulated with PRN code and navigation message.

2.4 GNSS Receiver

GNSS receivers are the user interface to GNSS services and enable the determination of Position Velocity Time (PVT) solutions. However, with a receiver alone, no measurements of the GNSS signals can be performed.

2.4.1 Receiver System Components

A GNSS receiver system is composed of the receiver itself and a receiving antenna, connected via a Radio Frequency (RF) cable. The antenna acts as physical interface between the electromagnetic waves sent by the GNSS satellites and the RF signals processed by the receiver. A GNSS receiver acquires and tracks the satellite signals, performs the distance measurements, demodulates the navigation message from the received signal and computes the navigation PVT solution. GNSS receivers perform measurements based on their own internal or externally provided time signal, referred to as receiver time scale or receiver clock. GNSS measurements are therefore time tagged with the measurement time given in the receiver time scale.

2.4.2 GNSS Measurements

The natural distance measurements of a GNSS receiver used for positioning are the replica signal code phase and replica carrier signal phase relative to the received satellite signal, as described in (Kaplan and Hegarty, 2017). A receiver also measures the carrier signal Doppler shift and Signal-to-Noise Ratio (SNR), these measurements however, are only mentioned for completeness and are not directly used for applications described in this work. An analysis of the received signal strength for multiple GNSS and signals is shown in section 7 to demonstrate the existence of GNSS signal interference for certain frequency bands, which is directly visible in the SNR measurements. The receiver signal acquisition and tracking Phase Lock Loop (PLL) continuously adjust the frequency of the replica signal generated by a GNSS receiver to the received satellite signal frequency. The code phase is measured by aligning the PRN code of the receiver generated replica signal with the received satellite signal, which is handled by the so called Delay Lock Loop (DLL). The code phase ambiguity of the PRN code length (1 ms ≈ 300 km for the GPS L1 C/A signal and 4 ms ≈ 1200 km for the Galileo E1 Open Service (OS) signal) is then solved by exploiting the navigation message structure.
The measured replica signal code phase can be used to determine the signal *time of generation* t^{tog} in the satellite time scale τ^s, measured at the *time of measurement* t_{tom} in the receiver time scale τ_r to form the so called pseudorange measurement in units of length, depicted in Figure 2.3

$$P_r^s(t_{tom}) = c \cdot \left[\tau_r(t_{tom}) - \tau^s(t^{tog})\right] + e_r^s(t_{tom}) \,, \tag{2.1}$$

with the pseudorange measurement noise $e_r^s(t_{tom})$, which is assumed to be a zero-mean random variable.

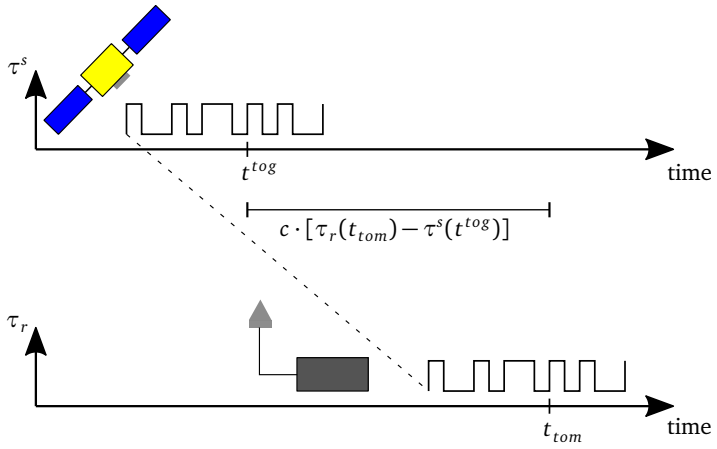

Figure 2.3: GNSS code phase (pseudorange) measurement, derived from the signal generation time in the satellite time scale $\tau^s(t^{tog})$ and the measurement time in the receiver time scale $\tau_r(t_{tom})$.

The measured replica carrier signal phase is used to generate a continuous cumulative carrier signal phase measurement in cycles

$$\phi_r^s(t_{tom}) = \Delta\phi_r^s(t_{tom}) + n_r^s(t_{tom}, t_{init}) + \eta_r^s(t_{tom}) \,, \tag{2.2}$$

where $\Delta\phi_r^s(t_{tom}) \in [0, 1)$ is the fractional phase measurement, $n_r^s(t_{tom}, t_{init})$ is the full cycle count of the measured replica carrier signal phase since initial signal acquisition at t_{init} and $\eta_r^s(t_{tom})$ is the carrier phase measurement noise, which is assumed to be a zero-mean random variable.
With the unknown number of carrier phase cycles at initial signal acquisition, the so called integer ambiguity N_r^s, the carrier phase measurement can be recognised as precise measure of the carrier phase pseudorange, depicted in Figure 2.4.

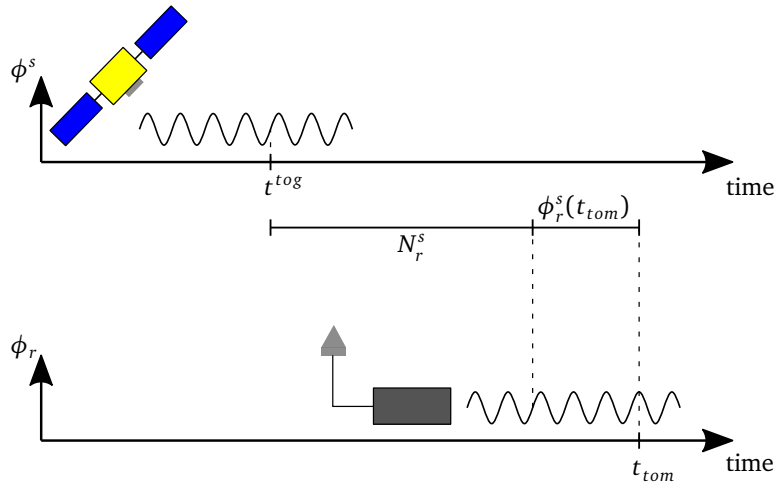

Figure 2.4: GNSS carrier phase measurement $\phi_r^s(t_{tom})$ of fractional and full cycles, recognised as precise measure of the carrier phase pseudorange by adding the unknown integer ambiguity term N_r^s.

3 Reference Systems

The determination of positions and time with GNSS and any other positioning or timing concept requires the definition of coordinate and time reference systems. The use of consistent reference systems is essential to compute accurate positions and time. A coordinate reference system is defined by a set of prescriptions, conventions and required models to define a triad of axes at any point in time (IERS, 2019a). The realisation of a coordinate reference system in the form of coordinates (and velocities) is referred to as coordinate reference frame. For time reference systems one could use a similar definition, however, it is uncommon to distinguish in the same way between reference time systems and reference time frames. Therefore, reference time systems are referred to as time scales in the course of this work. The following sections describe the relevant coordinate reference systems and time scales used in GNSS processing.

3.1 Coordinate Systems

A reference system co-rotating with the Earth, referred to as terrestrial reference system, is most suitable to express user coordinates on Earth, whereas it is convenient to describe positions and velocities of satellites in a non-rotating inertial reference system, referred to as celestial reference system. The relation between these two systems and the transformation of positions given in the corresponding reference frames is based on the so called Earth Orientation Parameters (EOP).

3.1.1 International Terrestrial Reference System

The International Terrestrial Reference System (ITRS) is a specific terrestrial reference system defined and provided by the International Earth Rotation and Reference Systems Service (IERS) with its origin located at the centre of mass of the whole Earth, including oceans and atmosphere (Petit and Luzum, 2010). The orientation of the geocentric ITRS is equatorial with its z-axis pointing towards the IERS Reference Pole (IRP). The direction of the x-axis is defined by the intersection point of the Earth's equator and the IERS Reference Meridian (IRM) and the y-axis completes the right-handed orthogonal system. The ITRS therefore is co-rotating with the Earth. The orientation was initially given by the Bureau International de l'Heure (BIH) orientation at epoch 1984.0 and the time evolution of the orientation is ensured by using a no-net-rotation condition with regards to horizontal tectonic motions over the whole Earth (Petit and Luzum, 2010). The unit of length is the International System of Units (SI) metre.

The ITRS is realised by the International Terrestrial Reference Frame (ITRF) which consists of a set of coordinates and velocities for a selected number of IERS tracking stations covering the whole Earth. The coordinates and velocities are determined from observations of the four main space geodesy techniques: GNSS, Very Long Baseline Interferometry (VLBI), Satellite Laser Ranging (SLR) and Doppler Orbitography and Radiopositioning Integrated by Satellite (DORIS). The set of coordinates and velocities defining the ITRF is updated on a regular basis and published by the IERS at (IERS, 2019b).

3.1.2 Celestial Reference Systems

The International Celestial Reference System (ICRS) is the celestial reference system defined and provided by the IERS with its origin located at the barycentre of our solar system (Petit and Luzum, 2010). It is a non-rotating inertial coordinate system, thus the directions of its axes are fixed with respect to the ensemble of distant extragalactic radio sources observed by VLBI. Its principal plane is defined to coincide as closely as possible with the mean equator at J2000.0 and the origin of right ascension is defined to coincide as closely as possible with the dynamical equinox at J2000.0 (from Petit and Luzum, 2010).

The ICRS is realised by the International Celestial Reference Frame (ICRF) which consists of a set of equatorial coordinates for extragalactic radio sources, estimated based on VLBI observations. The set of coordinates defining the ICRF is updated on a regular basis and published by the IERS at (IERS, 2019a).

The Geocentric Celestial Reference System (GCRS) is a specific celestial reference system used to describe the motion of satellites orbiting Earth. It is oriented in the same way as the ICRS, but its origin is shifted from the barycentre of our solar system to the centre of the Earth. Hence, the GCRS is a geocentric non-rotating quasi-inertial reference system, as the origin performs an accelerated motion.

3.1.3 Earth Orientation Parameters

The IERS Earth Orientation Parameters (EOP) describe the irregularities of the rotation of the Earth and provide the rotation of the ITRS to the ICRS as a function of time (from IERS, 2019c). The five EOPs measured by space geodetic techniques and provided by the IERS are (IERS, 2019c)

- $d\psi$, $d\epsilon$: The celestial pole offsets, defined as observed residual corrections to the conventional pole position defined by the International Astronomical Union (IAU) precession and nutation models
- UT1-UTC (described in section 3.2), also called Length Of Day (LOD): The excess revolution time of the Earth relative to 86400 SI seconds describes the variation in the rotation rate of the Earth
- x_p, y_p: The terrestrial coordinates of the Celestial Intermediate Pole (CIP) in the ITRS, ie. relative to the IRP, also referred to as polar motion

As the GCRS is oriented the same way as the ICRS, EOPs can be used to transform coordinates from the rotating ITRS to the GCRS. According to Petit and Luzum (2010), the transformation of a position vector $\boldsymbol{X}(t)$ from ITRS to GCRS at time t can be written as

$$\boldsymbol{X}_{GCRS}(t) = \boldsymbol{Q}(t)\,\boldsymbol{R}(t)\,\boldsymbol{W}(t)\,\boldsymbol{X}_{ITRS}(t)\,, \tag{3.1}$$

where $\boldsymbol{Q}(t)$, $\boldsymbol{R}(t)$ and $\boldsymbol{W}(t)$ are the transformation matrices for the celestial motion of the CIP in the GCRS due to precession and nutation including celestial pole offsets, the rotation of the Earth around the axis of the CIP including LOD and the polar motion respectively. The detailed procedure and algorithms for the ITRS to GCRS transformation are given in (Petit and Luzum, 2010).

3.2 Time Scales

The basic distance measurement required for positioning with GNSS practically is a measurement of different points in time. As described in section 2.4.2, these time measurements are realised on different time scales, which are not synchronised. The following section therefore provides an overview of the most important time scales used in GNSS signal processing.

3.2.1 International Atomic Time

International Atomic Time (TAI) is a uniform and stable time scale calculated at the International Bureau of Weights and Measures (BIPM) from atomic clocks in over eighty national laboratories (BIPM, Bureau International des Poids et Mesures, 2019b). The unit of TAI is the SI second and TAI therefore does not follow the irregular rotation of the Earth. For practical purposes however, it is convenient to use time scales which are linked to the actual rotation of the Earth.

3.2.2 Universal Time

Universal Time (UT1) is defined as the mean solar time at 0 deg longitude and therefore directly follows the rotation of the Earth. As the Earth rotation rate varies, UT1 is neither uniform nor stable. For practical purposes however, time scales should be based on a constant progress of time.

3.2.3 Coordinated Universal Time

Coordinated Universal Time (UTC) combines the definitions of TAI and UT1 and serves as the global reference time scale. The unit of UTC is the SI second, however, from time to time a leap second is added to ensure that UTC follows UT1 within 0.9 s. UTC therefore is a uniform and stepwise stable time scale. The insertion of UTC leap seconds is decided by the IERS.

3.2.4 GNSS System Time

Each GNSS maintains its own system time scale, which is broadcast via the navigation satellites to the users to enable PNT applications. However, each GNSS has its own definition of "time" and provides different levels of timing accuracy with respect to UTC.

GPS Time (GPST) is a continuous time scale (ie. no leap seconds applied) established by the GPS control segment and referenced to the physical UTC realisation at the U.S. Naval Observatory UTC(USNO) (IS-GPS-200, 2015). The GPST start epoch is midnight UTC in the night from January 5 to 6, 1980 with a difference TAI-UTC = 19 s. Hence the offset between GPST and UTC is defined by GPS-UTC = $n_{\text{leap}} - 19$ with the number of UTC leap seconds n_{leap}. GPST shall be synchronized to be within 1 μs of UTC (modulo one second) (IS-GPS-200, 2015).

Galileo System Time (GST) is a continuous time scale (ie. no leap seconds applied) established by the Galileo control segment from a selection of European timing laboratories (Stehlin et al., 2006). The GST start epoch is 23:59:47 UTC on 21 August 1999 with a difference TAI-UTC = 32 s (Galileo OS SIS ICD, 2016). As GST is defined to start 13 seconds before midnight UTC, the offset between GST and UTC is given (as for GPST) by GST-UTC = $n_{\text{leap}} - 19$. This definition supports the Galileo-GPS interoperability, as no integer second offset exists between GST and GPST. GST shall be steered to be within 50 ns of UTC (modulo one second) (Teunissen and Montenbruck, 2017). Detailed information on the physical generation of GST are given in (Stehlin et al., 2006).

BeiDou Time (BDT) is a continuous time scale (ie. no leap seconds applied) referenced to the physical UTC realisation at the National Time Service Center UTC(NTSC) (BeiDou OS B1I SIS ICD, 2019). The BDT start epoch is 00:00:00 UTC on 1 January 2006 with a difference TAI-UTC = 33 s. Hence the offset between BDT and UTC is defined by BDT-UTC = $n_{\text{leap}} - 33$. BDT shall be synchronised to be within 50 ns of UTC (modulo one second) (BeiDou OS B1I SIS ICD, 2019).

GLONASS Time (GLOT) is a discontinuous time scale with leap seconds applied as for UTC, generated by the GLONASS Central Synchronizer and referenced to the Russian national time realisation UTC(SU) plus a constant three hour offset (GLONASS ICD, 2008). GLOT therefore directly relates to UTC, which is why GLONASS satellites do not transmit any information on UTC leap seconds in their navigation messages. GLOT shall be synchronized to be within 1 μs of UTC(SU) plus three hours (GLONASS ICD, 2008).

Figure 3.1 shows the relationship between TAI, UT1, UTC and the different GNSS system times.

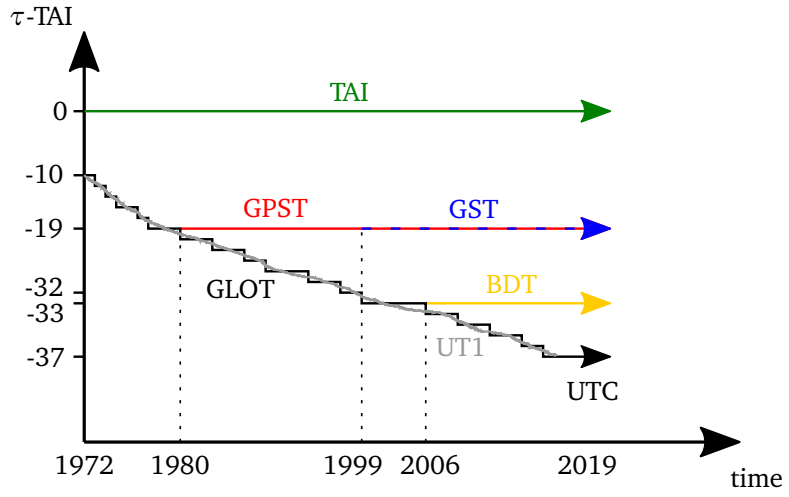

Figure 3.1: Relationship between TAI, UT1, UTC and GNSS system times (adopted from Ley et al., 2019).

3.2.5 Clock Offsets, Epochs and Points in Time

The proper handling of different time scales and clock offsets is essential whenever dealing with GNSS and especially important for multi-GNSS applications. The general definition and nomenclature of clock offsets, epochs and arbitrary points in time used in this work is therefore introduced.

An arbitrary point in time shall be defined by t, which can be expressed in different time scales τ_i. The clock reading $\tau_i(t)$ at time t on the clock which defines the time scale τ_i will be referred to as an Epoch in time scale τ_i. If one point in time is expressed in different time scales $\tau_i(t)$ and $\tau_j(t)$ it still refers to the exact same point in time. However, as long as the two time scales (their respective clocks) are not synchronised, the clock readings at this point in time will be different and their difference defines the clock offset between the two time scales (their respective clocks): $dt_{i,j}(t) = \tau_i(t) - \tau_j(t)$. Two independent clocks show the same clock reading (Epoch) at different points in time $\tau_i(t) = \tau_j(t + dt_j)$. It is assumed, that the time offset dt_j applied at one clock to show the same clock reading as another clock at a different time and the clock offset between two time scales at the same point in time $dt_{i,j}(t)$ are identical $dt_{i,j}(t) = dt_j$.

The value of a time varying quantity measured at a certain point in time $P_{meas}(\tau_i(t)) = P_{meas}(\tau_j(t)) = P_{meas}(t)$ is invariant to a change in the time scale, whereas the Epoch at which the quantity was measured differs for every time scale. However, in practice the measurement time is always driven by a certain time scale and therefore is performed at a certain Epoch $\tau_i(t)$. If the same measurement is triggered twice, at the same Epoch but from two different unsynchronised clocks (time scales), the measurement values of the time varying quantity will be different. In fact, the measurement was taken at the same Epoch, but at different points in time $P_{meas}(\tau_i(t)) \neq P_{meas}(\tau_j(t + dt_j))$.

This principle can be transferred to taking measurements and processing observations in GNSS applications. Whereas GNSS measurements are taken at a certain epoch, triggered by the GNSS receiver clock time scale τ_r, observations might be processed at the same epoch, but in a reference time scale τ_Ξ, see 4.1.4.

For GNSS positioning applications this reference time scale is realised and provided to the user in form of the so called navigation satellite clock offsets. As described above, a clock offset is the difference between two clock readings from independent time scales at a certain point in time. For GNSS applications, both the navigation satellite clock offset $dt^s_\Xi = \tau^s(t) - \tau_\Xi(t)$ and the receiver clock offset $dt_{r,\Xi} = \tau_r(t) - \tau_\Xi(t)$ need to be considered. In Figure 3.2 the general relationship of independent time scales τ_r and τ_Ξ and the offset between them is shown.

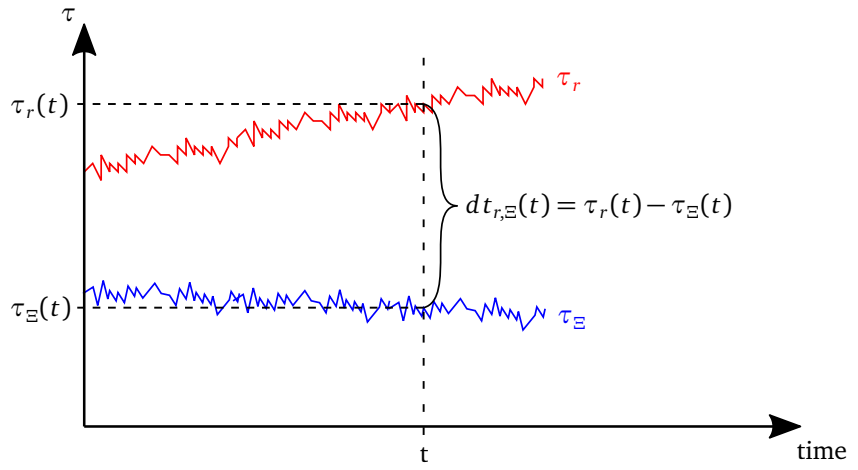

Figure 3.2: Schematic representation of the relationship between GNSS receiver clock time scale τ_r, reference time scale τ_Ξ and the receiver clock offset $dt_{r,\Xi}$.

4 GNSS Observation Model

The GNSS measurements introduced in section 2.4.2 form the set of observables, available to a GNSS receiver to estimate geodetic parameters like station coordinates, satellite orbits and time. The pseudorange and carrier phase observables for each individual signal are modelled by the so called raw observation equations, indicating that these equations describe the uncombined raw observable per signal measured by the GNSS receiver.

4.1 GNSS Raw Observables

The basic GNSS observable is the travel time T_r^s of the signal to propagate from a navigation satellite s to a receiver r. The apparent range or pseudorange between satellite and receiver is the signal travel time multiplied by the speed of light $P_r^s = c \cdot T_r^s$. It is called pseudorange, since GNSS observables are affected by numerous effects, described in the following section, which prevent the direct measurement of the correct geometric distance between satellite and receiver. There are many publications and textbooks on modelling GNSS observables (Hofmann-Wellenhof et al., 1992; Kleusberg and Teunissen, 1998; Kaplan and Hegarty, 2017) with different depth of detail. The observation equations derived in this work are based on (Teunissen and Kleusberg, 1998), however, they have been refined to describe a rigorous handling of all involved points in time. This allows to define all components of the observation equation with proper time arguments and discuss necessary assumptions, which usually are missing or not sufficiently explained in the literature.
The measurements are triggered by the receiver clock and therefore are taken at the *time of measurement* t_{tom} in the receiver clock time scale τ_r, called the measurement epoch $\tau_r(t_{tom})$. The concept of time scales and epochs has been introduced in section 3.2. It is assumed, that GNSS receivers take a set of measurements at the same epoch (Kaplan and Hegarty, 2017), resulting in a measurement epoch independent of tracked satellites and signals. On the satellite side, all signals originate from the same on-board oscillator and are realisations of the same satellite clock. Without loss of generality it can therefore be assumed that the signal *time of generation* t^{tog} in the satellite clock time scale τ^s is identical for all signals.

4.1.1 Pseudorange Observation Equation

The pseudorange measurement between receiver r and navigation satellite s is given by the difference of the time of measurement t_{tom}, given by the measurement epoch in the receiver time scale $\tau_r(t_{tom})$ and the time of signal generation t^{tog}, given by the generation epoch in the navigation satellite time scale $\tau^s(t^{tog})$

$$P_r^s(t_{tom}) = c \cdot \left[\tau_r(t_{tom}) - \tau^s(t^{tog})\right] + e_r^s(t_{tom})\,, \tag{4.1}$$

where c is the speed of light in vacuum and $e_r^s(t_{tom})$ the pseudorange measurement noise, which is assumed to be a zero-mean random variable. It should be emphasised, that in order to consistently describe all involved points in time, the time arguments used in (4.1) are the time of signal *generation* and *measurement*, instead of the time of signal *transmission* and *reception*, as usually found in the literature (cf. Teunissen and Kleusberg, 1998). The signal dependent transmission and reception time arguments are introduced in (4.4) and Figure 4.1 shows the relation between the four time arguments.
Expanding the pseudorange equation (4.1) by the receiver measurement time and the signal generation time both given in an independent reference time scale τ_Ξ and rearranging the terms gives

$$\begin{aligned} P_r^s(t_{tom}) &= c \cdot [\tau_r(t_{tom}) + \tau_\Xi(t_{tom}) - \tau_\Xi(t_{tom}) - \tau^s(t^{tog}) + \tau_\Xi(t^{tog}) - \tau_\Xi(t^{tog})] + e_r^s(t_{tom}) \\ &= c \cdot [\tau_\Xi(t_{tom}) - \tau_\Xi(t^{tog}) + dt_{r,\Xi}(t_{tom}) - dt^s_{\Xi,rel}(t^{tog})] + e_r^s(t_{tom}) \\ &= c \cdot T_r^s + c \cdot [dt_{r,\Xi}(t_{tom}) - dt^s_{\Xi,rel}(t^{tog})] + e_r^s(t_{tom}) \end{aligned} \tag{4.2}$$

where

$T_r^s = \tau_\Xi(t_{tom}) - \tau_\Xi(t^{tog})$ is the total signal travel time, between the moment of signal generation on-board the navigation satellite and the moment the signal is measured in the receiver, determined in a common reference time scale τ_Ξ

$dt_{r,\Xi}(t_{tom}) = \tau_r(t_{tom}) - \tau_\Xi(t_{tom})$ is the receiver clock offset from the reference time scale at the time of measurement

$dt^s_{\Xi,rel}(t^{tog}) = \tau^s(t^{tog}) - \tau_\Xi(t^{tog})$ is the satellite clock offset from the reference time scale at the time of signal generation including relativistic effects

The satellite on-board clock is affected by periodic relativistic effects due to the eccentricity of the noncircular satellite orbits, namely time dilation and frequency shifts due to Earth's gravitational potential, described in the theory of relativity by Albert Einstein. These effects can be modelled analytically as described in section 4.1.4 and are therefore separated from the satellite clock offset $dt^s_\Xi(t^{tog})$ by subtracting the periodic relativistic correction term $\delta_{rel}(t^{tog})$

$$dt^s_{\Xi,rel}(t^{tog}) = dt^s_\Xi(t^{tog}) - \delta_{rel}(t^{tog}) \tag{4.3}$$

The total signal travel time T^s_r not only depends on the receiver and satellite but also on the signal itself. As introduced in section 2.3, a navigation satellite signal Σia is defined by the system Σ, frequency index i and signal identifier a. The total signal travel time $T^s_{r,\Sigma ia}$ can be split into three parts

$$T^s_{r,\Sigma ia} = d^s_{ia} + \Delta T^s_{r,\Sigma ia} + d_{r,\Sigma ia} \tag{4.4}$$

where

$d^s_{ia} = t^{tot}_{ia} - t^{tog}$ is the (code) delay between the time of signal generation t^{tog} and transmission t^{tot}_{ia} on-board the navigation satellite

$\Delta T^s_{r,\Sigma ia} = t_{tor,\Sigma ia} - t^{tot}_{ia}$ is the free space travel time of signal Σia from the time of transmission t^{tot}_{ia} at the navigation satellite antenna to the time of reception $t_{tor,\Sigma ia}$ at the receiver antenna

$d_{r,\Sigma ia} = t_{tom} - t_{tor,\Sigma ia}$ is the (code) delay between the time of signal reception $t_{tor,\Sigma ia}$ and time of measurement t_{tom} at the receiver

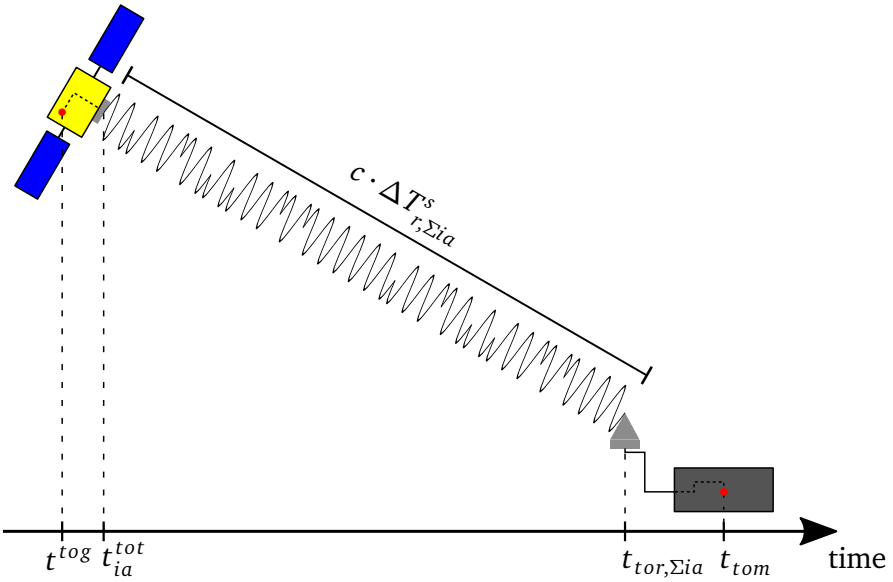

Figure 4.1: Representation of the relationship between the four time arguments: signal generation time t^{tog}, signal transmission time t^{tot}_{ia}, signal reception time $t_{tor,\Sigma ia}$ and time of measurement t_{tom}.

From the definition of the signal dependent (code) delay of electronic equipment on-board the navigation satellite follows, that signals generated at the same time are not transmitted at the same time, as described in (GSA, European GNSS Agency, 2019a). On the receiver side, signal dependent (code) delays of electronic equipment cause signals measured at the same time not being received at the same time.
Although the signal (code) delays physically are time differences, they are often referred to and modelled as instantaneous biases, which do not affect the receiver-satellite geometry. As discussed in detail in section 4.1.4, this assumption is valid for signal delays $d < \approx 1\mu s$ when dealing with receivers on Earth and signal delays $d < \approx 0.1\mu s$ for GNSS receivers on-board of LEO satellites. In order not to introduce significant ranging errors due to changes in the receiver-satellite geometry for precise multi-signal applications, the (code) delay difference between signals generated at the same time or measured at the same time should not exceed these limits.

In addition, it is a valid assumption to consider signal (code) delays to be constant over the signal travel time interval. The time argument of the satellite and receiver signal delays can therefore be set to the time of measurement

$$d_{ia}^{s} = d_{ia}^{s}(t_{ia}^{tot}) = d_{ia}^{s}(t_{tom})$$
$$d_{r,\Sigma ia} = d_{r,\Sigma ia}(t_{tom})$$

The free space signal travel time $\Delta T_{r,\Sigma ia}^{s}$ is affected by atmospheric and relativistic delays along the signal path and is disturbed by signal Multipath. It can be modelled in units of length by

$$c \cdot \Delta T_{r,\Sigma ia}^{s} = \rho_{r,\Sigma ia}^{s}(t_{ia}^{tot}, t_{tor,\Sigma ia}) + dtro_{r}^{s} + dion_{r,i}^{s} + c \cdot \delta_{stc} + dm_{r,\Sigma ia}^{s} \tag{4.5}$$

where

$\rho_{r,\Sigma ia}^{s}(t_{ia}^{tot}, t_{tor,\Sigma ia})$ is the geometric distance between the point of signal transmission at the navigation satellite antenna at time t_{ia}^{tot} and the point of signal reception at the receiver antenna at time $t_{tor,\Sigma ia}$, both described in an inertial coordinate system

$dtro_{r}^{s}$ models tropospheric delays in units of length

$dion_{r,i}^{s}$ models ionospheric delays in units of length

δ_{stc} is the relativistic time delay due to space-time curvature

$dm_{r,\Sigma ia}^{s}$ is the code signal multipath

The difference in signal transmission time $t_{ia}^{tot} - t_{jb}^{tot}$ and signal reception time $t_{tor,\Sigma ia} - t_{tor,\Sigma jb}$ for different signals are typically small $|d_{\Sigma ia} - d_{\Sigma jb}| << 1\,\mu s$, see example in section 5.2.2. This allows to neglect their effect on the receiver-satellite geometry and therefore model the geometric range with signal independent time arguments.

$$\rho_{r,\Sigma ia}^{s}(t_{ia}^{tot}, t_{tor,\Sigma ia}) = \rho_{r,\Sigma ia}^{s}(t^{tot}, t_{tor}) \tag{4.6}$$

As for the signal delays, it is a valid assumption to consider the atmospheric delays, relativistic corrections and signal multipath to be constant over the signal travel time interval and therefore set their time arguments to the time of measurement

$$dtro_{r}^{s} = dtro_{r}^{s}(t_{tom})$$
$$dion_{r,i}^{s} = dion_{r,i}^{s}(t_{tom})$$
$$\delta_{rel}(t^{tog}) = \delta_{rel}(t_{tom})$$
$$\delta_{stc} = \delta_{stc}(t_{tom})$$
$$dm_{r,\Sigma ia}^{s} = dm_{r,\Sigma ia}^{s}(t_{tom})$$

The formulas applied to model the geometric range, atmospheric delays and relativistic corrections are described in detail in section 4.1.4.
Instead of using the points of signal transmission and reception at the respective antenna, the geometric distance can be described by the difference between two Point Of Interest (POI), usually the centre of mass at the navigation satellite and the reference/marker point at the receiver. Therefore the geometric range as defined above is split to account for the offset between the points of interest and the points of signal transmission and reception respectively

$$\begin{aligned}\rho_{r,\Sigma ia}^{s}(t^{tot}, t_{tor}) &= \|\boldsymbol{r}^{s}(t^{tot}) + d\boldsymbol{r}_{ia}^{s}(t^{tot}) - \left[\boldsymbol{r}_{r}(t_{tor}) + d\boldsymbol{r}_{r,\Sigma ia}(t_{tor})\right]\| \\ &= \|\boldsymbol{r}^{s}(t^{tot}) - \boldsymbol{r}_{r}(t_{tor})\| + dr_{ia}^{s}(t^{tot}) - dr_{r,\Sigma ia}(t_{tor})\end{aligned} \tag{4.7}$$

where

$\boldsymbol{r}^{s}(t^{tot})$ is the geocentric position vector to the centre of mass of navigation satellite s at time of signal transmission, described in an inertial coordinate system

$\boldsymbol{r}_{r}(t_{tor})$ is the geocentric position vector to the reference/marker point of receiver r at time of signal reception, described in an inertial coordinate system

$d\boldsymbol{r}^s_{ia}(t^{tot})$ is the code signal dependent satellite antenna offset vector, ie. the vector between satellite centre of mass and the point of signal transmission

$d\boldsymbol{r}_{r,\Sigma ia}(t_{tor})$ is the code signal dependent receiver antenna offset vector, ie. the vector between receiver reference/marker point and the point of signal reception

As the vector between the POIs and the point of signal transmission/reception respectively does not change significantly during the signal travel time interval, the time argument of the antenna offset range corrections, see section 4.1.4 for details, can be set to the time of measurement

$$\begin{aligned} dr^s_{ia}(t^{tot}) &= dr^s_{ia}(t_{tom}) \\ dr_{r,\Sigma ia}(t_{tor}) &= dr_{r,\Sigma ia}(t_{tom}) \end{aligned}$$

With the receiver coordinate displacement correction $disp_r(t_{tom})$, required for precise applications on Earth, the pseudorange observation equation for raw signal Σia measured at time $t = t_{tom}$ is given by

$$\begin{aligned} P^s_{r,\Sigma ia}(t) = \|\boldsymbol{r}^s(t^{tot}) - \boldsymbol{r}_r(t_{tor})\| + dr^s_{ia}(t) - dr_{r,\Sigma ia}(t) + disp_r(t) + c\cdot[dt_{r,\Xi}(t) - dt^s_{\Xi}(t^{tog}) + \delta_{rel}(t)] \\ + dtro^s_r(t) + dion^s_{r,i}(t) + c\cdot\delta_{stc}(t) + c\cdot[d^s_{ia}(t) + d_{r,\Sigma ia}(t)] + \epsilon^s_{r,\Sigma ia}(t) \end{aligned} \tag{4.8}$$

where $\epsilon^s_{r,\Sigma ia}(t)$ contains the pseudorange measurement noise, the code signal multipath and residual modelling errors.

4.1.2 Carrier Phase Observation Equation

The theoretical carrier phase pseudorange measurement between receiver r and satellite s is given by the phase difference between the carrier signal replica at measurement time t_{tom}, generated in the receiver and the received carrier signal at generation time $\phi^s(t^{tog})$ generated on-board the navigation satellite in carrier wavelength cycles

$$\phi^{s*}_r(t_{tom}) = \phi_r(t_{tom}) - \phi^s(t^{tog}) + \eta^s_r(t_{tom}) \tag{4.9}$$

where $\phi_r(t_{tom})$ and $\phi^s(t^{tog})$ are the receiver and satellite unwrapped (continuous) carrier signal phase respectively and $\eta^s_r(t_{tom})$ is the carrier phase measurement noise. However, due to the ambiguity of sinusoidal carrier signals, a receiver can only measure the wrapped (fractional) phase difference of the receiver and satellite carrier signals and count the full phase cycles of the measured fractional phase difference after the initial signal acquisition to provide a continuous cumulative phase measurement, as described in section 2.4.2. The actual carrier phase measurement may therefore be written by modifying (4.9) as

$$\phi^s_r(t_{tom}) = \left[\phi_r(t_{tom}) - \phi^s(t^{tog})\right] mod\ 1 + n^s_r(t_{tom}, t_{init}) + \eta^s_r(t_{tom})\,, \tag{4.10}$$

where the modulo operator indicates the measured fractional phase difference constrained to the interval $[0, 1)$ cycles or $[0, 2\pi)$ radians and $n^s_r(t_{tom}, t_{init})$ denotes the integer value at measurement time t_{tom} incremented by the receiver since the initial signal acquisition at t_{init}.
The carrier signal frequency and unwrapped instantaneous phase, which is a continuous function of time are linked (cf. Teunissen and Kleusberg, 1998) by

$$\begin{aligned} f(t) &= \tfrac{d\phi(t)}{dt} \\ \phi(t) &= \phi(t_0) + \textstyle\int_{t_0}^{t} f(\tau)d\tau \end{aligned} \tag{4.11}$$

The carrier signal phase is therefore given by the interval of a time varying frequency, due to Doppler shift and drift of the underlying oscillator clock. For short time intervals $(t - t_0)$ the equation for carrier signal phase can be simplified, assuming constant frequency, by

$$\phi(t) = \phi(t_0) + f\cdot(t - t_0) \tag{4.12}$$

Time and phase can only be perceived as relative quantities and therefore are defined relative to the initial values t_0 and $\phi(t_0)$ respectively. However, as the initial values in (4.12) can not be separated, they can mathematically be lumped into one initial phase offset, which is equivalent to setting the initial time to zero $t_0 = 0$:

$$\phi(t) = \tilde{\phi}(t_0) + f\cdot t \tag{4.13}$$

The unwrapped signal phase realisations of the receiver and satellite oscillators can be written as

$$\begin{aligned}\phi_r(t_{tom}) &= \tilde{\phi}_r(t_0) + f_r \cdot \tau_r(t_{tom}) \\ \phi^s(t^{tog}) &= \tilde{\phi}^s(t^0) + f^s \cdot \tau^s(t^{tog})\end{aligned} \tag{4.14}$$

where f_r and f^s are the receiver and satellite clock frequencies respectively, $\tau_r(t_{tom})$ is the measurement time in the receiver time scale and $\tau^s(t^{tog})$ is the signal generation time in the satellite time scale. As described in section 2.4.2, the receiver signal acquisition and tracking loops constantly adjust the frequency of the receiver generated carrier signal replica, so a common frequency f can be used to formulate the carrier phase measurement.
The full unwrapped carrier phase pseudorange of the signal path is given by the difference between the unwrapped receiver and satellite signal phase (4.14) and making use of the time difference expansion in (4.2)

$$\begin{aligned}\phi_r(t_{tom}) - \phi^s(t^{tog}) &= \tilde{\phi}_r(t_0) - \tilde{\phi}^s(t^0) + f \cdot [\tau_r(t_{tom}) - \tau^s(t^{tog})] + pwu_r^s(t_{tom}) \\ &= \tilde{\phi}_r^s(t_0, t^0) + f \cdot [T_r^s + dt_{r,\Xi}(t_{tom}) - dt_{\Xi,rel}^s(t^{tog})] + pwu_r^s(t_{tom})\end{aligned} \tag{4.15}$$

where $\tilde{\phi}_r^s(t_0, t^0)$ is the combined initial phase offset and the phase wind-up $pwu_r^s(t_{tom})$ was added to account for changes in the relative orientation of transmitting and receiving antennas, see section 4.1.4 for details.
As described above, a receiver measures the wrapped (fractional) phase difference of the receiver and satellite carrier signals and counts the full phase cycles of the measured fractional phase difference after the initial signal acquisition to provide a continuous cumulative phase measurement. However, the initial number of full phase cycles at the time of signal acquisition, the so called carrier phase integer ambiguity term N_r^s is unknown.
The carrier phase measurement in (4.10) can be written in terms of the initial integer ambiguity at the time of signal acquisition N_r^s and the full unwrapped carrier phase pseudorange (4.15) as shown in Figure 2.4, to model the carrier phase observation for signal frequency i

$$\begin{aligned}\phi_{r,i}^s(t_{tom}) &= \phi_{r,i}(t_{tom}) - \phi_i^s(t^{tog}) - N_{r,i}^s + \eta_{r,i}^s(t_{tom}) \\ &= \tilde{\phi}_r^s(t_0, t^0) + f_i \cdot [T_{r,i}^s + dt_{r,\Xi}(t_{tom}) - dt_{\Xi,rel}^s(t^{tog})] + pwu_r^s(t_{tom}) - N_{r,i}^s + \eta_{r,i}^s(t_{tom})\end{aligned} \tag{4.16}$$

Multiplying equation (4.16) with the signal wavelength $\lambda_i = c/f_i$ and expanding the total signal travel time as shown in equations (4.4) and (4.5) yields the full carrier phase observation equation for the time of measurement $t = t_{tom}$ in units of length

$$\begin{aligned}\Phi_{r,i}^s(t) &= \lambda_i \cdot \phi_{r,i}^s(t) \\ &= \|\boldsymbol{r}^s(t^{tot}) - \boldsymbol{r}_r(t_{tor})\| + \delta r_i^s(t) - \delta r_{r,i}(t) + disp_r(t) + c \cdot [dt_{r,\Xi}(t) - dt_\Xi^s(t^{tog}) + \delta_{rel}(t)] \\ &\quad + dtro_r^s(t) - dion_{r,i}^s(t) + c \cdot \delta_{stc}(t) + \lambda_i \left[\delta_i^s(t) + \delta_{r,i}(t) + pwu_r^s(t) - N_{r,i}^s\right] + \eta_{r,i}^s(t)\end{aligned} \tag{4.17}$$

Comparing equation (4.17) with (4.8) reveals the following differences between modelling GNSS carrier phase and pseudorange observations

- Antenna offsets mapped to line of sight $\delta r_i^s(t)$ and $\delta r_{r,i}(t)$ are given with respect to the Antenna Phase Center (APC) instead of the Antenna Code Phase Center (ACPC).
- The ionospheric delay has opposite sign as described in section 4.1.4
- Instead of code signal delays, carrier phase signal delays $\delta_i^s(t)$ and $\delta_{r,i}(t)$ in cycles are used, see section 4.1.3 for details
- The phase wind-up effect $pwu_r^s(t)$ in cycles needs to be corrected as described in section 4.1.4
- The carrier phase integer ambiguity $N_{r,i}^s$ in cycles, which is constant for a satellite pass without cycle slip, ie. reacquisition of the carrier phase signal
- $\eta_{r,i}^s(t)$ contains the carrier phase measurement noise, the carrier phase signal multipath $\delta m_{r,i}^s(t)$ and residual modelling errors. Note that compared to (4.16) it is multiplied with the signal wavelength, but the same notation is kept.

4.1.3 GNSS Signal Delays

GNSS signal delays, as introduced in (4.4) and (4.17) are usually unknown and often referred to as Uncalibrated Signal Delays (USD) or more specific Uncalibrated Code Delays (UCD) and Uncalibrated Phase Delays (UPD) (Schönemann, 2014). Whereas the definition of UCDs is comprehensive and straight forward due to the measurable code signal dependent difference in propagation time through electronic equipment, UPDs are not as well defined and different definitions can be found in the literature (cf. Hofmann-Wellenhof et al., 1992; Kleusberg and Teunissen, 1998; Schönemann, 2014). An important part of the analysis of signal delays performed in this work is based on the use of calibrated signal delays, see section 7.1, thus the term *uncalibrated* used in UCD and UPD is omitted. Hence, signal delays considered in the pseudorange (4.8) and carrier phase (4.17) observation equations are referred to as signal code delay and signal phase delay respectively. The general definition and understanding of code and phase delays for multi-GNSS and multi-signal raw observation processing in this work is described in the following paragraphs.

Observable-specific Code Biases

As defined in section 4.1.1, code delays physically are time differences, whereas the satellite signal code delay d^s_{ia} accounts for the time delay between signal generation and transmission on-board the navigation satellite and the receiver signal code delay $d_{r,\Sigma ia}$ accounts for the time delay between signal reception and the time of measurement. They are caused by the antenna cable and signal dependent delays in the electronic equipment on-board the navigation satellite and in the GNSS receiver. Despite the physical definition, signal code delays may be referred to as instantaneous code biases which do not affect the receiver-satellite geometry. In analogy with the *bias type identifier* in (Schaer, 2016), the term Observable-specific Code Bias (OCB) is therefore used in this work. Signal delays on-board the navigation satellite before signal transmission or signal delays on the receiver side after signal reception might influence the computed receiver-satellite geometry due to the fact that these delays are usually unknown and therefore are part of the applied or estimated clock offsets. As described in sections 4.1.4 and 5.2.2, depending on the application signal code delays might be treated as biases for signal delays $d < \approx 1\,\mu s$ when dealing with receivers on Earth and signal delays $d < \approx 0.1\,\mu s$ for GNSS receivers on-board of LEO satellites.

Observable-specific Phase Biases

Signal phase delays have been introduced in section 4.1.2 similar to the definition of signal code delays. However, due to the nature of carrier phase signals and the resulting measurements, signal phase delays cannot be defined as absolute time differences caused by signal dependent delays in the electronic equipment on-board the navigation satellite and in the GNSS receiver. Satellite and receiver phase delays in (4.17) can physically be described as a combination of the oscillator initial phase offsets $\tilde{\phi}_r(t_0)$ and $\tilde{\phi}^s(t^0)$ from (4.14) and frequency dependent carrier phase delays on-board the navigation satellite and in the GNSS receiver hardware. However, as full cycles of phase delays are indistinguishable from integer values of the carrier phase ambiguity term, signal phase delays in this work are defined as the digits behind the decimal point, also referred to as fractional value, of the float (non-integer) carrier phase ambiguity $M^s_{r,i}$. As the magnitude of signal phase delays thereby is limited to one cycle of the carrier signal wavelength, they are referred to as Observable-specific Phase Bias (OPB) in analogy with the *bias type identifier* in (Schaer, 2016). Satellite phase biases δ^s_i and receiver phase biases $\delta_{r,i}$ are fully correlated with the carrier phase integer ambiguity term $N^s_{r,i}$, so from a raw carrier phase observation without additional information only their lump sum, also referred to as carrier phase float ambiguity $M^s_{r,i} = N^s_{r,i} - \delta^s_i - \delta_{r,i}$ can be determined. The existence of phase biases prevents the direct determination of integer ambiguities from raw carrier phase observations, even if all other parameters, corrections and errors would be accurately known.

4.1.4 Correction and Error Modelling

This section describes corrections and mathematical models applied in (4.8) and (4.17), which are required by the described GNSS raw observation processing scheme for precise applications.

Satellite Position Travel Time Correction

The geometric range between the navigation satellite center of mass and receiver reference/marker point is given by

$$\begin{aligned}\rho^s_r(t^{tot}, t_{tor}) &= \|\boldsymbol{r}^s(t^{tot}) - \boldsymbol{r}_r(t_{tor})\| \\ &= \sqrt{[X^s(t^{tot}) - X_r(t_{tor})]^2 + [Y^s(t^{tot}) - Y_r(t_{tor})]^2 + [Z^s(t^{tot}) - Z_r(t_{tor})]^2}\,,\end{aligned} \tag{4.18}$$

where X, Y, Z are the cartesian components of the geocentric position vectors in an inertial reference frame.

As the free space signal travel time $\Delta T_r^s = t_{tor} - t^{tot}$ in (4.5) also appears implicitly in

$$\rho_r^s(t^{tot}, t_{tor}) = \|\boldsymbol{r}^s(t_{tor} - \Delta T_r^s) - \boldsymbol{r}_r(t_{tor})\| \,, \tag{4.19}$$

the geometric range and therefore satellite position has to be determined either iteratively or by developing the satellite position in a Taylor series around the signal reception time t_{tor}.

Whereas most single point positioning algorithms implemented in commercial devices use an iterative approach to determine the satellite position at signal transmission time, the approach used in this work is based on developing the satellite position in a Taylor series around the signal reception time, mainly to avoid the time consuming iterative process and to handle both receiver and satellite positions at the same time.

With the Taylor series expansion of the satellite position around the signal reception time

$$\boldsymbol{r}^s(t_{tot}) = \boldsymbol{r}^s(t_{tor} - \Delta T_r^s) = \boldsymbol{r}^s(t_{tor}) - \left.\frac{d\boldsymbol{r}^s(t)}{dt}\right|_{t_{tor}} \cdot \Delta T_r^s(t_{tor}) + \mathcal{O}^2(\Delta T_r^s) \tag{4.20}$$

and neglecting second order and higher terms, the signal travel time correction for the satellite position mapped to the signal Line Of Sight (LOS) is given by

$$corr_{\Delta T_r^s}(t_{tor}) = \frac{\boldsymbol{r}^s(t_{tor}) - \boldsymbol{r}_r(t_{tor})}{\rho_r^s(t_{tor})} \cdot \boldsymbol{v}^s(t_{tor}) \cdot \frac{\rho_r^s(t_{tor})}{c} \,, \tag{4.21}$$

where the free space signal travel time is approximated by $\Delta T_r^s(t_{tor}) = \frac{\rho_r^s(t_{tor})}{c}$ and all geocentric position and velocity vectors $\boldsymbol{r}(t)$ and $\boldsymbol{v}(t)$ are given in an inertial reference frame.

The geometric range between the navigation satellite center of mass and receiver reference/marker point can then be written as:

$$\rho_r^s(t^{tot}, t_{tor}) = \rho_r^s(t_{tor}) + corr_{\Delta T_r^s}(t_{tor}) \,, \tag{4.22}$$

where both the receiver and satellite positions are treated at signal reception time

$$\rho_r^s(t_{tor}) = \|\boldsymbol{r}^s(t_{tor}) - \boldsymbol{r}_r(t_{tor})\| \,. \tag{4.23}$$

Range Rate Correction

The range rate correction is applied to account for changes in the receiver-satellite geometry and has two main use cases. The first one is to define a criterion to distinguish between the terms delay and bias, as noted in section 4.1.3. The second use case is to unify the time of measurement for a global network of GNSS receivers to estimate precise GNSS satellite orbits and clock offsets at a common processing time.

The change in the receiver-satellite geometry mapped to the signal LOS is given by the time derivative of the geometric range, referred to as range rate

$$\frac{d\rho_r^s(t)}{dt} = -\frac{\boldsymbol{r}^s(t) - \boldsymbol{r}_r(t)}{\rho_r^s(t)} \cdot (\boldsymbol{v}^s(t) - \boldsymbol{v}_r(t)) \tag{4.24}$$

where all geocentric position and velocity vectors $\boldsymbol{r}(t)$ and $\boldsymbol{v}(t)$ are given in an inertial reference frame.

Figure 4.2a shows the range rate computed for GPS and Galileo satellites tracked by ESA's GNSS Observation Network (EGON) receivers on 2019-05-26. Typical values for the range rate between GPS satellites and receivers on Earth are $d\rho_{EGON}^{GPS}/dt \in [-800, 800]\,\mathrm{m\,s^{-1}}$. For Galileo satellites typical range rate values are $d\rho_{EGON}^{GAL}/dt \in [-600, 600]\,\mathrm{m\,s^{-1}}$, whereas for the two satellites in elliptical orbits (GAL-201 and GAL-202) higher values of $d\rho_{EGON}^{GAL*}/dt \in [-1.36, 1.36]\,\mathrm{km\,s^{-1}}$ are observed. The magnitude of the range rate depends on the orbit and therefore velocity of the navigation satellites and differs slightly for the different GNSS.

For GNSS receivers on-board of LEO satellites, the range rate is significantly higher, compared to receivers on Earth, due to the much higher receiver velocity $\boldsymbol{v}_r(t)$. Figure 4.2b shows the range rate computed for GPS satellites, tracked by the receiver on-board the Jason-1 satellite on 2002-06-09. The semi-major axis of the Jason-1 orbit was determined to be $a_J = 7712.097\,\mathrm{km}$ with an orbital velocity of $v_J = 7.186\,\mathrm{km\,s^{-1}}$. Typical values for the range rate between GPS satellites and the Jason-1 satellite are $d\rho_J^{GPS}/dt \in [-7.6, 7.6]\,\mathrm{km\,s^{-1}}$.

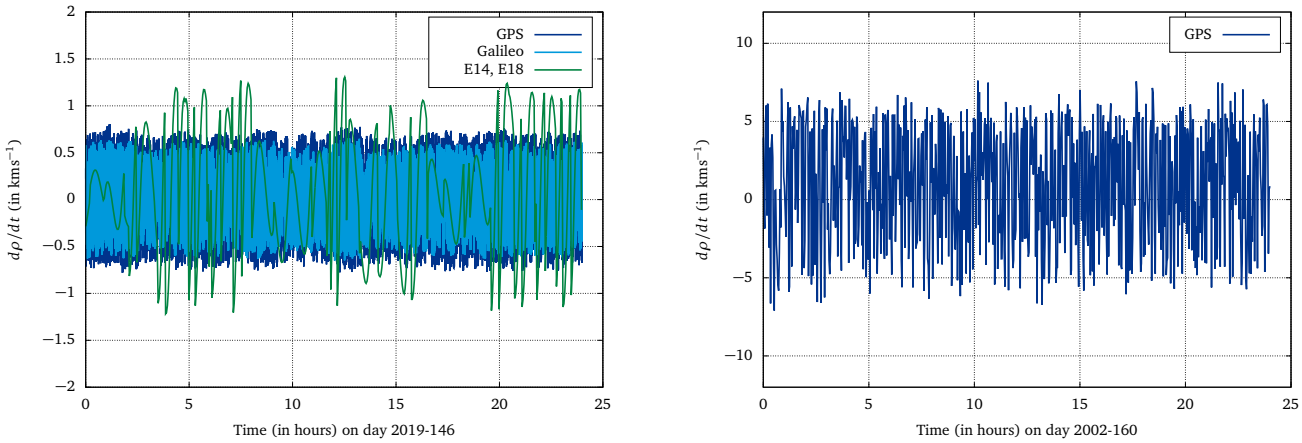

(a) EGON receivers tracking Galileo and GPS satellites

(b) Receiver on-board of Jason-1 tracking GPS satellites

Figure 4.2: Computed time derivatives of the geometric range between GNSS satellites and receivers for different applications.

In order to specify a criterion to distinguish between the terms delay and bias, a limit for the acceptable range error has to be defined. Assuming that range errors due to changes in the receiver-satellite geometry of $\Delta\rho < 1\,\text{mm}$ can be neglected, a time delay d may be treated as instantaneous bias if the following condition is fulfilled:

$$\Delta\rho = d \cdot \frac{d\rho_r^s}{dt} < 1\,\text{mm}\,. \tag{4.25}$$

Applying this condition to the range rate values found above, reveals the limits for treating signal delays as biases to be $d < \approx 1\,\mu s$ when dealing with receivers on Earth and $d < \approx 0.1\,\mu s$ for GNSS receivers on-board of LEO satellites.

When processing data of a global network of GNSS receiver in order to estimate precise navigation satellite orbits and clock offsets, the range rate correction can be applied to unify the time of measurement among different receivers. Since GNSS receiver perform measurements in their own time scale, observations from different receivers are usually time tagged with the same epoch, but they are not measured at the exact same point in time. This prevents the determination of satellite orbit and clock offsets at a common time. The range rate correction can be used to bring observations from different receivers measured at the same epoch to a common point in time, defined by the exact same epoch in the reference time scale τ_Ξ. This allows to consistently process all observations of a certain epoch from different receivers at a single point in time. It is important to note, that this range rate correction based on clock offsets including signal code delays might introduce significant ranging errors, if these receiver signal code delays including antenna cable exceed the limits described above.
The receiver clock range rate correction due to a receiver clock offset with respect to the reference time scale τ_Ξ is given by

$$corr_{rcr}(t, dt_{r,\Xi}(t)) = -\frac{d\rho_r^s(t)}{dt} \cdot dt_{r,\Xi}(t)\,. \tag{4.26}$$

For receiver clock offsets $dt_{r,\Xi}(t) = 500\,\mu s$, the receiver clock range rate correction can have a magnitude of up to $corr_{rcr}(t, dt_{r,\Xi}(t)) \approx 40\,\text{cm}$ for ground applications and up to $corr_{rcr}(t, dt_{r,\Xi}(t)) \approx 3.8\,\text{m}$ for LEO applications.
Applying the receiver clock range rate correction can be interpreted as a change in the time argument of the observation equation from receiver dependent time of measurement to a receiver independent common point in time, referred to as processing time t_{top}:

$$\begin{aligned} P_{r,\Sigma ia}^s(t_{top}) &= P_{r,\Sigma ia}^s(t_{tom}) + corr_{rcr}(t, dt_{r,\Xi}(t)) \\ \Phi_{r,i}^s(t_{top}) &= \Phi_{r,i}^s(t_{tom}) + corr_{rcr}(t, dt_{r,\Xi}(t))\,, \end{aligned} \tag{4.27}$$

where it is assumed that this change in time argument only affects the receiver satellite geometry, while other parameters of the observation equations remain unchanged.
It is important to emphasise that although they refer to different points in time, the receiver dependent time of measurement and the common processing time by definition refer to the same epoch $\tau_r(t_{tom}) = \tau_\Xi(t_{top})$.

For Precise Point Positioning (PPP) applications the receiver clock range rate correction can be used to unify the argument of time for applied precise GNSS orbits and clock offsets, applied corrections and estimated parameters and refer all to a common reference time scale. In combination with the satellite position travel time correction (4.21) this allows to directly use precise satellite state vectors given at a certain epoch in a reference time scale without iterative computation of the satellite position at signal transmission time. Depending on how many GNSS and satellites are processed, this approach might therefore improve the efficiency of PPP real-time applications.
Ignoring this correction in precise GNSS applications on ground, where satellite orbits and clock offsets given in a certain reference time scale are applied directly, can lead to range errors up to $\Delta\rho \approx 80\,\mathrm{cm}$ for receiver clock offsets of $dt_{r,\Xi}(t) = 1\,\mathrm{ms}$.
It should be noted, that this approach usually still requires the interpolation of precise satellite orbits to the receiver measurement epoch, in addition to applying the afore mentioned corrections. In case a receiver measurement epoch differs by several seconds from the available precise GNSS clock offset epochs, also all GNSS clock offsets would have to be interpolated to the measurement epoch, which requires highly stable atomic clocks on-board the navigation satellites, analysed for example in (Hauschild et al., 2013; Peng et al., 2019). This is especially important for PPP applications involving LEO satellites.

Relativistic Effects

The described relativistic effects for precise GNSS applications are split in four parts. The first relativistic effect is a constant satellite clock frequency offset due to the combined effects of time dilation and gravitational redshift. Time delation causes fast moving satellite clocks to appear to run slow relative to a user on Earth, whereas the difference in gravitational potential causes satellite clocks to run fast relative to a user on Earth. The combined effect depends on the orbit semi-major axis a, Galileo satellite clocks for example appear to run fast by $\approx 40.8\,\mu\mathrm{s\,d}^{-1}$ relative to a user on Earth. The constant satellite clock frequency offset is applied to the satellite clock hardware prior to launch, so that on average the apparent satellite clock rate for a user on Earth is the nominal frequency $f_0 = 10.23\,\mathrm{MHz}$. Table 4.1 shows the constant satellite clock frequency offsets for different GNSS.

Table 4.1: The constant satellite clock frequency offsets due to time delation and gravitationl redshift for different GNSS, applied to the satellite clock hardware prior to launch (Ashby, 2003).

GNSS	a (in km)	Δf (in Hz)
Galileo	29 599.80	-4.83×10^{-3}
BeiDou (MEO)	27 910.20	-4.69×10^{-3}
GPS	26 562.76	-4.57×10^{-3}
GLONASS	25 509.64	-4.46×10^{-3}

The second relativist effect is a periodic variation of the satellite clock frequency due to the eccentricity of noncircular satellite orbits. The classical periodic satellite clock correction (in units of length) can be described by (cf. Ashby, 2003)

$$\delta_{\mathrm{rel,ecc}}(t) = 2\frac{\boldsymbol{r}_I^s(t) \cdot \boldsymbol{v}_I^s(t)}{c} \tag{4.28}$$

where $\boldsymbol{r}_I^s(t)$ and $\boldsymbol{v}_I^s(t)$ are the geocentric satellite position and velocity vectors in an intertial reference frame.
The third relativist effect accounts for the satellite clock traveling through a varying gravitational potential due to Earth's oblateness, described by the J_{20} term of the gravitational field expansion. The additional periodic satellite clock correction (in units of length) can be described by (cf. Kouba, 2004)

$$\delta_{\mathrm{rel,J2}}(t) = \mathrm{J}_2\frac{3}{2}\frac{a_\oplus^2}{c}\sqrt{\frac{\mu_\oplus}{a^3}}\sin^2 i \sin 2u(t) \tag{4.29}$$

where $J_2 = J_{20} = 1.083 \times 10^{-3}$, $a_\oplus$ is the semi-major axis of the mean Earth, $\mu_\oplus$ is the Earth's gravitational constant, a is the orbit semi-major axis, i and u are the orbit inclination and the argument of latitude $u(t) = \omega + \nu(t)$, the sum of the argument of perigee ω and the true anomaly $\nu(t)$.
The combined periodic relativistic correction for the satellite clock is then given by

$$\delta_{\mathrm{rel}}(t) = \delta_{\mathrm{rel,ecc}}(t) + \delta_{\mathrm{rel,J2}}(t) \tag{4.30}$$

The fourth relativist effect is a propagation delay of the satellite signal due to the presence of the Earth's gravitational field. The Shapiro effect due to space-time curvature (cf. Zhu and Groten, 1988; Ashby, 2003; IERS, 2010) can be described in units of length by

$$\delta_{\text{stc}}(t) = \frac{2\mu_{\oplus}}{c^2} \ln\left(\frac{\|\boldsymbol{r}^s(t)\| + \|\boldsymbol{r}_r(t)\| + \rho_r^s(t)}{\|\boldsymbol{r}^s(t)\| + \|\boldsymbol{r}_r(t)\| - \rho_r^s(t)}\right) \tag{4.31}$$

Sagnac Effect

In classical PVT algorithms, positions of navigation satellites and receivers on ground are computed in a non-inertial Earth fixed coordinate system, see section 3.1 for details. In these algorithms, the Sagnac correction must be applied to account for the rotation of the Earth (fixed coordinate system) during the signal travel time (Teunissen and Montenbruck, 2017). It is assumed that all signals are received at a common time t_{tor} at the receiver, whereas in classical PVT algorithms the corresponding positions of different satellites s are computed in Earth fixed coordinate system at different signal transmission times $t^{s,tot}$. If the receiver position is to be determined in an Earth fixed coordinate system at the common reception time, the positions of all satellites need to be transformed to properly describe the geometric distances between receiver and satellites in a consistent coordinate system. The Sagnac correction therefore can be considered as transformation of the satellite positions at signal transmission time $\boldsymbol{r}^s(t^{s,tot})$ given in an Earth fixed coordinate system at signal transmission time $E(t^{s,tot})$ to a common Earth fixed coordinate system at signal reception time $E(t_{tor})$

$$\boldsymbol{r}^s_{E(t_{tor})}\left(t^{s,tot}\right) = \boldsymbol{R}_{\oplus}(\Delta\omega_{\oplus}) \cdot \boldsymbol{r}^s_{E(t^{s,tot})}\left(t^{s,tot}\right) \tag{4.32}$$

where the matrix $\boldsymbol{R}_{\oplus}(\Delta\omega_{\oplus})$ describes a rotation around the Earth rotation axis by an angle $\Delta\omega_{\oplus} = \omega_{\oplus} \cdot (t_{tor} - t^{s,tot})$ with the angular velocity of the Earth $\omega_{\oplus}$. Another possibility is to apply the Sagnac correction as range correction given by (cf. Ashby, 2004)

$$\Delta\rho_r^s = -\frac{\boldsymbol{r}^s(t^{s,tot}) - \boldsymbol{r}_r(t_{tor})}{c} \cdot \boldsymbol{\omega}_{\oplus} \times \boldsymbol{r}_r(t_{tor})\,, \tag{4.33}$$

where $\boldsymbol{\omega}_{\oplus}$ is the vector of Earth's angular velocity along the Earth rotation axis.
The Sagnac correction becomes irrelevant, when position and velocity vectors are handled in an inertial coordinate system (Ashby, 2003) which is independent of the rotation of the Earth. However, as for practical reasons positions on Earth always are expressed in an Earth fixed coordinate system, the transformation between the rotating Earth fixed and an inertial coordinate system described in section 3.1.3 has to be applied instead. Details of the Sagnac correction can be found in (Ashby, 2003, 2004).

Tropospheric Delay

According to Davis et al. (1993), the tropospheric signal delay between receiver r and satellite s can be modelled in a linear form by

$$dtro_r^s(t) = m_h(e) \cdot ZHD_r(t) + m_w(e) \cdot ZWD_r(t) + m_g(e)\left[G_{r,N}(t) \cdot \cos(a) + G_{r,E}(t) \cdot \sin(a)\right]\,, \tag{4.34}$$

where m_h, m_w and m_g are the hydrostatic, wet and gradient mapping functions, $e(t)$ and $a(t)$ are the satellite elevation and azimuth as seen from the receiver, $ZHD_r(t)$ and $ZWD_r(t)$ are the receiver dependent zenith hydrostatic and wet delay and $G_{r,N}(t)$ and $G_{r,E}(t)$ are the North and East tropospheric gradients. Different models for the mapping functions exist, for example the Neill Mapping Function (NMF), Vienna Mapping Function (VMF) or the Global Mapping Function (GMF) and as these functions are all elevation depend, they also are implicitly time dependent. The Zenith Hydrostatic Delay (ZHD) accounts for approximately 90 % of the tropospheric delay and as the dry part of the troposphere is quite homogeneous over different height and geographic regions (Bauer, 2011), it can be quite accurately modelled by for example the Saastamoinen model (Saastamoinen, 1973)

$$ZHD_{r,Saast}(t) = 0.002277 \cdot \left[P + \left(\frac{1255}{T} + 0.05\right)E\right] \tag{4.35}$$

where P is the atmospheric pressure in hPa, T is the temperature in K and E is the partial vapour pressure in hPa, derived for a specific receiver location from a Global Pressure Temperature (GPT) model.
The Zenith Wet Delay (ZWD) accounts for approximately 10 % of the tropospheric delay and shows a large regional and temporal variation (Bauer, 2011). It is therefore estimated per receiver as additional parameter $ZWD_r(t)$ in the least squares adjustment, as are the tropospheric gradients $G_{r,N}(t)$ and $G_{r,E}(t)$.

Ionospheric Delay

The first order ionospheric slant delay along the signal path between receiver r and satellite s for frequency f_i can be expressed (in m) by (cf. Bauer, 2011)

$$dion^s_{r,i}(t) = \frac{A}{f_i^2} \cdot STEC^s_r(t)\,, \tag{4.36}$$

with the ionospheric constant $A = 40.28\,\mathrm{m^3\,s^{-2}}$ and the time dependent slant total electron content $STEC^s_r(t)$, given in Total Electron Content Unit (TECU) (1 TECU $= 1 \times 10^{16}\,\mathrm{e^-/m^2}$). The Slant Total Electron Content (STEC) is defined as the number of electrons within a cylinder of cross sectional area of $1\,\mathrm{m^2}$ along the signal path (Newby, 1992).

The different phase and group velocities, relevant to derive the signal delays in the dispersive ionosphere for carrier phase and pseudorange observations respectively, lead to opposite signs for the ionospheric delay in the corresponding observation equations (Hofmann-Wellenhof et al., 2008), compare (4.8) and (4.17).

The first order ionospheric term accounts for 99.9 % of the ionospheric delay (Hernandez-Pajares et al., 2007) and satisfies the relation

$$\frac{dion^s_{r,i}(t)}{dion^s_{r,j}(t)} = \frac{f_j^2}{f_i^2} \tag{4.37}$$

In this work, second order terms of the ionospheric delay are not considered. A detailed analysis of second order ionospheric effects on GNSS signals can be found in (Hernandez-Pajares et al., 2007).

There are different ways of handling ionospheric delays in GNSS applications. The classical approaches are either to correct the ionospheric delay by models, mainly used for single-frequency observations or form the so-called ionosphere-free (IF) linear combination from dual-frequency observations, see section 4.2.2.

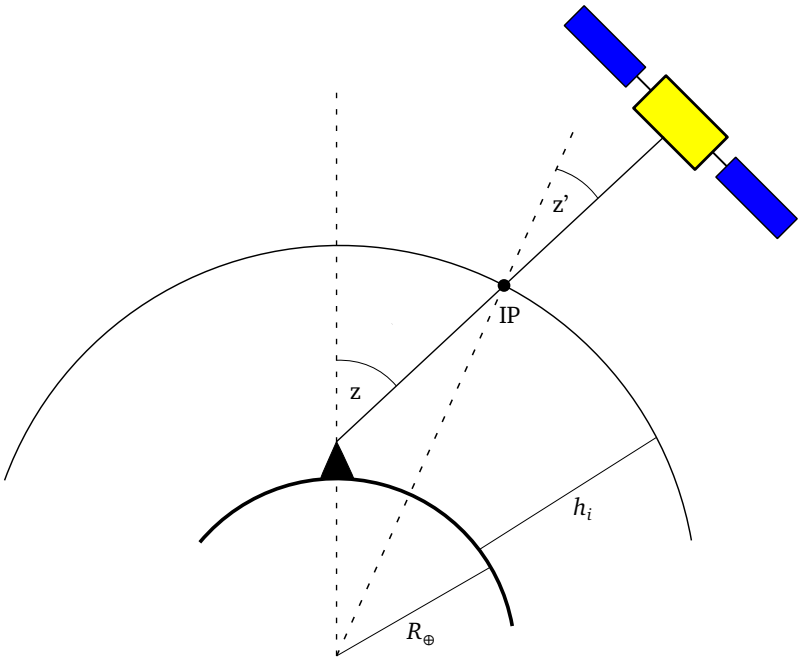

Figure 4.3: Geometric relation between zenith angle z at receiver position and z′ at the Ionospheric Pierce Point (IP) with the radius of the Earth $R_\oplus$ and the single layer height h_i of the ionospheric model.

The ionospheric delay can be modelled by either using ionosphere models provided by the GNSS themselves, like (Klobuchar, 1987) for GPS and NeQuick-G (European Commission, 2016) for Galileo, or using observation based models in the form of Vertical Total Electron Content (VTEC) maps (Hernández-Pajares et al., 2009). Global or regional VTEC maps, published in the Ionosphere Map Exchange (IONEX) format (Schaer et al., 1998), need to be combined with a zenith angle dependent mapping function $m_i(z)$ in order to map the vertical ionospheric delay to the slant signal path

$$STEC^s_r(t) = m_i(z) \cdot VTEC_r(t) = \frac{VTEC_r(t)}{\cos(z')} \tag{4.38}$$

where z' is the zenith angle at the ionospheric pierce point (IP), which is related to the zenith angle z at the receiver position (see Figure 4.3) by

$$\sin(z') = \frac{R_\oplus}{R_\oplus + h_i} \sin(z)\,, \tag{4.39}$$

with the radius of the Earth $R_\oplus$ and the VTEC map single layer model mean ionospheric height h_i. The receiver position zenith angle dependent ionosphere mapping function is then given by

$$m_i(z) = \left[1 - \left(\frac{R_\oplus}{R_\oplus + h_i} \sin z\right)^2\right]^{-1/2}\,. \tag{4.40}$$

In GNSS raw observation processing, the ionospheric delay can be estimated from multi-frequency observations by adding $STEC_r^s(t)$ to the list of parameters estimated in the least squares adjustment. This can be done by either estimating the absolute ionospheric slant delay or using (4.38) together with a VTEC map as a priori ionosphere model to estimate constrained residual STEC values. The handling of ionospheric delay estimation with GNSS raw observations in this work is described in section 5.2.3.

Antenna Offsets

The code signal dependent antenna offset vector $d\boldsymbol{r}_{\Sigma ia}(t)$ can be split into three parts, the constant and signal independent offset vector between the POI and the Antenna Reference Point (ARP) $d\boldsymbol{r}_{ARP}$, the signal dependent constant group delay offset $\boldsymbol{gdo}_{\Sigma ia}$ and the signal azimuth and zenith angle dependent scalar group delay variation $gdv_{\Sigma ia}(a,z)$ relative to the ACPC, see Figure 4.4. The antenna offset vector mapped to the signal LOS with unit vector $\boldsymbol{e}_{LOS}$ gives the antenna offset range correction for pseudorange observations

$$dr_{\Sigma ia}(t) = \boldsymbol{e}_{LOS}(t) \cdot d\boldsymbol{r}_{\Sigma ia}(t) = \boldsymbol{e}_{LOS}(t) \cdot d\boldsymbol{r}_{ARP} + \boldsymbol{e}_{LOS}(t) \cdot \boldsymbol{gdo}_{\Sigma ia} + gdv_{\Sigma ia}(a,z)\,, \tag{4.41}$$

where the Group Delay Variation (GDV) term $gdv_{\Sigma ia}(a,z)$ is implicitly time dependent due to the changing azimuth and zenith angles.

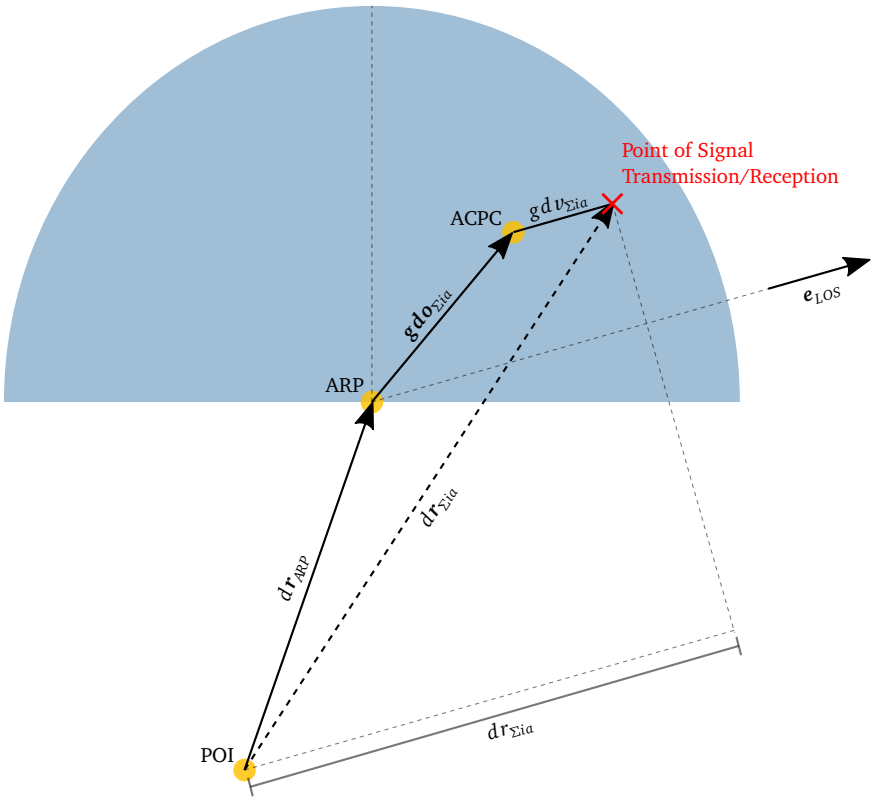

Figure 4.4: Antenna offset and variation corrections used for modelling GNSS pseudorange observations.

For carrier phase observations the antenna offset range correction $\delta r_i(t)$ is given with respect to the APC instead of the ACPC. It includes the constant and frequency independent offset between the POI and the ARP, the frequency dependent constant Phase Center Offset (PCO) and the signal azimuth and zenith angle and implicitly time dependent scalar Phase Center Variation (PCV), see Figure 4.5

$$\delta r_i(t) = \boldsymbol{e}_{LOS}(t) \cdot d\boldsymbol{r}_i(t) = \boldsymbol{e}_{LOS}(t) \cdot d\boldsymbol{r}_{ARP} + \boldsymbol{e}_{LOS}(t) \cdot \boldsymbol{pco}_i + pcv_i(a,z)\,. \tag{4.42}$$

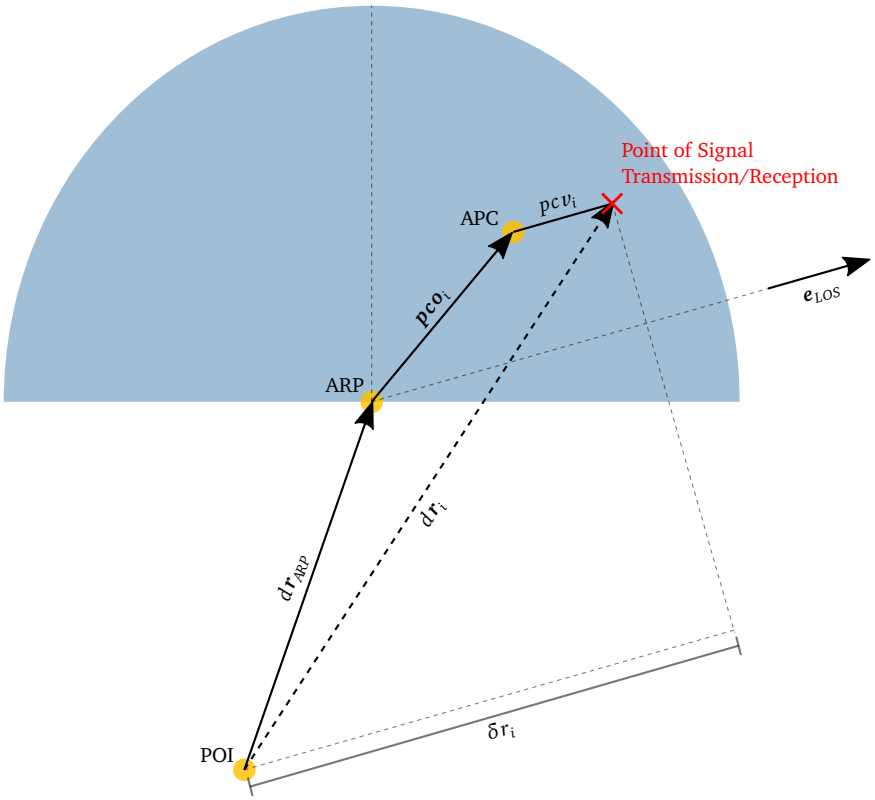

Figure 4.5: Antenna offset and variation corrections used for modelling GNSS carrier phase observations.

For precise GNSS applications, the antenna offset range corrections for pseudorange and carrier phase observations have to be applied for both, the transmitting and receiving antenna.

Ground Receiver Coordinate Displacements

Receiver coordinates on ground vary in time due to tide effects introduced by the Earth's changing topography. In order to estimate stable and precise receiver coordinates, the effects due to solid and permanent Earth tides, pole tides of the Earth and ocean loading tides need to be modelled and corrected in the observation equation.
The applied receiver coordinate displacement correction is given by

$$disp_r(t_{tom}) = disp_{r,spt}(t_{tom}) + disp_{r,pot}(t_{tom}) + disp_{r,olt}(t_{tom})\,, \tag{4.43}$$

with the components described in (IERS, 2010)

$disp_{r,spt}(t)$ considers solid and permanent tides of the Earth, caused by lunar and solar gravitational attraction

$disp_{r,pot}(t)$ considers pole tides of the Earth based on EOP data and Earth's mean pole

$disp_{r,olt}(t)$ considers loading effects due to ocean tides caused by lunar gravitational attraction

Phase Wind-Up

The phase wind-up effect describes the relative change of the orientation between transmitting and receiving antennas in carrier wavelength cycles. The phase wind-up correction derived by Wu et al. (1992) is given in cycles by

$$pwu_r^s(t) = 2\pi N + \delta pwu_r^s(t)\,, \tag{4.44}$$

where the number of full wavelength cycles N needs to be continuously tracked and the fractional part of a cycle is given by

$$\delta pwu_r^s(t) = \text{sign}(\gamma)\arccos\left(\frac{\boldsymbol{D}^s \cdot \boldsymbol{D}_r}{\|\boldsymbol{D}^s\|\,\|\boldsymbol{D}_r\|}\right). \tag{4.45}$$

The term γ is defined as

$$\gamma = \boldsymbol{k} \cdot (\boldsymbol{D}^s \times \boldsymbol{D}_r) \tag{4.46}$$

with the unit vector $\boldsymbol{k}$ pointing from transmitter to receiver, see Figure 4.6, the effective dipole vector of the receiving antenna with the dipole unit vectors $\boldsymbol{a}_r$ and $\boldsymbol{b}_r$

$$\boldsymbol{D}_r = \boldsymbol{a}_r - \boldsymbol{k}(\boldsymbol{k} \cdot \boldsymbol{a}_r) + \boldsymbol{k} \times \boldsymbol{b}_r \tag{4.47}$$

and the effective dipole vector of the transmitting antenna with the dipole unit vectors $\boldsymbol{a}^s$ and $\boldsymbol{b}^s$

$$\boldsymbol{D}^s = \boldsymbol{a}^s - \boldsymbol{k}\,(\boldsymbol{k} \cdot \boldsymbol{a}^s) - \boldsymbol{k} \times \boldsymbol{b}^s\,. \tag{4.48}$$

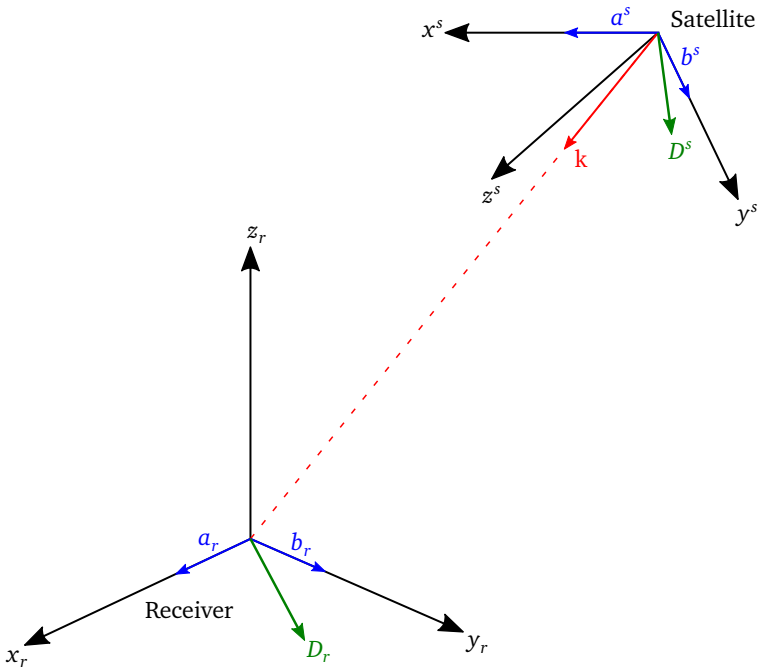

Figure 4.6: Dipole vectors D^s and D_r of the transmitting and receiving antennas respectively, used to compute the phase wind-up correction.

The correct knowledge of the navigation satellite attitude and especially the rate of the changing attitude is crucial to calculate the phase wind up effect. Taken the phase wind-up effect into account for precise GNSS applications therefore requires to accurately model the changing attitude of all involved navigation satellites. In this context it is important to note that for PPP applications, users must calculate the phase wind up correction using the same navigation satellite attitude model used by the service provider generating the precise satellite orbit and clock offsets.

4.1.5 Reduced Raw Observation Equations

Separating the correction terms described in section 4.1.4 from the parameters estimated in the least squares adjustment, the reduced functional model for raw pseudorange observations at the processing time $t = t_{top}$ (measurement epoch in reference time scale) can be written as

$$\begin{aligned}\tilde{P}^s_{r,\Sigma ia}(t) &= P^s_{r,\Sigma ia}(t) - Pcorr^s_{r,\Sigma ia}(t) \\ &= \rho^s_r(t) + c \cdot \left[\tilde{dt}_{r,\Xi}(t) - dt^s_{\Xi}(t^{tog})\right] + dtro^s_{r,wg}(t) \\ &\quad + 40.28/f_i^2 \cdot STEC^s_r(t) + c \cdot \left[d^s_{ia}(t) + d_{r,\Sigma ia}(t)\right] + \epsilon^s_{r,\Sigma ia}(t)\,,\end{aligned} \tag{4.49}$$

with

$$\begin{aligned}\rho^s_r(t) &= \|\boldsymbol{r}^s(t) - \boldsymbol{r}_r(t)\| \\ \tilde{dt}_{r,\Xi}(t) &= \left(1 - 1/c\; d\rho^s_r/dt\right) dt_{r,\Xi}(t) \\ dtro^s_{r,wg}(t) &= m_w(e) \cdot ZWD_r(t) + m_g(e)\left[G_{r,N}(t) \cdot \cos(a) + G_{r,E}(t) \cdot \sin(a)\right]\end{aligned} \tag{4.50}$$

and the computed pseudorange correction

$$Pcorr^s_{r,\Sigma ia}(t) = corr_{\Delta T^s_r}(t_{tor}) + dr^s_{ia}(t) - dr_{r,ia}(t) + disp_r(t) + \delta_{rel}(t) + m_h(e) \cdot ZHD_r(t) + c \cdot \delta_{stc}(t)\,. \tag{4.51}$$

The reduced functional model for raw carrier phase observations at processing time $t = t_{top}$ can be written as

$$\begin{aligned}\tilde{\Phi}^s_{r,i}(t) &= \Phi^s_{r,i}(t) - \Phi corr^s_{r,i}(t) \\ &= \rho^s_r(t) + c \cdot \left[\tilde{dt}_{r,\Xi}(t) - dt^s_{\Xi}(t^{tog})\right] + dtro^s_{r,wg}(t) \\ &\quad - 40.28/f_i^2 \cdot STEC^s_r(t) - \lambda_i M^s_{r,i}(t) + \eta^s_{r,i}(t)\,,\end{aligned} \tag{4.52}$$

with the carrier phase float ambiguity

$$M^s_{r,i}(t) = N^s_{r,i} - \delta^s_i(t) - \delta_{r,i}(t)\,, \tag{4.53}$$

which is the same formulation as used in (Blewitt, 1997). The computed carrier phase correction is given by

$$\Phi corr^s_{r,i}(t) = corr_{\Delta T^s_r}(t) + \delta r^s_i(t) - \delta r_{r,i}(t) + disp_r(t) + \delta_{rel}(t) + m_h(e) \cdot ZHD_r(t) + c \cdot \delta_{stc}(t) + \lambda_i pwu^s_r(t)\,. \tag{4.54}$$

The combined parameter vector for precise processing of raw pseudorange and phase observations is given by

$$\boldsymbol{X} = \left[\boldsymbol{r}^s(t), \boldsymbol{r}_r(t), dt_{r,\Xi}(t), dt^s_{\Xi}(t^{tog}), ZWD_r(t), G_{r,N}(t), G_{r,E}(t), STEC^s_r(t), d^s_{ia}(t), d_{r,\Sigma ia}(t), M^s_{r,i}(t)\right]^T\,. \tag{4.55}$$

It should be noted, that parameters estimated at every processing epoch, so called epoch parameters like the clock offsets $dt_{r,\Xi}$ and dt^s_{Ξ} and for raw observation processing the slant ionospheric delay $STEC^s_r$, are pre-eliminated from the normal equation system to reduce the dimension of the system without loosing any information, see (Dach et al., 2015b) for details.

Depending on the application, certain parameters might be introduced as known. For PPP applications for example the satellite position vector $\boldsymbol{r}^s(t)$ and clock offsets $dt^s_{\Xi}(t^{tog})$ are given by the precise product service provider and therefore are not part of the estimated parameter vector.

4.2 Linear Combinations of GNSS Observables

This section gives an overview of commonly used linear combinations of GNSS observables and describes the corresponding functional models and estimable parameters. The observation equations of linear combinations given in this section are based on the full raw observation equations described in section 4.1, as the corrections needed to form reduced observation equations depend on the type of linear combination.

4.2.1 Geometry-Free

The reduced observation equation for the Geometry-Free (GF) linear combination of two code observables for signals Σia and Σjb is given by

$$\begin{aligned}\tilde{P}^s_{r,GF(\Sigma ia,\Sigma jb)}(t) &= P^s_{r,\Sigma ia}(t) - P^s_{r,\Sigma jb}(t) - Pcorr^s_{r,GF(\Sigma ia,\Sigma jb)}(t) \\ &= 40.28 \cdot (1/f_i^2 - 1/f_j^2) \cdot STEC^s_r(t) + c \cdot \left[d^s_{ia-jb}(t) + d_{r,\Sigma ia-\Sigma jb}(t) \right] + \epsilon^s_{r,\Sigma ia}(t) - \epsilon^s_{r,\Sigma jb}(t)\,,\end{aligned} \tag{4.56}$$

with

$$Pcorr^s_{r,GF(\Sigma ia,\Sigma jb)}(t) = dr^s_{ia}(t) - dr^s_{jb}(t) - dr_{r,ia}(t) + dr_{r,jb}\,, \tag{4.57}$$

considering the differences of the signal dependent antenna offset range corrections.

The reduced geometry-free observation equation (in m) of two phase observables with frequencies i and j is given by

$$\begin{aligned}\tilde{\Phi}^s_{r,GF(i,j)}(t) &= \Phi^s_{r,i}(t) - \Phi^s_{r,j}(t) - \Phi corr^s_{r,GF(i,j)}(t) \\ &= 40.28 \cdot (1/f_j^2 - 1/f_i^2) \cdot STEC^s_r(t) + \lambda_j M^s_{r,j}(t) - \lambda_i M^s_{r,i}(t) + \eta^s_{r,i}(t) - \eta^s_{r,j}(t)\,,\end{aligned} \tag{4.58}$$

with

$$\Phi corr^s_{r,GF(i,j)}(t) = \delta r^s_i(t) - \delta r^s_j(t) - \delta r_{r,i}(t) + \delta r_{r,i}(t) + \left(\lambda_i - \lambda_j\right) pwu^s_r(t) \tag{4.59}$$

The reduced observation equations of the geometry-free linear combination contain the slant ionospheric delay $STEC^s_r(t)$, for code observations the so called satellite and receiver Differential Code Bias (DCB) of the used signal combination $d^s_{ia-jb}(t)$ and $d_{r,\Sigma ia-\Sigma jb}(t)$ respectively and for phase observations the difference (in units of length) of the carrier phase float ambiguities $\lambda_i M^s_{r,i}(t)$ and $\lambda_j M^s_{r,j}(t)$.

The DCBs are defined as the difference between code biases of two different signals. As for the raw code biases, DCBs are defined separately by satellite differential code biases

$$d^s_{jb-ia} = d^s_{jb} - d^s_{ia}\,, \tag{4.60}$$

and receiver differential code biases

$$d_{r,\Sigma jb-\Sigma ia} = d_{r,\Sigma jb} - d_{r,\Sigma ia}\,. \tag{4.61}$$

4.2.2 Ionosphere-Free

The reduced observation equation for the ionosphere-free (IF) linear combination of two code observables for signals Σia and Σjb is given by

$$\begin{aligned}\tilde{P}^s_{r,IF(\Sigma ia,\Sigma jb)}(t) &= \tfrac{f_i^2}{f_i^2 - f_j^2} \cdot P^s_{r,\Sigma ia}(t) - \tfrac{f_j^2}{f_i^2 - f_j^2} \cdot P^s_{r,\Sigma jb}(t) - Pcorr^s_{r,IF(\Sigma ia,\Sigma jb)}(t) \\ &= \rho^s_r(t) + c[\tilde{dt}_{r,\Xi}(t) - dt^s_\Xi(t^{tog})] + dtro^s_{r,wg}(t) \\ &\quad + c \cdot \left[d^s_{IF(ia,jb)}(t) + d_{r,IF(\Sigma ia,\Sigma jb)}(t) \right] + \epsilon^s_{r,IF(\Sigma ia,\Sigma jb)}(t)\,,\end{aligned} \tag{4.62}$$

with the correction term

$$\begin{aligned}Pcorr^s_{r,IF(\Sigma ia,\Sigma jb)}(t) &= corr_{\Delta T^s_r}(t_{tor}) + dr^s_{IF(ia,jb)}(t) - dr_{r,IF(\Sigma ia,\Sigma jb)}(t) \\ &\quad + disp_r(t) + \delta_{rel}(t) + m_h(e) \cdot ZHD_r(t) + c \cdot \delta_{stc}(t)\,,\end{aligned} \tag{4.63}$$

considering the ionosphere-free combination of the antenna offset range corrections. The reduced observation equation of the ionosphere-free linear combination (4.62) contains the same geometric terms as the individual observation equation (4.49) but no ionospheric delay.

The ionosphere-free code biases are defined by the IF linear combination of the raw code biases of the corresponding signals. As for the raw code biases, IF code biases are defined separately by ionosphere-free satellite code biases

$$d^s_{IF(ia,jb)} = \frac{f_i^2}{f_i^2 - f_j^2} \cdot d^s_{ia} - \frac{f_j^2}{f_i^2 - f_j^2} \cdot d^s_{jb} \,, \tag{4.64}$$

and ionosphere-free receiver code biases

$$d_{r,IF(\Sigma ia,\Sigma jb)} = \frac{f_i^2}{f_i^2 - f_j^2} \cdot d_{r,\Sigma ia} - \frac{f_j^2}{f_i^2 - f_j^2} \cdot d_{r,\Sigma jb} \,. \tag{4.65}$$

The reduced ionosphere-free observation equation of two phase observables (in m) with frequencies i and j is given by

$$\begin{aligned} \tilde{\Phi}^s_{r,IF(i,j)}(t) = \lambda_n \tilde{\phi}^s_{r,IF(i,j)}(t) &= \tfrac{f_i^2}{f_i^2 - f_j^2} \cdot \Phi^s_{r,i}(t) - \tfrac{f_j^2}{f_i^2 - f_j^2} \cdot \Phi^s_{r,j}(t) - \Phi corr^s_{r,IF(i,j)}(t) \\ &= \rho^s_r(t) + c[\tilde{dt}_{r,\Xi}(t) - dt^s_{\Xi}(t^{tog})] + dtro^s_{r,wg}(t) \\ &\quad - \lambda_n M^s_{r,IF(i,j)} + \eta^s_{r,IF(i,j)}(t) \end{aligned} \tag{4.66}$$

with the correction term

$$\begin{aligned} \Phi corr^s_{r,IF(i,j)}(t) = corr_{\Delta T^s_r}(t) &+ \delta r^s_{IF(i,j)}(t) - \delta r_{r,IF(i,j)}(t) \\ &+ disp_r(t) + \delta_{rel}(t) + m_h(e) \cdot ZHD_r(t) + c \cdot \delta_{stc}(t) + \lambda_n pwu^s_r(t) \,, \end{aligned} \tag{4.67}$$

considering the ionosphere-free combination of the antenna offset range corrections and the combined effect of the phase wind up $\lambda_n pwu^s_r(t)$ with the so called NL wavelength $\lambda_n = c/(f_i + f_j)$.

The float ambiguity of the ionosphere-free phase observation equation is given by

$$M^s_{r,IF(i,j)} = N^s_{r,IF(i,j)} - \delta_{r,IF(i,j)} - \delta^s_{IF(i,j)} \tag{4.68}$$

where the ionosphere-free combination of the integer ambiguities $N^s_{r,i}$ and $N^s_{r,j}$ is defined by

$$\begin{aligned} \lambda_n N^s_{r,IF(i,j)} &= \tfrac{f_i^2}{f_i^2 - f_j^2} \cdot \lambda_i N^s_{r,i} - \tfrac{f_j^2}{f_i^2 - f_j^2} \cdot \lambda_j N^s_{r,j} \\ N^s_{r,IF(i,j)} &= \tfrac{f_i}{f_i - f_j} \cdot N^s_{r,i} - \tfrac{f_j}{f_i - f_j} \cdot N^s_{r,j} = N^s_{r,i} + \tfrac{f_j}{f_i - f_j} \cdot (N^s_{r,i} - N^s_{r,j}) = N^s_{r,i} + \tfrac{\lambda_w}{\lambda_j} \cdot N^s_{r,w} \,, \end{aligned} \tag{4.69}$$

with the so called WL wavelength $\lambda_w = c/(f_i - f_j)$ and widelane integer ambiguity $N^s_{r,w} = N^s_{r,i-j} = N^s_{r,i} - N^s_{r,j}$.

The definition in (4.69) also applies to the ionosphere-free combination of the phase biases δ_i and δ_j to form $\delta_{IF(i,j)}$, hence from inserting (4.69) into (4.68) follows

$$M^s_{r,IF(i,j)} = M^s_{r,i} + \frac{\lambda_w}{\lambda_j} M^s_{r,i-j} \,. \tag{4.70}$$

with $M^s_{r,i-j} = M^s_{r,i} - M^s_{r,j} = N^s_{r,w} - \delta_{r,i-j} - \delta^s_{i-j}$. From (4.69) it is obvious, that the ionosphere free carrier phase ambiguity $N^s_{r,IF(i,j)}$ is not an integer number. This prevents the integer ambiguity resolution from this type of observation alone in all common processing algorithms making use of the ionosphere-free linear combination. As described in section 5.1.3, this issue is commonly solved by using an additional linear combination of two code and two phase observations, the so called Melbourne-Wuebbena (MW) linear combination.

4.2.3 Melbourne-Wuebbena

The reduced observation equation for the Melbourne-Wuebbena (MW) linear combination of two code observables for signals Σia and Σjb and the corresponding phase observables (in m) with frequencies i and j is given by

$$\begin{aligned}\widetilde{MW}^{s}_{r,(\Sigma ia,\Sigma jb)}(t) &= \tfrac{f_i}{f_i-f_j}\cdot\Phi^{s}_{r,i}(t)-\tfrac{f_j}{f_i-f_j}\cdot\Phi^{s}_{r,j}(t)-\left[\tfrac{f_i}{f_i+f_j}\cdot P^{s}_{r,\Sigma ia}(t)+\tfrac{f_j}{f_i+f_j}\cdot P^{s}_{r,\Sigma jb}(t)\right]-MWcorr^{s}_{r,MW(\Sigma ia,\Sigma jb)}(t)\\ &= -\lambda_w M^{s}_{r,i-j}-c\cdot\left[d_{r,MW(\Sigma ia,\Sigma jb)}(t)+d^{s}_{MW(ia,jb)}(t)\right]+\epsilon^{s}_{r,MW(\Sigma ia,\Sigma jb)}(t)\end{aligned} \tag{4.71}$$

with the correction term

$$\begin{aligned}MWcorr^{s}_{r,MW(\Sigma ia,\Sigma jb)}(t) = \tfrac{1}{f_i-f_j}&\left[f_i\cdot\left(\delta r^{s}_{i}(t)-\delta r_{r,i}(t)\right)-f_j\cdot\left(\delta r^{s}_{j}(t)-\delta r_{r,j}(t)\right)\right]\\ -\tfrac{1}{f_i+f_j}&\left[f_i\cdot\left(dr^{s}_{ia}(t)-dr_{r,ia}(t)\right)+f_j\cdot\left(dr^{s}_{jb}(t)-\delta r_{r,jb}(t)\right)\right]\end{aligned} \tag{4.72}$$

considering the Melbourne-Wuebbena combination of the antenna offset range corrections. Signal independent corrections and the phase wind-up effect cancel in the Melbourne-Wuebbena linear combination and therefore do not need to be applied. The receiver and satellite MW code biases are given by

$$\begin{aligned}d_{r,MW(\Sigma ia,\Sigma jb)} &= \tfrac{f_i}{f_i+f_j}d_{r,\Sigma ia}+\tfrac{f_j}{f_i+f_j}d_{r,\Sigma jb}\\ d^{s}_{MW(ia,jb)} &= \tfrac{f_i}{f_i+f_j}d^{s}_{ia}+\tfrac{f_j}{f_i+f_j}d^{s}_{jb}\,.\end{aligned} \tag{4.73}$$

The Melbourne-Wuebbena linear combination (4.71) contains the widelane integer ambiguity $N^{s}_{r,w}$ with the corresponding differential phase biases $\delta_{i-j}(t)$ and a linear combination of code biases. Therefore only a biased widelane integer ambiguity can be retrieved from the MW linear combination. As described in section 5.1.2, this issue can be solved by forming double differences of the Melbourne-Wuebbena linear combination with the assumption that the MW code biases cancel.

4.3 Summary of Different Observation Models

Table 4.2 provides a summary of the components in the raw observation model described in section 4.1 and the observation models of linear combinations of GNSS observables described in section 4.2, where ∅ indicates that a component is eliminated by forming the corresponding linear combination.

Table 4.2: Summary of the components in the raw observation model and observation models of linear combinations of GNSS observables. The symbol ∅ indicates that a component is eliminated by forming the corresponding linear combination.

Obs. Model	Pos_r	Pos^s	Clk_r	Clk^s	Tropo	Iono	CodeBias_r	CodeBias^s	Ambiguity
RAW	$\boldsymbol{r}_r$	$\boldsymbol{r}^s$	$dt_{r,\Xi}$	dt^{s}_{Ξ}	$dtro^{s}_{r,wg}$	$STEC^{s}_{r}$	$d_{r,\Sigma ia}$	d^{s}_{ia}	$\lambda_i M^{s}_{r,i}$
GF	∅	∅	∅	∅	∅	$STEC^{s}_{r}$	$d_{r,\Sigma ia-\Sigma jb}$	d^{s}_{ia-jb}	$\lambda_i M^{s}_{r,i}-\lambda_j M^{s}_{r,j}$
IF	$\boldsymbol{r}_r$	$\boldsymbol{r}^s$	$dt_{r,\Xi}$	dt^{s}_{Ξ}	$dtro^{s}_{r,wg}$	∅	$d_{r,IF(\Sigma ia,\Sigma jb)}$	$d^{s}_{IF(ia,jb)}$	$\lambda_n\left(M^{s}_{r,i}+\lambda_w/\lambda_j M^{s}_{r,i-j}\right)$
MW	∅	∅	∅	∅	∅	∅	$d_{r,MW(\Sigma ia,\Sigma jb)}$	$d^{s}_{MW(ia,jb)}$	$\lambda_w M^{s}_{r,i-j}$

5 GNSS Observation Processing

The GNSS observables introduced in section 4 can be used to estimate a variety of geodetic parameters like station coordinates, satellite orbits, orientation of the Earth and time. This section describes the conventional processing approach for precise geodetic applications based on the dual-frequency IF linear combination, introduces the GNSS raw observation processing approach, referred to as RAW and outlines the fundamentals of the parameter estimation algorithms applied in this work.

5.1 Conventional GNSS Observation Processing

The conventional processing approach for precise dual-frequency applications is based on the IF linear combination described in 4.2.2. The main advantage of this approach is the cancelation of the first order ionospheric delay up to 99.9 % (Hernandez-Pajares et al., 2007). It should be noted that the term ionosphere-free is not fully correct, as several approximations are involved in the derivation of the first order ionospheric slant delay (4.36), as described in (Hofmann-Wellenhof et al., 1992; Seeber, 1993).
The formation of the IF linear combination of code and phase observations, described in (4.62) and (4.66), leads to an increase of the observation noise due to the law of error propagation by a factor of $\approx 2.5 - 3.5$, compared to the raw observation noise. Table 5.1 shows the factors of observation noise increase of the IF linear combination for different GNSS and signal combinations.

Table 5.1: Observation noise increase factor of the IF linear combination relative to the raw observation noise for different GNSS and signal combinations.

GNSS	IF LC	Noise Factor
Galileo	E1/E5a	2.59
	E1/E5b	2.81
GPS	L1/L2	2.98
	L1/L5	2.59
BeiDou	B1I/B2I	2.90
	B1I/B3I	3.53

As the IF linear combination is based on dual-frequency observations only, the usage of available multi-frequency signals for this commonly used processing approach is limited by definition. One option to make use of multi-frequency observations is to form different dual-frequency IF linear combinations, as shown in Table 5.1. However, this implies the cancelation of different dual-frequency data based ionospheric delays for the different IF signal combinations. Therefore, the dual-frequency IF linear combination is not the preferred method for processing all available multi-signal observations. The following sections describe the state-of-the-art methods for the handling of code biases, phase biases and ambiguity resolution in the conventional IF linear combination processing approach.

5.1.1 Code Bias Handling

When dealing with a single dual-frequency IF signal combination, as it was the case in the past decades for GPS L1/L2 only applications, signal code biases as introduced in section 4.1.3 did not play an important role and could be ignored for standard positioning applications. With multiple GNSS and signals on multiple frequencies available today, the handling of signal delays becomes a crucial part of the parameter estimation process when combining observations from more than two signals. in (Villiger et al., 2019) a detailed analysis of observable specific signal biases, ionosphere-free signal biases and differential signal biases has been performed.
However, when processing the conventional dual-frequency IF linear combination of code and phase observations, the corresponding code biases can be ignored for most PVT applications. Satellite clock offsets broadcast in the Galileo and GPS navigation messages, provided by the International GNSS Service (IGS) and most other service providers are based on the ionosphere-free linear combination of dual-frequency observations (Galileo OS SIS ICD, 2016; IS-GPS-200, 2015; Dach et al., 2015a). This implies that the provided satellite clock offsets $dt^s_{IF(ia,jb),\Xi}(t)$ contain the ionosphere-free linear combination of the respective code biases $d^s_{IF(ia,jb)}$, defined in (4.64)

$$dt^s_{IF(ia,jb),\Xi}(t) = dt^s_{\Xi}(t) - d^s_{IF(ia,jb)}(t)\,, \tag{5.1}$$

where $dt^s_{\Xi}(t)$ is the unbiased satellite clock offset, defined in (4.3). For the broadcast satellite clock offsets, the reference time scale is given by Ξ=GST for Galileo and Ξ=GPST for GPS. As the satellite IF code biases are included in the broadcast satellite clock offsets and other service providers, they are implicitly applied when these satellite clock products are used and do not need to be considered by the user. Receiver IF code biases are typically ignored for standard PVT solutions, except for precise timing applications, and are estimated as part of the receiver clock offset

$$dt_{r,IF(\Sigma ia,\Sigma jb),\Xi}(t) = dt_{r,\Xi}(t) - d_{r,IF(\Sigma ia,\Sigma jb)}(t)\,. \tag{5.2}$$

Equation (5.2) indicates that for multi-GNSS applications an additional parameter, referred to as ISB, needs to be determined as the estimated receiver clock contains GNSS and signal dependent biases. A description of the ISB is given in section 7.3.2.

Compared to Galileo and GPS, the satellite clock offsets broadcast in the BeiDou navigation message are an exception, as the B3I signal is selected as reference signal (BeiDou OS B3I SIS ICD, 2018). This implies that the broadcast BeiDou satellite clock offsets $dt^s_{brdc,BDT}(t)$ contain the B3I signal satellite code bias

$$dt^s_{brdc,BDT}(t) = dt^s_{BDT}(t) - d^s_{C6I}(t)\,. \tag{5.3}$$

Using these satellite clock offsets in the conventional IF linear combination processing approach, would require the user to apply additional satellite code biases, described in section 5.2.4.

In order to support single-frequency PVT applications in combination with the broadcast IF satellite clock offsets, or based on signal B3I for BeiDou, all GNSS satellites transmit so called satellite group delay (Satellite Group Delay (SGD)) parameters as part of their navigation message, also referred to as Broadcast Group Delay (BGD) (Galileo OS SIS ICD, 2016; IS-GPS-200, 2015; BeiDou OS SIS ICD, 2016). Single-frequency users, except for BeiDou signal B3I, are required to apply the additional satellite BGDs, whereas the corresponding receiver code biases are typically ignored. A detailed description of BGDs is provided in section 5.2.4.

In addition to satellite code bias parameters broadcast in the GNSS navigation messages and to support multi-signal applications, different institutes (e.g. Deutsches Zentrum für Luft- und Raumfahrt (DLR) and Chinese Academy of Sciences (CAS)) generate multi-signal satellite DCB products, available at (CDDIS, Crustal Dynamics Data Information System, 2019a). These satellite DCBs are commonly determined from GF linear combinations of GNSS observations, described in (4.56) by applying a zero-mean constraint on satellite DCBs per constellation to separate receiver-specific and satellite-specific signal code biases (Montenbruck et al., 2014). These satellite DCBs $\tilde{d}^s_{ia-jb}$ deviate from the physical satellite DCB d^s_{ia-jb} by the constellation DCB mean value

$$\tilde{d}^s_{ia-jb} = d^s_{ia-jb} - \frac{1}{n}\sum_s^n d^s_{ia-jb}\,. \tag{5.4}$$

The zero-mean constraint is applied to remove a rank deficiency in the conventional DCB estimation process, which is needed as GF observations only contain the sum of receiver- and satellite-specific DCBs, as shown in (4.56).

The impact of (re)defining satellite DCBs according to (5.4) will be analysed in section 7.1.2.

5.1.2 Observation Differences

As described in section 4.2.3, the MW linear combination formed by phase and code observations contains a linear combination of code biases and therefore only provides a biased widelane ambiguity. This issue is commonly solved by forming double differences of the Melbourne-Wuebbena linear combination with the assumption that the MW code biases cancel. This allows to retrieve a double difference widelane ambiguity with integer nature, which is used in the conventional integer ambiguity resolution approach described in section 5.1.3. The double difference MW observation equation is given by the difference of the MW linear combination in (4.71) for receivers A, B and satellites k, l

$$\begin{aligned}\widetilde{MW}^{kl}_{AB,(\Sigma ia,\Sigma jb)}(t) &= \widetilde{MW}^{k}_{A,(\Sigma ia,\Sigma jb)}(t) - \widetilde{MW}^{k}_{B,(\Sigma ia,\Sigma jb)}(t) - \widetilde{MW}^{l}_{A,(\Sigma ia,\Sigma jb)}(t) + \widetilde{MW}^{l}_{B,(\Sigma ia,\Sigma jb)}(t) \\ &= -\lambda_w M^{kl}_{AB,i-j} + \epsilon^{kl}_{AB,MW(\Sigma ia,\Sigma jb)}(t)\end{aligned} \tag{5.5}$$

As shown in (6.3), the expected value of a double difference float ambiguity is given by the corresponding integer ambiguity, which also applies to the double difference widelane ambiguity in (5.5).

However, in order to make use of the double difference widelane ambiguity, double differences also have to be formed for the corresponding ionosphere-free linear combination. The ambiguity term of the double difference carrier phase IF linear combination follows from (4.70) and is given by

$$M^{kl}_{AB,IF(i,j)} = M^{kl}_{AB,i} + \frac{\lambda_w}{\lambda_j} \cdot M^{kl}_{AB,i-j} \,. \tag{5.6}$$

Equations 5.5 and 5.6 form the basis of the conventional carrier phase integer ambiguity resolution approach for the ionosphere-free linear combination.

5.1.3 Carrier Phase Integer Ambiguity Resolution

The resolution of integer values for the carrier phase ambiguity term is the key to high-precision GNSS applications as it allows to exploit the precision of the carrier phase measurement in the form of precise phase pseudoranges. The resolution of integer ambiguities therefore is not a goal in itself, but to achieve an improvement in the estimation of other parameters of interest. To whole process of exploiting the increased precision due to resolved integer ambiguities is usually performed in three steps:

1. Float solution: The standard least squares adjustment is performed with the carrier phase ambiguities estimated as float values

2. Integer Ambiguity Resolution: The float ambiguities are mapped to the corresponding integer values

3. Fixed Solution: The least squares adjustment is repeated with fixed values for the resolved integer ambiguities

The second step involves the actual mapping, also referred to as fixing, of the float ambiguities to integer values, which has been an active field of research in the past decades and still is today. Various methods for the determination of integer ambiguities based on float ambiguity estimates have been proposed in the literature. Discussions of these methods can be found in standard GNSS textbooks, such as (Hofmann-Wellenhof et al., 1992), (Teunissen, 1998), (Kaplan and Hegarty, 2017) and (Teunissen, 2017). Integer ambiguity resolution methods can generally be divided in three different approaches (cf. Teunissen, 2017)

Integer Rounding

The simplest way of mapping float ambiguities to integer values is to round each float ambiguity to its nearest integer, referred to as Integer Rounding (IR). This method does not take any correlations between ambiguities into account and therefore cannot be considered a serious method for resolving correct integer ambiguities (Teunissen et al., 2002).

Integer Bootstrapping

The sequential conditional integer rounding method, also referred to as Integer Bootstrapping (IB) is an advanced integer ambiguity resolution approach, as it takes some of the correlations between ambiguities into account. The IB method performs a sequential conditional Least Squares (LSQ) adjustment by rounding individual ambiguities to their nearest integer and in sequential steps taking the correlation of the formed integer ambiguities with other ambiguities into account (Teunissen, 1998).

Integer Least-Squares

The concept of performing a least-squares optimisation based on the integer nature of ambiguity parameters by minimising the squared norm of the deviation of float ambiguities from their corresponding integer value is referred to as Integer Least Squares (ILS) and was first introduced in (Teunissen, 1993). In contrast to the other methods IR and IB, no direct computation of the integer values can be performed. Instead, an integer search is necessary to obtain a solution of the ILS method. Due to high correlations between carrier phase ambiguities in GNSS processing, the integer ambiguity search space is large. The ILS method is therefore shifting the problem of fixing integer ambiguities to finding integer ambiguities. Detailed information on the ILS method can be found in (Teunissen, 1999) and (Teunissen, 2001).

The most common utilisation of the ILS concept is the Least-Squares AMBiguity Decorrelation Adjustment (LAMBDA) method (Teunissen, 1995), where the integer ambiguity search space is refined by performing a decorrelation transformation of the ambiguities, referred to as Z-transformation. Various efficiency improvements due to integer ambiguity search space refinements are described in e.g. (Teunissen, 1995), (De Jonge and Tiberius, 1996) and (Chang et al., 2005).
Other realisations of the integer ambiguity resolution methods described above are summarised in (Verhagen, 2005), where all methods except two are relying on the ILS concept and therefore only differ in the way the search space is defined. The other two methods, namely Three-Carrier Ambiguity Resolution (TCAR) (Vollath et al., 1998) and Cascading Integer Resolution (CIR), are based on IB and are compared to LAMBDA in (Teunissen et al., 2002). Other comparisons of the different integer ambiguity resolution methods can be found in e.g. (Kim and Langley, 2000), (Joosten and Verhagen, 2003), (Teunissen, 2003) and (Verhagen and Joosten, 2004).

The fundamental prerequisite, which has to be fulfilled to successfully apply any of the integer ambiguity resolution methods, is that the carrier phase ambiguities of the functional model used as input for the ambiguity resolution algorithm are of integer nature. In general this is not the case for the carrier phase float ambiguity of raw observations and other undifferenced observations (cf. Table 4.2), which is not an integer number as it includes unknown instrumental phase biases of the satellite and receiver (Blewitt, 1997). By applying these phase biases as additional corrections, theoretically an integer nature could be constructed for the raw observation ambiguities. All other undifferenced observation models in Table 4.2 would require additional corrections or assumptions to construct an integer nature ambiguity term. Conventional phase bias handling and applications making use of their corrections are described in section 5.1.4. The handling of raw phase biases in this work and proposed applications are described in sections 6.3 and 7.5.3.

In order to fulfil the fundamental prerequisite of using carrier phase ambiguities of integer nature for the resolution of integer ambiguities, the methods described above are all based on Double Difference (DD) phase observations and the estimation of DD carrier phase ambiguities, which according to Teunissen et al. (2002) are *known* to be integers. As shown in (6.3), the expected value of a double difference carrier phase float ambiguity, as defined in (4.53), is indeed integer, however, this implies the cancelation of all phase biases in the double difference. in (Teunissen, 2017) the so called mixed-integer functional model described in (Teunissen et al., 2002) is introduced, but in contrast to (Teunissen et al., 2002), without explicitly mentioning the formation of double difference observations. It is important to note, that with the mixed-integer functional model a general system of linear(ized) equations is described, in which some of the parameters are real numbers and others are of integer nature. Therefore, the mixed-integer functional model either describes double differences of observations, or undifferenced observations with additionally applied corrections, which is not explicitly mentioned in (Teunissen, 2017).

For the resolution of integer ambiguity values in the conventional dual-frequency ionosphere-free linear combination processing approach, forming double differences alone is not sufficient. As shown in section 4.2.2, the carrier phase ambiguity of the IF linear combination is not an integer number, which prevents the resolution of ambiguity integer values from this type of observation alone. In fact, the carrier phase ambiguity of the IF linear combination contains two integer ambiguities, therefore a second observation is required to resolve both integer numbers. This issue is commonly solved by using the Melbourne-Wuebbena (MW) linear combination in addition, introduced in section 4.2.3. However, as shown in section 5.1.2, only the double difference of the MW linear combination contains carrier phase ambiguities with integer nature. Therefore, the conventional carrier phase integer ambiguity resolution approach is based on double differences of the dual-frequency ionosphere-free linear combination and double differences of the Melbourne-Wuebenna linear combination of two code and phase observables.
Starting from equations 5.5 and 5.6, the conventional carrier phase integer ambiguity resolution approach first resolves the double difference widelane integer ambiguities $N^{kl}_{AB,i-j}$ and forms the so called double difference narrowlane ambiguities

$$M^{kl}_{AB,n} \equiv M^{kl}_{AB,i} = M^{kl}_{AB,IF(i,j)} - \frac{\lambda_w}{\lambda_j} \cdot N^{kl}_{AB,i-j} \,, \tag{5.7}$$

based on the estimated real-valued DD IF ambiguities $M^{kl}_{AB,IF(i,j)}$ and the resolved DD MW integer ambiguities $N^{kl}_{AB,i-j}$.
After resolving the integer values of the double difference narrowlane ambiguities $N^{kl}_{AB,i}$, the so called *fixed*, integer ambiguity based but still real-valued DD IF ambiguities can be computed by

$$\bar{M}^{kl}_{AB,IF(i,j)} = N^{kl}_{AB,i} + \frac{\lambda_w}{\lambda_j} \cdot N^{kl}_{AB,i-j} \,, \tag{5.8}$$

which are then used to compute the fixed solution.

5.1.4 Phase Bias Handling and PPP-RTK

Carrier phase biases, as introduced in (4.17), are eliminated in the conventional integer ambiguity resolution approaches described in section 5.1.3 by forming double difference observations. In order to enable integer ambiguity resolution in PPP applications, referred to as PPP Real Time Kinematic (PPP-RTK) (Wübbena et al., 2005; Mervart et al., 2008; Teunissen et al., 2010), corrections based on phase biases are required (amongst others) in addition to precise GNSS satellite orbit and clock products to recover the integer nature of the PPP user carrier phase ambiguity term. Depending on the applied method, different PPP-RTK corrections of clock parameters, phase biases or ambiguities are computed in a network-level integer ambiguity fixed solution and provided to the PPP-RTK user.

Table 5.2: Overview of commonly used PPP-RTK methods.

PPP-RTK Method	Observations	DD User Ambiguities	PPP-RTK Corrections
Integer Recovery Clock (IRC) (Laurichesse et al., 2009)	Iono-Free	WL/NL	Sat. code/phase clocks WL bias
Decoupled Clock Model (DCM) (Collins et al., 2010)	Iono-Free	WL/NL	Sat. code/phase clocks WL bias
Uncalibrated Phase Delays (UPD) Fractional Cycle Bias (FCB) (Ge et al., 2008; Geng et al., 2011, 2012)	Iono-Free	WL/NL	Sat. clock WL/NL ambiguity fractionals of a reference station
Common Clock (CC) (Zhang et al., 2011)	Raw	Per frequency	Sat. clock Sat. bias per freq
Distinct Clocks (DC) (De Jonge, 1998; Teunissen et al., 2010)	Raw	Per frequency	Sat. code clock Sat. phase clock per freq

Different PPP-RTK approaches have been developed in recent years and Table 5.2 provides a summary of commonly used methods. While some of these PPP-RTK approaches are based on dual-frequency ionosphere-free observations, the CC and DC models are formulated to be applied (in theory) to multi-frequency undifferenced (raw) observations. However, the examples provided in the corresponding references (Teunissen et al., 2010; Zhang et al., 2011) are only based on dual frequency observations. It should be noted, that the PPP-RTK corrections in Table 5.2 are re-parameterised estimable versions of the original clock offset, bias and ambiguity parameters.

An extensive review and discussion of PPP-RTK methods and a comprehensive derivation of the corrections shown in Table 5.2 is provided in (Teunissen and Khodabandeh, 2014), where it is demonstrated that the corrections computed by different methods provide the same information content and can be transformed from one to the other, making the methods practically equivalent. According to Teunissen and Khodabandeh (2014), the lack of the ionospheric delay in the IF linear combination is considered the bottleneck for fast ambiguity resolution with the corresponding methods. This motivates the use of raw observations to achieve faster ambiguity resolution by applying ionospheric corrections in addition, which has been demonstrated in (Zhang et al., 2011). Teunissen and Khodabandeh (2014) also demonstrate that due to the parameterisation of the different methods the PPP user ambiguities are standard double difference ambiguities and no undifferenced ambiguities as sometimes stated. According to Teunissen and Khodabandeh (2014), "*the integer ambiguity resolution at the PPP-RTK user side is always that of double difference ambiguities*". Hence, the required integer nature double difference ambiguities on network-level, as discussed in section 5.1.3, intrinsically lead to double difference ambiguities at the PPP-RTK user side, realised by the additional PPP-RTK corrections.

5.2 Multi-GNSS Multi-Signal Raw Observation Processing

GNSS raw observation processing is the most straightforward approach of exploiting GNSS observables for the estimation of geodetic parameters. The raw observation processing approach (Schönemann et al., 2011; Schönemann, 2014), also referred to as raw method, makes use of the original (raw) observations generated by a GNSS receiver. No linear combinations and observation differences are formed, thus treating the observation equations in their original form as specified in (4.8) and (4.17). This implies, that several effects and biases eliminated by linear combinations or observation differences remain in the observation equation and need to be properly handled. In the raw method ionospheric delays and signal biases need to be either corrected or estimated, whereas in the conventional IF linear combination processing

approach biases are usually absorbed by the clock offsets, as shown in section 5.1.1, or eliminated by differencing as described in section 5.1.2. In multi-GNSS and multi-signal raw observation processing, all available original multi-signal observations from satellites of multiple GNSS are processed together to estimate all parameters in a joint least-squares adjustment, see section 5.3 for details.

5.2.1 Benefits and Challenges

The increasing number of signals available from the continuously modernised GNSS motivates the usage of multiple signals to exploit their individual characteristics. Conventional dual-frequency IF linear combination processing limits the number of usable signals and poses the problem of having to choose between different possible dual-signal combinations. In raw observation processing, there is no inherent limitation on the number of signals, therefore allowing to benefit from the increase in the number of signals already available today and in future. The use of the original (raw) observations preserves the individual signal characteristics and allows to analyse the individual effects like signal biases or signal measurement noise. The formation of (IF) linear combinations amplifies the noise of the resulting observation, as shown in section 5.1, whereas in raw observation processing the original noise characteristics of the individual signals can be analysed and used. This allows for example the explicit weighting and editing of individual observations based on the corresponding signal characteristics. Figure 5.1 shows the code observation residual Root Mean Square (RMS) daily mean values of individual Galileo signals and the ionosphere-free linear combination IF(E1,E5a) for station CEBR from the multi-GNSS and multi-signal POD analysed in section 7.4.

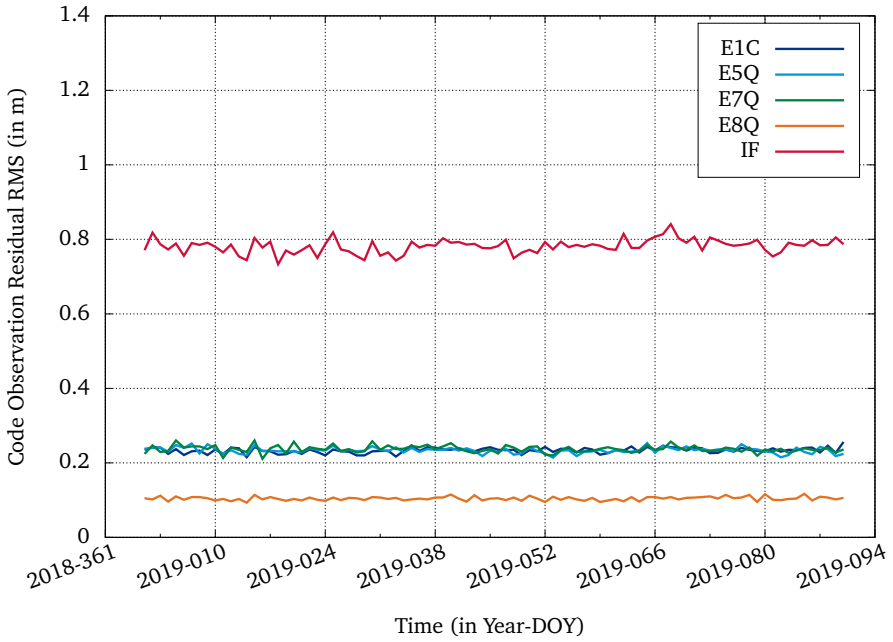

Figure 5.1: Code observation residual RMS daily mean values of individual Galileo signals and the ionosphere-free linear combination IF(E1,E5a) for station CEBR from analyses described in section 7.4.

The required handling of the ionospheric delay in raw observation processing can be recognised as benefit and challenge at the same time. The ionospheric delay remains in the raw observation equations, enabling the estimation of ionospheric effects in addition to common geodetic parameters (Odijk, 2002). Applying ionosphere corrections to raw observations instead of using the IF linear combination is also regarded beneficial in the context of PPP-RTK applications, as described in section 5.1.4. However, as the ionospheric delay is changing rapidly, it usually has to be estimated per processing epoch, thus generating a considerable amount of additional parameters. In addition there is a strong correlation between clock offset parameters, signal biases and the ionospheric delay, requiring a proper treatment of the additional parameters in order to solve the induced rank deficiency in the normal equation system, see section 5.3 for details.

5.2.2 Handling of Raw Observation Biases

In raw observation processing all signal biases remain in the observation equation and if more then one signal is processed, these biases need to be properly handled. They can not (all) be absorbed by the clock offset parameters, as it is usually done in the IF linear combination processing approach, as described in section 5.1.1. Although the raw

observation equations (4.8) and (4.17) only contain the sum of a receiver-satellite signal bias, it is commonly assumed that the signal bias can be separated in a satellite-specific and a receiver-specific bias. Due to the correlation of signal biases with clock offsets and the ionospheric delay, different constraints are necessary in order to eliminate the rank deficiency and successfully process raw observations from multiple signals and GNSS. For the code biases, this is typically done by setting the satellite and receiver code bias of a reference signal to zero, thereby redefining the remaining code biases to be differential code biases (DCBs), as shown in the example for the Galileo IOV satellite code biases below. This redefinition of code biases is required if no absolute raw observation code biases are available, which typically is not the case for both, GNSS receivers and satellites. Exceptions are GNSS receivers used for precise timing applications where absolute code biases are required as shown in section 7.3, as well as the Galileo IOV satellites where satellite-specific absolute code biases, measured by the satellite manufacturer, have been published. Thus, by setting a reference signal code bias to zero the respective clock offset is redefined by absorbing the reference signal code bias. However, instead of handling code biases in the commonly used differential approach, where the used signals have to be known a priori in order to provide a linear independent set of biases, they are still treated as observable specific biases. For multi-GNSS processing, this approach allows to determine a common receiver clock offset by selecting reference signals with similar (almost identical) receiver code biases (for example Galileo E1C and GPS G1C, as described in (Defraigne et al., 2013)), or by estimating a receiver-specific DCB between the two reference signals of different GNSS. In order to eliminate the rank deficiency and estimate ionospheric delays, the satellite and receiver DCBs of at least one additional signal have to be constrained to a priori values. However, if the estimation of physically meaningful ionospheric delays is of interest, the constrained signal DCBs also have to be physically correct. The estimation of physically meaningful satellite-specific DCBs and their application for the estimation of physically meaningful ionospheric delays is shown in sections 7.1 and 7.2.

Galileo is the first GNSS to publish satellite metadata (GSA, European GNSS Agency, 2019a) and reveals that raw signal absolute code biases of the IOV satellites are on the order of approximately $1\,\mu s$ - $3\,\mu s$. The so called satellite group delay (SGD) of for example signal band E1 on the primary subsystem of Galileo satellite GAL-103 (E19) has been measured by the spacecraft manufacturer on-ground prior to the satellite launch to be $d_{E1}^{GAL-103} = 3.1493\,\mu s$, as shown in Table 5.3.

Table 5.3: Galileo IOV satellite group delays (SGD) for the primary and redundant subsystems measured by the spacecraft manufacturer on-ground prior to launch (taken from GSA, European GNSS Agency, 2019a).

GSAT	Primary (in ns)			Redundant (in ns)		
	E1	E5	E6	E1	E5	E6
GAL-101	1214.8	1205.1	1208.9	1215.2	1204.9	1206.7
GAL-102	1218.9	1212.0	1211.2	1218.9	1212.5	1211.7
GAL-103	3149.3	3146.9	3149.8	3150.3	3149.3	3150.1
GAL-104	3150.1	3148.1	3148.3	3151.9	3150.7	3149.8

Selecting E1 as the reference signal for the code bias values of GAL-103 from Table 5.3, would modify the satellite clock offset by 3149.3 ns and redefine the observable specific code biases to be $d_{E1}^{GAL-103} = 0\,\text{ns}$, $d_{E5}^{GAL-103} = -2.4\,\text{ns}$ and $d_{E6}^{GAL-103} = 0.5\,\text{ns}$. However, as these code biases have been redefined relative to the reference signal E1 code bias, they actually are satellite DCBs.

As defined in (4.4), the magnitude of satellite DCBs is equivalent to the difference in signal transmission time $t_{ia}^{tot} - t_{jb}^{tot}$ for different signals. The measured DCB values for the Galileo IOV satellites satisfy the condition $|d_{ia} - d_{jb}| << 1\,\mu s$, derived in section 4.1.4, meaning that no geometric change due to the different times of signal transmission has to be accounted for, which confirms the assumption made in (4.6). As DCBs are relative biases between different signals and no absolute signal delays through cables and electronic equipment, it can be assumed that the above condition is also satisfied for GNSS receivers. This assumption is analysed in detail in section 7.1 for satellites of multiple GNSS and different receiver types.

As described in section 4.1.4, the absorption of the reference signal code bias by the respective clock offset parameter might introduce receiver-satellite geometry related ranging errors. For satellite clock offsets this might be the case, depending on the application, when the modified clock offset is used to iteratively compute the satellite position at the signal transmission epoch in the applied reference time scale. As the satellite reference signal code bias implicitly is introduced in the computation of the signal transmission time, the satellite position might be computed at an undesired point in time. Whether or not this effect is significant depends on the application and the magnitude of the reference signal code bias. Ignoring the modification of the GAL-103 satellite clock offset by the measured absolute code bias for signal E1 from Table 5.3 would introduce a maximum ranging error of 2 mm ($= 600\,\text{m}\,\text{s}^{-1} \cdot 3.15\,\mu s$) for a receiver on

Earth and 2.4 cm ($= 7.6\,\mathrm{km\,s^{-1}} \cdot 3.15\,\mu s$) for a receiver onboard of a LEO satellite, using the typical range rate values computed in section 4.1.4. Therefore this effect can usually be neglected in standard PVT applications on Earth.

For GNSS receivers, the modification of the clock offset might introduce ranging errors, if combined with the receiver clock range rate correction described in (4.26). Therefore, absolute signal code delays including antenna cable for a GNSS receiver system used in a global network adjustment with applied receiver clock range rate correction should not exceed the $1\,\mu s$ limit, as described in section 4.1.4.

5.2.3 Handling of Ionospheric Delay

As described in section 4.1.4, the first order ionospheric slant delay along the signal path between receiver r and satellite s for frequency f_i can be expressed (in m) by

$$dion^s_{r,i}(t) = \frac{40.28}{f_i^2} \cdot STEC^s_r(t)\,, \tag{5.9}$$

where $STEC^s_r(t)$ represents the slant total electron content along the signal path. In the raw method ionospheric delays can be determined from multi-signal raw observations by estimating the slant total electron content $STEC^s_r(t)$ in addition to common geodetic parameters in the least squares adjustment (Odijk, 2002). This can be done by either estimating the absolute ionospheric slant delay or using a VTEC map as a priori ionosphere model to estimate constrained residual STEC values. The STEC parameters are estimated per processing epoch and pre-eliminated from the normal equation system as described in (Dach et al., 2015b).

Depending on the setup of code bias parameters, physically not meaningful (biased) ionospheric delays might be determined. This could lead to negative STEC values, as demonstrated in section 7.2, which physically does not make sense as the STEC represents the number of electrons along the signal path.

5.2.4 Raw Observation Processing with Ionosphere-Free Products

All commonly available satellite orbit and clock products from broadcast navigation messages, provided by the IGS and most other service providers are based on the ionosphere-free linear combination of dual-frequency observations (Dach et al., 2015a). As described in section 5.1.1, this implies that the provided satellite clock offsets contain the ionosphere-free linear combination of the respective raw code biases $d^s_{IF(jb,kc)}$, defined in (4.64). An exception are the satellite clock offsets broadcast in the BeiDou navigation message, where the B3I signal is selected as reference signal, (cf. BeiDou OS B3I SIS ICD, 2018).

Applying the IF satellite clock offsets to the reduced raw code observation equation 4.49 at receiver measurement time $t = t_{tom}$ leads to a modification of satellite-specific code biases

$$\begin{aligned}\tilde{P}^s_{r,\Sigma ia}(t) = \rho^s_r(t) &+ c \cdot \left[dt_{r,\Xi}(t) - dt^s_{IF,\Xi}(t^{tog}) \right] \\ &+ dtro^s_{r,wg}(t) + 40.28/f_i^2 \cdot STEC^s_r(t) \\ &+ c \cdot \left[d^s_{ia}(t) - d^s_{IF(jb,kc)}(t) \right] + c\, d_{r,\Sigma ia}(t) + \epsilon^s_{r,\Sigma ia}(t)\,.\end{aligned} \tag{5.10}$$

The modified satellite-specific code biases, sometimes referred to as pseudo-absolute code biases (Villiger et al., 2019) can be expressed as a combination of differential code biases for the general case of signal ia

$$\begin{aligned} d^s_{ia} - d^s_{IF(jb,kc)} &= d^s_{ia} - \tfrac{f_j^2 \cdot d^s_{jb} - f_k^2 \cdot d^s_{kc}}{f_j^2 - f_k^2} \\ &= \tfrac{1}{f_k^2 - f_j^2} \left[f_k^2 \left(d^s_{ia} - d^s_{kc} \right) - f_j^2 \left(d^s_{ia} - d^s_{jb} \right) \right] \\ &= \tilde{\alpha}_{j,jk} \cdot d^s_{ia-kc} - \tilde{\alpha}_{k,jk} \cdot d^s_{ia-jb} \\ &= d^s_{ia-jb} + \tilde{\alpha}_{j,jk} \cdot d^s_{jb-kc}\,, \end{aligned} \tag{5.11}$$

where the equality $\tilde{\alpha}_{j,jk} - \tilde{\alpha}_{k,jk} = 1$ has been used and time arguments are neglected for clarity. The frequency dependent factor is given in the general form

$$\tilde{\alpha}_{i,jk} = \frac{f_j^2 f_k^2}{f_i^2 (f_k^2 - f_j^2)}\,. \tag{5.12}$$

For the special case of processing raw observations jb or kc, which have been used in the ionosphere-free linear combination $IF(jb,kc)$ to generate satellite orbit and clock offsets, the modified satellite-specific code biases are given by

$$\begin{aligned} d^s_{jb} - d^s_{IF(jb,kc)} &= \tilde{\alpha}_{j,jk} \cdot d^s_{jb-kc} = \frac{f_k^2}{f_k^2 - f_j^2} \cdot d^s_{jb-kc} \\ d^s_{kc} - d^s_{IF(jb,kc)} &= \tilde{\alpha}_{k,jk} \cdot d^s_{jb-kc} = \frac{f_j^2}{f_k^2 - f_j^2} \cdot d^s_{jb-kc} \,, \end{aligned} \tag{5.13}$$

which agrees with the general definition in (5.11), as $d^s_{jb-jb} = 0$. The modified satellite code biases in (5.13) are equivalent to the definition of the satellite BGD values broadcast in the Galileo and GPS navigation messages (cf. Galileo OS SIS ICD, 2016; IS-GPS-200, 2015)

$$\begin{aligned} BGD^s_{(E1,E5a)} &= \tilde{\alpha}_{1,15} \cdot d^s_{E1C-E5Q} \\ BGD^s_{(E1,E5b)} &= \tilde{\alpha}_{1,17} \cdot d^s_{E1C-E7Q} \\ T^s_{GD(L1P(Y),L2P(Y))} &= \tilde{\alpha}_{1,12} \cdot d^s_{G1W-G2W} \,, \end{aligned} \tag{5.14}$$

where the frequency indices refer to the signal frequencies of the corresponding GNSS, described in section 2.2.
For BeiDou, no clear mathematical definition of the broadcast group delay (group delay differential) is given in any of the Interface Control Document (ICD) (BeiDou OS SIS ICD, 2016; BeiDou OS B1I SIS ICD, 2019; BeiDou OS B3I SIS ICD, 2018). However, as it is stated that the B3I signal equipment group delay is included in the broadcast satellite clock offsets, it is assumed that the BeiDou satellite BGD values broadcast in the navigation messages are given by the DCBs relative to signal B3I

$$\begin{aligned} T^s_{GD1(B1I,B3I)} &= d^s_{C2I-C6I} \\ T^s_{GD2(B2I,B3I)} &= d^s_{C7I-C6I} \,, \end{aligned} \tag{5.15}$$

Whereas satellite group delays are broadcast to the users only to enable single frequency applications, the general concept in (5.11) can be applied to multi-signal GNSS raw observation processing, as used in the analysis described in section 7.3. As an example, the definitions of modified satellite code biases are given, applicable for multi-signal Galileo raw observation processing with satellite clock offsets derived from the Galileo F/NAV message, based on $IF(E1,E5a)$ (Galileo OS SIS ICD, 2016)

$$\begin{aligned} d^s_{E1C} - d^s_{IF(E1C,E5Q)} &= \tilde{\alpha}_{1,15} \cdot d^s_{E1C-E5Q} \\ d^s_{E5Q} - d^s_{IF(E1C,E5Q)} &= \tilde{\alpha}_{5,15} \cdot d^s_{E1C-E5Q} \\ d^s_{E7Q} - d^s_{IF(E1C,E5Q)} &= d^s_{E7Q-E1C} + \tilde{\alpha}_{1,15} \cdot d^s_{E1C-E5Q} \\ d^s_{E8Q} - d^s_{IF(E1C,E5Q)} &= d^s_{E8Q-E1C} + \tilde{\alpha}_{1,15} \cdot d^s_{E1C-E5Q} \\ d^s_{E6C} - d^s_{IF(E1C,E5Q)} &= d^s_{E6C-E1C} + \tilde{\alpha}_{1,15} \cdot d^s_{E1C-E5Q} \end{aligned} \tag{5.16}$$

It should be noted, that multi-signal pseudo-absolute satellite code biases are consistent with satellite clock offsets and absolute ionospheric delays only if the computation is based on physically meaningful satellite DCBs. The impact of not using physically meaningful satellite DCBs is analysed in sections 7.2 and 7.3.

5.3 Parameter Estimation Applied in Raw Method

As derived in section 4.1, the relation between the vector of observations $\boldsymbol{Y}(t)$ and vector of parameters $\boldsymbol{X}(t)$ is described by the nonlinear functional model $\boldsymbol{f}(\boldsymbol{X}(t),t)$

$$\boldsymbol{Y}(t) = \boldsymbol{f}(\boldsymbol{X}(t),t) = \begin{pmatrix} f_1(\boldsymbol{X}(t),t) \\ f_2(\boldsymbol{X}(t),t) \\ \vdots \\ f_l(\boldsymbol{X}(t),t) \end{pmatrix} \tag{5.17}$$

where $\boldsymbol{f}(\boldsymbol{X}(t),t)$ is the l-dimensional vector of observation equations (4.8) and (4.17) at time t. In this formulation and GNSS processing in general, the Gauss-Markov model (Niemeier, 2008) is used, relating the parameters to only one observation per equation $f_i(\boldsymbol{X}(t),t)$. The observations $\boldsymbol{Y}(t)$ are associated with the weight matrix $\boldsymbol{P}(t)$ to account for the difference in precision of code and phase measurements or code measurements of different signals and apply other

signal or elevation dependent weighting schemes. If the observations are assumed to be uncorrelated, the weight matrix is diagonal.
While the observation equations are nonlinear, commonly used parameter estimation approaches require linear models and therefore a linearisation of the functional model. Linearisation of the system equations implies that only approximate solutions are found, thus the best estimates $\hat{\boldsymbol{X}}(t)$ of the parameters need to be found in an iterative way, where the term "best" will be defined in the section 5.3.2. In this work, the estimation of parameters is based on the principle of *Linearised Iterative Weighted Batch LSQ Adjustment with Soft Constraints*, where the individual parts of this approach are explained in the following section.

5.3.1 Linearisation of the Functional Model

The functional model (5.17) is linearised by a Taylor series expansion, which requires nominal values $\boldsymbol{X}^*(t)$ for the estimated parameters, used to evaluate the partial derivatives of the functional model with respect to the parameters. The Taylor series expansion of a function $\boldsymbol{f}(\boldsymbol{X}(t),t)$ is given by:

$$\boldsymbol{f}(\boldsymbol{X}(t),t) = \boldsymbol{f}(\boldsymbol{X}^*(t)+\boldsymbol{x}(t),t) = \boldsymbol{f}(\boldsymbol{X}^*(t),t) + \left.\frac{\delta \boldsymbol{f}}{\delta \boldsymbol{X}}\right|_{X^*(t)} \boldsymbol{x}(t) + \mathcal{O}^2(\boldsymbol{x}(t)) \tag{5.18}$$

where $\boldsymbol{x}(t) = \boldsymbol{X}(t) - \boldsymbol{X}^*(t)$ is the vector of parameter deviations from the nominal values and represents the actual estimated parameters in a linearised LSQ adjustment, $\boldsymbol{f}(\boldsymbol{X}^*(t),t)$ is the nonlinear function of the nominal parameter values, often referred to as *computed or reconstituted observation*, which also includes all modelled effects not part of the estimated set of parameters. Second and higher order terms $\mathcal{O}^2(\boldsymbol{x}(t))$ are neglected.
The partial derivatives of the functional model or observation equations with respect to the parameters, evaluated at the nominal parameter values can be written in matrix notation as the so called design matrix

$$\boldsymbol{A}(t) = \left.\frac{\delta \boldsymbol{f}}{\delta \boldsymbol{X}}\right|_{X^*(t)} \tag{5.19}$$

For GNSS applications using code and phase observations with the functional models described in section 4.1, the design matrix is given by

$$\boldsymbol{A}(t) = \left[\left.\frac{\delta \boldsymbol{P}^s_{r,\Sigma ia}(t)}{\delta \boldsymbol{X}}\right|_{X^*(t)} \quad \left.\frac{\delta \boldsymbol{\Phi}^s_{r,i}(t)}{\delta \boldsymbol{X}}\right|_{X^*(t)} \right]^T , \tag{5.20}$$

where $\boldsymbol{P}^s_{r,\Sigma ia}(t)$ and $\boldsymbol{\Phi}^s_{r,i}(t)$ are the vectors of code and phase observation equations corresponding to all available observations at time t. With (5.17) and (5.18) the linearised system of equations can be written as

$$\boldsymbol{y}(t) = \boldsymbol{A}(t)\boldsymbol{x}(t) + \boldsymbol{v}(t) \tag{5.21}$$

where $\boldsymbol{y}(t) = \boldsymbol{Y}(t) - \boldsymbol{f}(\boldsymbol{X}^*(t),t)$ is the observation deviation vector, often referred to as *observed-minus-computed* vector and $\boldsymbol{v}(t)$ is the error or residual vector.

5.3.2 Solution of the Weighted Linearised System

The solution of (5.21) can be derived by the method of least squares (Gauss, 1809), which defines the term "best" estimate as the minimum of the weighted sum of squared residuals

$$\Omega(t) = \boldsymbol{v}^T(t)\boldsymbol{P}(t)\boldsymbol{v}(t) \rightarrow min\,. \tag{5.22}$$

Skipping the time arguments for clarity and inserting (5.21) in (5.22) gives:

$$\Omega = [\boldsymbol{y} - \boldsymbol{A}\,\boldsymbol{x}]^T\,\boldsymbol{P}\,[\boldsymbol{y} - \boldsymbol{A}\,\boldsymbol{x}] \rightarrow min\,. \tag{5.23}$$

The minimum condition is fulfilled for

$$0 \stackrel{!}{=} \frac{\delta\,\Omega}{\delta\,\boldsymbol{x}} = -2\boldsymbol{A}^T\boldsymbol{P}\,\boldsymbol{y} + 2\boldsymbol{A}^T\boldsymbol{P}\boldsymbol{A}\,\boldsymbol{x}\,, \tag{5.24}$$

and

$$0 \stackrel{!}{<} \frac{\delta^2\,\Omega}{\delta^2\,\boldsymbol{x}} = 2\boldsymbol{A}^T\boldsymbol{P}\boldsymbol{A}\,. \tag{5.25}$$

The solution of the weighted linear least squares problem at time t is given by multiplying (5.24) by the inverse of the so called normal equation matrix $\boldsymbol{N} = \boldsymbol{A}^T\boldsymbol{P}\boldsymbol{A}$

$$\hat{\boldsymbol{x}}(t) = \boldsymbol{N}^{-1}(t)\,\boldsymbol{A}^T(t)\,\boldsymbol{P}(t)\,\boldsymbol{y}(t) \tag{5.26}$$

5.3.3 Sequential Batch Least Squares

The term *sequential batch* refers to the combination of multiple successive sets (batches) of data into one system of equations, such that the data sets are not solved individually, but instead one combined solution is generated. Mathematically, successive observation data sets with linearised system of equations (5.21) at times $t_1, t_2, \ldots, t_p$ can be combined in matrix vector form:

$$\begin{pmatrix} \boldsymbol{y}_1 \\ \boldsymbol{y}_2 \\ \vdots \\ \boldsymbol{y}_p \end{pmatrix} = \begin{pmatrix} \boldsymbol{A}_1 \\ \boldsymbol{A}_2 \\ \vdots \\ \boldsymbol{A}_p \end{pmatrix} \boldsymbol{x} + \begin{pmatrix} \boldsymbol{v}_1 \\ \boldsymbol{v}_2 \\ \vdots \\ \boldsymbol{v}_p \end{pmatrix}, \tag{5.27}$$

where $\boldsymbol{y}_i = \boldsymbol{y}(t_i)$, $\boldsymbol{A}_i = \boldsymbol{A}(t_i)$, $\boldsymbol{v}_i = \boldsymbol{v}(t_i)$. The deviation vector $\boldsymbol{x}$ contains all parameters needed to derive the functional models at all times $t_1, t_2, \ldots, t_p$. It is important to note, that only parameters estimated per epoch contribute p parameters to the combined vector $\boldsymbol{x}$, whereas other (constant) parameters might only contribute 1 parameter for the entire time interval. Therefore the time argument of the combined parameter deviation vector $\boldsymbol{x}$ and also the combined absolute parameter vector $\boldsymbol{X}$ and combined vector of nominal parameter values $\boldsymbol{X}^*$ will be omitted for the batch least squares problem. Equation (5.27) can be written as:

$$\tilde{\boldsymbol{y}} = \tilde{\boldsymbol{A}}\boldsymbol{x} + \tilde{\boldsymbol{v}}\,, \tag{5.28}$$

which gives the linearised system of equations for solving the batch least squares adjustment. As this formulation has the drawback of creating huge matrices, when combining for example observation data with 30 second sampling of a full day, the following method called *normal equation stacking* is usually applied to keep the dimensions of involved matrices at a limited size and therefore reduce the computational load of the algorithm. Neglecting correlations in time between observations, the combined weight matrix can be written with $\boldsymbol{P}_i = \boldsymbol{P}(t_i)$ in block diagonal form

$$\tilde{\boldsymbol{P}} = \begin{pmatrix} \boldsymbol{P}_1 & 0 & \ldots & 0 \\ 0 & \boldsymbol{P}_2 & \ldots & 0 \\ \vdots & \vdots & \ddots & \vdots \\ 0 & 0 & \ldots & \boldsymbol{P}_p \end{pmatrix}. \tag{5.29}$$

The solution of the sequential batch least squares problem (5.28) can then be written in the same form as (5.26) as

$$\hat{\boldsymbol{x}} = \tilde{\boldsymbol{N}}^{-1}\tilde{\boldsymbol{A}}^T\tilde{\boldsymbol{P}}\tilde{\boldsymbol{y}} \tag{5.30}$$

where

$$\tilde{\boldsymbol{N}} = \tilde{\boldsymbol{A}}^T\tilde{\boldsymbol{P}}\tilde{\boldsymbol{A}} = \sum_{i=1}^{p} \boldsymbol{A}_i^T\boldsymbol{P}_i\,\boldsymbol{A}_i = \sum_{i=1}^{p} \boldsymbol{N}(t_i) \tag{5.31}$$

is referred to as stacked normal equation matrix, derived by the sum of the normal equation matrices computed at times t_i with $i = 1, \ldots, p$. Similar, the stacked right hand side of the normal equation system 5.30 is given by the sum of the right hand side computed at times t_i

$$\tilde{\boldsymbol{A}}^T\tilde{\boldsymbol{P}}\tilde{\boldsymbol{y}} = \sum_{i=1}^{p} \boldsymbol{A}_i^T\boldsymbol{P}_i\,\boldsymbol{y}_i\,. \tag{5.32}$$

5.3.4 Solution of the Linearised Iterative Weighted Batch Least Squares Problem

As the linearised system of equations (5.30) does not model the exact relation between observations and parameters, iterations are needed to improve the parameter estimates. The iterative process is finished if the weighted sum of squared

residuals Ω is no longer improving with respect to the previous iteration or when a predefined number of iteration steps has been reached.
The batch linearised system of equations from (5.28) at iteration step k is given by

$$\tilde{\boldsymbol{y}}_{k-1} = \tilde{\boldsymbol{A}}_{k-1}\boldsymbol{x}_k + \tilde{\boldsymbol{v}}_{k-1}\,, \tag{5.33}$$

where $\tilde{\boldsymbol{v}}_{k-1}$ is the combined residual vector and

$$\tilde{\boldsymbol{y}}_{k-1} = \tilde{\boldsymbol{Y}} - \tilde{\boldsymbol{f}}(\boldsymbol{X}^* = \hat{\boldsymbol{X}}_{k-1}) = \begin{pmatrix} \boldsymbol{Y}(t_1) \\ \boldsymbol{Y}(t_2) \\ \vdots \\ \boldsymbol{Y}(t_p) \end{pmatrix} - \begin{pmatrix} \boldsymbol{f}(\hat{\boldsymbol{X}}_{k-1}(t_1), t_1) \\ \boldsymbol{f}(\hat{\boldsymbol{X}}_{k-1}(t_2), t_2) \\ \vdots \\ \boldsymbol{f}(\hat{\boldsymbol{X}}_{k-1}(t_p), t_p) \end{pmatrix} \tag{5.34}$$

is the combined deviation vector of the observations from all batches $1,\ldots,p$. The *computed observations* $\tilde{\boldsymbol{f}}(\boldsymbol{X}^*)$ of iteration step k are derived by the nonlinear functional model evaluated at the parameter best estimates from the previous iteration $\boldsymbol{X}^* = \hat{\boldsymbol{X}}_{k-1}$, which in the first iteration are the initial parameter values $\boldsymbol{X}_0$. The solution of the iterative weighted batch least squares problem for iteration step k is the best estimate of the parameter deviations vector given by:

$$\hat{\boldsymbol{x}}_k = \tilde{\boldsymbol{N}}_{k-1}^{-1}\tilde{\boldsymbol{A}}_{k-1}^T\tilde{\boldsymbol{P}}_{k-1}\tilde{\boldsymbol{y}}_{k-1}\,. \tag{5.35}$$

The solution of the best estimates for the absolute parameter values in iteration step k is derived by:

$$\hat{\boldsymbol{X}}_k = \hat{\boldsymbol{X}}_{k-1} + \hat{\boldsymbol{x}}_k\,, \tag{5.36}$$

with the a posteriori residual vector

$$\tilde{\boldsymbol{v}}_k = \tilde{\boldsymbol{y}}_k - \tilde{\boldsymbol{A}}_k\hat{\boldsymbol{x}}_k\,, \tag{5.37}$$

where $\tilde{\boldsymbol{y}}_k = \tilde{\boldsymbol{Y}} - \tilde{\boldsymbol{f}}(\boldsymbol{X}^* = \hat{\boldsymbol{X}}_k)$ and $\tilde{\boldsymbol{A}}_k = \frac{\delta\tilde{\boldsymbol{f}}}{\delta\boldsymbol{X}}\Big|_{\hat{\boldsymbol{X}}_k}$ are both evaluated at the absolute parameter values $\hat{\boldsymbol{X}}_k$.

5.3.5 Constrained Least Squares Adjustment

The batch linearised system of equations in (5.33) may be expanded by introducing additional information in order to remove a rank deficiency of the normal equation matrix or simply constrain a certain parameter to a given value. In this work constrained parameter values $\boldsymbol{X}_c$ are added to the linearised system of equations in the form of pseudo observations, also called fictitious observations (Dach et al., 2015b). These pseudo observations are associated with a covariance matrix and the corresponding weight matrix $\boldsymbol{R}$ for the constrained parameters. Hence this approach of introducing parameter constraints may also be referred to as soft constraints or Bayesian constraints.
The batch linearised system of equations for parameter constraints in the form of pseudo observations at iteration step k is given by

$$\boldsymbol{z}_{k-1} = \boldsymbol{B}_{k-1}\boldsymbol{x}_k + \boldsymbol{\xi}_{k-1}\,, \tag{5.38}$$

where $\boldsymbol{\xi}_{k-1}$ is the residual vector of the parameter constraints and

$$\boldsymbol{z}_{k-1} = \boldsymbol{X}_c - \boldsymbol{X}^* \tag{5.39}$$

is the deviation vector of the parameter constraints from the nominal parameter values $\boldsymbol{X}^* = \hat{\boldsymbol{X}}_{k-1}$. The matrix $\boldsymbol{B}_{k-1}$ contains only zeros and ones and relates the parameters to the corresponding constraints.
This allows to add different types of constraints to the linearised system of equations. An absolute constraint of parameter X_i to its nominal value is introduced by setting the corresponding element $z_i = 0$, which constrains the parameter deviation to zero by introducing a fictitious observation of the form $x_i = 0$. Relative constraints between two parameters X_i and X_j may be introduced by adding a fictitious observation of the form $x_i - x_j = 0$. A zero-mean constraint for a group of parameters $1,\ldots,m$ may be introduced by adding a fictitious observation of the form $\sum_{i=1}^{m} x_i = 0$.

With the normal equation matrix of the fictitious observations from parameter constraints

$$\boldsymbol{M} = \boldsymbol{B}^T\boldsymbol{R}\boldsymbol{B}\,, \tag{5.40}$$

the solution of the linearised iterative weighted batch least squares problem with soft constraints is given by

$$\hat{\boldsymbol{x}} = \left(\tilde{\boldsymbol{N}} + \boldsymbol{M}\right)^{-1} \left(\tilde{\boldsymbol{A}}^T \tilde{\boldsymbol{P}} \tilde{\boldsymbol{y}} + \boldsymbol{B}^T \boldsymbol{R} \boldsymbol{z}\right) , \tag{5.41}$$

where the iteration subscripts have been omitted to improve readability.

5.3.6 Stochastic Model

The observations of the combined vector $\boldsymbol{Y}$ for the batch least squares adjustment are described by the stochastic model

$$\boldsymbol{C}_{yy} = \sigma_0^2 \boldsymbol{Q}_{yy} = \sigma_0^2 \tilde{\boldsymbol{P}}^{-1} , \tag{5.42}$$

where

$\boldsymbol{C}_{yy}$ is the covariance matrix of the observations

$\boldsymbol{Q}_{yy}$ is the cofactor matrix of the observations

$\tilde{\boldsymbol{P}}$ is the weight matrix of the observations

σ_0^2 is the a priori variance factor

If the observations are uncorrelated, $\tilde{\boldsymbol{P}}$ is a diagonal matrix with the elements

$$\tilde{P}_{yy} = \frac{\sigma_0^2}{\sigma_y^2} , \tag{5.43}$$

where σ_y is the standard deviation of the corresponding observation.
The weight matrix of the fictitious observations from parameter constraints is given in the same diagonal form for uncorrelated parameter constraints

$$R_{xx} = \frac{\sigma_0^2}{\sigma_x^2} , \tag{5.44}$$

where σ_x is the standard deviation of the corresponding parameter constraint.
The weighted sum of squared residuals, also referred to as loss function for the batch least squares adjustment is given for the unconstrained solution by

$$\tilde{\Omega} = \tilde{\boldsymbol{v}}^T \tilde{\boldsymbol{P}} \tilde{\boldsymbol{v}} \tag{5.45}$$

and for the solution with parameter constraints by

$$\tilde{\Omega} = \tilde{\boldsymbol{v}}^T \tilde{\boldsymbol{P}} \tilde{\boldsymbol{v}} + \boldsymbol{\xi}^T \boldsymbol{R} \boldsymbol{\xi} . \tag{5.46}$$

The a posteriori variance factor is computed by

$$\sigma^2 = \frac{\tilde{\Omega}}{f} , \tag{5.47}$$

where $f = n - u$ is the degree of freedom for the least squares adjustment with the number of observations n and number of estimated parameters u. The square root of the a posteriori variance factor is often referred to as sigma of unit weight (Koch, 2004)

$$\sigma = \sqrt{\frac{\tilde{\Omega}}{f}} . \tag{5.48}$$

The a posteriori covariance matrix of the estimated parameters with soft constraints is then given by

$$\boldsymbol{C}_{\hat{x}\hat{x}} = \sigma^2 \boldsymbol{Q}_{\hat{x}\hat{x}} = \sigma^2 \left(\tilde{\boldsymbol{N}} + \boldsymbol{M}\right)^{-1} , \tag{5.49}$$

where

$\boldsymbol{Q}_{\hat{x}\hat{x}}$ is the cofactor matrix of the estimated parameters

$\tilde{\boldsymbol{N}}$ is the stacked normal equation matrix (5.31) of the observations

$\boldsymbol{M}$ is the normal equation matrix (5.40) of the parameter constraints

The diagonal elements $C_{\hat{x}\hat{x}}$ of the parameter covariance matrix contain the standard deviations of the estimated parameters

$$\sigma_{\hat{x}} = \sqrt{C_{\hat{x}\hat{x}}}\,, \tag{5.50}$$

whereas the off-diagonal elements of the parameter covariance matrix can be used to determine the correlation coefficients between two estimated parameters

$$\rho_{ij} = \frac{C_{ij}}{\sigma_i \sigma_j}\,. \tag{5.51}$$

5.4 Satellite Orbit Determination

The classical orbit determination problem assumes the motion of bodies due to a central force or point mass. However, for human-made satellites orbiting the Earth, nongravitational forces and the deviation from a central force (point mass) are significant (Tapley et al., 2004). Table 5.4 (adopted from Flohrer, 2008) shows a list of perturbing forces acting on Earth orbiting satellites ordered by decreasing acceleration values computed for GPS satellites by Beutler (2005). In addition, the impact on satellite orbits after one day is shown.

Table 5.4: Perturbing forces acting on GNSS satellites ordered by decreasing acceleration values, computed for GPS satellites (adopted from Flohrer, 2008)

Perturbing force	Acceleration (in $\mathrm{m\,s^{-2}}$)	Orbit error after one day (in m)
Earth's monopole	0.57	330000000
Earth's oblateness	5.1×10^{-5}	35500
Lunar attraction	4.5×10^{-6}	1800
Solar attraction	2.0×10^{-6}	1300
Geopotential harmonics (higher terms)	4.2×10^{-7}	450
Direct Solar Radiation Pressure (SRP)	9.7×10^{-8}	200
Y-bias	1.0×10^{-9}	8
Solid Earth tides	5.0×10^{-9}	0.4
Thermal reradiation and Earth albedo	$\approx 1.3 \times 10^{-9}$	≈ 0.1
Planet attraction and ocean tides	$\approx 1.3 \times 10^{-10}$	≈ 0.01

A satellite orbit is described by the so called state vector $\boldsymbol{X}(t)$ containing the satellite's position and velocity at time t in an Earth centred inertial reference frame. If the differential equations of motion of the satellite are known, an initial state vector $\boldsymbol{X^0} = \boldsymbol{X}(t_0)$ can be used to determine the position and velocity of the satellite at any given time. In order to achieve the highest accuracy, the gravitational and nongravitational perturbing forces (see Table 5.4) need to be considered by mathematical models in the differential equations of motion of the satellite. They are crucial in the determination of the initial state vector as well as for the propagation of the orbit in order to compute satellite positions and velocities at any point in time. As both, the exact initial state vector as well as the exact forces defining the differential equations of motion are unknown, observations such as range, azimuth and elevation from known positions on Earth are used to improve the estimate of the satellite orbit. The process of orbit determination is described in (Tapley et al., 2004) as

> "*The problem of determining the best estimate of the state of a spacecraft, whose initial state is unknown, from observations influenced by random and systematic errors, using a mathematical model that is not exact.*"

In general the orbit determination problem is linearised by a Taylor series expansion as described in section 5.3.1. The difference to simple point positioning is that in the dynamical orbit determination process not only the relationship between observations and state parameters is linearised about a nominal state vector at the time of observation. Also the equations of motion describing the relationship between the state parameters at the time of observation and the initial

time need to be linearised about a nominal orbit trajectory. The nonlinear equations of motion of the state vector $\boldsymbol{X}(t)$ can be written in the form:

$$\dot{\boldsymbol{X}}(t) = \boldsymbol{F}(\boldsymbol{X}(t), t)\,, \tag{5.52}$$

which can be linearised as shown in (5.18) by

$$\boldsymbol{F}(\boldsymbol{X}(t), t) = \boldsymbol{F}(\boldsymbol{X}^*(t), t) + \left.\frac{\delta \boldsymbol{F}}{\delta \boldsymbol{X}}\right|_{X^*(t)} \boldsymbol{x}(t) + \mathscr{O}^2(\boldsymbol{x}(t))\,, \tag{5.53}$$

where $\boldsymbol{x}(t) = \boldsymbol{X}(t) - \boldsymbol{X}^*(t)$ is the vector of parameter deviations from the nominal values $\boldsymbol{X}^*(t)$, obtained by integrating (5.52) with the initial values $\boldsymbol{X}^*(t_0)$, which in an iterative solution are given by the best estimates of the initial state vector from the previous iteration

$$\boldsymbol{X}^*(t_0) = \hat{\boldsymbol{X}}_{k-1}(t_0) \equiv \hat{\boldsymbol{X}}^0_{k-1}\,.$$

With the time derivative of the parameter deviation vector $\dot{\boldsymbol{x}}(t) = \dot{\boldsymbol{X}}(t) - \boldsymbol{F}(\boldsymbol{X}^*(t), t)$ and $\boldsymbol{D}(t) = \left.\frac{\delta \boldsymbol{F}}{\delta \boldsymbol{X}}\right|_{X^*(t)}$, equation (5.53) can be written in the form

$$\dot{\boldsymbol{x}}(t) = \boldsymbol{D}(t)\boldsymbol{x}(t)\,, \tag{5.54}$$

where second and higher order terms $\mathscr{O}^2(\boldsymbol{x}(t))$ have been neglected. Equation (5.54) describes the linearised system of equations of motion with the general solution (cf. Tapley et al., 2004) expressed by

$$\boldsymbol{x}(t) = \boldsymbol{\Phi}(t, t_0)\boldsymbol{x}^0\,, \tag{5.55}$$

where $\boldsymbol{\Phi}(t, t_0)$ is the so called state transition matrix, relating the state parameter deviations at the time of observation t with the state parameters deviations $\boldsymbol{x^0} = \boldsymbol{x}(t_0)$ at initial time t_0.
The full linearised model for the orbit determination process is given by the linearised observation equations with observation deviation vector $\boldsymbol{y}(t)$ from (5.21) and the general solution for the linearised equations of motion for the state deviation vector $\boldsymbol{x}(t)$:

$$\begin{aligned} \boldsymbol{y}(t) &= \boldsymbol{A}(t)\boldsymbol{x}(t) + \boldsymbol{v}(t) \\ \boldsymbol{x}(t) &= \boldsymbol{\Phi}(t, t_0)\boldsymbol{x}^0\,. \end{aligned} \tag{5.56}$$

The combined linearised equation for the orbit determination process can be written as:

$$\boldsymbol{y}(t) = \boldsymbol{H}(t)\boldsymbol{x}^0 + \boldsymbol{v}(t)\,, \tag{5.57}$$

with the combined design matrix

$$\boldsymbol{H}(t) = \boldsymbol{A}(t)\boldsymbol{\Phi}(t, t_0)\,. \tag{5.58}$$

In analogy to section 5.3.4, the best estimate solution of the orbit determination process 5.57 using iterative weighted batch least squares is given for iteration step k by

$$\hat{\boldsymbol{x}}^0_k = \tilde{\boldsymbol{N}}^{-1}_{k-1}\tilde{\boldsymbol{H}}^T_{k-1}\tilde{\boldsymbol{P}}_{k-1}\tilde{\boldsymbol{y}}_{k-1}\,, \tag{5.59}$$

where the stacked normal equation matrix for the orbit determination problem is given by

$$\tilde{\boldsymbol{N}}_{k-1} = \tilde{\boldsymbol{H}}^T_{k-1}\tilde{\boldsymbol{P}}_{k-1}\tilde{\boldsymbol{H}}_{k-1}\,. \tag{5.60}$$

The combined design matrix at iteration step k is given by

$$\tilde{\boldsymbol{H}}_{k-1} = \begin{pmatrix} \boldsymbol{H}_{k-1}(t_1) \\ \boldsymbol{H}_{k-1}(t_2) \\ \vdots \\ \boldsymbol{H}_{k-1}(t_p) \end{pmatrix} = \begin{pmatrix} \boldsymbol{A}_{k-1}(t_1)\boldsymbol{\Phi}_{k-1}(t_1, t_0) \\ \boldsymbol{A}_{k-1}(t_2)\boldsymbol{\Phi}_{k-1}(t_2, t_0) \\ \vdots \\ \boldsymbol{A}_{k-1}(t_p)\boldsymbol{\Phi}_{k-1}(t_p, t_0) \end{pmatrix}, \tag{5.61}$$

where $\boldsymbol{A}_{k-1}(t_i)$ and $\boldsymbol{\Phi}_{k-1}(t_i, t_0)$ are both evaluated at the nominal state vector $\boldsymbol{X}^*(t_i)$, derived by integrating the best estimates of the initial parameter values from the previous iteration $\hat{\boldsymbol{X}}^0_{k-1}$.

6 Carrier Phase Integer Ambiguity Resolution with Raw Observations

The main objective of this work was to analyse the resolution of integer ambiguity values based on multi-GNSS and multi-signal raw observation processing and to successfully implement the developed approach in the NAvigation Package for Earth Observation Satellites (NAPEOS), a software package developed at the European Space Operations Centre (ESOC) for processing a variety of geodetic observation data and estimating geodetic parameters including precise satellite orbit determination and prediction. As the resolution of integer ambiguities is not a goal in itself, but used to exploit the precision of the carrier phase measurements in the form of precise phase pseudoranges, the implemented approach was applied to the problem of multi-GNSS precise orbit determination (POD), described in section 7.4.

The process used in this work to obtain the so called ambiguity fixed solution based on processing multi-GNSS and multi-signal raw observations involves three steps:

1. Float solution: The iterative weighted batch least squares adjustment, described in section 5.3 is performed with raw carrier phase ambiguities estimated as float values $M^s_{r,i}$, without forming any linear combinations or observation differences

2. Integer Ambiguity Resolution (IAR): The iterative integer ambiguity resolution algorithm, described in sections 6.1 and 6.2 is used to resolve integer values for ambiguities of all GNSS on all frequencies

3. Fixed Solution: The iterative weighted batch least squares adjustment is repeated with fixed values for multi-GNSS and multi-signal raw observation ambiguities

The second step involves the actual resolution of integer ambiguity values based on carrier phase ambiguity estimates from multi-GNSS and multi-signal raw observations.

6.1 Concept of Raw Observation Ambiguity Resolution

The concept of resolving carrier phase integer ambiguities from raw observations implemented in the course of this work is based on an iterative ambiguity fixing approach making use of raw observation float ambiguity estimates. In general, the approach is based on the procedure described in (Springer, 2009), which originates from the AMBIGON method described in (Blewitt, 1989) and can not be categorised as one of the methods described in section 5.1.3. As no search of integer values is performed, the integer ambiguity resolution method described here could be viewed as advanced integer bootstrapping (IB), however, instead of only a few ambiguities, in this method multiple ambiguities of different frequencies are fixed at once.
As described in section 5.1.3 and shown in (4.53), the carrier phase ambiguity term of raw observations is not of integer nature as it includes unknown instrumental phase biases of the satellite and receiver (Blewitt, 1997). Without additional information integer ambiguity resolution can only be performed on double difference (DD) ambiguities (Ge et al., 2005). In order to fix multi-signal ambiguities to integer values, double differences (DDs) of raw float ambiguity estimates are formed on parameter level for all frequencies as only those are of integer nature, described mathematically in section 6.2.1. It will be analysed whether the formation of double differences from raw float ambiguity estimates really is of integer nature, as the raw float ambiguity estimates might include other residual errors besides the instrumental phase biases. The advantage of generating integer nature ambiguities on parameter level is that the raw method, see section 5.2, can be applied to process all available multi-signal raw observations and estimate all geodetic parameters of interest, including ionospheric delays per receiver-satellite link. Therefore, no preselection of observations is necessary for example based on baseline length, as commonly applied in conventional double difference observation processing approaches.

The iterative integer ambiguity resolution scheme for double differences of multi-GNSS and multi-signal raw float ambiguity estimates is shown as flowchart diagram in Figure 6.1 and based on the following steps:

1. For all existing receiver baselines (a combination of two receivers) form all possible double difference ambiguities on all frequencies from raw ambiguity estimates with overlapping time intervals

2. For each receiver baseline
   a) Compute the fixing probability for double difference ambiguities of all frequencies, as described in section 6.2.3
   b) Select *fixable* double difference ambiguities based on two criteria: fixing probability and fractional value, see section 6.2.3 for details

c) Sort the *fixable* double difference ambiguities by fixing probability and check for independence using the modified Gram-Schmidt process (Golub and Van Loan, 1996)

3. Sort the *fixable* double difference ambiguities from all receiver baselines by fixing probability and check for independence using the modified Gram-Schmidt process

4. Introduce integer constraints for the selected *fixable* double difference ambiguities, as described in section 6.2.3 and solve the normal equation system including the estimation of raw ambiguity values

5. Repeat steps 2.-4. (next iteration) or finish, if
   a) All ambiguities are fixed, or
   b) No additional ambiguities were fixed in the last iteration, or
   c) The maximum number of iterations has been reached

It is important to note, that the described method does not involve the formation of any linear combination or difference on observation level. The estimation of all parameters, also in the ambiguity fixed solution is fully based on GNSS raw observations. Only for the resolution of ambiguity integer values, double differences of raw float ambiguity estimates are formed and once fixed, additional constraints are introduced to the normal equation system as described in section 6.2.3. This process inevitably also involves the fixing of wrong double difference integer values. This issue however, is solved in the least squares adjustment of the fixed solution, where wrong integer constraints of individual ambiguities are filtered out by checking the respective raw phase observation residuals.
Raw observation float ambiguity estimates of the final double difference integer constrained solution are fixed, if they belong to a fixable double difference integer ambiguity. Raw observation float ambiguities not belonging to a fixable double difference integer ambiguity remain in the fixed solution as float ambiguity parameter estimates. The application of fixed raw ambiguity values simplifies the introduction of double difference ambiguity integer constraints in the fixed solution of the iterative weighted batch least squares adjustment for operational reasons.
The advantage of this method, together with raw observation processing, is that fixed raw observation ambiguities of the final double difference integer constrained solution can directly be used to resolve undifferenced raw integer ambiguities and determine raw observation phase biases for all involved frequencies, as described in section 6.3.

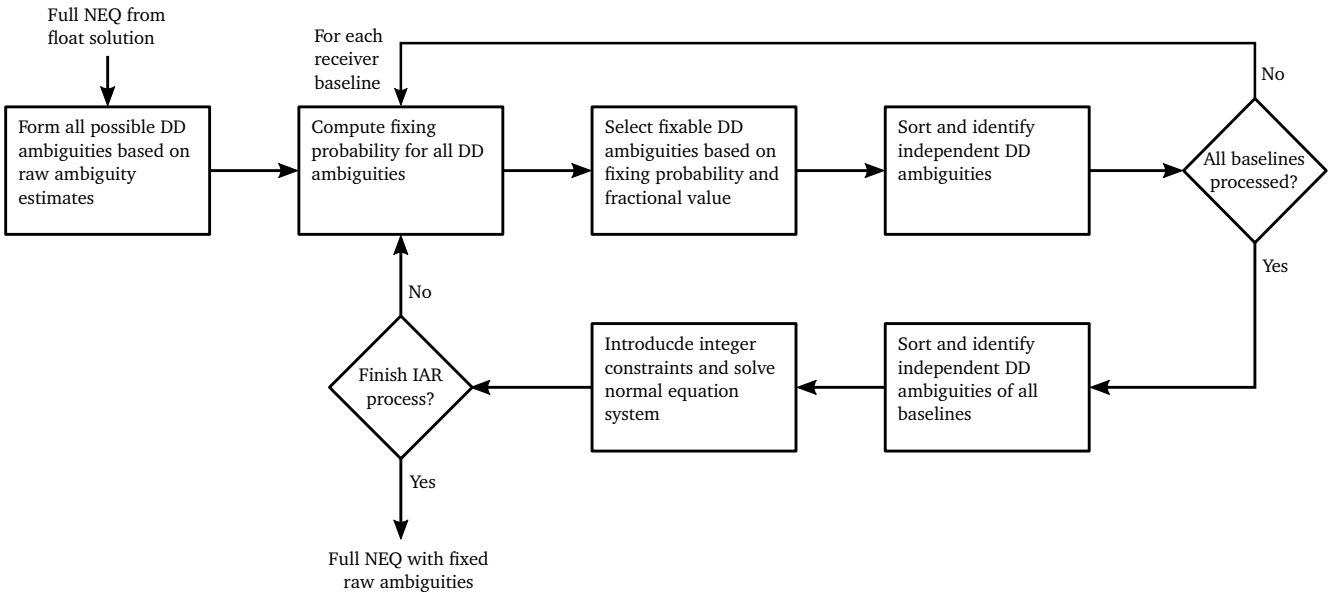

Figure 6.1: Flowchart diagram of the iterative integer ambiguity resolution scheme for double difference ambiguities based on multi-GNSS and multi-signal raw observation float ambiguity estimates.

6.2 Multi-Frequency Double Difference Integer Ambiguity Resolution

The described iterative integer ambiguity resolution scheme for double differences of raw float ambiguities is applied simultaneously to all processed phase observations on multiple frequencies and for multiple GNSS. The details of forming double difference ambiguities, fixing them to integer values and applying integer constraints to the normal equation system is described in the following sections.

6.2.1 Forming Double Difference Ambiguities

The double difference ambiguity for raw signal frequency i in carrier wavelength cycles is formed from raw observation float ambiguity estimates $\hat{M}^s_{r,i}$ of receivers A, B and satellites k, l by:

$$M^{kl}_{AB,i} = \hat{M}^k_{A,i} - \hat{M}^k_{B,i} - \hat{M}^l_{A,i} + \hat{M}^l_{B,i} \,. \tag{6.1}$$

The fractional part of the double difference ambiguity is given in cycles by

$$f^{kl}_{AB,i} = M^{kl}_{AB,i} - N^{kl}_{AB,i} \tag{6.2}$$

where $N^{kl}_{AB,i} = NINT\left[M^{kl}_{AB,i}\right]$ is the nearest integer of $M^{kl}_{AB,i}$, which leads to fractional values $f^{kl}_{AB,i} \in [-0.5, 0.5]$ cycles.

From the definition of raw observation float ambiguities in (4.53) follows, that the expected value of a double difference ambiguity is given by

$$\begin{aligned} E\left[M^{kl}_{AB,i}\right] &= N^k_{A,i} - \delta^k_i(t) - \delta_{A,i}(t) - N^k_{B,i} + \delta^k_i(t) + \delta_{B,i}(t) \\ &\quad - N^l_{A,i} + \delta^l_i(t) + \delta_{A,i}(t) + N^l_{B,i} - \delta^l_i(t) - \delta_{B,i}(t) \\ &= N^k_{A,i} - N^k_{B,i} - N^l_{A,i} + N^l_{B,i} \,, \end{aligned} \tag{6.3}$$

which is the double difference combination of the raw observation integer ambiguities and therefore also is an integer number.
The analysis of double difference ambiguity fractionals $f^{kl}_{AB,i}$ computed from the raw observation float ambiguity estimates $\hat{M}^s_{r,i}$ reveals, whether double difference ambiguities are close to an integer value and therefore can be fixed to the nearest integer. The criteria used to decide whether a double difference ambiguity should be fixed to an integer value are described in section 6.2.3.

6.2.2 Histogram of Double Difference Ambiguity Fractionals

An intuitive way of visualising whether double difference (DD) ambiguities for a certain application are close to an integer value, is the so called histogram of double difference ambiguity fractionals. It shows the number of fractional values within a certain bin size over the fractional value range $[-0.5, 0.5]$ cycles. The fact that values for both interval boundaries ± 0.5 cycles are computed leads to a reduction of 50 % in the number of fractionals for these bins, as from an integer point of view they are practically identical, see Figure 6.2. As the number of fractionals for a certain signal depends on the number of available ambiguity parameters, the histogram also indicates the differences in the number of available DD ambiguities for different signals. The fractionals of multiple signals are colour coded and stacked on top of each other per GNSS to show the individual signal and combined DD ambiguity fractional characteristics. The histogram reveals whether a significant part of all computable (dependent) double difference ambiguities is close to integer, which corresponds to a fractional value close to zero. If the ambiguity fractional histogram is shaped Gaussian like with a mean value of 0 it can be assumed that integer ambiguity resolution can be performed properly and it will strengthen the overall solution.
In multi-GNSS and multi-signal raw observation processing, the histogram of all computable double difference ambiguity fractionals formed from raw observation float ambiguity estimates can be used to

- Compare the general consistency of raw float ambiguity estimates for different GNSS
- Compare the quality of different signal frequencies for a certain GNSS
- Check for potential consistency of inter-system raw float ambiguities to facilitate inter-system integer ambiguity resolution

Figure 6.2 shows an example of a double difference ambiguity fractional histogram from raw observation float ambiguity estimates for Galileo raw phase observations from signals E1C, E5Q, E7Q, E8Q and E6C.
In addition, the histogram of all computable (dependent) double difference ambiguity fractionals from integer constraint solutions, ie. after fixing integer ambiguities, see section 6.2.3, indicates whether the fixing of double difference ambiguities to integer values was successful. An increased number of zero fractionals shows the impact of fixing independent double difference ambiguities to integer values. As the histogram shows fractional values for all computable double difference ambiguities and not just independent ones, it also indicates whether all double difference ambiguities converge to integer values by introducing the integer constraints in the ambiguity fixing algorithm, described in section

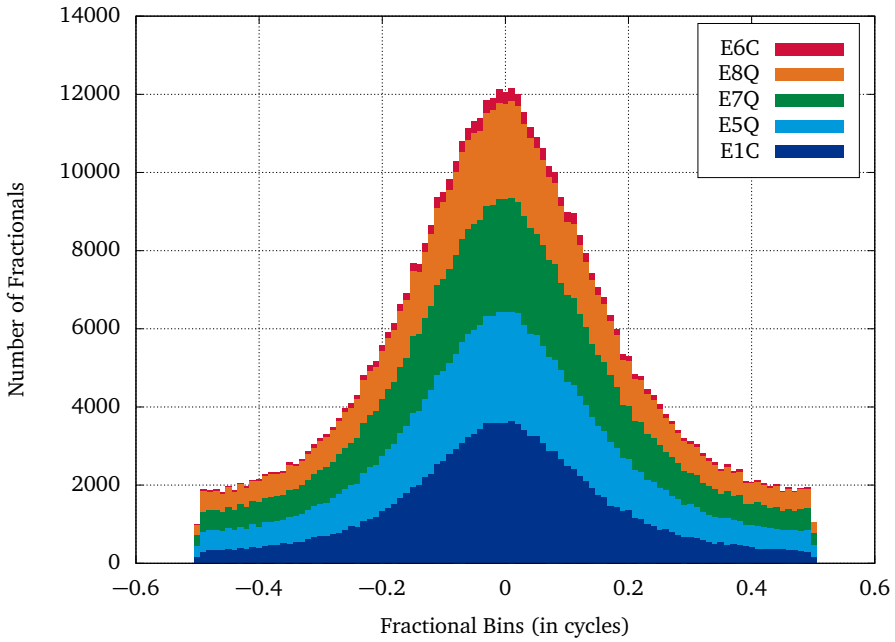

Figure 6.2: Double difference ambiguity fractional histogram based on raw observation float ambiguity estimates for all Galileo signals.

6.2.3. Remaining non-zero fractionals indicate, that due to inconsistencies in the raw observation float ambiguity estimates, the corresponding double difference ambiguities do not converge to integer values, despite the introduced integer constraints.

The double difference ambiguity fractional histograms for different GNSS and signals are shown in section 7.4.2 and the impact of introduced integer constraints in the ambiguity fixing process is analysed.

6.2.3 Fixing Double Difference Integer Ambiguities

The decision whether a double difference ambiguity can be fixed to an integer value is based on two criteria, its fixing probability and its fractional value. The probability P_0 of fixing a double difference ambiguity to its nearest integer is computed by the formula of Dong and Bock (1989), which is also used in (Ge et al., 2005):

$$P_0\left(M_{AB,i}^{kl}\right) = 1 - \sum_{n=1}^{\infty} erfc\left(\frac{n - f_{AB,i}^{kl}}{\sqrt{2}\sigma_{M_{AB,i}^{kl}}}\right) - erfc\left(\frac{n + f_{AB,i}^{kl}}{\sqrt{2}\sigma_{M_{AB,i}^{kl}}}\right) \tag{6.4}$$

with

$$erfc(x) = \frac{2}{\sqrt{\pi}} \int_x^{\infty} e^{-t^2} dt \,, \tag{6.5}$$

where $\sigma^2_{M_{AB,i}^{kl}}$ is the double difference ambiguity variance in cycles, computed from the variances $\sigma^2_{M_{r,i}^{s}}$ of the raw observation float ambiguity estimates.

The threshold used in this work to select the fixable double difference ambiguities based on their fixing probability P_0 is set to 94 %. The fractional value interval used in this work to select the fixable double difference ambiguities based on their fractional value $f_{AB,i}^{kl}$, computed by (6.2) is set to $[-0.05, +0.05]$ cycles of the carrier wavelength λ_i.

The double difference ambiguities, which satisfy the fixing probability and fractional value criteria are fixed to the nearest integer value, which can be summarised by

$$\text{If} \quad \left(P_0\left(M_{AB,i}^{kl}\right) > 0.94 \quad \text{and} \quad \left|f_{AB,i}^{kl}\right| < 0.05\right) \quad \text{then} \quad M_{AB,i}^{kl} := NINT\left[M_{AB,i}^{kl}\right] \tag{6.6}$$

Applying Integer Constraints to the Normal Equation System

The information of integer fixed double difference ambiguities is added to the normal equation system as an additional constraint for the double difference combination of the raw observation ambiguity parameters, as described in section 5.3.5 and therefore represents a relative constraint between four parameters

$$M_{A,i}^{k} - M_{B,i}^{k} - M_{A,i}^{l} + M_{B,i}^{l} = N_{AB,i}^{kl} \tag{6.7}$$

However, as in the linearised least squares adjustment deviations of parameter are estimated, the equivalent formulation for the double difference combination of the raw observation ambiguity parameter deviations $m_{r,i}^{s} = M_{r,i}^{s} - M_{r,i}^{s\,*}$ is used

$$m_{A,i}^{k} - m_{B,i}^{k} - m_{A,i}^{l} + m_{B,i}^{l} = f_{AB,i}^{kl} \tag{6.8}$$

where $M_{r,i}^{s\,*}$ are the nominal values of the raw observation ambiguity parameters and the fractional value $f_{AB,i}^{kl}$ is the difference needed to be applied to the computed double difference ambiguity to make it an integer value.

Assuming that the parameter deviation vector x is ordered in such a way, that the raw observation ambiguity parameter deviations contributing to a fixed double difference ambiguity are at the end of the parameter deviation vector, the normal equation system in (5.35) can be written in block matrix form

$$\begin{bmatrix} \boldsymbol{N}_{11} & \boldsymbol{N}_{12} \\ \boldsymbol{N}_{21} & \boldsymbol{N}_{22} \end{bmatrix} \begin{bmatrix} \boldsymbol{x}_1 \\ \boldsymbol{x}_2 \end{bmatrix} = \begin{bmatrix} \boldsymbol{A}_1^T \boldsymbol{P} \boldsymbol{y} \\ \boldsymbol{A}_2^T \boldsymbol{P} \boldsymbol{y} \end{bmatrix} \tag{6.9}$$

where $\boldsymbol{x}_2$ is the vector of raw observation ambiguity parameter deviations $m_{r,i}^{s}$ contributing to a fixed double difference ambiguity. The integer constraint (6.8) can be written in matrix vector notation

$$\boldsymbol{DD}\, \boldsymbol{x}_2 = \boldsymbol{f} \tag{6.10}$$

where $\boldsymbol{DD}$ is the double difference operator forming the fixed double difference ambiguities and $\boldsymbol{f}$ is the vector of all fixed double difference ambiguity fractionals.

The integer constraints (6.10) are applied to the normal equation system in the form of fictitious observations or soft constraints as in (5.41), which for the block matrix notation (6.9) can be written as (Springer, 2009)

$$\begin{bmatrix} \boldsymbol{N}_{11} & \boldsymbol{N}_{12} \\ \boldsymbol{N}_{21} & \boldsymbol{N}_{22} + \frac{\sigma_0^2 \boldsymbol{DD}^T \boldsymbol{DD}}{\sigma_m^2} \end{bmatrix} \begin{bmatrix} \boldsymbol{x}_1 \\ \boldsymbol{x}_2 \end{bmatrix} = \begin{bmatrix} \boldsymbol{A}_1^T \boldsymbol{P} \boldsymbol{y} \\ \boldsymbol{A}_2^T \boldsymbol{P} \boldsymbol{y} + \frac{\sigma_0^2 \boldsymbol{DD}^T \boldsymbol{f}}{\sigma_m^2} \end{bmatrix} \tag{6.11}$$

where the standard deviation of the raw observation ambiguity parameter deviations σ_m is set to a small value (typically 1×10^{-9}) to give the integer constraints a strong weight. However, care must be taken when choosing this value to avoid numerical problems when solving the normal equation system.

The constrained system of normal equations is used to re-estimate the raw observation ambiguities and all other parameters in an iterative way. As will be shown in section 7.4.2, the additional integer constraints improve the solution and therefore in consecutive iterations even more double difference ambiguities can be fixed to an integer value. The double difference integer ambiguity fixing described in section 6.2.3 is repeated until one of the following criteria is met:

- All double difference ambiguities have been fixed to integer
- No additional double difference ambiguities have been fixed to an integer value in the last iteration
- The maximum number of iterations has been reached

After the double difference integer ambiguity fixing is finished, the raw ambiguity estimates belonging to a fixed double difference ambiguity are kept fix to compute the fixed solution of the iterative weighted batch least squares adjustment.

6.2.4 Inter-Frequency Consistency Check

In addition to the formation of double difference ambiguities per frequency, as described in section 6.2.1, the difference between two double difference ambiguities on different frequencies, so called widelane double difference ambiguities can be used to check the consistency of double difference ambiguities on different frequencies.

The widelane double difference ambiguity for frequencies i and j is formed from double difference ambiguities (6.13) by:

$$M^{kl}_{AB,i-j} = M^{kl}_{AB,i} - M^{kl}_{AB,j} \,. \tag{6.12}$$

In theory, widelane double difference ambiguities are associated with the widelane wavelength $\lambda_w = c/(f_i - f_j)$, which is much larger than the wavelength of individual carrier signals $\lambda_i = c/f_i$. The histogram of widelane double difference ambiguity fractionals $f^{kl}_{AB,i-j}$ should therefore be more confined, if the double difference ambiguities on different frequencies have been formed consistently without additional unmodelled frequency dependent errors.
Figure 6.3 shows an example of a widelane double difference ambiguity fractional histogram based on raw observation float ambiguity estimates for Galileo phase observations on signal frequencies E5a, E5b, E5 and E6 with respect to signal frequency E1. The confined shape of the histogram, compared to Figure 6.2 confirms the consistency of the used double difference ambiguities on different frequencies. Almost 70 % of all widelane double difference ambiguity fractionals from raw observation float ambiguity estimates are within $[-0.1, +0.1]$ widelane cycles.

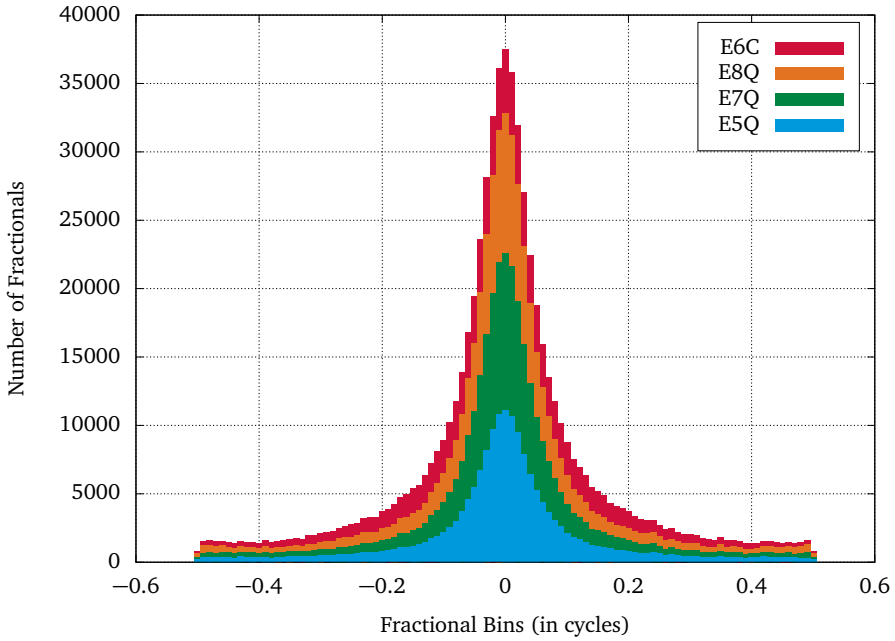

Figure 6.3: Widelane double difference ambiguity fractional histogram based on raw observation float ambiguity estimates for Galileo signals relative to E1C.

6.2.5 Inter-System Integer Ambiguity Resolution

The integer ambiguity fixing approach described so far, was based on double differences formed from raw observation float ambiguity estimates of receivers A, B and satellites k, l, where both satellites belong to the same GNSS.
As in the raw observation processing approach all ambiguities are handled per frequency, double difference ambiguities can also be formed for satellites k, l belonging to different GNSS, as long as they are transmitting signals on the same carrier frequency.
Inter-System (IS) double difference ambiguities for Galileo and GPS and a common signal frequency i are formed from raw observation float ambiguity estimates of receivers A, B, Galileo satellite E_k and GPS satellite G_l by

$$M^{E_k G_l}_{AB,i} = \hat{M}^{E_k}_{A,i} - \hat{M}^{E_k}_{B,i} - \hat{M}^{G_l}_{A,i} + \hat{M}^{G_l}_{B,i} \,. \tag{6.13}$$

The histogram of inter-system double difference ambiguity fractionals reveals whether raw observation float ambiguity estimates from different GNSS can be combined consistently. A distorted shape of the fractional histogram and/or a non-zero mean value indicate, that residual errors in the raw observation float ambiguity estimates from different GNSS prevent the consistent combination of inter-system double difference ambiguities. In this case, the additional fixing of inter-system double difference ambiguities to integer values might not be performed properly and might weaken the overall solution.
Figure 6.4 shows an example of an inter-system double difference ambiguity fractional histogram for Galileo phase observations on signals E1C and E5Q and GPS phase observations on signals G1C and G5Q. The histogram shows that

the formation of double difference ambiguities between Galileo and GPS satellites does not provide any statistically significant integer ambiguities for the combination of E5Q and G5Q. For the combination of E1C and G1C, the shape of the histogram reveals a better consistency between raw observation float ambiguity estimates from Galileo and GPS, however, the histogram shows a non-zero mean value.

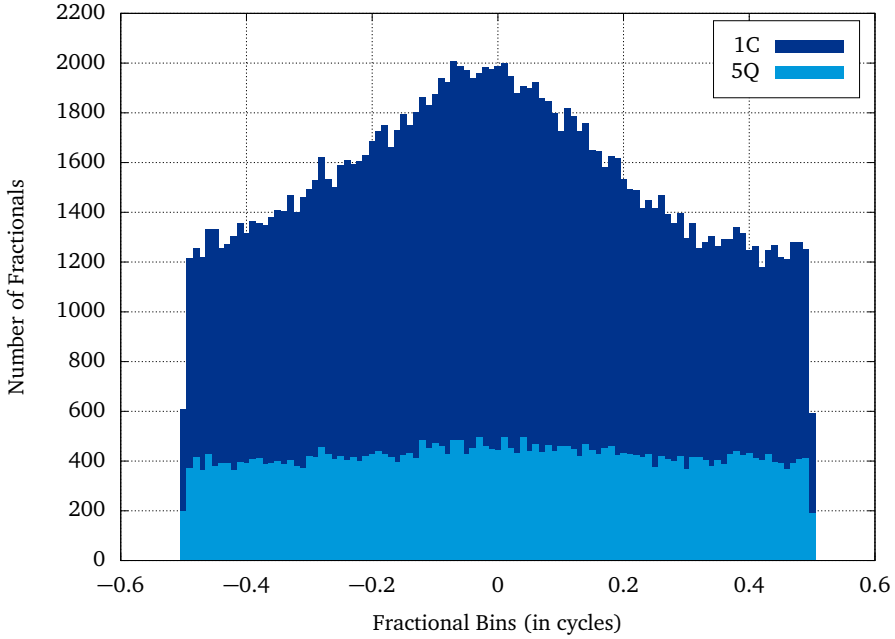

Figure 6.4: Inter-system double difference ambiguity fractional histogram based on raw observation float ambiguity estimates for Galileo signals E1C and E5Q and GPS signals G1C and G5Q.

In section 7.4.2 inter-system double difference ambiguity fractional histograms for Galileo, GPS and BeiDou and different carrier frequency combinations are shown. The impact of the additional fixing of Galileo-GPS inter-system double difference ambiguities to integer values on the precise orbit determination of GNSS satellites is analysed in section 7.4.3.

6.3 Undifferenced Raw Integer Ambiguities and Phase Biases

Raw observation float ambiguity estimates of the final iteration of the integer ambiguity resolution algorithm are referred to as fixed raw ambiguities $\bar{M}^s_{r,i}$, if they belong to a fixable double difference integer ambiguity. These fixed raw ambiguities are assumed to include only phase biases in addition to the raw integer ambiguity and no or very little other residual errors. Therefore, they are used to resolve undifferenced raw integer ambiguities and determine raw observation phase biases for all involved frequencies.
As described in section 4.1.3, full cycles of phase biases are indistinguishable from integer values of the raw observation ambiguity term and raw observation phase biases per receiver satellite link can therefore be defined as the fractional value of the final raw observation float ambiguity estimates

$$\delta^s_{r,i} = \delta^s_i + \delta_{r,i} = \bar{M}^s_{r,i} - NINT\left[\bar{M}^s_{r,i}\right], \tag{6.14}$$

with the undifferenced raw integer ambiguity

$$N^s_{r,i} = NINT\left[\bar{M}^s_{r,i}\right]. \tag{6.15}$$

In order to make use of raw observation phase biases, determined with the described approach, for applications enabling single receiver integer ambiguity resolution with multi-signal raw observations, satellite phase biases need to be determined from the link phase biases in (6.14). One option to separate satellite and receiver phase biases is to introduce a zero-mean constraint per frequency or fix the phase bias for all signals of a selected reference receiver or satellite. However, this might cause similar issues as the zero-mean based determination of satellite code biases, described in section 7.1.2. Another option to separate satellite phase biases from the available phase biases per receiver satellite link (6.14),

is to form between satellite Single Difference (SD) phase biases per receiver.
The between satellite SD phase bias on frequency i for satellites k and l determined from fixed raw observation ambiguity estimates of receiver A are given by

$$\delta_i^{kl} = \delta_i^k - \delta_i^l = \delta_{A,i}^k - \delta_{A,i}^l = \left(\bar{M}_{A,i}^k - N_{A,i}^k\right) - \left(\bar{M}_{A,i}^l - N_{A,i}^l\right) , \tag{6.16}$$

where it is assumed that the raw observation receiver phase bias $\delta_{A,i}$ cancels in the between satellite single difference of phase biases per receiver satellite link.
The stability of multi-frequency between satellite SD phase biases from fixed raw observation ambiguity estimates is analysed in section 7.5.2. Aspects for the use of multi-frequency between satellite SD phase biases in single receiver integer ambiguity resolution applications is discussed in section 7.5.3.

7 Analyses, Results and Applications

This section describes the analyses performed in the course of this work together with the main results related to the following objectives: Handling of physically meaningful GNSS code biases in multi-GNSS and multi-signal raw observation processing and integer ambiguity resolution based on multi-GNSS and multi-signal raw observation processing. The first approach is used to demonstrate applications using multi-GNSS and multi-signal raw observations related to single receiver absolute ionospheric delay estimation and GNSS system time and inter-system time offset determination. The latter approach is applied to the problem of multi-GNSS precise orbit determination from a global network of receivers.

7.1 Multi-GNSS Multi-Signal Raw Observation Code Biases

As described in section 5.2.2, GNSS signal code biases need to be properly handled in multi-signal raw observation processing. The proper handling of code biases in a physically meaningful way is especially important for multi-signal applications related to ionosphere estimation and time transfer. Section 7.1.1 therefore describes the performed analyses and calibrations of receiver system code biases, which is needed for the performed analyses and estimation of physically meaningful GNSS satellite code biases in section 7.1.2. The achieved receiver and satellite code bias results are then applied to single receiver absolute ionosphere estimation in section 7.2 and timing applications in section 7.3.

7.1.1 Receiver System Code Biases

Receiver system code biases are defined as signal dependent delays in all components of the receiver system, containing of the receiving antenna, signal splitter, other hardware components like lightning protector and most important the receiver itself. When signal dependent antenna offset corrections, as described in section 4.1.4 are applied to code observations, the receiver system code biases should only contain residual signal dependent antenna delays. In order to estimate physically meaningful navigation satellite code biases, receiver system code biases need to be determined. The most consistent way of estimating navigation satellite code biases is to use a global GNSS receiver network with identical receivers. ESA's GNSS Observation Network (EGON) shown in Figure 7.1 is equipped with the same receiver type and mostly with the same antenna. This setup makes receiver specific code bias calibration feasible and allows for the estimation of physically meaningful satellite code biases.

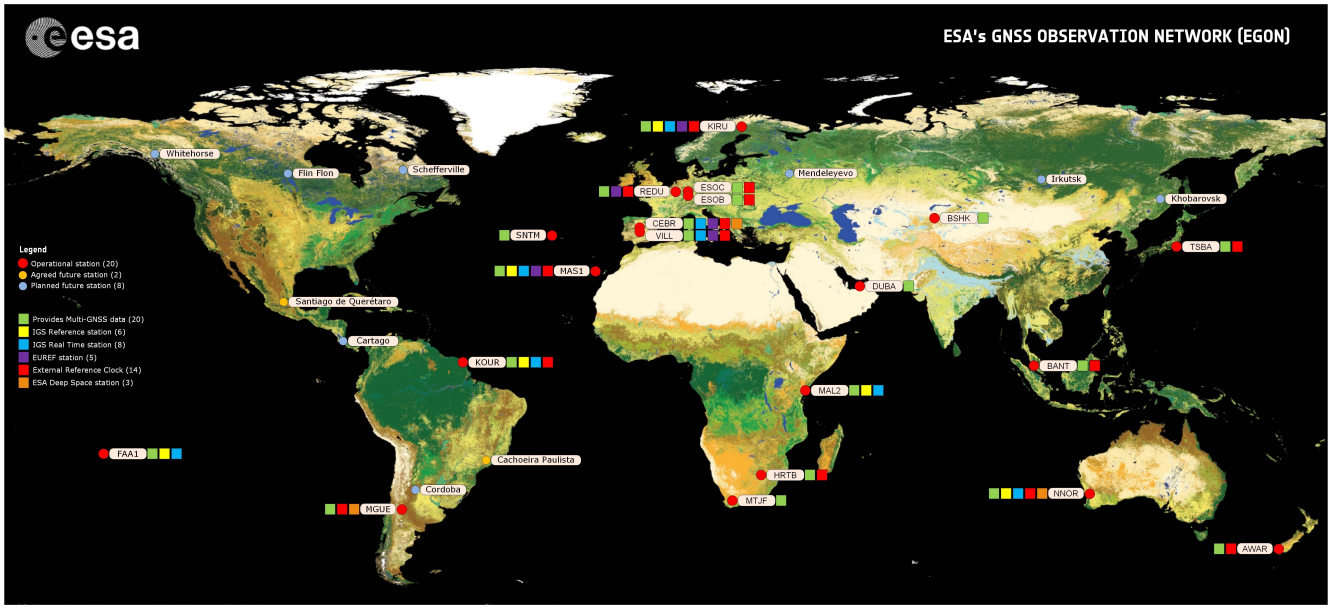

Figure 7.1: ESA's GNSS Observation Network (EGON) (Navigation Support Office, 2019)

Code Bias Calibration with GNSS Signal Simulator

For most multi-signal applications it is adequate to handle GNSS signal code biases in the form of differential code biases with respect to a reference signal, as discussed in section 5.2.2. In order to separate receiver and satellite code

biases without introducing additional zero-mean constraints in the estimation process, receiver differential code biases are calibrated with a multi-GNSS and multi-signal simulator (Reckeweg et al., 2016, 2018).

The simulator was set up to generate signals of all four GNSS (Galileo, GPS, BeiDou, GLONASS) for a static position on Earth with all constellations in the full nominal configuration. Signal dependent atmospheric effects were not simulated and signal dependent satellite code biases and transmitting antenna offsets were set to zero. The difference between raw code observations of different signals measured by a receiver directly connected to the multi-GNSS multi-signal simulator is given by:

$$P^{SIM}_{r,\Sigma ia}(t) - P^{SIM}_{r,\Sigma jb}(t) = c \cdot d_{r,\Sigma ia-\Sigma jb}(t) + \epsilon^{s}_{r,\Sigma ia}(t) - \epsilon^{s}_{r,\Sigma jb}(t)\,. \tag{7.1}$$

Equation (7.1) reveals that the described GNSS signal simulator setup allows to directly measure receiver specific differential code biases for all simulated GNSS signals. The receiver type deployed in EGON was used to measure differential code biases for 14 different signals from four different GNSS. The measured raw code observation differences (7.1) for simulated Galileo and GPS signals are shown in Figure 7.2, for simulated BeiDou and GLONASS signals they are shown in Figure 7.3. Figures 7.2a, 7.2b and 7.3a for Galileo, GPS and BeiDou signals show constant receiver DCBs over the full simulated time interval. The mean values and standard deviations of the calibrated receiver DCBs are summarised in Table 7.1.

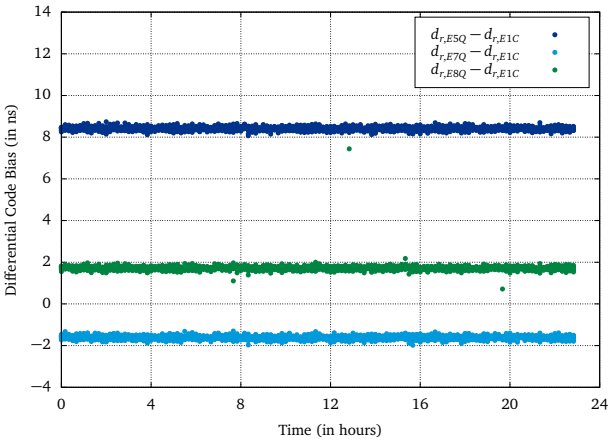

(a) Galileo signal receiver DCBs relative to $d_{r,E1C}$

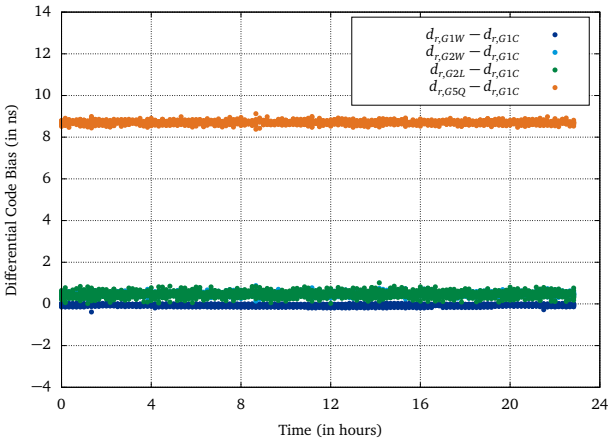

(b) GPS signal receiver DCBs relative to $d_{r,G1C}$

Figure 7.2: EGON receiver specific differential code biases (DCBs) from simulated multi-signal GNSS raw observations.

Table 7.1: Differential code bias calibration values for the EGON receiver type determined from simulated multi-GNSS and multi-signal raw observations, shown in Figures 7.2 and 7.3a.

GNSS	DCB	Mean Value (in ns)
Galileo	$d_{r,E5Q-E1C}$	8.42 ± 0.1
	$d_{r,E7Q-E1C}$	-1.61 ± 0.1
	$d_{r,E8Q-E1C}$	1.72 ± 0.2
GPS	$d_{r,G1W-G1C}$	-0.07 ± 0.1
	$d_{r,G2W-G1C}$	0.48 ± 0.1
	$d_{r,G2L-G1C}$	0.46 ± 0.1
	$d_{r,G5Q-G1C}$	8.70 ± 0.1
BeiDou	$d_{r,C7I-C2I}$	-1.11 ± 0.1

The measured raw code observation differences for GLONASS signals show as expected no constant receiver DCBs, as the FDMA satellites do not transmit their signals at the same carrier frequency, as described in section 2.2.4. For consistency reasons in the handling of GNSS signal code biases applied in this work, GLONASS satellites are therefore excluded in all further analyses.

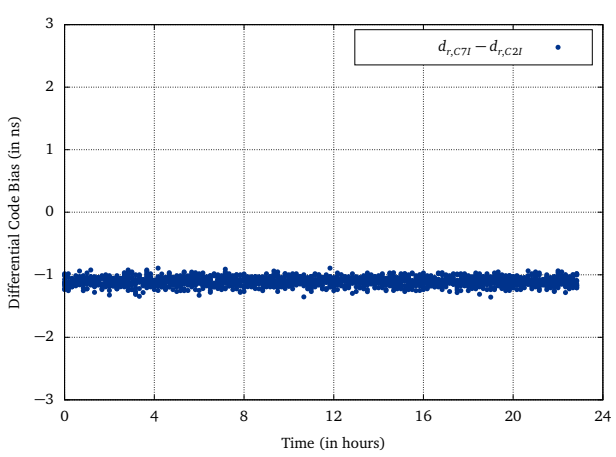

(a) BeiDou signal receiver DCBs relative to $d_{r,C2I}$

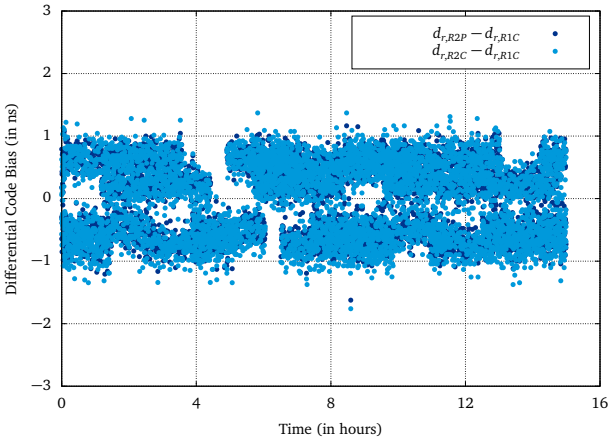

(b) GLONASS signal receiver DCBs relative to $d_{r,R1C}$ for satellite PRN numbers R0*

Figure 7.3: EGON receiver specific differential code biases (DCBs) from simulated multi-signal GNSS raw observations.

To demonstrate the universal validity of the described receiver DCB calibration approach with simulated GNSS raw observations and also to include the Galileo E6 signal, the DCBs of other receiver types were calibrated. Figure 7.4 shows the measured raw code observation differences (7.1) for simulated Galileo and GPS signals of the receiver type used to update the current EGON receivers in the near future. The mean values and standard deviations of the calibrated DCBs for this receiver type are summarised in Table 7.2.

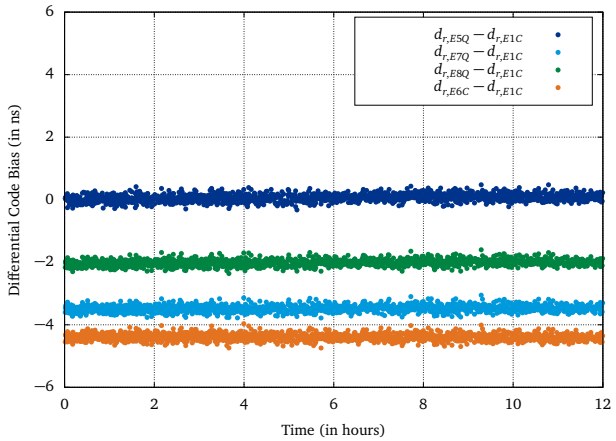

(a) Galileo signal receiver DCBs relative to $d_{r,E1C}$

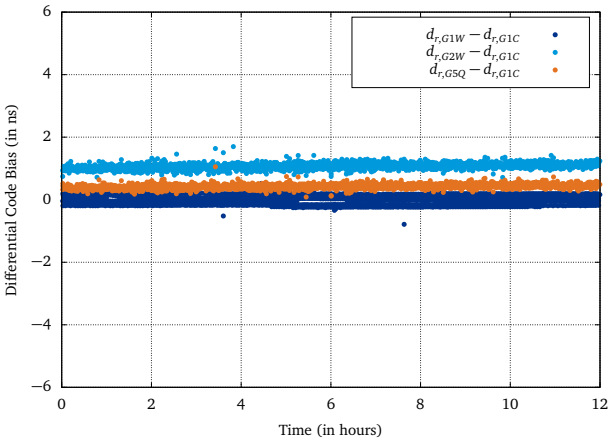

(b) GPS signal receiver DCBs relative to $d_{r,G1C}$

Figure 7.4: Future EGON receiver specific differential code biases (DCBs) from simulated multi-signal GNSS raw observations.

Receiver System Code Bias Variations

During its lifetime, the receiver system DCBs might not be as constant, as it was shown in the calibration with simulated GNSS raw observations. Multiple factors might impact the overall receiver system code bias values although the receiver itself is not changed. The main important factors are: receiver firmware or software setting changes, temperature drifts and splitter or antenna hardware changes.

Updates to the receiver firmware or software settings causing changes in the correlator settings might impact the receiver code biases as described in (Hauschild and Montenbruck, 2016), where it is shown that the satellite-dependent inter-receiver differential bias RMS doubles for most of the analysed GPS, Galileo and BeiDou signals when multipath mitigation is switched on for one of the receivers. Maximum values for the change in satellite-dependent inter-receiver bias rms values due to a change of the correlator/multipath settings are approximately 7 cm - 12 cm for GPS signals, 6 cm for Galileo signals and 7 cm - 10 cm for BeiDou signals, indicating that the lowest code bias inconsistencies were found for Galileo signals.

Table 7.2: Differential code bias calibration values for the future EGON receiver type determined from simulated multi-GNSS and multi-signal raw observations, shown in Figure 7.4.

GNSS	DCB	Mean Value (in ns)
Galileo	$d_{r,E5Q-E1C}$	0.07 ± 0.1
	$d_{r,E7Q-E1C}$	-3.48 ± 0.1
	$d_{r,E8Q-E1C}$	-2.01 ± 0.1
	$d_{r,E6C-E1C}$	-4.39 ± 0.1
GPS	$d_{r,G1W-G1C}$	-0.01 ± 0.1
	$d_{r,G2W-G1C}$	1.07 ± 0.1
	$d_{r,G5Q-G1C}$	0.42 ± 0.1

However, these results mainly show the impact on receiver code biases when different type of receivers with different correlator settings are used. As only EGON receivers with identical settings are used in the code bias analysis of this work, no differences in the receiver code biases discussed in (Hauschild and Montenbruck, 2016) are to be expected and can therefore be neglected. As a result, the separation of signal code biases in a receiver-specific and satellite-specific part performed in this work is a valid approach, as only identical receivers are used.

Electric components usually show temperature dependent behaviour, therefore it is likely that changes in the receiver temperature also lead to changes in the receiver GNSS signal code biases. The impact of temperature drifts on receiver code biases has been analysed in (Schönemann, 2014). It was shown that the temperature induced drift of differential code biases reaches maximum values of approximately $6\,\mathrm{mm\,°C^{-1}}$ for the analysed GPS and Galileo signals. This corresponds to a change in differential code biases of 1 ns for a temperature change of at least 50 °C. Therefore, the temperature effect on receiver code biases is neglected in the analysis performed in this work.

The impact of an additional signal splitter in the receiver system as well as the selection of the splitter output on receiver DCBs was analysed with two different types of splitters. Both are 4-way passive multi-signal capable splitters, but from different manufacturers.
The GNSS signal simulator scenario described above was used repeatably to measure multi-GNSS and multi-signal raw observations with the EGON receiver connected to different signal splitters and splitter outputs. Figure 7.5 shows the measured raw code observation differences for simulated Galileo and GPS signals with the receiver being connected to each of the four outputs of the first splitter in test.

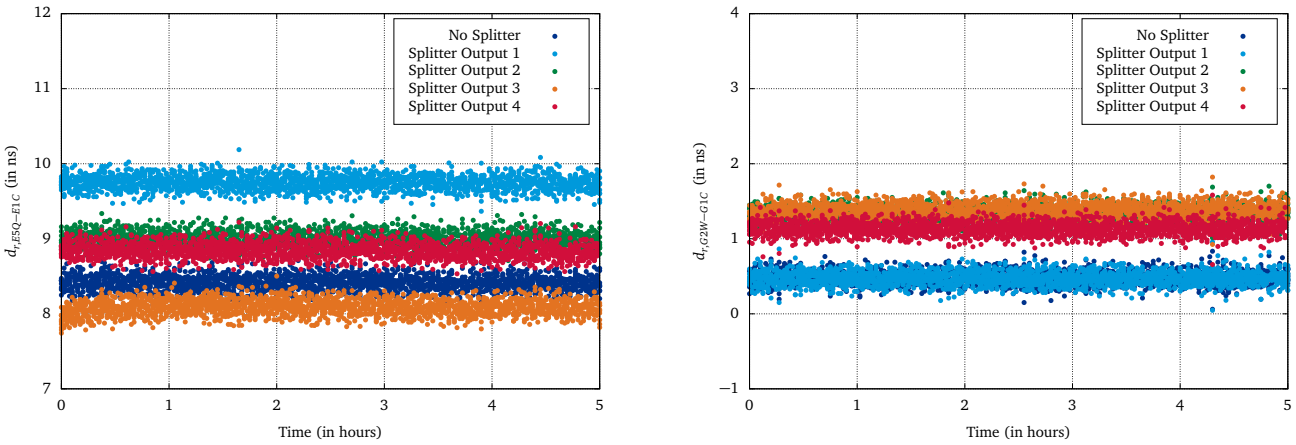

(a) Galileo signal receiver system DCB $d_{r,E5Q} - d_{r,E1C}$

(b) GPS signal receiver system DCB $d_{r,G2W} - d_{r,G1C}$

Figure 7.5: Impact of the 4-way GNSS splitter type A output selection on receiver system differential code biases.

Figure 7.6 shows the measured raw code observation differences for simulated Galileo and GPS signals with the receiver being connected to each of the four outputs of the second splitter in test.

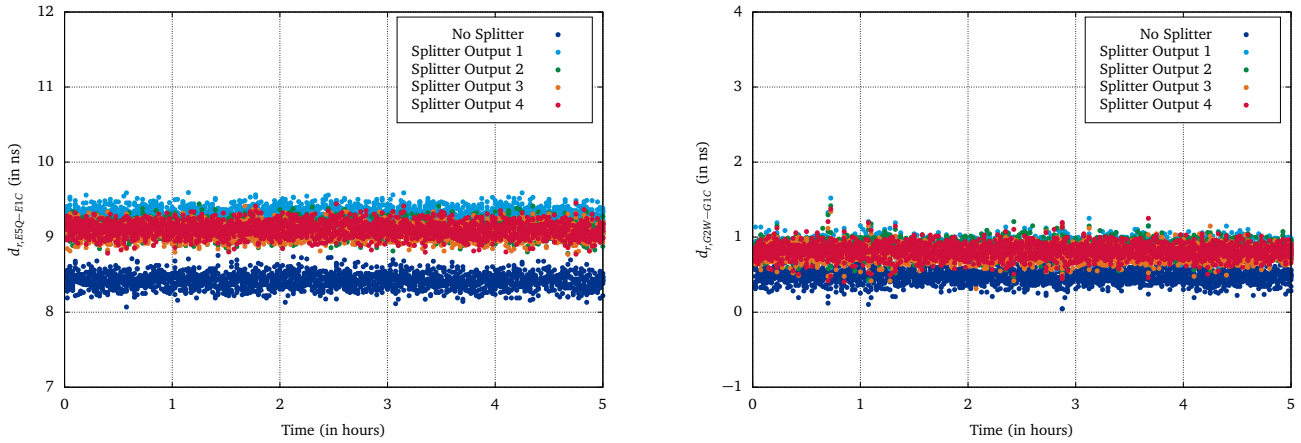

(a) Galileo signal receiver system DCB $d_{r,E5Q} - d_{r,E1C}$

(b) GPS signal receiver system DCB $d_{r,G2W} - d_{r,G1C}$

Figure 7.6: Impact of the 4-way GNSS splitter type B output selection on receiver system differential code biases.

Table 7.3 summarises the mean values and standard deviations of the splitter and selected output dependent receiver system DCBs. The analysis shows, that significant receiver system DCB differences up to 1.7 ns were measured for Galileo $d_{r,E5Q} - d_{r,E1C}$ between different outputs of splitter A. For this splitter type, different signal outputs show different receiver DCB measurements, which is most prominent for Galileo signals, shown in Figure 7.5a. The splitter output dependency is not as pronounced for GPS $d_{r,G2W} - d_{r,G1C}$ with receiver system DCB differences up to 0.9 ns. Splitter B does not show a signal output dependency on the measured receiver DCBs. Instead all splitter outputs induce a common receiver system DCB offset with respect to the scenario without splitter of approximately 0.7 ns for Galileo $d_{r,E5Q} - d_{r,E1C}$ and 0.4 ns for GPS $d_{r,G2W} - d_{r,G1C}$.

Table 7.3: Receiver system differential code bias dependency on selected splitter and signal output, determined from simulated multi-GNSS and multi-signal raw observations, shown in Figures 7.5 and 7.6.

Splitter Output	Mean Values Splitter A (in ns)		Mean Values Splitter B (in ns)	
	$d_{r,E5Q-E1C}$	$d_{r,G2W-G1C}$	$d_{r,E5Q-E1C}$	$d_{r,G2W-G1C}$
No Splitter	8.42 ± 0.1	0.48 ± 0.1	8.42 ± 0.1	0.48 ± 0.1
Output 1	9.75 ± 0.1	0.47 ± 0.1	9.29 ± 0.1	0.87 ± 0.1
Output 2	9.01 ± 0.1	1.35 ± 0.1	9.10 ± 0.1	0.90 ± 0.1
Output 3	8.09 ± 0.1	1.39 ± 0.1	9.07 ± 0.1	0.78 ± 0.1
Output 4	8.84 ± 0.1	1.14 ± 0.1	9.10 ± 0.1	0.81 ± 0.1

For the EGON receiver systems, identical splitters of type B are used and the selected splitter output is not changed. Therefore, no splitter hardware induced differences in receiver system DCBs can be assumed. However, the fact that the use of a splitter might induce receiver system DCB offsets with respect to not using any splitter needs to be accounted for when applying the calibrated receiver DCBs from Table 7.1.

The relative impact of the receiving antenna with a certain Low Noise Amplifier (LNA) on receiver system DCBs was analysed with real multi-GNSS and multi-signal raw observations, by manually switching the used antenna of a GNSS test site at ESOC. Receiver system DCBs were estimated for the test site as well as other EGON sites in a common adjustment. Figure 7.7 shows the impact of the antenna switch on day of year 2018-256. The estimated receiver system DCBs of the test site show antenna induced differences of up to approximately 7 ns for $d_{r,E7Q} - d_{r,E1C}$, whereas estimated receiver system DCBs of the EGON sites do not show any differences, as expected.

The EGON receiver network used for the analysis in section 7.1.2 did not exhibit any antenna change during the processed time interval. Therefore, the relative impact of a receiving antenna switch on receiver system DCBs can be neglected in the performed analysis. However, the fact that the receiving antenna with a certain LNA might induce receiver system DCB offsets with respect to feeding the GNSS signals directly from a simulator to the receiver needs to be accounted for when applying the calibrated receiver DCBs from Table 7.1.

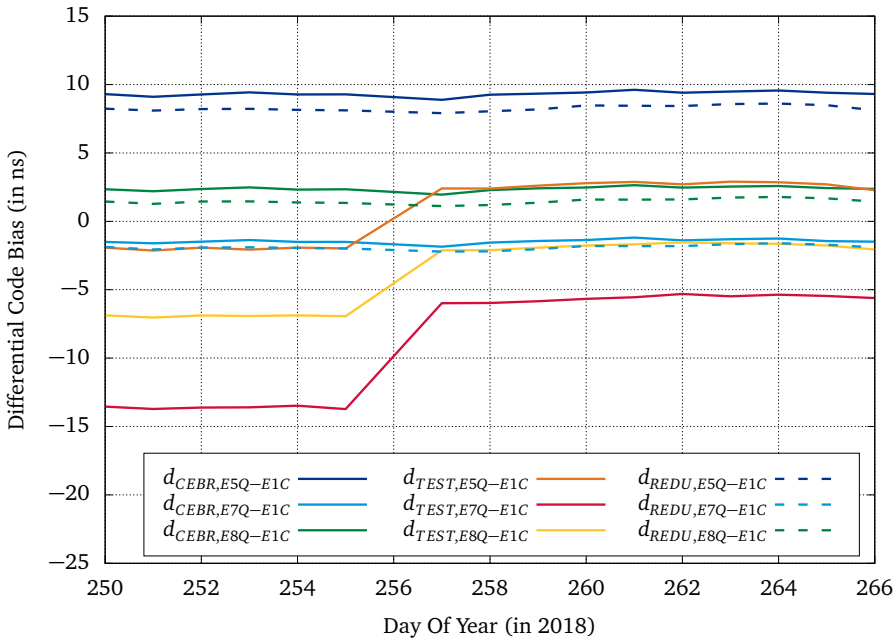

Figure 7.7: Impact of an antenna switch on estimated receiver system differential code biases (DCBs) for different Galileo signals.

Calibration of Absolute Code Biases with Real Data

The calibration of absolute raw observation code biases is only required for timing applications. The common processing approach however, is based on the ionosphere-free linear combination of dual-frequency observations, and therefore only the IF combination of dual-frequency absolute code biases needs to be applied in conventional timing applications. In order to use multi-GNSS and multi-signal raw observations for GNSS system time offset analyses shown in section 7.3, absolute receiver system code biases need to be determined for all processed GNSS and signals.
For the operational ESOC timing laboratory, contributing with two hydrogen masers to the derivation of UTC, absolute code bias calibration values are available for the used GNSS timing receiver. This EGON type receiver has been calibrated at Physikalisch-Technische Bundesanstalt (PTB) for GPS only code signals G1W and G2W, which are commonly used in the IF linear combination, as described above.

Table 7.4: Multi-GNSS multi-signal absolute code bias calibration values for the ESOC timing receiver used in the time offset analyses in section 7.3.

GNSS	Code Bias	Calibration Value (in ns)
Galileo	$d_{r,E1C}$	80.70
	$d_{r,E5Q}$	87.24
	$d_{r,E7Q}$	79.46
	$d_{r,E8Q}$	81.44
GPS	$d_{r,G1W}$	80.70
	$d_{r,G2W}$	79.45
	$d_{r,G1C}$	80.70
	$d_{r,G5Q}$	86.72
BeiDou	$d_{r,C2I}$	80.70
	$d_{r,C7I}$	79.83

Analyses have shown, that the receiver code bias of Galileo signal E1C is very close to the GPS signal G1W receiver code bias, with a difference not exceeding 1 ns (Defraigne et al., 2013), which was confirmed in (Elwischger et al., 2013) and

(Fonville et al., 2012). The similarity of these receiver code biases was assumed for the antenna as well (Defraigne et al., 2013). In order to process multi-GNSS and multi-signal raw observations, the GPS signal absolute calibration values are therefore used together with the calibrated DCBs in Table 7.1, to infer absolute receiver system code biases for Galileo and BeiDou signals.

Table 7.4 shows the calibrated absolute GPS signal code biases together with the determined multi-GNSS multi-signal absolute code biases, which were used in the multi-GNSS system time offset analyses in section 7.3.

7.1.2 GNSS Satellite Code Biases

The main goal of determining receiver system code biases in section 7.1.1 was to enable the estimation of physically meaningful navigation satellite code biases. The proper handling of receiver and physically meaningful satellite code biases is crucial for applications involving multiple GNSS and signals, like absolute ionosphere estimation and timing applications based on the raw observation processing approach as demonstrated in sections 7.2 and 7.3 and described in (Reckeweg et al., 2018). The subject of physically meaningful code biases will be of importance for future multi-GNSS and multi-signal applications based on receiver code bias calibrations, as the use of currently available satellite bias products can introduce significant inconsistencies.

This section describes and discusses satellite code bias products based on the conventional code bias determination approach, described in section 5.1.1, and presents the results of the estimation of physically meaningful multi-GNSS multi-signal satellite code biases performed in this work. As argued in section 5.2.2, it is adequate to handle GNSS signal code biases in the form of differential code biases with respect to a reference signal, which is also the case for the conventional satellite code bias determination approach.

Satellite code biases determined with the conventional approach $\tilde{d}^s_{ia-jb}$, described in section 5.1.1, deviate from the physical satellite DCB d^s_{ia-jb} by the constellation DCB mean value. Due to this re-definition of satellite DCBs, a change in the satellite constellation, ie. increasing or decreasing number of satellites or a change in the code bias of a single satellite, impacts the estimated DCBs of all satellites. Conventional satellite code bias products therefore show occasional common jumps for all satellite DCBs, which are processing artefacts mostly caused by satellites joining or leaving the constellation. Although these jumps can be seen in the satellite DCB time series, they have no physical meaning as the individual satellite on-board hardware bias did not change. This motivated the estimation of so called physically meaningful satellite DCBs with the multi-GNSS and multi-signal raw observation processing approach, described below.

Broadcast Satellite Group Delays

All GNSS satellites transmit so called satellite group delay (SGD) parameters as part of their navigation message, also referred to as BGD (Galileo OS SIS ICD, 2016; IS-GPS-200, 2015; BeiDou OS SIS ICD, 2016). As described in section 5.1.1, the main reason for the transmission of SGDs is to enable PVT services for single-frequency users, nevertheless these group delays could also be used for GNSS raw observation processing. For Galileo and GPS the definition of satellite BGDs is not equivalent to satellite differential code biases, however, BGDs can be transformed to satellite DCBs as shown in (5.14).

Figure 7.8 shows the DCBs $\tilde{d}^s_{E1-E5a}$ derived from satellite BGDs of signals E1 and E5a for different Galileo satellites for about 2.5 years. The time series shows significant jumps in the DCBs of all satellites at common points in time. This clearly indicates the zero-mean approach used by the Galileo control centre to generate satellite BGD values. An exception are the two jumps for satellite PRN numbers E18 (between 2019-048 and 2019-058) and E14 (between 2019-076 and 2019-083). As these were intentional changes of the individual satellite code biases, manually induced by the Galileo control centre, the satellite BGDs of only those two satellites show the respective change. Apparently, these two satellite code bias jumps were accounted for in the determination of the satellite BGDs of all other satellites. This however, was not the case for other satellite code bias products, as can be seen in Figure 7.11 and will be discussed below. The DCB values derived from satellite BGDs for the IOV satellites deviate from the measured calibration values in (GSA, European GNSS Agency, 2019a) by up to 6 ns, as shown in Table 7.5.

A similar behaviour of the satellite BGD time series can be seen for other GNSS, indicating that all system provider apply the zero-mean approach to determine broadcast satellite group delays. Figure 7.9a shows the DCBs $\tilde{d}^s_{L1P(Y)-L2P(Y)}$ derived from satellite BGDs of signals L1P(Y) and L2P(Y) for different GPS satellites. It can be seen that the zero-mean constraint applied for GPS satellites does not introduce huge jumps of satellite BGDs, which is mainly due to the fact that the GPS constellation is not changing significantly and it contains more satellites than Galileo or BeiDou. The change of GPS satellite DCB for PRN number G18 around 2018-022 is due to the fact, that the PRN number was assigned from satellite vehicle number GPS-054 to GPS-034. Figure 7.9b shows the DCBs $\tilde{d}^s_{B1I-B3I}$ derived from satellite BGDs of signals B1I and B3I for different BeiDou satellites.

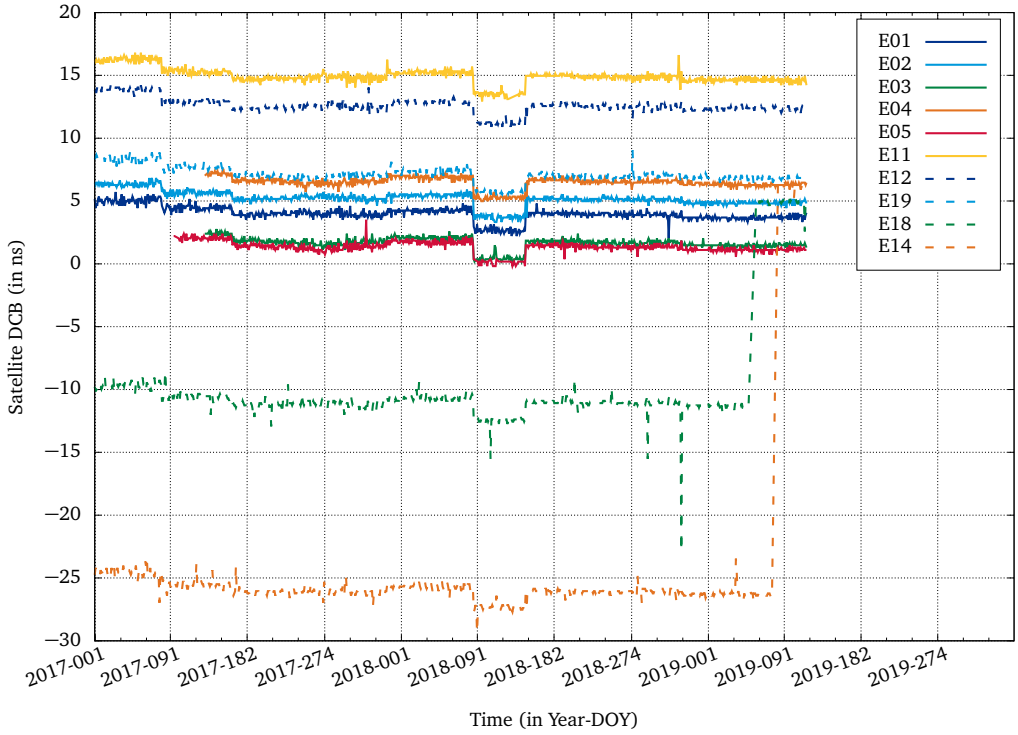

Figure 7.8: Galileo IOV and FOC satellite DCBs $\tilde{d}^{s}_{E1-E5a}$, derived from broadcast satellite group delays for signals E1/E5a.

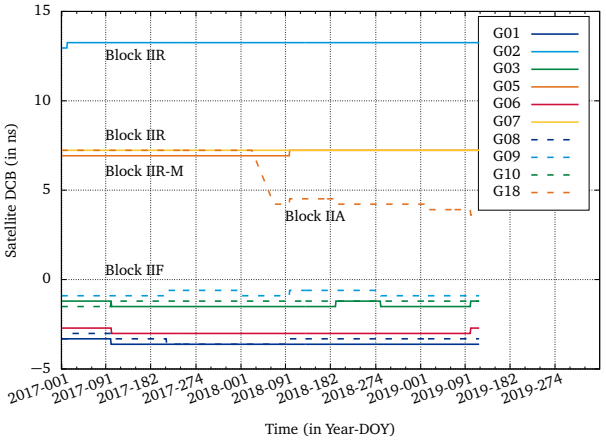

(a) GPS satellite DCBs $\tilde{d}^{s}_{L1P(Y)-L2P(Y)}$, derived from broadcast satellite group delays for signals L1P(Y)/L2P(Y).

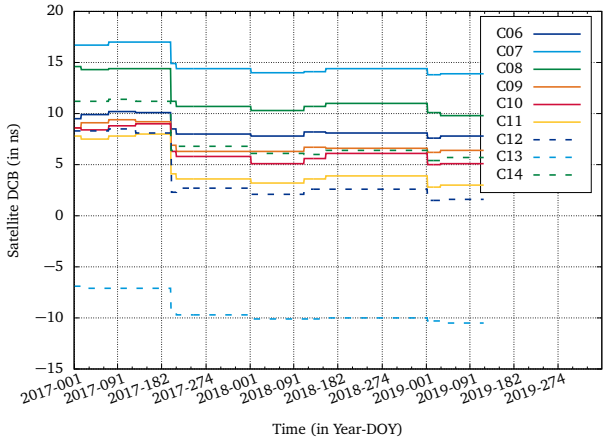

(b) BeiDou satellite DCBs $\tilde{d}^{s}_{B1I-B3I}$, derived from broadcast satellite group delays for signals B1I/B3I.

Figure 7.9: Satellite DCBs derived from satellite broadcast group delays.

Realignment of Galileo Satellite BGDs

Galileo is the only GNSS which provides satellite group delays measured on-ground by the spacecraft manufacturer (GSA, European GNSS Agency, 2019a), see values in Table 5.3. These measured SGD calibration values, provided for the Galileo IOV satellites, allow to generate physically meaningful DCBs for all Galileo satellites, by realigning the satellite BGDs.
The realignment is done by splitting the whole satellite BGD time series in intervals without jumps and then perform the following steps for each time interval:

- Compute the DCB mean value for each IOV satellite with $s \in$ [E11, E12, E19] and the number of epochs N in a certain time interval $t_i \in [t_1, \ldots, t_N]$

$$\bar{d}^s = 1/N \sum_{i=1}^{N} d^s(t_i)$$

- Compute the difference between determined IOV satellite DCB mean value and calibration value from (GSA, European GNSS Agency, 2019a) with $s \in$ [E11, E12, E19]

$$\Delta d^s = \bar{d}^s - d^s_{cal}$$

- Compute the realignment value as the mean of the IOV deviations from the calibration values with $s \in$ [E11, E12, E19]

$$\Delta d_{\text{realgn}} = 1/3 \sum_s \Delta d^s$$

- Apply the realignment value to all Galileo satellites to generate physically meaningful DCBs

$$d^s_{E1-E5a} = \tilde{d}^s_{E1-E5a} - \Delta d_{\text{realgn}}$$

As shown in Figure 7.10, the realignment of Galileo satellite BGDs with IOV satellite group delay calibration values generates physically meaningful DCBs for all Galileo satellites and removes all jumps in the Galileo satellite DCB time series.

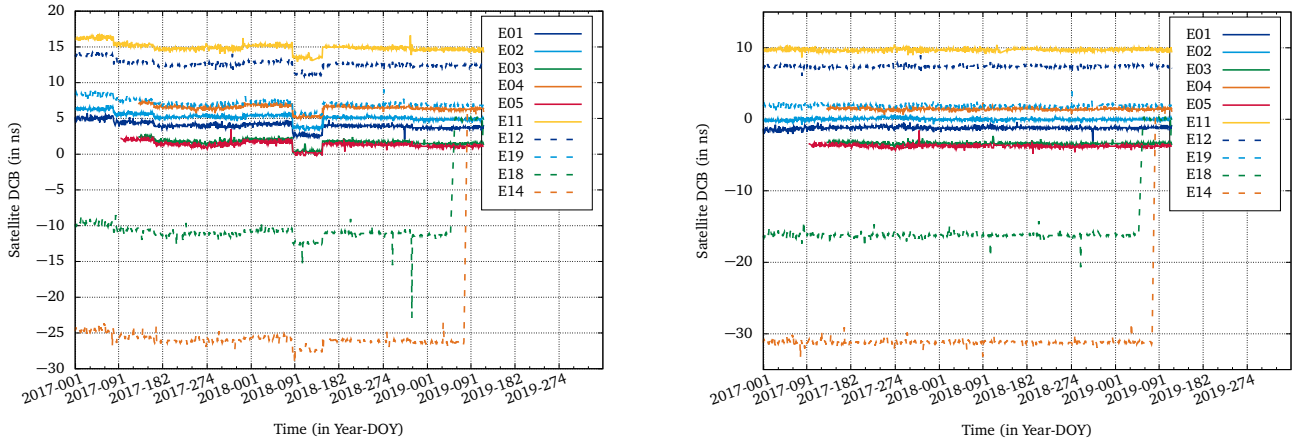

(a) Original Galileo satellite DCBs $\tilde{d}^s_{E1-E5a}$

(b) Realigned Galileo satellite DCBs d^s_{E1-E5a}

Figure 7.10: Galileo IOV and FOC satellite DCBs derived from broadcast satellite group delays for signals E1/E5a.

The realignment values computed from Galileo IOV satellite BGDs and the corresponding DCB calibration values are given in Table 7.5.

Available Satellite Code Bias Products

In addition to the broadcast satellite group delays, other multi-GNSS multi-signal satellite code bias products have been analysed. DLR and CAS both provide multi-GNSS DCB products derived from observations of the IGS Multi-GNSS Experiment (MGEX) network (Montenbruck et al., 2017), available from (CDDIS, Crustal Dynamics Data Information System, 2019a). Both centres determine daily DCB solutions and apply a zero-mean condition per satellite constellation to separate satellite- and receiver-specific differential code biases. Details of the DCB estimation process used by DLR are described in (Montenbruck et al., 2014), whereas Wang et al. (2016) and Li et al. (2012) provide a description of the method used by CAS.

Table 7.5: Galileo satellite BGD realignment values to generate physically meaningful satellite DCBs and remove jumps in the time series of Galileo satellite DCBs derived from broadcast satellite group delays.

Time Interval (in Year-DOY)	Realignment value Δd_{realgn} (in ns)
2017-001 - 2017-081	6.49 ± 0.45
2017-082 - 2017-164	5.64 ± 0.35
2017-166 - 2017-348	5.07 ± 0.38
2017-351 - 2018-086	5.49 ± 0.40
2018-088 - 2018-148	3.81 ± 0.44
2018-152 - 2018-330	5.17 ± 0.44
2018-335 - 2019-120	4.87 ± 0.42

Figure 7.11 shows the daily Galileo satellite DCB estimates $\tilde{d}^s_{E1C-E5Q}$ from DLR for the same Galileo satellites and time interval as used for the satellite BGDs. Compared to DCBs derived from satellite BGDs in Figure 7.8, the daily satellite DCB estimates show different but still common jumps for all satellites in the time series and an agreement of the DCB values within 1 ns for most of the analysed time interval. Comparing the DCB estimates of the IOV satellites with the calibration values in (GSA, European GNSS Agency, 2019a) however, reveals that the Galileo satellite DCB estimates are offset with respect to the measured values on-ground by approximately 6 ns. In addition, the intentional changes of the satellite BGDs for satellite PRN numbers E14 and E18 in the beginning of 2019, lead to significant jumps of all Galileo satellite DCBs. It should be emphasised, that the status of the two Galileo satellites in eccentric orbit GSAT0201 (E18) and GSAT0202 (E14) is set to *testing* and they are not part of the *usable* Galileo constellation. The fact that a change of the satellites under test impacts satellite code biases of all active Galileo satellites is questionable and particular care must be taken when making use of these satellite code bias products.

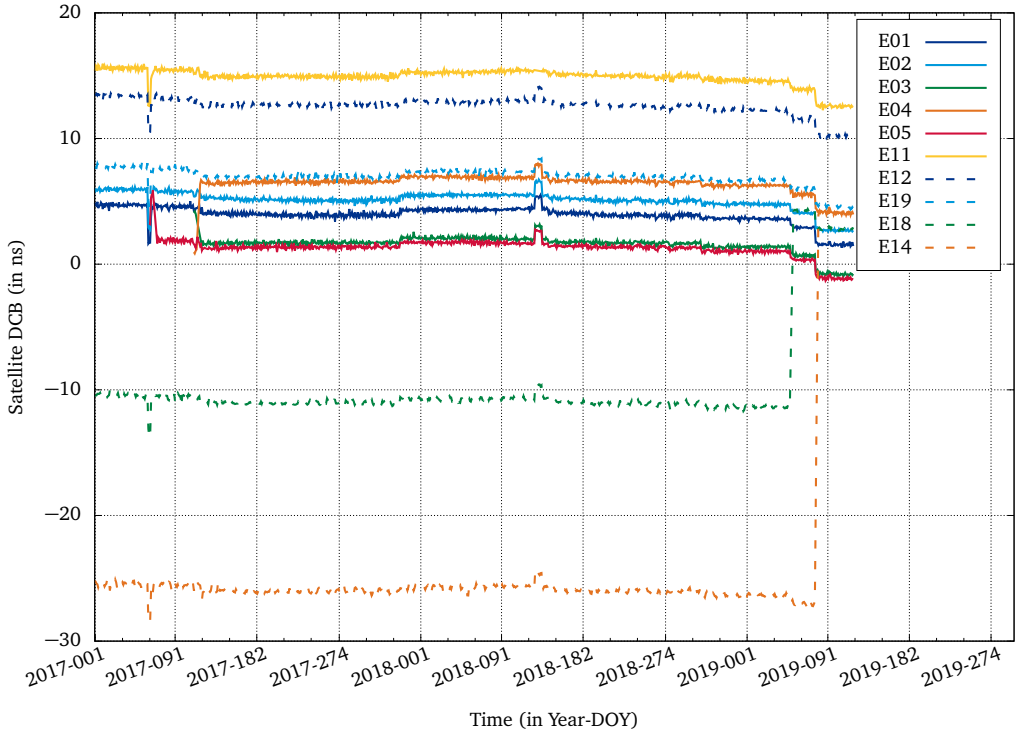

Figure 7.11: Galileo satellite $\tilde{d}^s_{E1C-E5Q}$ DCB estimates by DLR (Daily IGS MGEX DCB solutions in Bias-SINEX format) from (CDDIS, Crustal Dynamics Data Information System, 2019a).

Figure 7.12 shows the daily GPS and BeiDou satellite DCB estimates from DLR for $\tilde{d}^s_{G1C-G2W}$ and $\tilde{d}^s_{C2I-C6I}$ respectively and for the same satellites and time interval as for the satellite BGDs in Figure 7.9. As for the broadcast values the zero-mean constraint applied for GPS satellites does not introduce huge jumps of satellite DCBs, whereas for BeiDou significant

jumps are visible for all shown satellites. The change in satellite DCB for PRN number G18 around 2018-022 is due to the fact, that the PRN number was assigned from satellite vehicle number GPS-054 to GPS-034, whereas a second change can be identified around 2018-320, which potentially is due to a hardware change on-board the satellite. Both changes are too small to have a significant impact on the estimation of other GPS satellite DCB values.
Unlike Galileo, the GPS and BeiDou satellite DCB estimates from DLR do not agree with the DCBs derived from satellite BGD values and deviate by up to 6 ns for GPS and 8 ns for BeiDou. It should be noted however, that for GPS satellites different signal combinations are compared, as DLR does not provide the satellite DCBs $\tilde{d}^s_{G1W-G2W}$. However, as DCBs between signals on the same carrier frequency, e.g. $\tilde{d}^s_{G1C-G1W}$, typically are on the 1-2 ns level only (CDDIS, Crustal Dynamics Data Information System, 2019a), a deviation of up to 6 ns for the GPS DCBs indicates a significant offset to the DCBs derived from satellite BGD values.

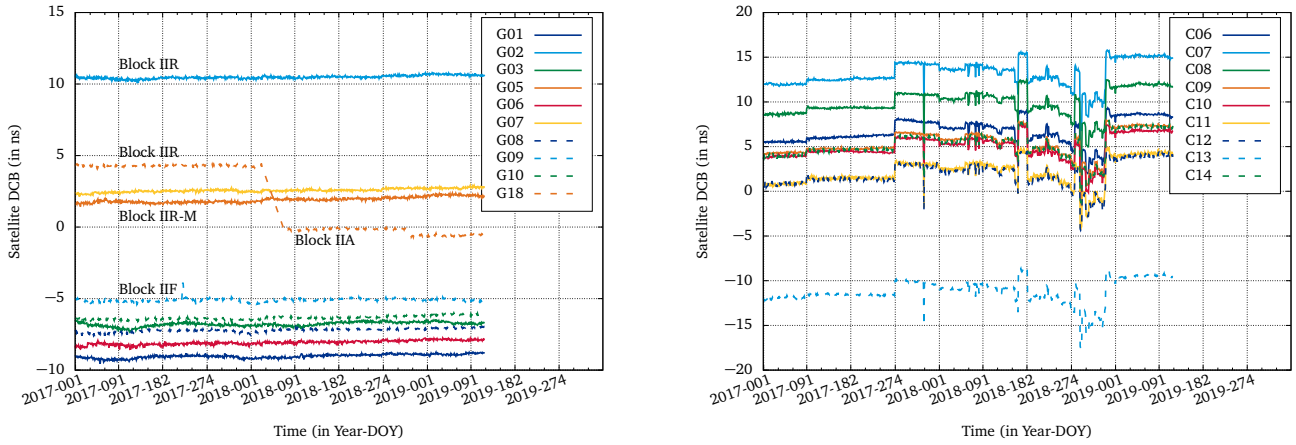

(a) GPS satellite DCB $\tilde{d}^s_{G1C-G2W}$

(b) BeiDou satellite DCB $\tilde{d}^s_{C2I-C6I}$

Figure 7.12: Satellite DCB estimates by DLR (Daily IGS MGEX DCB solutions in Bias-SINEX format) from (CDDIS, Crustal Dynamics Data Information System, 2019a).

Satellite Code Bias Estimation with Raw Method

The estimation of physically meaningful multi-GNSS multi-signal satellite code biases performed in this work is based on the raw observation processing approach with GNSS observation data from ESA's GNSS Observation Network (EGON), shown in Figure 7.1. As described in section 5.2.2 GNSS signal code biases are handled in the form of differential code biases with respect to a reference signal. However, besides fixing the reference signal absolute code bias to zero, all satellite code biases are estimated free, without additional (zero-mean) constraints.
As GNSS raw observation contain the sum of satellite- and receiver-specific code biases, calibrated receiver differential code biases are used to separate satellite and receiver code biases. The receiver DCBs however, are not fixed to the values measured in section 7.1.1. In order to allow for variations of the estimated receiver system DCB values with respect to the calibration values, the receiver code bias parameters are constrained with a standard deviation of 1 ns, as described in section 5.3.5. Residual ionosphere slant Total Electron Content (TEC) values are estimated with respect to applied ionospheric delays from IONEX files, generated by ESOC.

Figure 7.13 shows the physically meaningful Galileo satellite DCBs $d^s_{E1C-E5Q}$ for the same Galileo satellites and time interval as used before, estimated with the raw observation processing approach.
Compared to DCBs derived from satellite BGDs and the DCB product from DLR in Figures 7.8 and 7.11, the daily satellite DCBs estimated with the raw observation processing approach do not show common jumps for all satellites in the time series, but a constant DCB value for most satellites with stabilities of 0.2 ns - 0.5 ns. The estimated DCB values for the IOV satellites agree with the measured calibration values in (GSA, European GNSS Agency, 2019a) within 1 ns, which is also true for the estimated DCB values of all Galileo satellites with respect to the realigned satellite DCBs derived from satellite BGDs shown in Figure 7.10b. This motivates to use the term *physically meaningful* satellite DCBs and confirms the consistency of the applied receiver system DCB calibration values determined in section 7.1.1 and the estimated residual ionosphere slant TEC values.

Figure 7.13 also reveals, that the intentional changes of the satellite BGDs for satellite PRN numbers E14 and E18 in the beginning of 2019 do not impact the estimation of other Galileo satellite DCBs, when the raw observation process-

Figure 7.13: Galileo satellite $d^s_{E1C-E5Q}$ DCB estimates based on the raw observation processing approach with constrained EGON receiver DCBs and estimated residual ionospheric delays.

ing approach described above is used. However, the manually induced jumps of the two Galileo satellite BGD values can properly be determined. It should be noted, that several points have to be considered when comparing estimated physically meaningful Galileo IOV satellite DCBs with the measured calibration values. For the comparison it is not clear which on-board subsystem ("primary" or "redundant") was active during the analysed time interval and whether a switch happened from one to the other. On-ground measurements of the IOV DCBs d^s_{E1-E5} deviate for the two subsystems by up to 1.4 ns (GSA, European GNSS Agency, 2019a). Another issue is the fact that on-ground measurements of the IOV DCBs are only available for the frequency bands E1, E5 and E6, without specifications for E5a and E5b. The last point is that aging effects of the measured DCBs for IOV satellites launched in 2011/2012 are ignored.

Still, the fact that the described raw observation processing approach could be used to estimate physically meaningful IOV satellite DCBs close to the measured calibration values in (GSA, European GNSS Agency, 2019a), supports the use of this method to also estimate physically meaningful DCBs for the other Galileo satellites, satellites of other GNSS and other signals.

Figure 7.14 shows the physically meaningful GPS and BeiDou satellite DCBs $d^s_{G1C-G2W}$ and $d^s_{C2I-C7I}$ respectively for the same satellites and time interval as used before, estimated with the raw observation processing approach. The daily estimates show constant satellite DCBs for most of the time interval. An exception are the DCB estimates of GPS satellite PRN number G18 and the BeiDou IGSO satellites in the end of 2018. The change in satellite DCB for PRN number G18 around 2018-022 is due to the fact, that the PRN number was assigned from satellite vehicle number GPS-054 to GPS-034, whereas the second change around 2018-320 potentially is due to a hardware change on-board the satellite. Whereas BeiDou MEO satellites (C11, C12 and C14) were not affected, BeiDou IGSO satellites were tracked by only one EGON receiver during days 2018-317 - 2018-330. This lead to an increase of the estimated satellite DCBs of approximately 2 ns and demonstrates the importance of using a network of receivers with calibrated DCB values.

As no measured calibration values of GPS and BeiDou satellites are available from the GNSS service providers, no independent validation of the estimated physically meaningful satellite DCBs can be performed, as it was done for Galileo.

The mean and standard deviation values of all estimated physically meaningful satellite DCBs shown in Figures 7.13 and 7.14 are given in Table 10.7. Estimates of physically meaningful satellite DCBs for other signals are shown in appendix section G.

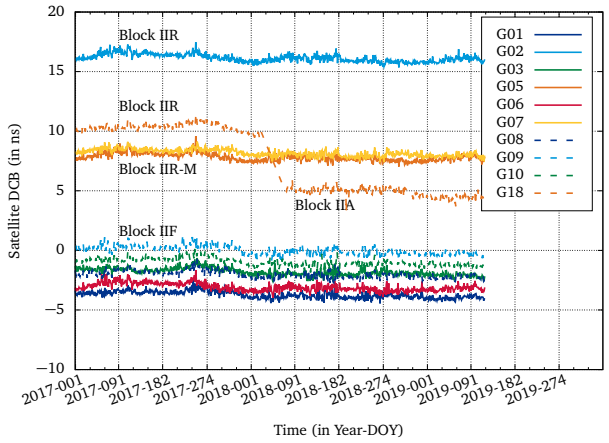

(a) GPS satellite DCB $d^s_{G1C-G2W}$

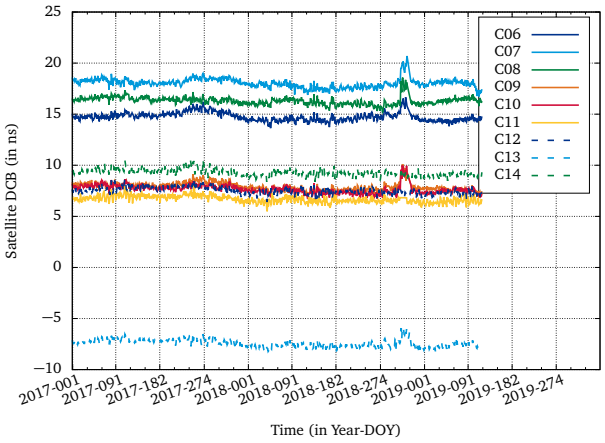

(b) BeiDou satellite DCB $d^s_{C2I-C7I}$

Figure 7.14: Satellite DCB estimates based on the raw observation processing approach with constrained EGON receiver DCBs and estimated residual ionospheric delays.

7.2 Ionospheric Delay Estimation

The estimation of slant ionospheric delay STEC parameters as an atmospheric research application is used to demonstrate and motivate the use of physically meaningful GNSS signal code biases. As described in section 5.2.3, in the raw method STEC parameters are estimated per processing epoch from multi-signal raw observations.

The estimation of physically meaningful ionospheric delays, also referred to as unbiased or absolute ionosphere estimation is based on constraining receiver DCBs to the calibrated values determined in section 7.1.1. In addition, physically meaningful satellite DCBs, derived in section 7.1.2, are applied. The impact on the ionospheric delay estimation when using satellite DCBs determined with zero-mean constraint instead is analysed (cf. Reckeweg et al., 2017).

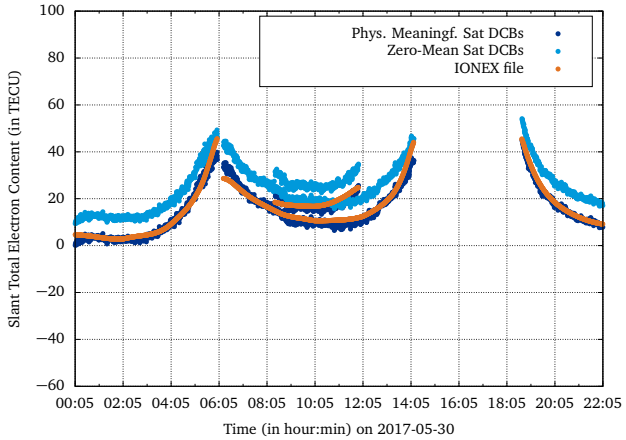

(a) STEC estimates for Galileo satellite PRN numbers E01, E07 and E09 based on multi-frequency raw observations.

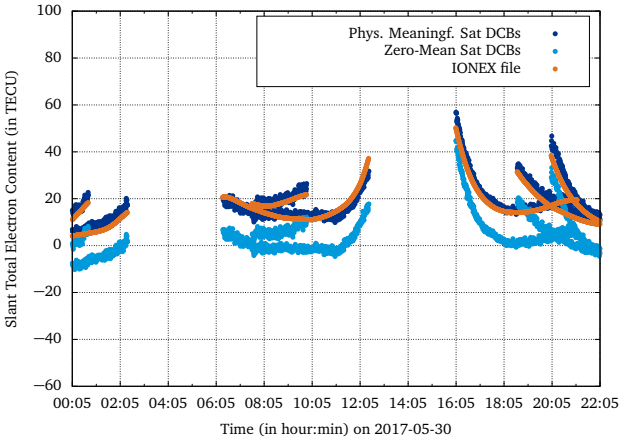

(b) STEC estimates for GPS satellite PRN numbers G01, G03, G10 and G24 based on triple-frequency raw observations.

Figure 7.15: Ionospheric delay estimates from multi-frequency raw observation processing compared to STEC values derived from IONEX files generated at ESOC.

Figure 7.15 shows the absolute ionosphere STEC estimates for an EGON type GNSS receiver at ESOC and different Galileo and GPS satellites, determined from multi-signal raw observations. The ionosphere estimates with applied physically meaningful and zero-mean satellite DCBs are compared to STEC values derived from an IONEX file, generated at ESOC. The Figures show, that STEC estimates from multi-signal raw observations determined with applied physically meaningful satellite DCBs agree well with the values derived from the IONEX file. The use of zero-mean constrained satellite DCBs leads to offsets in the ionospheric delay estimation. In the case of GPS this even leads to the estimation of negative STEC values, which is physically impossible, as the slant total electron content is defined as the number of electrons within a certain cross-section along the signal path, described in section 4.1.4.

Figure 7.16 shows the absolute ionosphere STEC estimates for the same receiver at ESOC and different GPS and BeiDou satellites, determined from dual-signal raw observations only. In principle the Figure also shows, that STEC estimates with applied physically meaningful satellite DCBs agree quite well with STEC values derived from the IONEX file and using zero-mean constrained satellite DCBs leads to physically impossible estimates. However, Figure 7.16 also shows that using only dual-frequency raw observations leads to STEC estimates, which do not agree as well with the reference STEC values derived from the IONEX file, compared to estimates from multi-frequency raw observations in Figure 7.15. In addition, the estimation of ionospheric delays for BeiDou satellites shows an increased noise compared to Galileo and GPS, which is partly reflected in the higher code observation residuals shown in Figure 7.19b. The increased noise for the left and centre satellite passes shown in Figure 7.16b might also reflect, that these are IGSO satellites, whereas the satellite pass on the right with lower noise belongs to a MEO satellite.

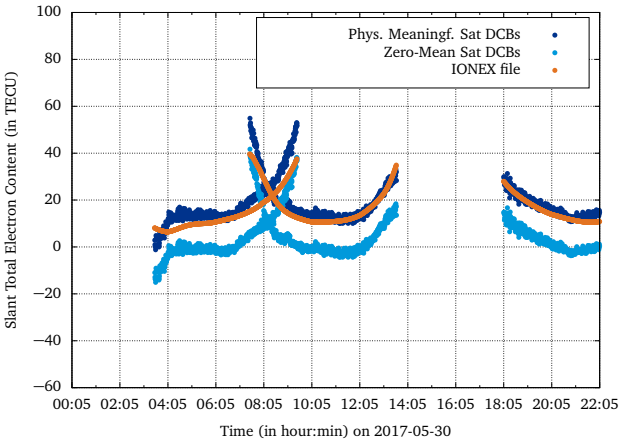

(a) STEC estimates for GPS satellite PRN numbers G11, G12 and G13.

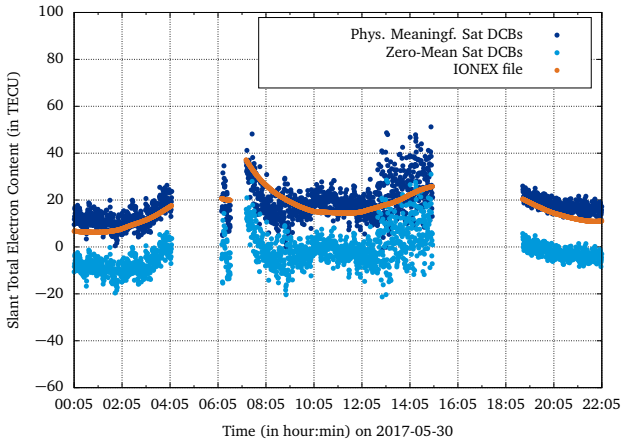

(b) STEC estimates for BeiDou satellite PRN numbers C07, C12 and C13.

Figure 7.16: Ionospheric delay estimates from dual-frequency raw observation processing compared to STEC values derived from IONEX files generated at ESOC.

7.3 GNSS Time Offset Analysis

The determined multi-GNSS multi-signal absolute code bias values shown in Table 7.4 were used to demonstrate the application of estimating GNSS system time and inter-system time offsets (Inter-System Time Offset (ISTO)) with the raw observation processing approach. This analysis is based on Galileo, GPS and BeiDou broadcast satellite orbits and clock offsets, as only these products refer the satellite clock offsets to the respective GNSS system time. In conventional multi-GNSS orbit and clock products all values are referred to a common time scale. Theoretically, these products could also be used to derive inter-system time offsets, however, due to the conventional way of handling ionosphere-free signal biases, the derived ISTO would not describe the actual offset between GNSS system times, as described in section 7.3.2.

7.3.1 System Time Offset to UTC

The GNSS system time offset relative to UTC is computed from receiver clock offset estimates, determined with the raw observation processing approach. multi-GNSS and multi-signal raw observations were used with applied absolute code bias calibration values for an EGON type timing receiver at ESOC, physically meaningful GNSS satellite DCBs, determined in section 7.1.2 and estimated absolute ionospheric delays. For BeiDou, determined physically meaningful GNSS satellite DCBs could not be used in this analysis, as the BeiDou broadcast satellite clock offsets refer to signal B3I, as described in section 5.1.1 and (BeiDou OS B3I SIS ICD, 2018). As no simulated BeiDou B3I signals were available, no receiver DCBs could be calibrated relative to signal B3I. Therefore, satellite BGD values were used instead to determine BeiDou system time offset relative to UTC. These are the BGD values, users would have to apply for BeiDou timing applications based on the standard single-frequency or dual-frequency ionosphere-free processing approach. For Galileo and GPS, the usage of broadcast satellite orbits and clock offsets determined with the conventional ionosphere-free processing approach prevent the direct usage of determined physically meaningful satellite DCBs. The applied satellite DCBs therefore need to be modified into pseudo-absolute code biases, as described in section 5.2.4.

The determination of GNSS system time offset relative to UTC is based on clock offset estimates of an EGON type timing receiver. This timing receiver is connected to a steered hydrogen maser, which defines the physical time realisation

UTC(ESOC). For clock offsets determined relative to each GNSS system time scale τ_{Ξ} with $\Xi \in$ [GST, GPST, BDT] the following steps are performed:

- Compute the daily receiver clock offset mean value with the number of processing epochs per day N and $t_i \in [t_1, \ldots, t_N]$

$$\overline{dt}_{ESOC,\Xi} = 1/N \sum_{i=1}^{N} dt_{ESOC,\Xi}(t_i)$$

- The clock offset mean value represents the daily offset between the local time realisation and GNSS system time, as described in section 3.2.5

$$\overline{dt}_{ESOC,\Xi} = \tau_{UTC(ESOC)} - \tau_{\Xi}$$

- Align the daily clock mean values to UTC by applying the offset between UTC and the physical time realisation UTC(ESOC), derived from the so called BIPM *Circular T* (BIPM, Bureau International des Poids et Mesures, 2019a)

$$\tau_{\Xi} - \tau_{UTC} = -\left(\overline{dt}_{ESOC,\Xi} + \left[\tau_{UTC} - \tau_{UTC(ESOC)}\right]\right)$$

It should be noted, that leap seconds have been accounted for in addition in order to be consistent with the initial definition of the different GNSS system times, shown in Figure 3.1. Figure 7.17 shows the GNSS system time offsets with respect to UTC (modulo 1 second) for Galileo (GST $= \tau_{GST} - \tau_{UTC}$), GPS (GPST $= \tau_{GPST} - \tau_{UTC}$) and BeiDou (BDT $= \tau_{BDT} - \tau_{UTC}$), determined with the raw observation processing approach from multi-GNSS and multi-signal raw observations. Absolute calibrated timing receiver code biases from Table 7.4 and satellite DCBs determined in 7.1.2 were applied and the absolute slant ionospheric delay was estimated.

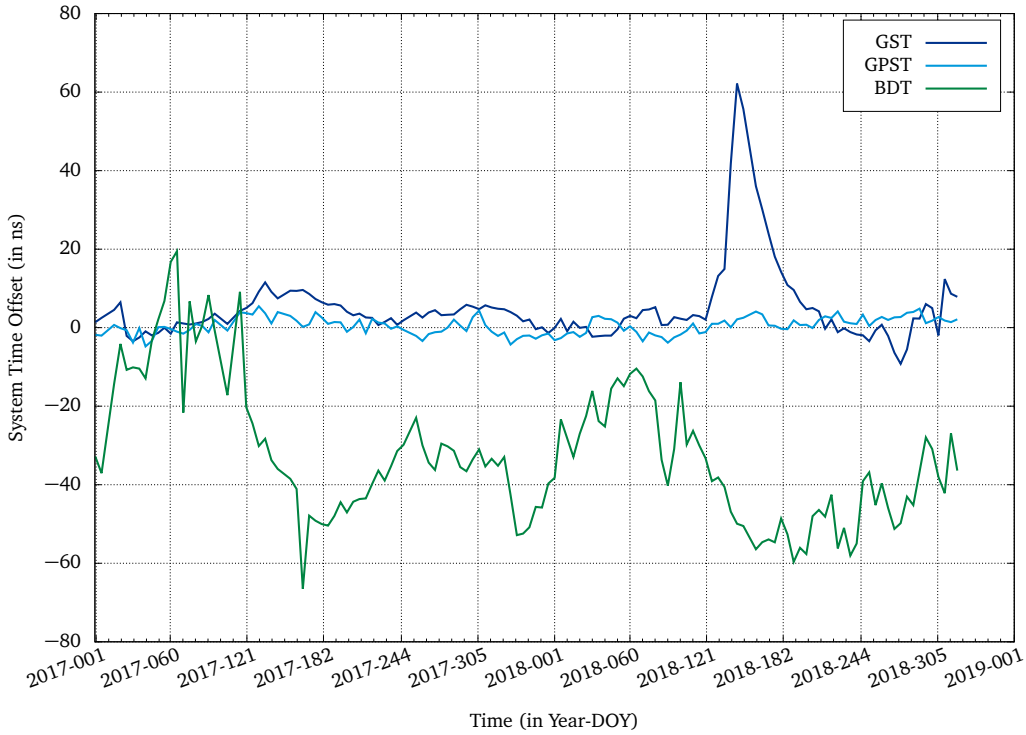

Figure 7.17: GNSS system time offset with respect to UTC determined with the raw observation processing approach from multi-GNSS and multi-signal raw observations.

Figure 7.17 shows, that for most of the analysed time interval GST and GPST stay within ±10 ns relative to UTC, whereas BDT deviates up to 60 ns. As discussed before, satellite BGD values were used instead of determined physically meaningful satellite DCBs for BeiDou. This however, can not explain the huge offset determined for BDT relative to UTC. As the daily code observation residual mean values for BeiDou signals shown in Figure 7.19b are reasonable, as are the estimated absolute ionospheric delays shown in Figure 7.16b, it may be concluded that the BeiDou system time has a mean offset relative to UTC of approximately 40 ns after day 2017-130.
The analysis also shows that around day 2018-146, Galileo system time encountered an unusual peak, which indicates a malfunction in the time transfer of the not yet fully operational GNSS. Events like that motivate the independent monitoring of different GNSS system times for multi-GNSS applications as demonstrated with the raw observation processing approach.

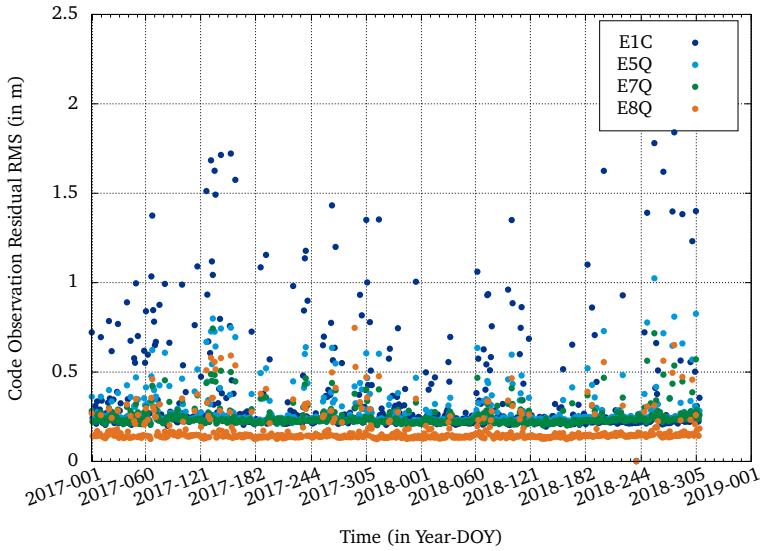

Figure 7.18: Galileo code observation residual RMS daily mean values for the EGON type timing receiver used to estimate the GNSS system times.

Figure 7.18 and 7.19 show the multi-GNSS and multi-signal code observation residual RMS daily mean values for the EGON type timing receiver used to estimate the GNSS system times.

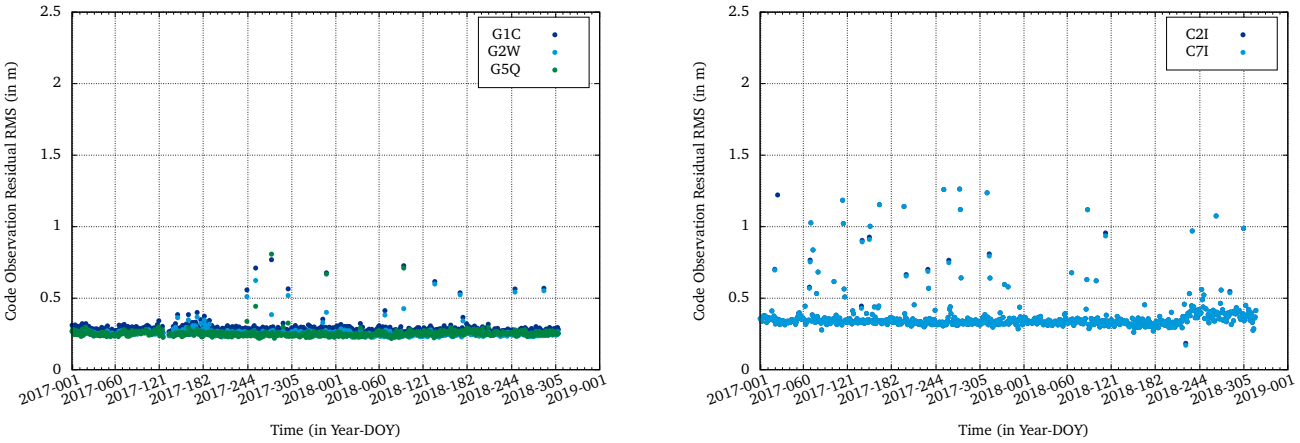

(a) GPS signals

(b) BeiDou signals

Figure 7.19: Code observation residual RMS daily mean values for the EGON type timing receiver used to estimate the GNSS system times.

The general code residual RMS level for all GNSS and signals is below 0.5 m, however, for Galileo and BeiDou signals more outlier are visible compared to GPS signals. The GPS signals show code residual RMS values around 27 cm, whereas BeiDou signal code residuals have an RMS mean value of 38 cm. Galileo signal code residuals are comparable to GPS except for the Galileo E5 AltBOC signal, which shows an RMS mean value of only 17 cm.

7.3.2 Inter-System Time Offset

Inter-System Time Offset (ISTO) is the general term for the system time difference between two GNSS. The inter-system time offset is crucial for multi-GNSS applications in combination with the GNSS broadcast satellite orbits and clocks, which all refer to their own GNSS system time.

To support multi-GNSS application, the difference between GST and GPST, referred to as Galileo-GPS Time Offset (GGTO) is broadcast in the Galileo navigation message. The *GPGA* parameter retrieved from mixed broadcast navigation RINEX files (CDDIS, Crustal Dynamics Data Information System, 2019b) refers to the Galileo minus GPS time

offset and was used as reference value in the GGTO analysis. It should be noted, that in RINEX 3.04, the label of the parameter was changed to *GAGP*, but its value still refers to the Galileo minus GPS time offset.
The Galileo and GPS system time offsets relative to UTC, determined in section 7.3.1 were used to compute the GGTO based on the raw observation processing approach with absolute ionospheric delay estimates. In addition, the GGTO was determined with residual ionospheric delay estimates, constrained with respect to applied ionospheric delays from IONEX files generated by ESOC to demonstrate the impact of absolute ionospheric delay estimation.
In conventional multi-GNSS precise satellite orbit and clock products generated with the ionosphere-free processing approach, all satellite clock offsets are referred to a common time scale and the ISTO is lumped together with receiver dependent IF signal code biases and estimated as the so called ISB. The ISB between Galileo and GPS determined with receiver r and ionosphere-free observables G_i [e.g. GPS IF(G1W,G2W)] and E_j [e.g. Galileo IF(E1C,E5Q)] can be defined as

$$\mathrm{ISB}_{r,E_jG_i}(t) = \mathrm{GGTO}(t) + d_{r,E_j}(t) - d_{r,G_i}(t)\,, \tag{7.2}$$

where $d_{r,X}(t)$ is the ionosphere-free linear combination X of the corresponding receiver code biases, as defined in (4.64). The ISB therefore is not (only) a time offset between two different GNSS and without knowledge of the receiver IF signal code biases, the parameter is not physically meaningful, especially for timing applications.
Figure 7.20 shows GPGA values of the Galileo navigation message, retrieved from mixed broadcast navigation RINEX files together with GGTO values computed from GNSS system time offsets relative to UTC, determined with the raw method as shown in section 7.3.1. In addition the GGTO values inferred from the standard multi-GNSS solution generated at ESOC based on the conventional dual-frequency ionosphere-free (IF) processing approach are shown.

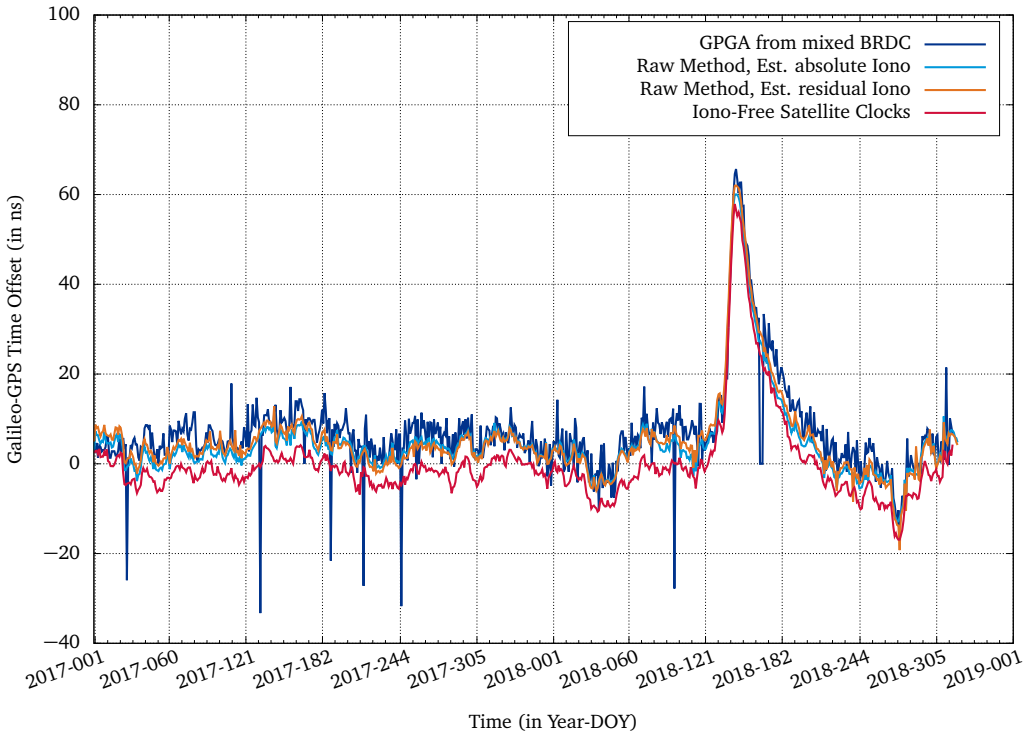

Figure 7.20: Galileo-GPS time offset (GGTO) comparison between GPGA parameter in mixed broadcast navigation RINEX files, computed GGTO values based on the raw method with absolute or residual ionospheric delay estimates and GGTO values computed from precise multi-GNSS ionosphere-free (IF) satellite clock products.

The GGTO values based on the raw observation processing approach are less noisy than the GPGA values from mixed broadcast navigation RINEX files, while the time offset values agree well for most of the analysed time interval. The raw observation processing approach can therefore be used to determine physically meaningful GGTO values from multi-signal raw observations with applied absolute code bias calibration values, physically meaningful GNSS satellite DCBs and estimated ionospheric delays. The two different raw observation processing approaches almost show identical results, demonstrating that the absolute estimation of ionospheric delays has no negative impact on the results compared to applying ionospheric delays from IONEX files. The GGTO values inferred from multi-GNSS precise satellite clocks generated with the conventional ionosphere-free processing approach however, show an almost constant offset of ap-

proximately 8 ns to the GGTO values determined with the other methods. This confirms the existence of additional receiver- and signal-specific biases in these GGTO values, as described in the ISB definition (7.2).

7.4 Multi-GNSS Precise Orbit Determination with Fixed Raw Carrier Phase Ambiguities

The integer ambiguity resolution approach based on multi-GNSS and multi-signal raw observation processing implemented in the course of this work and described in section 6, is applied to precise orbit determination of multi-GNSS satellites with raw observation data from global receiver networks. The general performance of the integer ambiguity resolution approach is analysed by comparing determined multi-GNSS satellite orbits of float ambiguity and fixed ambiguity solutions. In addition results are compared to available products from IGS and multi-GNSS products from ESOC, both based on the conventional ionosphere-free dual-frequency processing and ambiguity fixing approach, described in section 5.1. The performance of the integer ambiguity resolution approach based on multi-GNSS and multi-signal raw observation processing is compared among the individual GNSS and for different signals and the impact of introducing inter-system integer ambiguity resolution is analysed.

7.4.1 Global Network Adjustment

Different global GNSS receiver networks have been used in this analysis, all based on a selection of EGON receivers and additional IGS stations. The receiver selection for the three different networks is based mostly on geometry to obtain a well distributed global network. For the first network, the number of receivers was limited to 100 stations (labeled GE^*_{100}) with a typical network geometry shown in Figure 7.21a, which includes some receivers tracking only GPS signals. For the other two networks used in the analysis, the selection was limited to receivers tracking (at least) both GPS and Galileo signals, whereas one network consists of 100 receivers (labeled GE_{100}) and another network consists of 60 receivers (labeled GE_{60}), shown in Figure 7.21b.

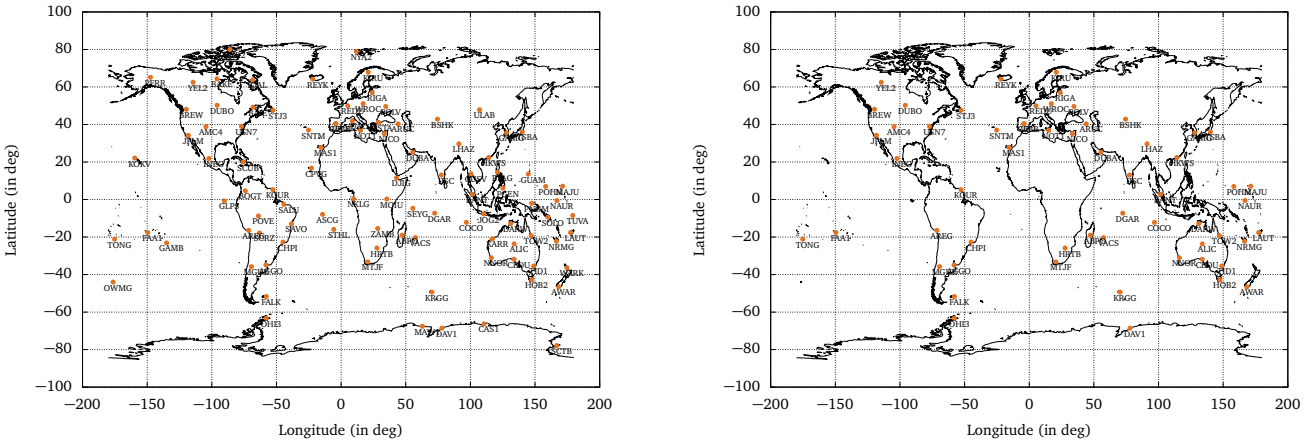

(a) Network with 100 receivers, some tracking only GPS signals (GE^*_{100})

(b) Network with 60 receivers, all tracking (at least) both GPS and Galileo signals (GE_{60})

Figure 7.21: Global receiver networks used for the analyses of multi-GNSS precise orbit determination with integer ambiguity resolution based on raw phase observations.

Table 7.6 summarises the different scenarios used in the multi-GNSS POD analysis with carrier phase integer ambiguity resolution. The first two scenarios (#1 and #2) serve as reference as they employ the conventional ionosphere-free (IF) processing approach, based on dual-frequency IF code and phase observations and Melbourne-Wuebbena observations. The carrier phase ambiguity resolution is based on the combination of widelane (WL) and narrowlane (NL) ambiguities, as described in section 5.1.3.

All other scenarios employ the raw method, based on multi-GNSS and multi-signal code and phase raw observations with a maximum of eleven signals from three different GNSS in scenario #9. The carrier phase ambiguity fixing for these scenarios is based on raw float ambiguities, as described in section 6, whereas in scenario #4 Galileo-GPS inter-system raw ambiguities for signals E1C/G1C and E5Q/G5Q have been fixed in addition.

The impact of the selected receiver network is analysed by comparing the results of scenarios #3, #5 and #6, whereas the single-GNSS scenarios (#7 and #8) are used to investigate potential differences to multi-GNSS scenarios.

Table 7.6: Summary of the analysed scenarios for multi-GNSS POD with fixed raw carrier phase ambiguities.

#	Processing Approach	Rec. Network (#Stations)	GNSS	Used Observations	Ambiguity Resolution
1	IF	GE_{60}	Galileo GPS	IF(E1C, E5Q), MW(E1C, E5Q) IF(G1W,G2W), MW(G1W,G2W)	WL + NL
2	IF	GE_{100}	Galileo GPS	IF(E1C, E5Q), MW(E1C, E5Q) IF(G1W,G2W), MW(G1W,G2W)	WL + NL
3	RAW	GE_{60}	Galileo GPS	E1C, E5Q, E7Q, E8Q, E6C G1C, G2W	RAW
4	RAW	GE_{60}	Galileo GPS	E1C, E5Q, E7Q, E8Q, E6C G1C, G2W	RAW + IS (1C)
5	RAW	GE_{100}	Galileo GPS	E1C, E5Q, E7Q, E8Q, E6C G1C, G2W	RAW
6	RAW	GE^{*}_{100}	Galileo GPS	E1C, E5Q, E7Q, E8Q, E6C G1C, G2W	RAW
7	RAW	GE_{100}	Galileo	E1C, E5Q, E7Q, E8Q, E6C	RAW
8	RAW	GE_{100}	GPS	G1C, G2W	RAW
9	RAW	GE_{100}	Galileo GPS BeiDou	E1C, E5Q, E7Q, E8Q, E6C G1C, G2W, G5Q C2I, C6I, C7I	RAW

Table 7.7 summarises the basic parameter setup used in the multi-GNSS POD analysis with carrier phase integer ambiguity resolution and reveals the differences between conventional dual-frequency ionosphere-free processing and the raw method with multi-signal raw observations. The symbol ✓indicates that a parameter is estimated, whereas brackets specify the constraint on the parameter, as described in section 5.3.5. The symbol ∅ indicates that the parameter is ignored in the LSQ adjustment.

Table 7.7: Summary of the parameter setup used in the multi-GNSS POD analyses with fixed raw carrier phase ambiguities.

Processing	$\boldsymbol{r}_r$	$\boldsymbol{r}^s$	dt_r	dt^s	$dtro^s_{r,wg}$	$STEC^s_r$	d_r	d^s	ISB	N^s_r	EOP	SRP
Approach	d^{-1}	d^{-1}	e^{-1}	e^{-1}	h^{-1}, d^{-1}	e^{-1}	d^{-1}	d^{-1}	d^{-1}	p^{-1}	d^{-1}	
IF	✓(1 cm)	✓	✓	✓	✓(2 m)	∅	∅	∅	✓(wrt. GPS)	✓	✓	✓
RAW	✓(1 cm)	✓	✓	✓	✓(2 m)	✓	✓	✓	∅	✓	✓	✓

The used global receiver networks are composed of multiple different receiver types for which no calibration values of the receiver DCBs are available. Therefore, as a trade-off to improve robustness, the receiver code biases $d_{r,\Sigma ia}$ of the first two signals for the first GNSS are fixed to zero, while the receiver code biases of the other signals are estimated without any constraint. For signals from other GNSS, only the receiver code bias of the first signal is fixed to zero, while the second signal receiver code bias is estimated with a zero-mean constraint and the other signal receiver code biases are estimated without any constraint. The satellite code biases d^s_{ia} of the first two signals are fixed to zero for all GNSS, while the other signal satellite code biases are estimated with a zero-mean constraint.

In section 7.4.2 the results of the multi-GNSS and multi-signal integer ambiguity resolution approach, described in section 6 are presented and analysed for different scenarios from Table 7.6.

The orbit and clock quality of the multi-GNSS satellite POD based on resolved integer ambiguities is analysed and discussed in sections 7.4.3 and 7.4.4.

7.4.2 Multi-GNSS Multi-Signal Integer Ambiguity Resolution

Different quality indicators can be used to analyse the success of the applied integer ambiguity resolution approach based on GNSS raw observation processing. As discussed in section 6, the histogram of double difference ambiguity fractionals, computed from raw observation float ambiguity estimates reveals whether a significant part of all formed (dependent) double difference ambiguities is close to integer, which corresponds to a fractional value close to zero. For consecutive iterations, the fractional histogram reveals the impact of fixed integer ambiguities on ambiguities which have not been fixed (yet). The second quality indicator used to analyse the success of the integer ambiguity resolution approach is the percentage of independent double difference ambiguities fixed to an integer value and the percentage of fixed raw ambiguities.
The following paragraphs compare the normalized histograms of double difference ambiguity fractionals from daily solutions, simply referred to as fractional histograms, and the percentage of fixed ambiguities for different GNSS, different signals, different receiver networks and inter-system double difference ambiguities.

Comparison of Galileo, GPS and BeiDou

Scenario #9 is used to analyse the characteristics of the raw observation integer ambiguity resolution performance for different GNSS. Figure 7.22 shows the fractional histogram, introduced in section 6.2.2, for Galileo raw phase observations from signals E1C, E5Q, E7Q, E8Q and E6C tracked by the GE_{100} network in the first iteration of the integer ambiguity resolution algorithm, where no ambiguities have been fixed to integer yet. The histogram shows that for Galileo signal E6C significant less DD ambiguities can be formed compared to the other signals, which can be explained by the limited number of GNSS receivers tracking signals on the Galileo E6 frequency band. However, the Gaussian shape of the histogram for all five signals with a mean value of 0 indicates good consistency among all computable (dependent) double difference ambiguities and suggests that integer ambiguity resolution can properly be performed.

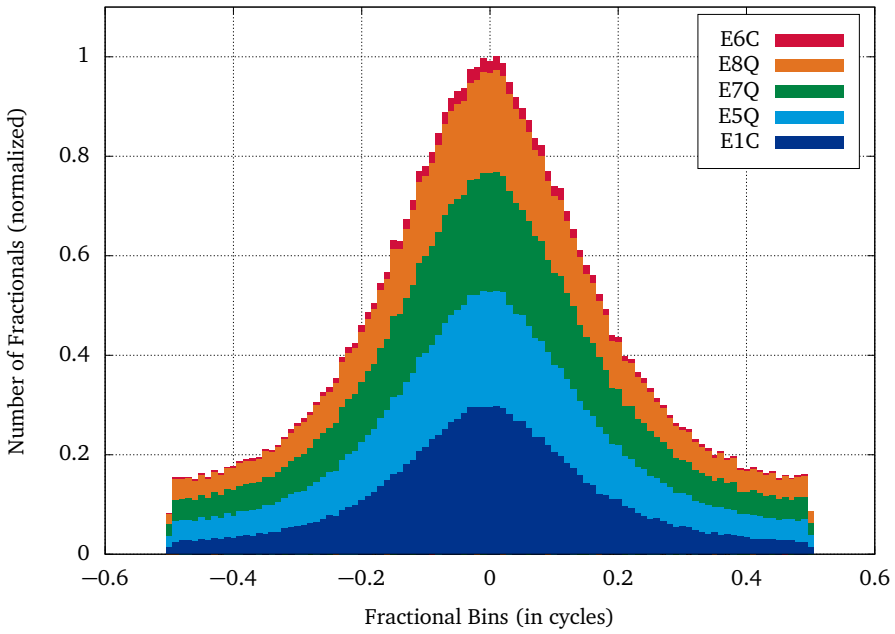

Figure 7.22: Normalized DD ambiguity fractional histogram based on raw observation float ambiguity estimates for Galileo signals tracked by the GE_{100} network in the first iteration of the integer ambiguity resolution (IAR) algorithm.

In Figure 7.23 the fractional histogram for Galileo signals is shown in the second and third iteration of the integer ambiguity resolution algorithm. The additional integer constraints of double difference ambiguities fixed to integer values, see (6.11) lead to a narrow fractional value peak centred at zero in the second iteration and an almost single peak centred at zero in the third iteration. This indicates a successful integer ambiguity resolution with almost all computable (dependent) double difference ambiguities fixed to an integer value after the third iteration.
The fractional histogram for GPS raw phase observations from signals G1C, G2W and G5Q tracked by the GE_{100} network is shown in Figure 7.24 for the first iteration of the integer ambiguity resolution algorithm, where no ambiguities have been fixed to integer yet. The histogram shows that for GPS signal G5Q significant less DD ambiguities can be formed

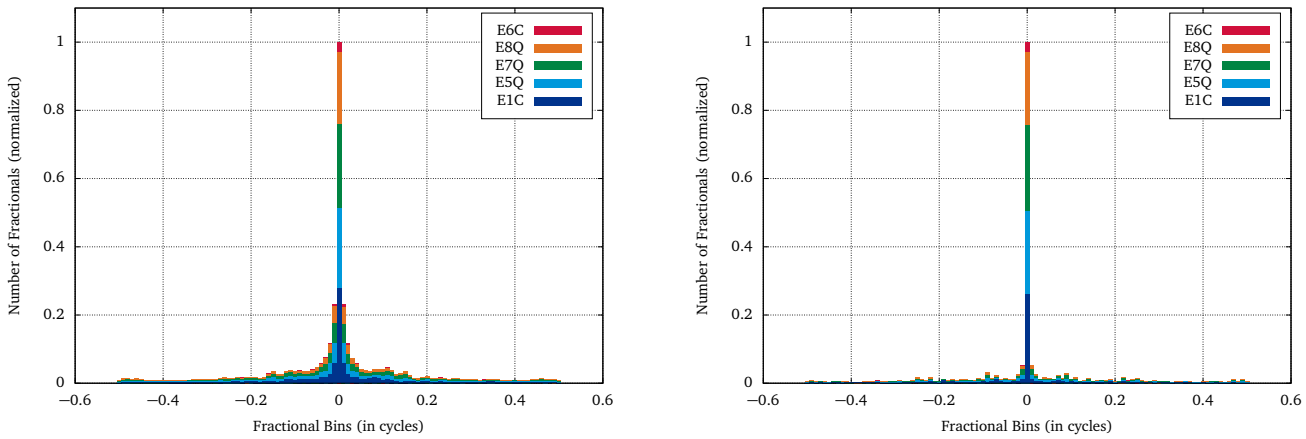

(a) Second iteration of the IAR algorithm.

(b) Third iteration of the IAR algorithm.

Figure 7.23: Normalized DD ambiguity fractional histograms based on raw observation float ambiguity estimates for Galileo signals tracked by the GE_{100} network.

compared to the other signals, which can be explained by the limited number of GPS satellites transmitting signals on the GPS L5 frequency band. Unlike Galileo, the histogram for GPS signals shows a significant number of fractionals at ±0.5 cycles for all signals, indicating inconsistencies in the raw observation float ambiguity estimates used to form all computable (dependent) double difference ambiguities. However, the fractional histogram shows a bulge centred at zero, suggesting a tendency of the double difference ambiguities towards an integer value.

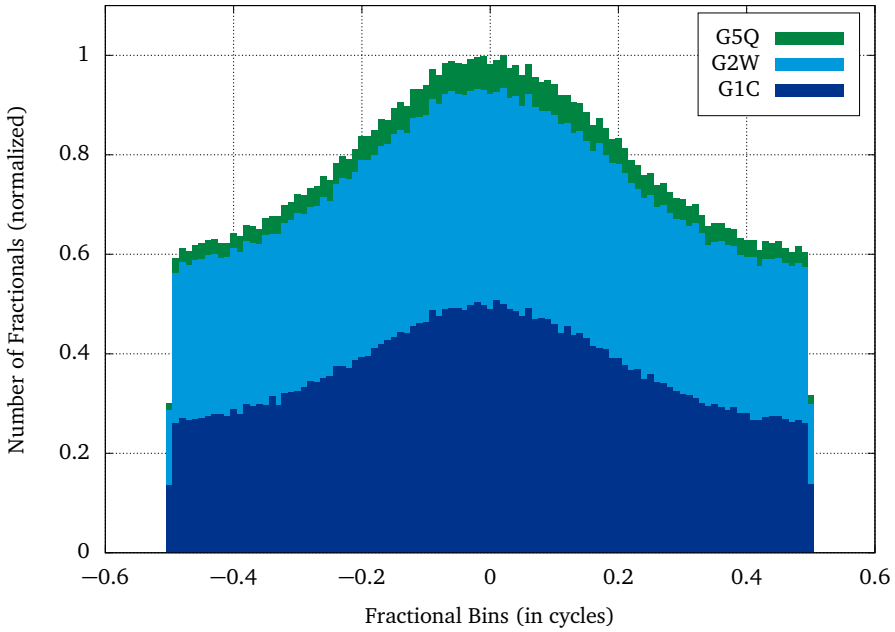

Figure 7.24: Normalized DD ambiguity fractional histogram based on raw observation float ambiguity estimates for GPS signals tracked by the GE_{100} network in the first iteration of the integer ambiguity resolution (IAR) algorithm.

In Figure 7.25 the fractional histogram for GPS signals is shown in the second and third iteration of the integer ambiguity resolution algorithm. The additional integer constraints of double difference ambiguities fixed to integer values lead to a narrow fractional value peak centred at zero in the second and third iteration, however, the remaining significant number of non-zero fractionals indicates, that due to inconsistencies in the raw observation float ambiguity estimates, the corresponding double difference ambiguities do not converge to integer values, despite the introduced integer constraints. It will be analysed in section 7.4.3 if and how this finding influences the determination of precise orbits for GPS satellites.

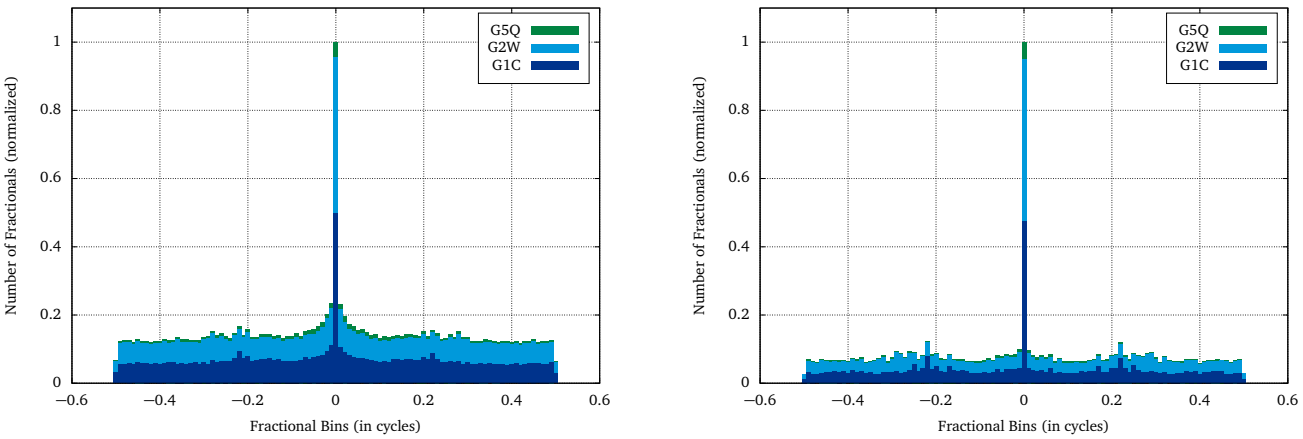

(a) Second iteration of the IAR algorithm.

(b) Third iteration of the IAR algorithm.

Figure 7.25: Normalized DD ambiguity fractional histograms based on raw observation float ambiguity estimates for GPS signals tracked by the GE_{100} network.

The fractional histogram for BeiDou raw phase observations from signals C2I, C7I and C6I tracked by the GE_{100} network is shown in Figure 7.26 for the first iteration of the integer ambiguity resolution algorithm, where no ambiguities have been fixed to integer yet.

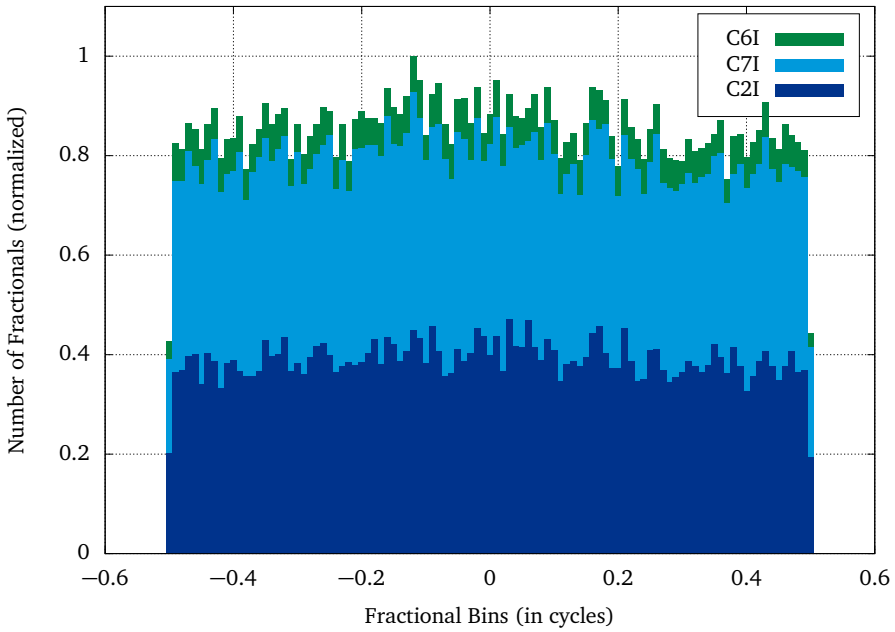

Figure 7.26: Normalized DD ambiguity fractional histogram based on raw observation float ambiguity estimates for BeiDou signals tracked by the GE_{100} network in the first iteration of the integer ambiguity resolution (IAR) algorithm.

The histogram shows that for BeiDou signal C6I significant less DD ambiguities can be formed compared to the other signals, which can be explained by the limited number of GNSS receivers tracking the BeiDou C6I signal. Unlike Galileo and GPS, the histogram for BeiDou signals does not show any tendency of the computable (dependent) double difference ambiguities towards an integer value, as the number of fractionals per bin are uniformly distributed over all fractional values. It is therefore questionable, whether the inter ambiguity resolution approach for BeiDou raw phase observations improves the solution, which will be analysed in section 7.4.3.

In Figure 7.27 the fractional histogram for BeiDou signals is shown in the second and third iteration of the integer ambiguity resolution algorithm. Although in the second iteration double difference ambiguities are fixed to integer

values, indicated by the peak centred at zero, there is no significant change between the second and third iteration with a high number of remaining non-zero fractionals. This indicates significant inconsistencies in the BeiDou raw observation float ambiguity estimates, with the corresponding double difference ambiguities not converging to integer values, despite the introduced integer constraints.

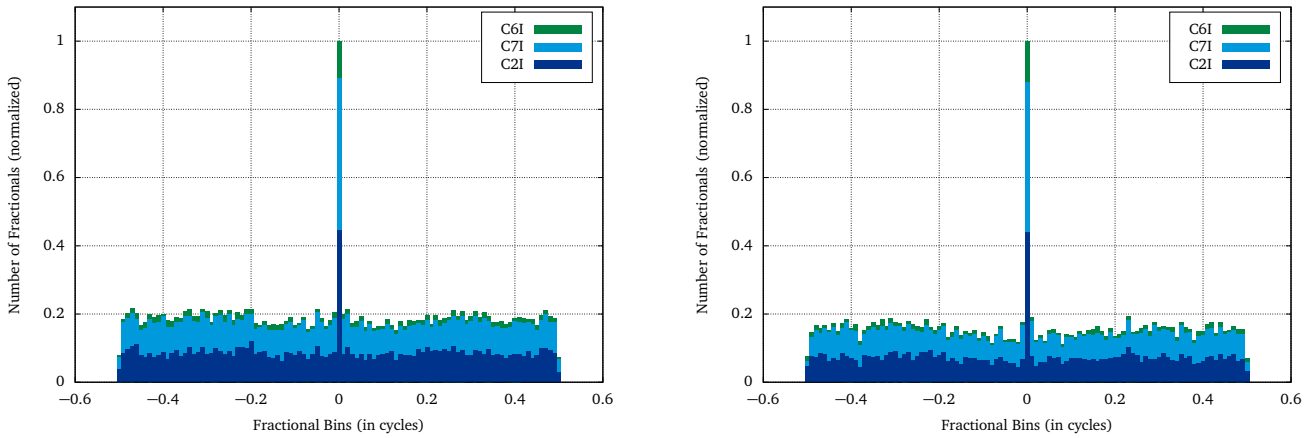

(a) Second iteration of the IAR algorithm.

(b) Third iteration of the IAR algorithm.

Figure 7.27: Normalized DD ambiguity fractional histograms based on raw observation float ambiguity estimates for BeiDou signals tracked by the GE_{100} network.

The second quality indicator used to analyse the success of the integer ambiguity resolution approach is the percentage of fixed integer ambiguities from the set of independent double difference ambiguities, determined as described in section 6.1, and the resulting percentage of fixed raw ambiguities.

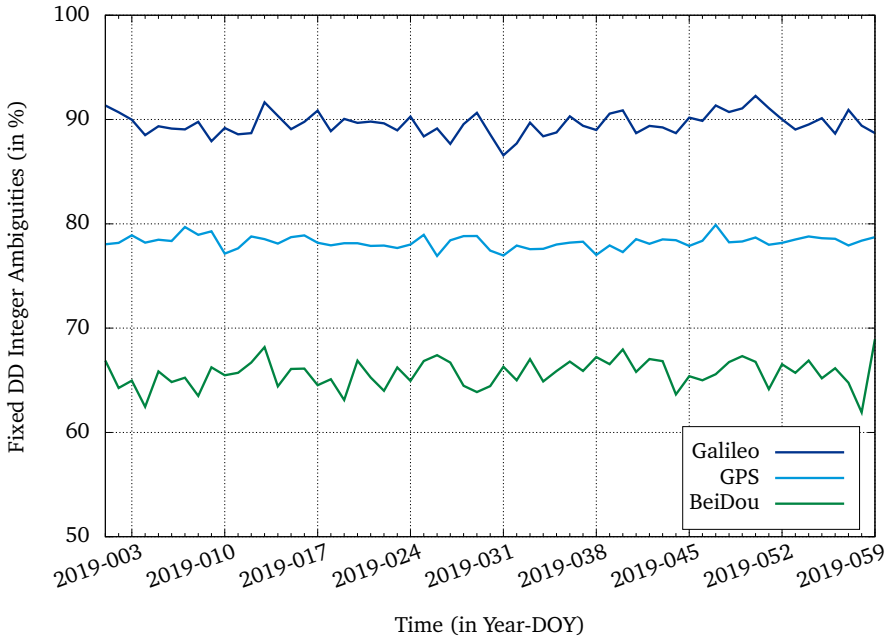

Figure 7.28: Percentage of fixed independent DD integer ambiguities per GNSS for daily solutions of scenario #9.

The percentage of fixed independent double difference integer ambiguities indicates the consistency of raw ambiguity estimates in terms of phase biases and the deviation from expected integer values, see equation 6.3, due to residual errors in the raw ambiguity estimates. It therefore reflects the shape of the fractional histograms described above and allows an even better comparison between the integer ambiguity resolution success rates of different GNSS. In agreement with the fractional histograms and the discussion above, Figure 7.28 shows the percentages of fixed independent DD integer ambiguities per GNSS for scenario #9.

It can be seen that Galileo has the highest percentage of fixed DD integer ambiguities of around 90 %, whereas for GPS around 79 % and for BeiDou around 65 % can be fixed on average. This indicates an advantage of the truly multi-frequency raw observation processing for Galileo, where the processed 24 satellites all are transmitting signals on five different centre frequencies. For GPS only 12 out of the processed 31 satellites are transmitting a third L5 signal, which is known to be affected by carrier phase variations (Montenbruck et al., 2010). For BeiDou only 9 out of the processed 17 satellites are transmitting a third B2 signal, the number of receivers tracking BeiDou signals is 10 % lower on average compared to the number of receivers tracking Galileo and GPS signals and there is a lack of information for the precise modelling of BeiDou satellites (for example PCV values) compared to Galileo and GPS. These effects in combination with the additional estimation of the ionospheric delays, especially for satellites transmitting signals on two frequencies only, lead to an increase of the residual errors in the raw ambiguity estimates and therefore to a deviation of the DD ambiguities from the expected integer values.

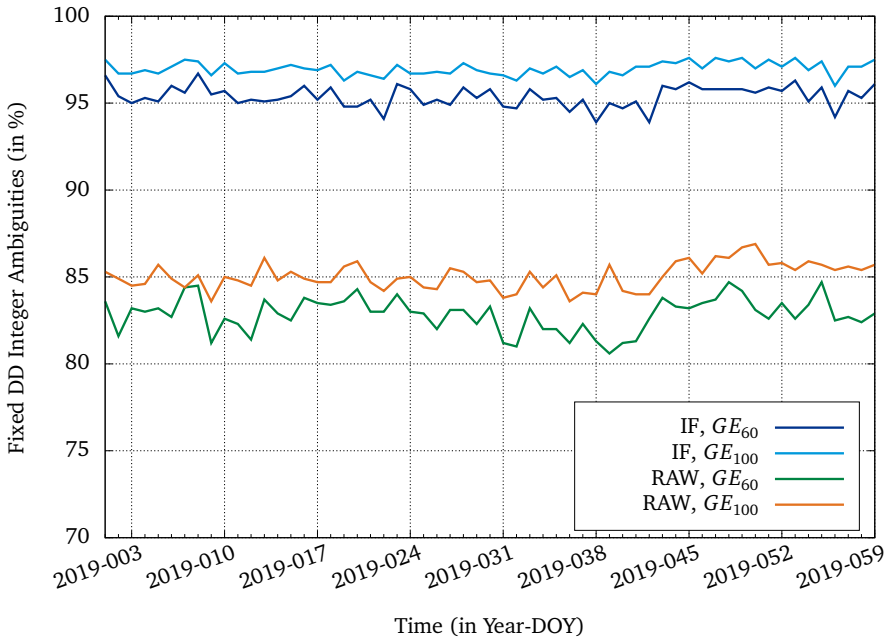

Figure 7.29: Percentage of total number of fixed independent DD integer ambiguities (Galileo+GPS) for daily solutions of scenarios #1, #2, #3 and #5.

Figure 7.29 shows the percentages of the total number of fixed independent DD integer ambiguities for different Galileo+GPS scenarios to demonstrate the impact of the size of the ground station network and the difference between conventional IF processing and the raw method for a combined processing of Galileo+GPS. For both processing approaches, the increase of the ground station network size from 60 to 100 stations leads to an increase in the percentage of fixed DD integer ambiguities of about 2 %. In general, the integer ambiguity resolution approach based on WL and NL ambiguities, used for the conventional IF processing, shows a significantly higher percentage of fixed DD integer ambiguities of about 97 % for the 100 station network, whereas the integer ambiguity resolution approach based on raw observation processing only achieves about 85 % of fixed DD integer ambiguities. The main reason for this difference is the worse performance of GPS signals in the integer ambiguity resolution based on raw observations, as shown in Figure 7.28. In addition, this indicates the existence of residual errors also in the raw observation ambiguity estimates for Galileo, most likely due to the additional estimation of the ionospheric delays. In the IF processing approach, the formation of WL ambiguities with a wavelength $3-4$ times larger then the raw carrier phase signal wavelength improves the resolution of correct integer ambiguities. As the raw method and the implemented integer ambiguity resolution algorithm renounce the formation of any linear combination, there is a disadvantage in terms of the wavelength associated with the ambiguity terms, which makes the resolution of correct integer ambiguities more difficult.

As described in section 6.3, the raw observation ambiguity estimates belonging to a fixable independent double difference integer ambiguity are referred to as fixed raw ambiguities. The same concept can be applied to the undifferenced IF ambiguity estimates introduced in (4.69), belonging to a fixable independent WL and NL DD integer ambiguity. Figure 7.30 shows the percentages of the fixed raw ambiguities per GNSS for scenario #9, corresponding to the percentages of fixed independent DD integer ambiguities in Figure 7.28. In addition the percentages of fixed undifferenced IF ambiguities are shown per GNSS for scenario #2.

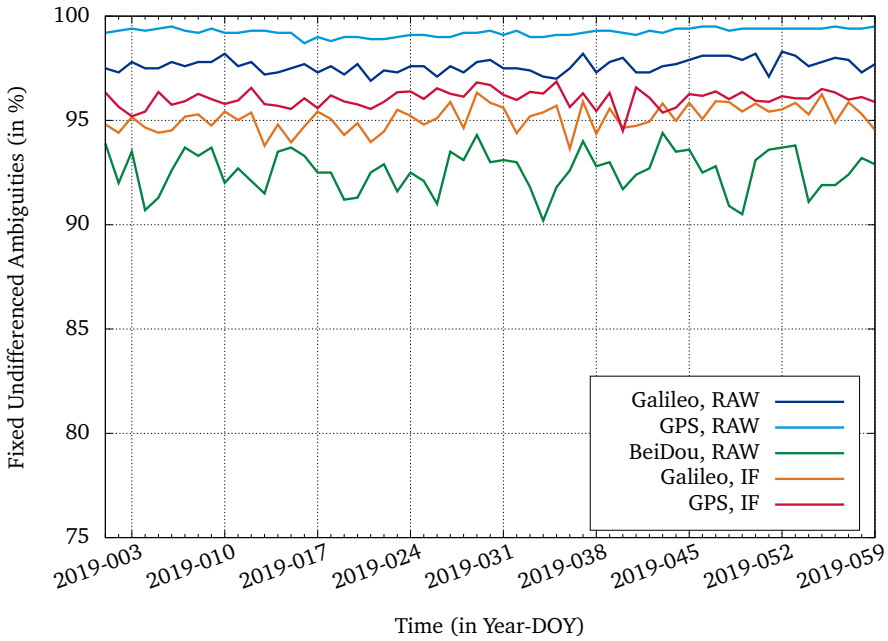

Figure 7.30: Percentage of fixed undifferenced ambiguities per GNSS for daily solutions of scenarios #2 and #9.

Despite the higher number of fixed DD integer ambiguities for the IF processing approach shown in Figure 7.29, it can be seen in Figure 7.30 that for the undifferenced ambiguities the percentage of fixed RAW ambiguities is above the percentage of fixed IF ambiguities for Galileo and GPS.
This indicates that despite inconsistencies between some of the raw ambiguity estimates leading to lower percentages of fixable DD integer ambiguities (see Figure 7.29) still most of the undifferenced Galileo and GPS raw ambiguities can be fixed. This fact could be explained for example by several groups of different receiver types within the processed network, where DD integer ambiguities from raw ambiguity estimates can be resolved within a certain group of receivers, but not between receivers of different groups due to receiver type inconsistencies. This theory is confirmed by the improvement of the DD ambiguity fractional histogram when using only raw ambiguity estimates of a single receiver type, as shown in Figure 7.36.
For both processing approaches (IF and RAW) the percentage of fixed undifferenced ambiguities is slightly higher for GPS compared to Galileo, which can be explained by the not yet full constellation of Galileo satellites and the fact that not all receivers are tracking signals on all five Galileo frequencies. Due to missing Galileo satellites and receivers tracking only a subset of the Galileo signals, some undifferenced raw ambiguities can simply not be used to form double differences which prevents them from being fixed. For BeiDou the percentage of fixed raw ambiguities is significantly less, as expected from previous results.

Figure 7.31 shows the percentage of fixed raw ambiguities per GNSS signal for scenario #9 and reveals individual signal characteristics. It can be seen that for Galileo all signals behave similar except E6C which shows a significantly smaller fixing rate. This can be explained by two major facts. Due to the limited number of receivers tracking a Galileo signal on E6, less raw ambiguity estimates can be used to form DD ambiguities compared to the other signals. The second factor which might influence the overall quality of the Galileo E6 signal is interference due to other transmitting sources on or close to the E6 carrier frequency.

Figure 7.32 shows the SNR measurements of different satellites tracked simultaneously by a multi-GNSS receiver at ESOC. While the SNR measurements for the GPS and BeiDou satellites in Figure 7.32b do not show any disturbances, there is a clear interference pattern in the E6 signal visible in Figure 7.32a.
This repetitive pattern was identified to belong to an amateur TV station close to ESOC, which transmits a signal close to the nominal E6 centre frequency. The reduced performance of the Galileo E6 signal compared to the other signals can also be visualised by the fractional histograms per signal, shown in section G.

For GPS the signal G5Q shows a smaller fixing rate compared to the fixed raw ambiguities on signals G1C and G2W as seen in Figure 7.31. This can be explained by the two facts already mentioned above, which are the reduced number

of satellites transmitting a signal on L5, therefore less raw ambiguity estimates are available to form DD ambiguities compared to the other signals, and the L5 carrier phase variations.

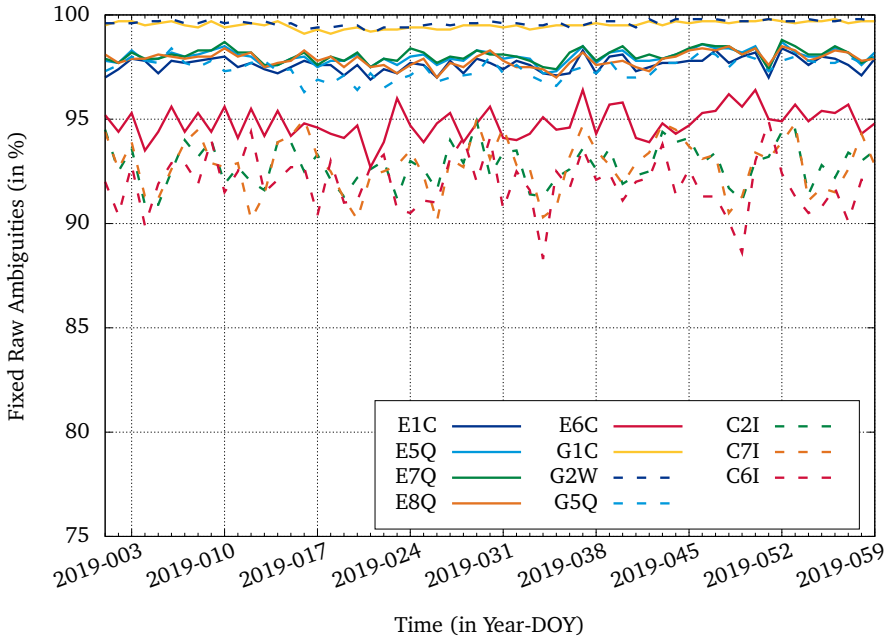

Figure 7.31: Percentage of fixed raw observation ambiguities per GNSS signal for daily solutions of scenario #9.

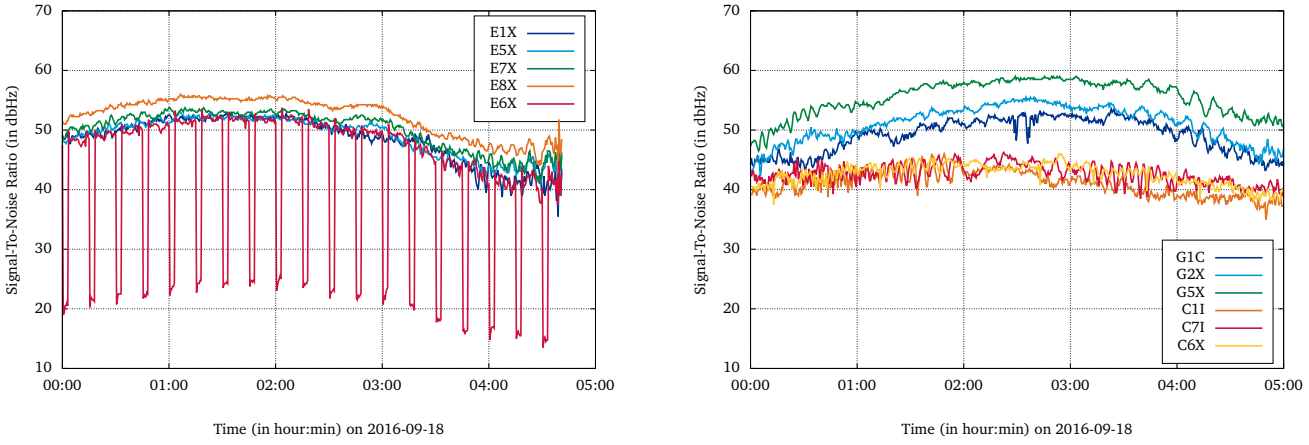

(a) Interference pattern for the E6 signal of Galileo satellite PRN number E08

(b) GPS satellite PRN number G24 and BeiDou satellite PRN number C08

Figure 7.32: SNR measurements of different satellites tracked simultaneously by a multi-GNSS receiver at ESOC.

As expected from previous results the BeiDou raw ambiguities per signal in Figure 7.31 show the smallest fixing rate. As for the Galileo signal on E6, there is only a limited number of receivers tracking BeiDou C6I signals, which explains the reduced fixing rate of the BeiDou C6I signal compared to the other two signals.

In section 7.4.3 the impact of the analysed integer ambiguity results on the precise orbit determination of multi-GNSS satellites will be investigated and discussed.

As described in section 6.2.4, the difference between two DD ambiguities based on raw ambiguity estimates on different frequencies can be used to check the consistency of double difference ambiguities on different frequencies. This approach is not used for the actual fixing of integer ambiguity values, as the implemented integer ambiguity resolution approach

renounces the use of inter-frequency linear combinations. However, it can be used to analyse the expected narrowing of the fractional histogram for widelane DD ambiguities.

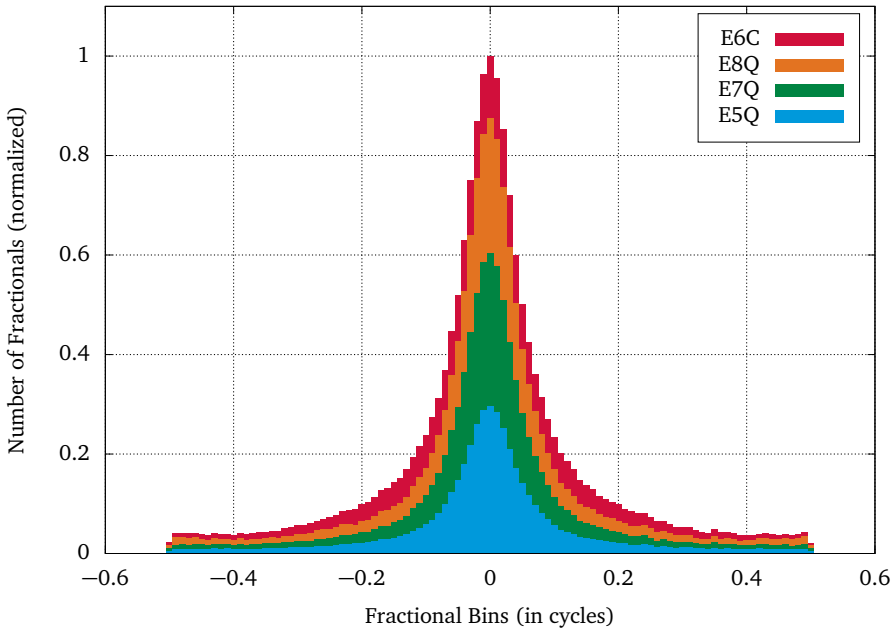

Figure 7.33: Normalized DD ambiguity widelane fractional histogram based on raw observation float ambiguity estimates for Galileo signals tracked by the GE_{100} network relative to E1C.

Figure 7.33 demonstrates that for Galileo the widelane DD ambiguities of all signals (relative to E1C) show a more confined and steeper fractional histogram as compared to the DD ambiguity histogram per signal in Figure 7.22, which suggests consistent double difference ambiguities on different frequencies.

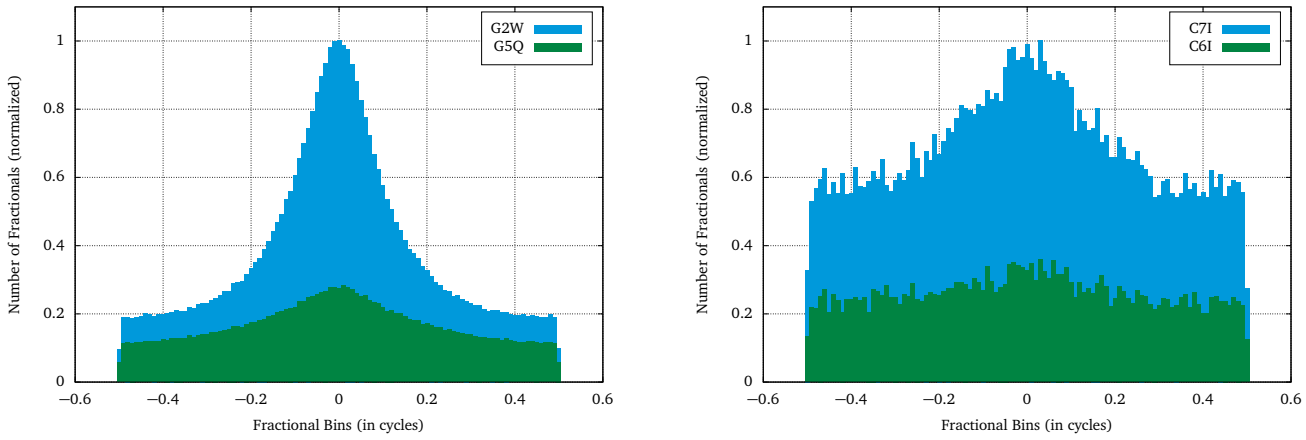

(a) GPS signals relative to G1C.

(b) BeiDou signals relative to C2I.

Figure 7.34: Normalized DD ambiguity widelane fractional histograms based on raw observation float ambiguity estimates for signals tracked by the GE_{100} network.

The widelane DD ambiguity fractionals for GPS and BeiDou shown in Figure 7.34 reveal, that consistent double difference ambiguities can only be combined for GPS signals G1C and G2W. The combination of DD ambiguities for GPS signals G1C and G5Q, as well as the BeiDou widelane DD ambiguities do not show the expected confined fractional histogram. This confirms the previous results and indicates signal dependent residual errors in the respective raw ambiguity estimates due to the aforementioned reasons of additional ionospheric delay estimation, limited number of transmitters or receivers for certain GNSS signals and a lack of information for the precise modelling of BeiDou satellites.

Inter-System Integer Ambiguity Fixing

In the raw observation processing approach all ambiguities are handled per frequency which enables the formation of double difference ambiguities for satellites belonging to different GNSS, as long as they are transmitting signals on the same carrier frequency. These inter-system (IS) double difference ambiguities have been formed for Galileo/GPS signals E1C/G1C and E5Q/G5Q, as well as for Galileo/BeiDou E7Q/C7I, shown in Figure 7.35.

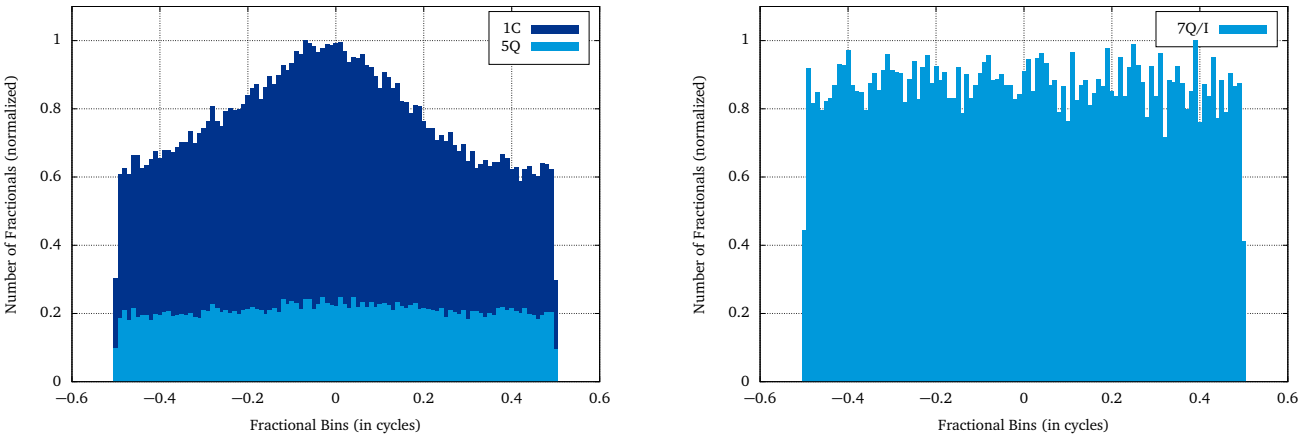

(a) Galileo-GPS inter-system DD ambiguities.

(b) Galileo-BeiDou inter-system DD ambiguities.

Figure 7.35: Normalized inter-system DD ambiguity fractional histograms based on raw observation float ambiguity estimates for signals tracked by the GE_{100} network.

The inter-system double difference ambiguity fractional histograms reveal that Galileo/GPS raw ambiguity estimates for signals E5Q/G5Q, as well as raw ambiguity estimates for Galileo/BeiDou can not be combined consistently. The corresponding histograms show an equal distribution of fractional values over the whole fractional range. The combination of Galileo/GPS raw ambiguity estimates for signals E1C/G1C, shown in Figure 7.35a, indicates a better consistency, however, instead of an integer tendency the histogram reveals common residual error differences in the raw ambiguity estimates of the two different GNSS in the form of a non-zero mean value. It is therefore questionable whether the additional fixing of inter-system double difference ambiguities to integer values strengthens the overall solution.
In scenario #4 the impact of the additional fixing of Galileo/GPS E1C/G1C inter-system double difference ambiguities to integer values on the POD of GNSS satellites has been analysed with the results shown in section 7.4.3.

Dependency on Receiver Network

The fractional histogram based on GPS raw ambiguity estimates shown in Figure 7.36a shows a significant number of fractionals at ±0.5 cycles for all signals, indicating inconsistencies in the raw ambiguity estimates used to form all computable (dependent) double difference ambiguities. To analyse the cause of these inconsistencies, the histogram was regenerated based on the same data set but using only one specific receiver type. Filtering the data set for this receiver type lead to a reduction in the number of receivers used to form DD ambiguities from 100 to 24. Figure 7.36b shows the resulting fractional histogram of all computable (dependent) double difference ambiguities based on a single receiver type. The improved, more Gaussian-like shape of the histogram indicates that the residual errors of the GPS raw ambiguity estimates are receiver type dependent, as using only a single receiver type shows a much better consistency among raw ambiguity estimates. This suggests that for GPS signals there is a stronger receiver type dependency than observed for Galileo signals, shown in Figure 7.22.

7.4.3 Multi-GNSS Satellite Orbit Quality

The resolution of DD integer ambiguities based on raw observation ambiguity estimates has been applied to the problem of precise orbit determination (POD) for multi-GNSS satellites. The different scenarios summarised in Table 7.6 were used to estimate orbits of Galileo, GPS and BeiDou satellites. The setup of the different scenarios allows to analyse the results of combined multi-GNSS processing with up to 72 GNSS satellites, compare the conventional IF processing approach with the raw observation processing approach and analyse the impact of fixing inter-system DD integer ambiguities.
Two quality indicators have been used to evaluate the GNSS satellite POD results. As the orbit determination is based on daily solutions, the common midnight epoch of two consecutive days is used to compute the RMS of the so called orbit midnight overlap. As the daily solutions are independent in terms of observations, a small midnight overlap indicates a

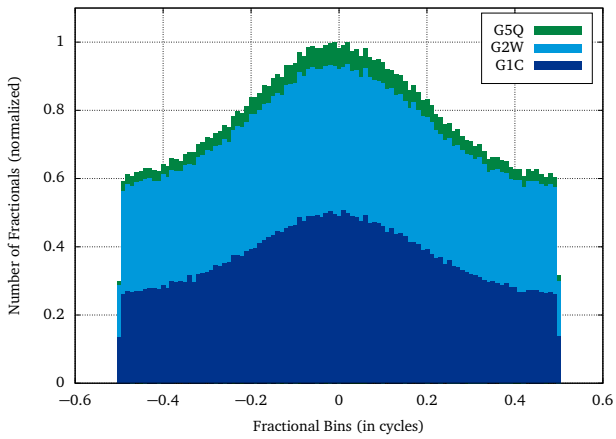

(a) Using all mixed receiver types of the GE_{100} network.

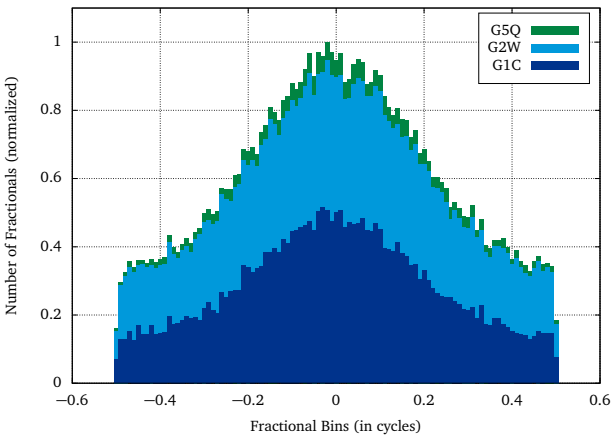

(b) Using only one specific receiver type of the GE_{100} network.

Figure 7.36: Comparison of normalized DD ambiguity fractional histograms based on raw observation float ambiguity estimates for GPS signals in the first iteration of the IAR algorithm.

better intrinsic orbit quality. In order to also obtain an external evaluation of the orbit quality, the estimated GNSS satellite orbits are compared with reference products from ESOC (Navigation Support Office, 2019) for multi-GNSS orbits, labeled ESOC MGNSS (ESM), and IGS for GPS orbits.

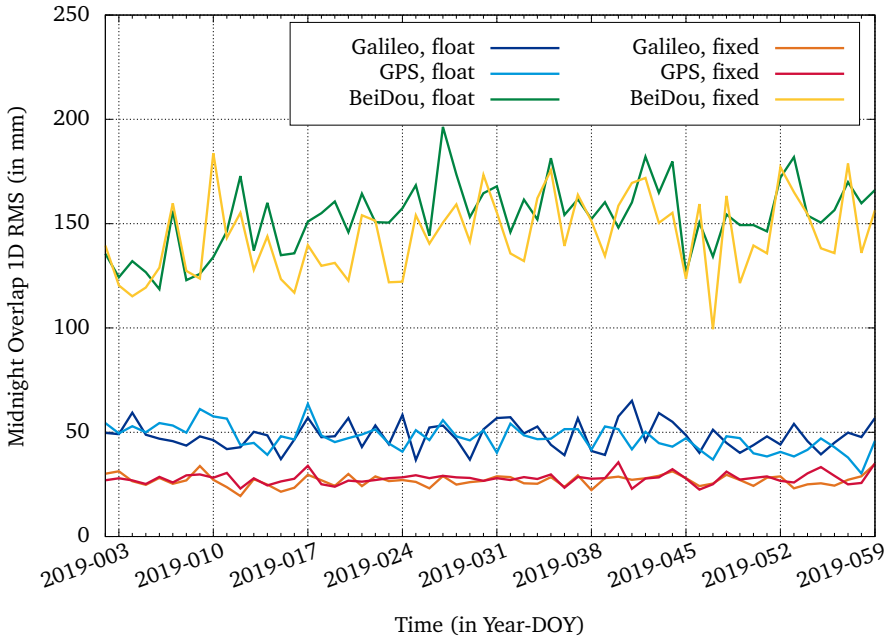

Figure 7.37: Midnight satellite orbit overlap 1D RMS constellation mean values for the daily float and fixed solutions of scenario #9.

Figure 7.37 shows the midnight overlap 1D RMS constellation mean values of Galileo, GPS and BeiDou satellite orbits for the float ambiguity solutions and the ambiguity fixed solutions of scenario #9. It can be seen that Galileo and GPS both show an intrinsic orbit quality of about 50 mm for the float solutions and 27 mm for the fixed solution. This factor of almost two for the improvement of the midnight overlaps indicates the successful application of the integer ambiguity resolution approach based on raw ambiguity estimates, described in section 6. Figure 7.37 also shows that for BeiDou the midnight overlaps of the float solution are a factor of 3 worse than for the other GNSS and indicates that the fixing of DD integer ambiguities based on raw ambiguity estimates does not improve the intrinsic orbit quality.
In order to compare the implemented integer ambiguity resolution approach based on raw observation processing with the conventional approach, two scenarios based on the IF linear combination have been processed, see Table 7.6.

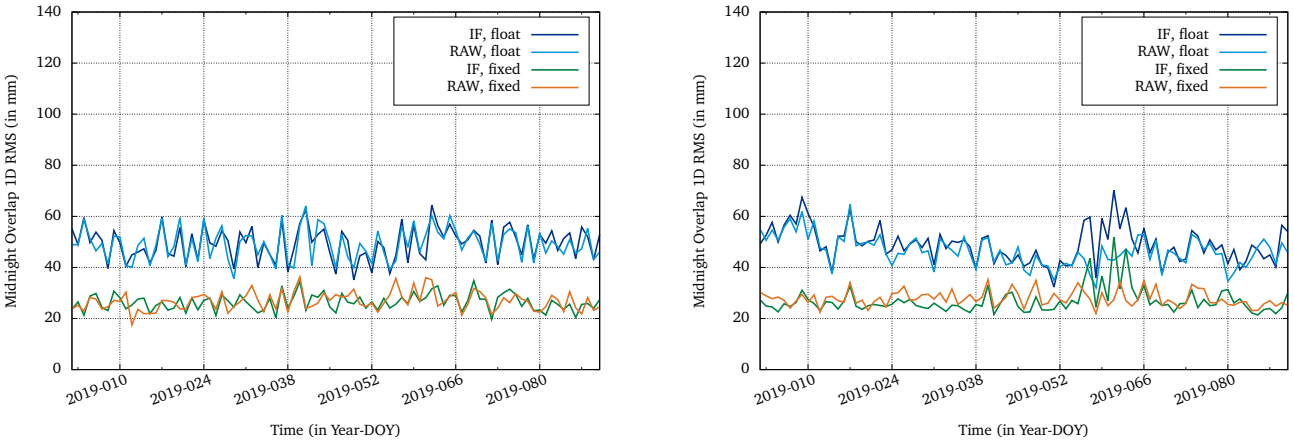

(a) Galileo **(b)** GPS

Figure 7.38: Midnight satellite orbit overlap 1D RMS constellation mean values for the daily float and fixed solutions of scenarios #2 and #5.

Figure 7.38 shows the comparison of the intrinsic orbit quality for scenarios #2 and #5 for the determined satellite orbits of both, Galileo and GPS. It can be seen that the fixing of integer ambiguity values improves the midnight overlaps by a factor of two for both, the conventional IF approach, as well as the RAW approach. The midnight overlaps of the fixed solutions for both approaches are around 26 mm for Galileo and 27 mm for GPS, indicating an at least equivalent quality of the GNSS satellite orbits, despite the differences of the percentage of fixed ambiguities discussed in section 7.4.2. Figure 7.38b indicates a more robust orbit determination based on the raw method, as the peaks in the midnight overlaps for the IF approach around day 2019-060 are not visible for the RAW approach.

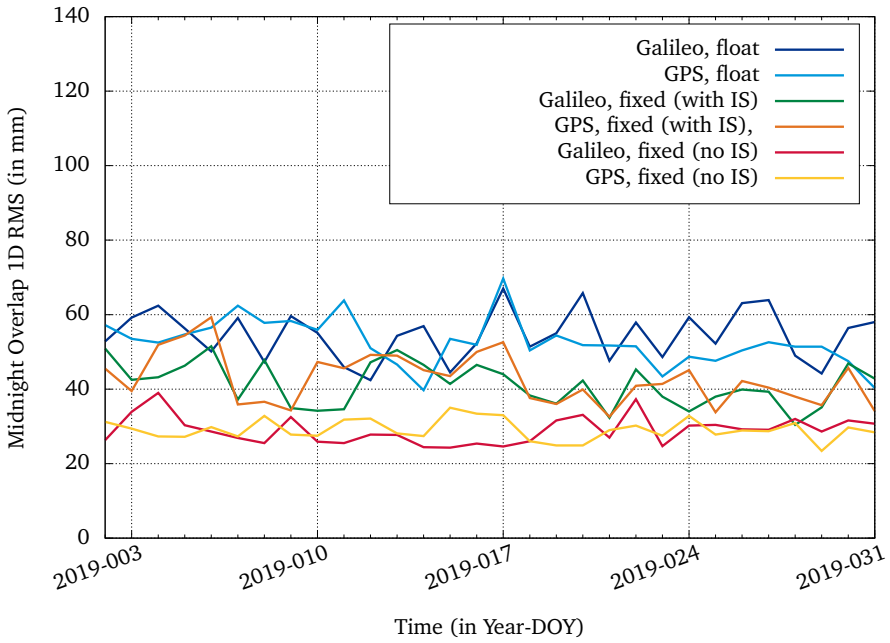

Figure 7.39: Midnight satellite orbit overlap 1D RMS constellation mean values for the daily float and fixed solutions of scenarios #3 and #4.

Figure 7.39 shows the impact of fixing Galileo-GPS inter-system DD integer ambiguities for signals E1C/G1C in addition to the integer ambiguity fixing per GNSS by comparing the results of scenarios #3 and #4. The midnight overlap 1D RMS constellation mean values for the fixed solutions increase from about 29 mm to 42 mm for both, Galileo and GPS when inter-system DD integer ambiguities are fixed in addition. This reveals a weakening of the fixed solution due to inter-system DD integer ambiguity fixing and confirms the inconsistencies of raw ambiguity estimates of the different

GNSS, already indicated in the fractional histogram shown in Figure 7.35a.

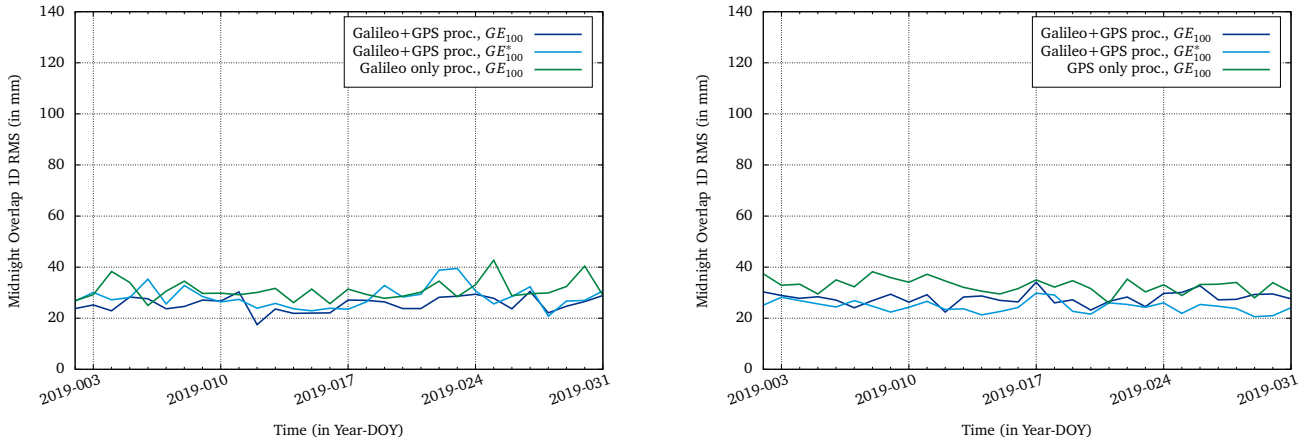

(a) Galileo **(b)** GPS

Figure 7.40: Midnight satellite orbit overlap 1D RMS constellation mean values for the daily fixed solutions of scenarios #5, #6, #7 and #8.

In Figure 7.40 the Galileo and GPS satellite orbit midnight overlap constellation mean values are compared for the fixed solutions of different scenarios with a network size of 100 receivers. For both GNSS it is shown that single GNSS processing generates about 20 % less accurate midnight orbit overlaps compared to multi-GNSS processing.
In addition Figure 7.40 reveals that the usage of the GE^*_{100} network, which includes some receivers tracking only GPS signals, decreases the midnight orbit overlap accuracy for Galileo by about 6 % on average, whereas the midnight orbit overlap accuracy for GPS increases by about 12 %.

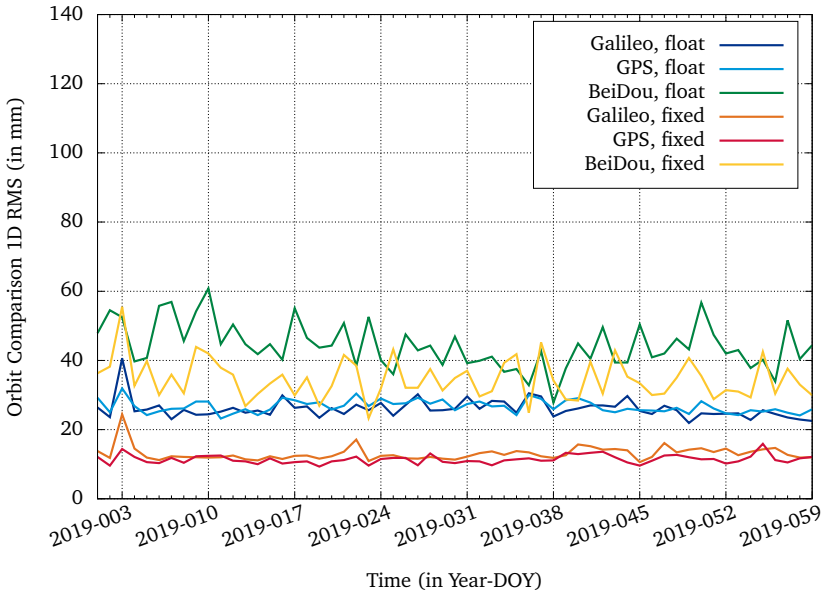

Figure 7.41: Orbit comparison 1D RMS constellation mean values for the daily float and fixed solutions of scenario #9 relative to the ESOC multi-GNSS orbits based on the IF processing approach.

An external evaluation of the orbit quality is performed by comparing the estimated GNSS satellite orbits with reference products from ESOC (for multi-GNSS orbits) and IGS in addition (for GPS orbits only).
Figure 7.41 shows the orbit difference 1D RMS constellation mean values of Galileo, GPS and BeiDou satellite orbits for the float and fixed solutions of scenario #9. The estimated satellite orbits were compared to the routinely generated ESOC multi-GNSS solution based on the conventional IF processing approach. Galileo and GPS both show an external orbit quality of about 26 mm for the float solutions and 12 mm for the fixed solutions, indicating a very good agreement

of the GNSS satellite orbits and the successful application of the integer ambiguity resolution approach based on raw ambiguity estimates. For BeiDou the difference to the ESOC reference orbit is a factor of 2-3 worse compared to Galileo and GPS. However, the fixing of DD integer ambiguities indicates an improvement of the external orbit quality with a BeiDou constellation mean value of 35 mm on average over the shown time interval.

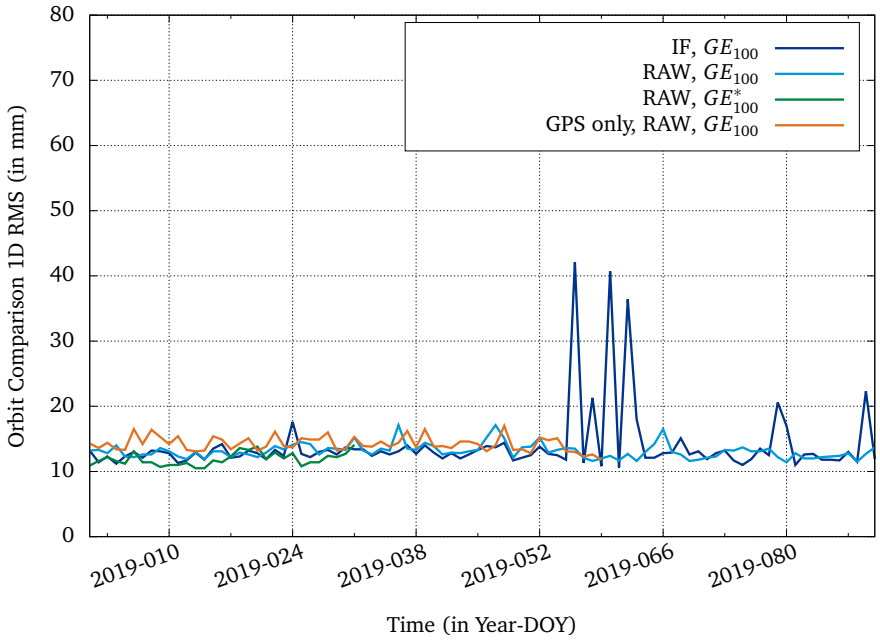

Figure 7.42: Orbit comparison 1D RMS constellation mean values for the daily GPS fixed solutions of scenarios #2, #5, #6 and #8 relative to the IGS final orbits based on the IF processing approach.

In addition the IGS final orbits are used to compare the GPS orbit quality of different fixed solutions from Table 7.6. Figure 7.42 reveals that the four different GPS fixed solutions of scenarios #2, #5, #6 and #8 all show a very good agreement with the IGS final orbits.
Among the four scenarios the GPS only processing scenario #8 performs worst with 14 mm 1D RMS orbit difference, which suggests an advantage of combined multi-GNSS processing, as already seen in Figure 7.40b. The combined Galileo and GPS processing scenario #6 including receivers tracking only GPS satellites (GE^{*}_{100}) performs best, as expected, with 12 mm 1D RMS orbit difference.
Figure 7.42 also indicates a more robust orbit determination based on the raw method, as the peaks for the IF approach around days 2019-060, 2019-080 and 2019-090 are not visible in the results based on the RAW approach.

These peaks are due to a single GPS satellite with PRN number G18, which can not be consistently processed with the IF processing approach. Figure 7.43 shows the orbit comparison 1D RMS relative to the IGS final orbits for the problematic satellite G18 and another GPS satellite with PRN number G19, determined from the GE_{60} network. It can be seen that the orbit comparison for satellite G19 does not show any significant peaks with the determination based on the raw method giving slightly more consistent results. The orbit comparison for satellite G18 shows differences to the IGS final orbits of up to 66 cm for the IF fixed solution, whereas the RAW fixed solution shows an average agreement of 16 mm with the IGS final orbits.

7.4.4 Multi-GNSS Satellite Clock Quality

The GNSS satellite clock quality is analysed by the RMS of the estimated clock offsets compared to a linear fit. The RMS therefore is an indicator of the stability of the estimated clock offsets. Figure 7.44 shows RMS constellation mean values of the estimated GNSS satellite clock offsets compared to a linear fit clock model.
Figure 7.44a indicates a significant improvement in the stability of the estimated satellite clocks for the integer ambiguity fixed solutions of both Galileo and GPS. The Galileo constellation RMS mean value is 118 ps on average and indicates an almost 4 times better satellite clock stability compared to the GPS constellation RMS mean value of 425 ps on average.
Figure 7.44b reveals that the satellite clock stability of the fixed solution of scenario #9 is almost identical to the ESM reference solution for Galileo and GPS with constellation RMS mean values of 116 ps and 433 ps on average respectively.

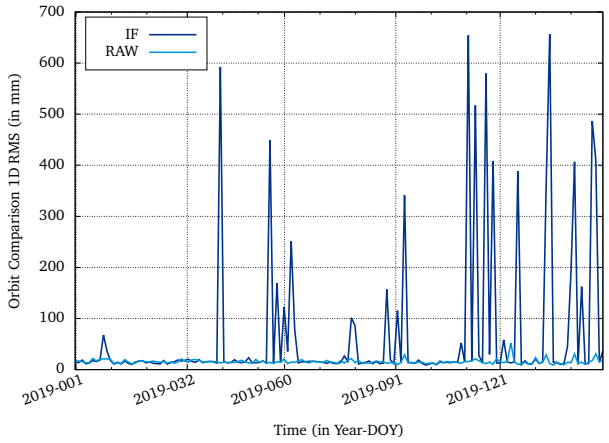

(a) GPS satellite PRN number G18

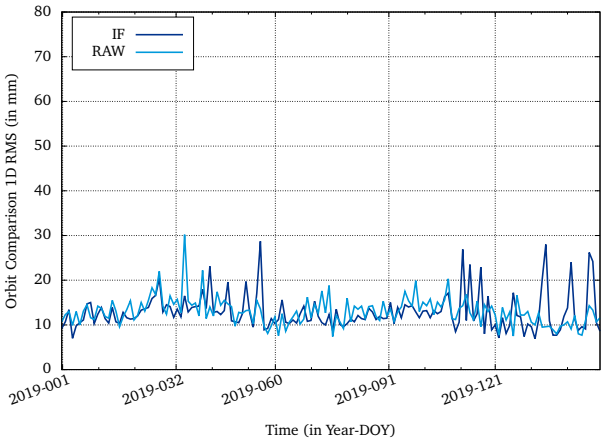

(b) GPS satellite PRN number G19

Figure 7.43: Orbit comparison 1D RMS for individual GPS satellites from daily fixed solutions of scenarios #1 and #3 relative to the IGS final orbits.

For BeiDou the raw method achieves a better stability then the ESM reference solution with a constellation RMS mean values of 735 ps on average.

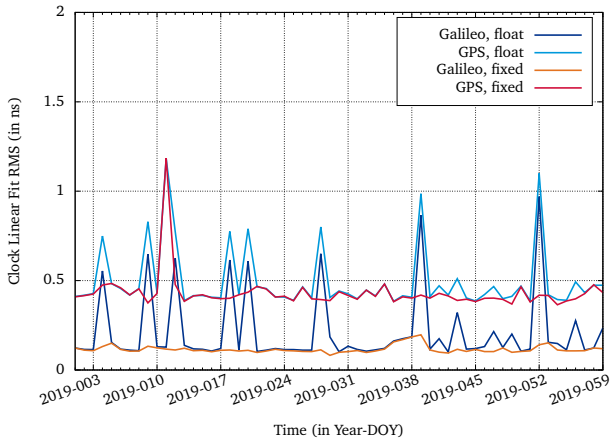

(a) Daily float and fixed solutions of scenario #5 for Galileo and GPS.

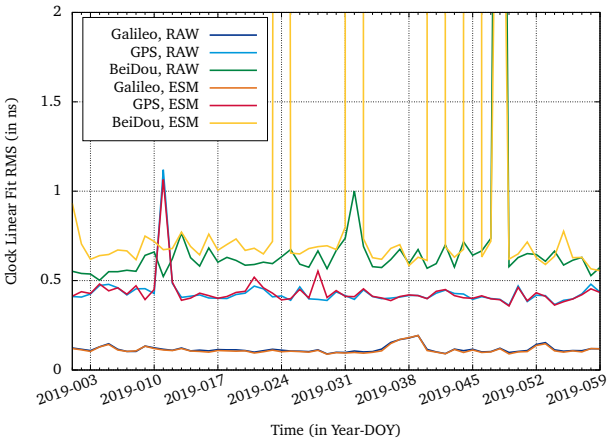

(b) Daily fixed solutions of scenario #9 and the ESM reference solution for Galileo, GPS and BeiDou.

Figure 7.44: RMS constellation mean values of the estimated GNSS satellite clock offsets compared to a linear fit clock model.

7.5 Multi-GNSS Multi-Signal Raw Observation Phase Biases

The existence of phase biases, as introduced in sections 4.1.2 and 4.1.3, prevents the direct determination of raw observation carrier phase integer ambiguity values. Phase biases are therefore of specific interest for precise GNSS applications, as described in section 5.1.4.
In this section the stability of receiver-specific and satellite-specific phase biases is analysed based on two different approaches, one making use of simulated GNSS signals, the other using the results of the fixed raw ambiguity solutions shown in section 7.4.

7.5.1 Receiver Phase Bias Analysis based on Simulated Observations

The stability of receiver-specific raw observation phase biases was analysed based on GNSS signals simulated without any atmospheric delays or antenna phase centre offsets and variations. The simulation setup comprised three different receiver types (A, B and C) connected to the multi-GNSS and multi-signal simulator at the same time via an RF signal

splitter. The equation for the observation difference of simulated phase and code signals with the same carrier frequency in cycles is given by

$$\phi_{r,i}^{SIM}(t) - P_{r,\Sigma jb}^{SIM}(t)/\lambda_i = \delta_i^s(t) + \delta_{r,i}(t) - N_{r,i}^s - f_i \cdot \left[d_{ia}^s(t) + d_{r,\Sigma ia}(t)\right] + \eta_{r,i}^s(t) - \epsilon_{r,\Sigma ia}^s(t)\,. \tag{7.3}$$

As the code biases were shown to be constant, see section 7.1, and the carrier phase integer ambiguity is constant for a carrier phase signal tracked without cycle slip, their sum can be considered constant (modulo an integer number of cycles) in this analysis

$$N_{r,i}^s + f_i \cdot \left[d_{ia}^s(t) + d_{r,\Sigma ia}(t)\right] = \text{const. (modulo an integer number of cycles)}$$

The difference between phase and code observations in (7.3) therefore allows to analyse the stability of the carrier phase bias term $\delta_i^s(t) + \delta_{r,i}(t)$.

In order to analyse the stability and separation of satellite-specific and receiver-specific phase biases, all three receivers have been manually restarted multiple times during the analysed time interval, indicated by vertical lines in the Figures below. Theoretically, satellite-specific phase biases should not be affected by a receiver restart, whereas receiver phase biases might change due to the reinitialisation of the signal tracking loops, described in section 2.4.2.

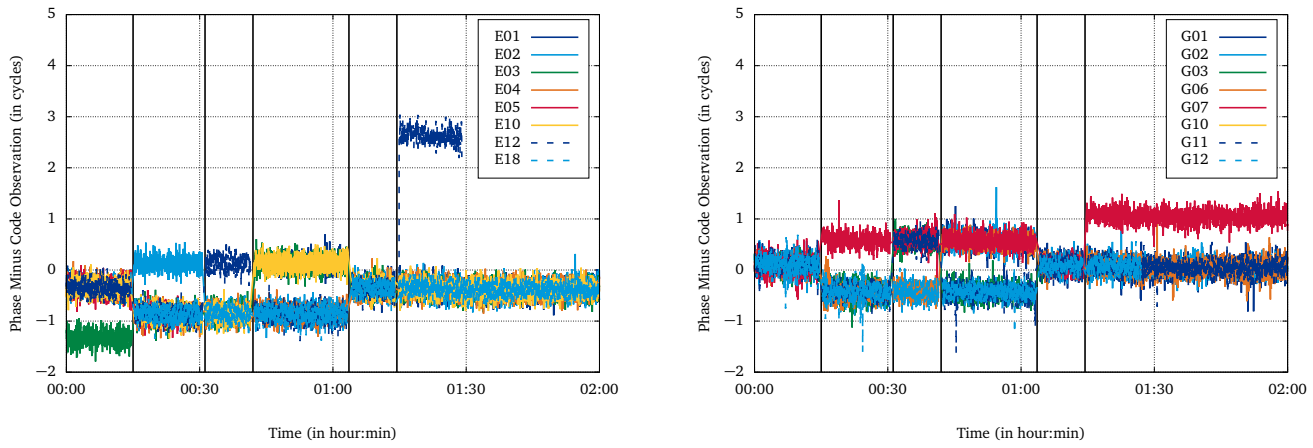

(a) Galileo signal E1C

(b) GPS signal G1C

Figure 7.45: Difference between phase and code observations for multiple satellites, generated by a multi-GNSS multi-signal simulator and measured by an EGON receiver type (A).

Figure 7.45 shows the difference between phase and code observations for multiple Galileo satellites for signal E1C and multiple GPS satellites for signal G1C, measured by an EGON type receiver (A). It can be seen that some receiver restarts induce jumps of fractions of one carrier wavelength cycle, whereas some restarts do not induce any jump or a jump of an integer number of cycles. However, the noise of the phase minus code observations for the Galileo E1C and GPS G1C signals prevent a useful analysis of the results.
Therefore, the Galileo AltBOC signal E8Q was used to improve the phase bias stability analysis. Figure 7.46a shows the phase minus code observation for the AltBOC signal E8Q tracked by an EGON receiver type (A) from multiple Galileo satellites.
The noise of the E8Q phase minus code observation is considerably smaller compared to the E1C/G1C observations and allows to analyse the phase bias stability in detail. Figure 7.46 shows that again some receiver restarts induce jumps of fractions of one carrier wavelength cycle, whereas other restarts do not induce any jump or a jump of an integer number of cycles. However, it can be seen that the change in phase bias due to receiver restarts is independent of the tracked satellites. This confirms the theoretical understanding of not inducing satellite dependent phase bias changes due to a receiver restart. The changes seen in Figure 7.46a can therefore be related to receiver-specific phase biases.

Figures 7.46b and 7.47 show the phase minus code observations for the AltBOC signal E8Q tracked by a future EGON receiver type (B) and a different receiver type (C) from multiple Galileo satellites. The general characteristics of phase bias changes as described before also apply to these receivers. Although the magnitude of the phase bias changes is different for each receiver, all three receiver types show a satellite independency of phase bias changes due to receiver restarts.

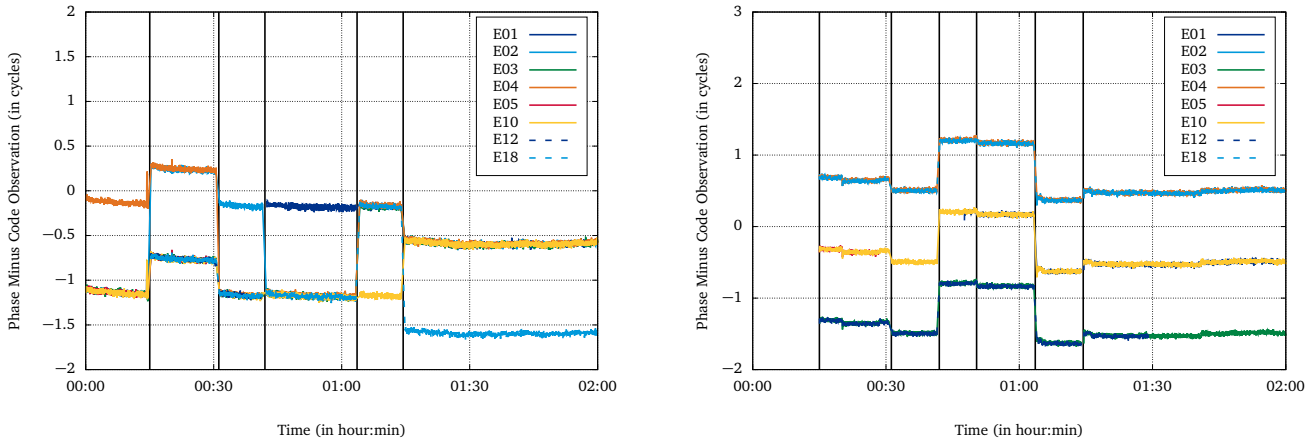

(a) EGON receiver type (A)

(b) Future EGON receiver type (B)

Figure 7.46: Difference between Galileo signal E8Q phase and code observations for multiple satellites, generated by a multi-GNSS multi-signal simulator.

All Figures shown in this section indicate that the phase bias term remains constant when no receiver restart is induced. This suggests that the receiver-specific phase bias (for the analysed receiver types) theoretically can be treated as a constant value, which will be further discussed in section 7.5.2.

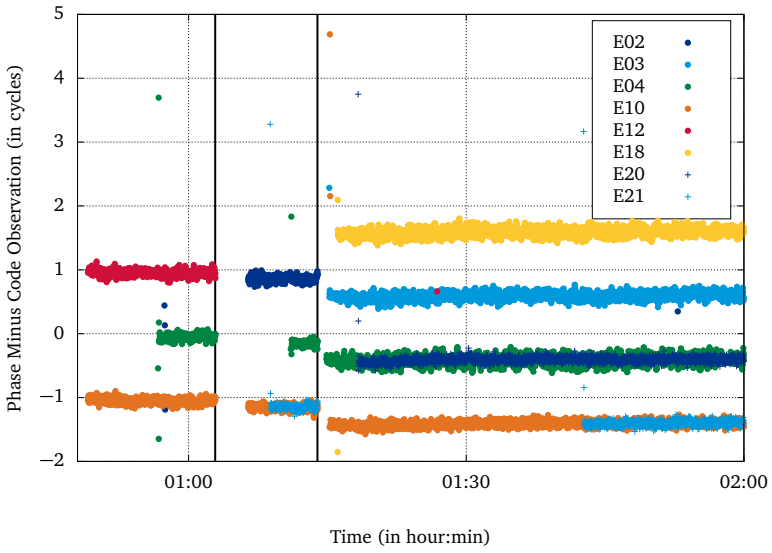

Figure 7.47: Difference between Galileo signal E8Q phase and code observations for multiple satellites, generated by a multi-GNSS multi-signal simulator and measured by receiver type C.

The change in receiver-specific phase biases induced by a receiver restart indicates (for the analysed receiver types) that the calibration of receiver-specific phase biases is impractical. This however, means that receiver-specific phase biases can not be corrected and remain in the raw observation equation, preventing the direct integer ambiguity resolution from GNSS raw observations. In order to be independent of receiver-specific phase biases, between satellite SD phase biases have been analysed with real observation data.

7.5.2 Satellite Phase Bias Analysis with Real Observations

As shown in section 7.5.1 it is impractical to calibrate receiver-specific raw observation phase biases as they can not be considered to have a constant value. Therefore, satellite-specific raw observation phase biases are analysed for between satellite single differences (SD), where the receiver-specific part has been eliminated. The single difference raw observa-

tion phase biases analysed in this section have been formed from fixed raw ambiguities, as described in section 6.3. The between satellite SD phase bias on frequency i for satellites k and l based on fixed raw ambiguities is given by

$$\delta_i^{kl} = \delta_i^k - \delta_i^l = \left(\bar{M}_{r,i}^k - N_{r,i}^k\right) - \left(\bar{M}_{r,i}^l - N_{r,i}^l\right) . \tag{7.4}$$

These between satellite SD phase biases per frequency are used to analyse the stability of satellite-specific phase biases based on estimates from multiple receivers. The results of scenario #9, described in section 7.4, are used to analyse multi-GNSS multi-frequency satellite SD phase biases. The analysis is based on the fixed raw ambiguities and is performed in the following steps:

1. Form undifferenced raw phase biases from fixed raw ambiguities, as shown in (6.14).
2. Form Pass-to-Pass (P2P) differences of all raw phase biases, ie. differences between raw phase biases $\delta_{r,i}^s$ determined from different satellite passes but belonging to the same receiver r, satellite s and frequency i
3. Select raw phase biases with a pass-to-pass stability better than 0.1 cycles.
4. Form satellite SD phase biases per frequency and per receiver from selected raw phase biases for overlapping satellite passes.

The selection of raw phase biases in step 3, based on the pass-to-pass stability, is motivated by the fact that theoretically receiver-specific phase biases should be constant, as discussed in section 7.5.1. The pass-to-pass stability can be visualised in the form of a fractional histogram, as introduced in section 6.2.2. The histogram shows the pass-to-pass differences of raw phase biases determined in step 2 and reveals GNSS and signal dependent characteristics. Figure 7.48 shows the pass-to-pass phase bias difference histogram for all Galileo and GPS signals on day 2019-001, based on the results of scenario #9.

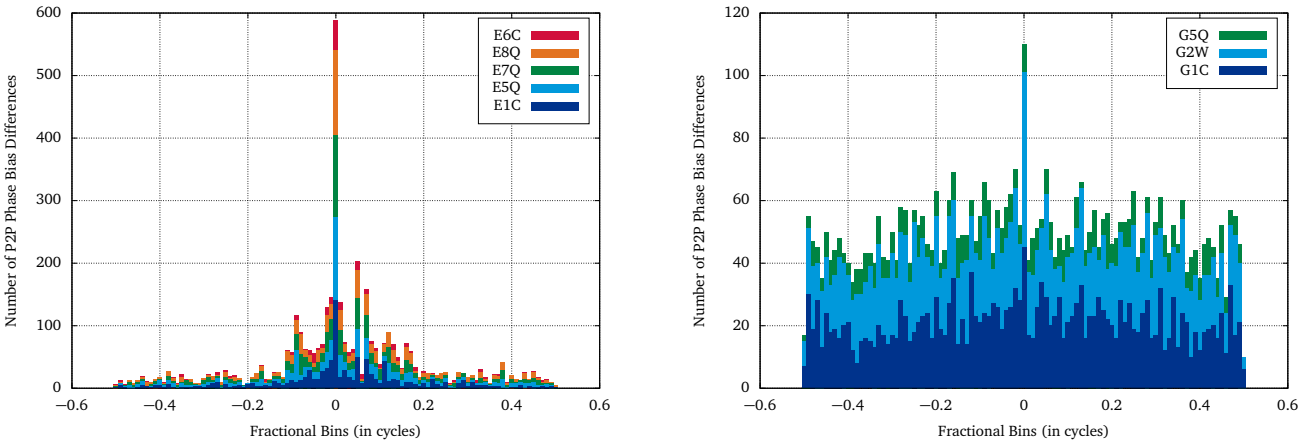

(a) Galileo **(b)** GPS

Figure 7.48: Pass-to-pass (P2P) phase bias difference histograms based on fixed raw observation ambiguities.

Figure 7.48 reveals that the most common value of the pass-to-pass phase bias differences is zero with most values within ± 0.1 cycles for Galileo signals and an almost even distribution over all fractional values for GPS. This indicates good pass-to-pass stability for the raw phase biases determined from Galileo signals and significant worse pass-to-pass stability for the raw phase biases determined from GPS signals.

Satellite SD phase biases per frequency are formed from raw phase biases for each receiver tracking a certain pair of satellites at the same time. In order to visualise the results, satellite SD phase biases are associated with the centre epoch of the corresponding satellite passes tracked by a certain receiver. Figure 7.49 shows the between satellite SD phase biases for different Galileo and GPS satellite pairs for signals E1C and G1C respectively, where each data point indicates a different receiver.
The Galileo satellite SD phase biases in Figure 7.49a show good consistency among the values determined from different receivers and indicate stable satellite-specific phase biases for the shown satellite passes. For GPS, the number of satellite SD phase biases shown in Figure 7.49b is considerably reduced, as already indicated in Figure 7.48b. Some satellite-specific phase biases show good consistency, like for G32 - G27, whereas for most satellite pairs no consistent values can

be determined. The Figures showing satellite SD phase biases determined for all other Galileo and GPS signals are given in section G.

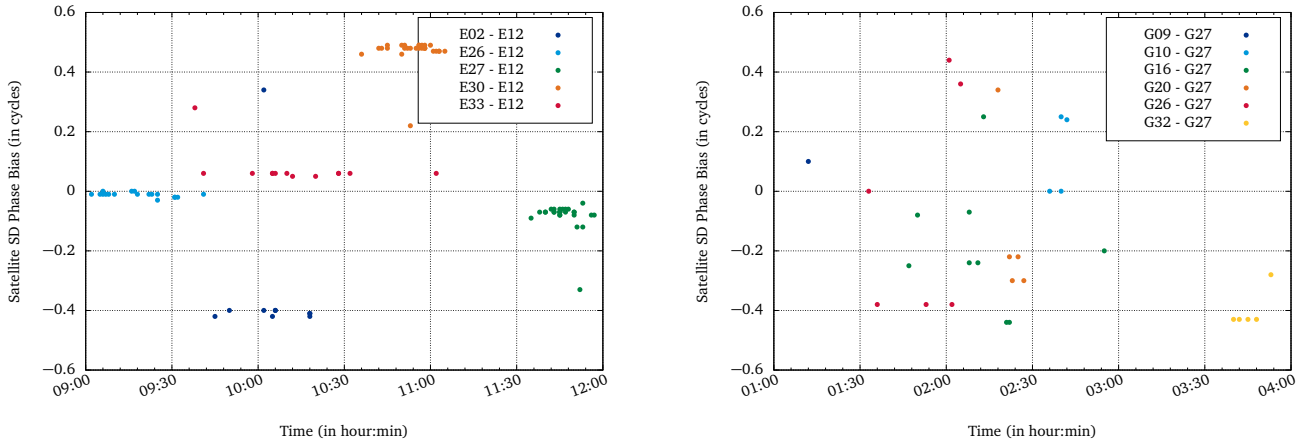

(a) Galileo signal E1C **(b)** GPS signal G1C

Figure 7.49: Between satellite SD phase biases for different pairs of satellites, determined from fixed raw observation ambiguities of multiple receivers, each tracking the respective pair of satellites at the same time.

Figure 7.50 shows the SD phase biases of satellite PRN numbers E26 and E12 for all Galileo signals and demonstrates that stable satellite SD phase biases can be determined for all five Galileo frequencies.

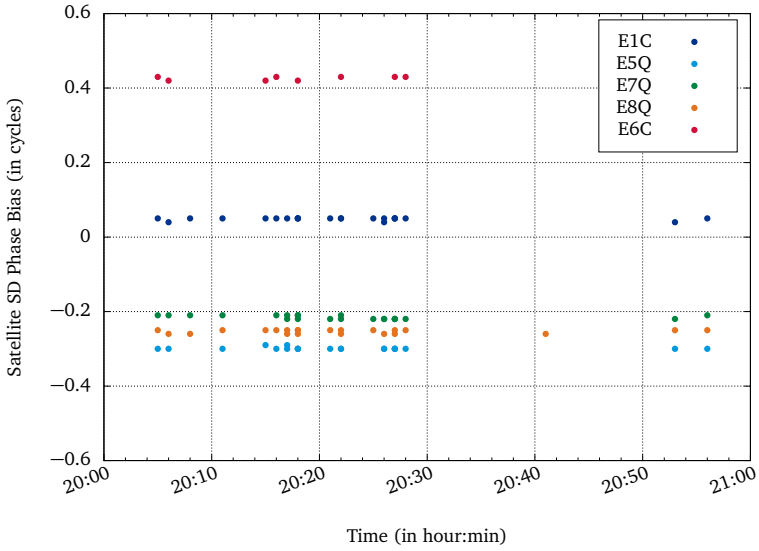

Figure 7.50: Between satellite SD phase biases of Galileo satellites E26 and E12 for all signals, determined from fixed raw observation ambiguities of multiple receivers, each tracking both satellites at the same time.

However, when looking at the satellite SD phase biases determined for satellite passes of multiple days, it becomes evident that the generation of independent daily solutions impacts the stability of satellite-specific phase biases. Figure 7.51 shows the SD phase biases of satellite PRN numbers E26 and E12 for four consecutive days and indicates significant phase bias jumps between individual days for all five Galileo frequencies, which would motivate the generation of daily satellite-specific phase bias products.

In order to improve the consistency among satellite SD phase biases over multiple days one could consider the determination of multi-day solutions or constrain satellite SD phase biases between independent daily solutions.

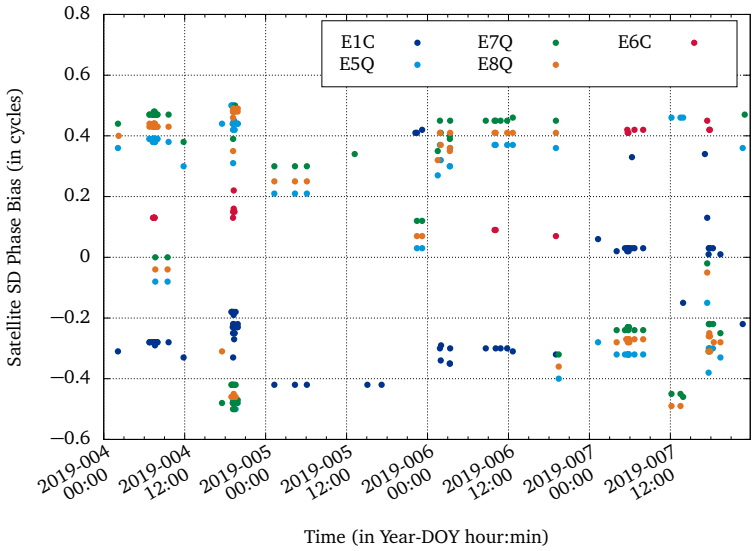

Figure 7.51: Between satellite SD phase biases of Galileo satellites E26 and E12 for all signals, determined from fixed raw observation ambiguities of multiple receivers, each tracking both satellites at the same time.

The determined multi-frequency satellite SD phase biases could aid the integer ambiguity resolution for a single receiver applying the raw observation processing approach and therefore enable PPP applications with integer ambiguity resolution (PPP-IAR), as introduced in section 5.1.4.

7.5.3 Aspects for PPP-IAR with Determined Satellite SD Phase Biases

A single receiver PPP approach with integer ambiguity resolution based on the multi-frequency satellite SD phase biases, as determined in section 7.5.2, would have to apply the raw observation processing approach without forming any linear combinations or observation differences.
In principle the user corrections needed for this PPP-IAR approach are similar to the ones of the CC model, described in section 5.1.4, namely precise satellite orbits and clock offsets and between satellite SD phase biases.
In contrast to the realisation of the CC model, demonstrated in (Teunissen and Khodabandeh, 2014) using a dual-frequency geometry-free/ionosphere-free decomposition where the single receiver ambiguities are in fact double-difference ambiguities, the PPP-IAR approach described here is not based on a specific re-parameterisation by fixing certain parameters of a single reference station in the network solution. Instead it is based on the final raw observation ambiguity estimates of the fixed network solution, as described in section 6.3. The user PPP algorithm would have to form between satellite SDs of the estimated multi-frequency raw observation float ambiguities and apply the satellite SD phase biases to construct ambiguities with integer nature. Fixing these ambiguities to the correct integer values and adding the corresponding integer constraints to the normal equation system, as described in section 6.2.3, would then strengthen and improve the standard PPP solution.
The implementation of a PPP-IAR approach based on the described method is outside the scope of this work, but offers an excellent opportunity to analyse an alternative to the PPP-RTK methods introduced in section 5.1.4 and to further exploit the potential of precise applications making use of the GNSS raw observation processing approach.

8 Conclusion

The analyses and results presented in this work motivate the use of a GNSS processing approach based on multi-GNSS and multi-signal raw observations without forming any linear combinations or observation differences. With the continuous modernisation of existing GNSS, the finalisation of Galileo and the fast-evolving BeiDou system, future GNSS applications will largely be based on multi-GNSS and multi-signal processing. The conventional dual-frequency ionosphere-free processing approach limits the number of usable signals and therefore does not provide the flexibility required for proper multi-GNSS and multi-signal applications. As the GNSS raw observation processing approach has no inherent limitation on the number of signals, it allows users to benefit from the expanding GNSS signal environment.
The simultaneous processing of multi-signal raw observations requires both a proper handling of all involved signal hardware biases and the estimation of ionospheric delay parameters, both of which become crucial parts of the parameter estimation process. As the ionospheric delay is changing rapidly, it usually is estimated per processing epoch, generating a considerable amount of additional parameters. The strong correlation between clock offset parameters, signal biases and the ionospheric delays requires a proper treatment of the additional parameters in order to solve the induced rank deficiency in the normal equation system.
The required handling of ionospheric delays in the raw observation processing approach enables the estimation of ionospheric effects in addition to common geodetic parameters. In addition, applying ionosphere corrections to raw observations instead of using the IF linear combination is regarded beneficial in the context of PPP-RTK applications, as described in section 5.1.4.
While the formation of IF linear combinations amplifies the noise of the resulting observations, using GNSS raw observations preserves the individual signal characteristics, allowing users to benefit from the original signal noise characteristics and analyse signal individual effects.
The raw method supports precise multi-GNSS and multi-signal applications with a physically meaningful handling of multi-signal code biases, ionospheric delays and multi-GNSS time offsets.

8.1 Signal Bias Handling in Multi-GNSS and Multi-Signal Raw Observation Processing

The calibration of receiver-specific multi-GNSS and multi-signal DCBs with simulated GNSS observations was demonstrated and successfully applied in the estimation of physically meaningful code biases for Galileo, GPS and BeiDou satellites. In addition, the calibration of multi-signal raw observation absolute code biases for a dedicated GNSS timing receiver allowed the analysis of GNSS system times and inter-system time offsets using the multi-signal raw observation processing approach.
Variations of receiver-system specific code biases due to the use of RF signal splitters and a change of the receiving antenna were analysed, showing an impact of up to 7 ns for the analysed receiver-antenna pair. This emphasises the importance of calibrating the complete receiver system chain for applications making use of mixed receiver and antenna types with applied corrections for receiver-specific code biases.
The comparison of estimated GNSS satellite DCBs with published Galileo IOV metadata reveals that the raw method is capable of determining physically meaningful GNSS satellite code biases and confirms the correct calibration of receiver-specific code biases for the EGON receiver network.
The determined receiver and satellite code biases were used to estimate absolute ionospheric delays with the raw method, showing excellent agreement with reference values computed from IONEX files and demonstrating the negative impact of not using physically meaningful code biases.

8.2 Integer Ambiguity Resolution Based on Multi-GNSS and Multi-Signal Raw Observations

A carrier phase integer ambiguity resolution approach based on multi-GNSS and multi-signal raw observation processing without forming any linear combinations or observation differences has been described and successfully implemented in the course of this work. It was demonstrated that this approach can be used to correctly resolve integer ambiguity values for multi-frequency Galileo signals, indicating a consistent handling of all signals for most receivers used in the global network adjustment. For dual- and triple-frequency GPS signals, the resolution of integer ambiguity values showed significant inconsistencies of the formed DD ambiguities, indicating a different handling of signals for different receiver types. For dual- and triple-frequency BeiDou signals, integer ambiguity values could not properly be resolved due to a lack of information on the modelling of BeiDou satellites and a reduced number of MEO satellites as well as receivers tracking all BeiDou signals.
In a Galileo+GPS scenario comparing the IAR approach based on raw observations with the conventional approach based on the IF linear combination and WL/NL ambiguities, the percentages of achieved fixed DD integer ambiguities

are about 85 % and 97 % respectively. This large discrepancy can be explained by receiver inconsistencies (mainly for GPS signals) and also reflects the renunciation of widelane ambiguities in the raw method. These ambiguities have a wavelength 3-4 times larger than raw signal ambiguities and therefore ease the integer ambiguity resolution in the conventional approach. This finding demonstrates that the raw method, as expected, is more sensitive to different GNSS signal characteristics and the methods of signal handling and tracking employed by different receiver types.
Despite this alleged drawback, the IAR approach based on raw observations achieves a higher percentage of fixed undifferenced ambiguities of 97-99 % for Galileo and GPS signals, whereas the conventional IF approach only achieves 95-96 %. This indicates that despite certain signal inconsistencies, almost all raw observation ambiguities can be fixed.
The IAR performance analysed for eleven different signals on eight frequencies from three different GNSS shows characteristics which can only be disclosed by the raw method, e.g. the reduced performance of the Galileo E6 signal. This reduced performance is mainly due to the lack of receivers tracking this signal, but potentially also due to interference issues in the E6 frequency band.
The resolution of inter-system DD integer ambiguities was demonstrated for common carrier signal frequencies, however, further investigations are required to analyse the presented issues of fixing correct integer values in order to improve the overall solution.

8.3 Multi-GNSS Precise Orbit Determination Based on Fixed Raw Observation Ambiguities

The IAR approach based on multi-GNSS and multi-signal raw observations has been applied to precise orbit determination of Galileo, GPS and BeiDou satellites. The successful implementation of the IAR approach based on raw observations has been demonstrated by a factor of two improvement of the Galileo and GPS satellite orbit overlaps for the ambiguity fixed solution with respect to the float solution.
Despite the differences in the resolution of integer ambiguity values, the POD for Galileo and GPS satellites shows a similar performance with orbit overlap 1D RMS values at the midnight epoch of about 27 mm for the ambiguity fixed solution. For BeiDou the orbit overlap 1D RMS values of the float and fixed solutions both are about 150 mm, which confirms that for BeiDou the resolution of integer ambiguity values based on raw observations could not properly be performed.
The comparison of satellite orbit quality between the IAR approach based on raw observations and the conventional approach based on the IF linear combination shows at least equivalent performance for the approach implemented in the course of this work. For some cases the IAR approach based on raw observations even provides a better performance in terms of orbit overlaps and orbit comparison to reference solutions from ESOC and the IGS final products.
The comparison of determined GNSS satellite orbits based on raw observations with the ESOC standard multi-GNSS solution based on the processing of the IF linear combination reveals orbit difference 1D RMS values of about 12 mm for Galileo and GPS satellites and about 35 mm for BeiDou satellites. The comparison of determined GPS orbits with IGS final products also reveals orbit difference 1D RMS values of about 12 mm.
In addition, it could be shown that the fixing of raw observation ambiguities also improves the stability of estimated satellite clock offsets. The determined constellation RMS mean values for the difference between the satellite clock offset estimates and a linear fit model are 116 ps for Galileo, 433 ps for GPS and 735 ps for BeiDou, demonstrating the high quality of the Galileo satellite on-board clocks.

The fixed raw observation ambiguities of the multi-GNSS POD analyses have further been used to analyse raw observation phase biases. While receiver specific phase biases, analysed with simulated GNSS observations for different receivers, were not found to be considered constant, the analysis of satellite SD phase biases based on fixed raw ambiguities reveals consistent and stable multi-frequency phase bias values for Galileo signals determined from different receivers. For GPS, most satellite SD phase biases determined from fixed raw ambiguities do not show consistent and stable values. The consistency of satellite-specific phase biases between independent daily solutions remains to be further analysed, as well as the use of these phase biases in PPP-IAR applications.

9 Outlook

The developments and analyses performed in the course of this work give rise to a variety of additional research topics to extend the presented analyses and further exploit the potential of the raw observation processing approach for precise GNSS applications.
In the context of code bias calibration and determination, the additional calibration of receiver DCBs for Galileo frequency E6 and BeiDou signal C6I is of interest in order to estimate physically meaningful satellite DCBs for these signals.
For the integer ambiguity resolution based on raw observations and precise GNSS satellite orbit determination, potential improvements due to an enhanced modelling of BeiDou satellites remain to be analysed once more details are made available by the system provider. In addition, further investigations of the resolution of inter-system integer ambiguities based on raw phase observations of common carrier frequencies and its impact on GNSS satellite POD are required.
With respect to satellite-specific phase biases, it remains to be confirmed whether constraining multi-frequency satellite SD phase biases between independent daily solutions is applicable to improve their consistency. The realisation of a PPP-IAR algorithm to perform single receiver integer ambiguity resolution based on the presented multi-frequency satellite-specific phase biases remains to be implemented. This would offer the opportunity to analyse alternative IAR enabled PPP approaches and compare their performance with existing PPP-RTK concepts. One of the major drawbacks of these existing concepts is the long convergence time due to the use of the ionosphere-free linear combination. It remains to be analysed whether the estimation of ionospheric delays from multi-signal raw observations, together with applied multi-frequency satellite-specific phase biases in the alternative IAR enabled PPP approach, can improve the convergence time and therefore further exploit the potential of the GNSS raw observation processing approach.

10 Appendix

A Notation and Symbols

GNSS Observation Model

Σ	Symbol of a generic GNSS
$\square^s$	Relates to satellite s
$\square_r$	Relates to GNSS receiver r
$\square_\oplus$	Relates to the Earth
Σia	3-character ID of a signal sent by a satellite of GNSS Σ with frequency index i and signal identifier a
f_i	Carrier signal frequency i
λ_i	Carrier signal wavelength corresponding to frequency i
τ_Ξ	Generic reference time scale used in GNSS observation processing
τ_r	Time scale of GNSS receiver r
τ^s	Time scale of satellite s
t^{tog}	Time of signal generation on-board the navigation satellite
t^{tot}_{ia}	Time of transmission for signal ia at the navigation satellite antenna
$t_{tor,\Sigma ia}$	Time of reception for signal Σia at the receiver antenna
t_{tom}	Time of measurement at the receiver, independent of tracked satellite and signal
$T^s_{r,\Sigma ia}$	Total signal travel time
$\Delta T^s_{r,\Sigma ia}$	Free space signal travel time
$P^s_{r,\Sigma ia}$	Functional model of a pseudorange observation measured by receiver r for signal Σia received from navigation satellite s
$\Phi^s_{r,i}$	Functional model of a carrier phase observation measured by receiver r for frequency i of a signal received from navigation satellite s
$\rho^s_{r,\Sigma ia}(t^{tot}, t_{tor})$	Geometric distance between the point of signal transmission at the navigation satellite antenna at time t^{tot} and the point of signal reception at the receiver antenna at time t_{tor}
$\boldsymbol{r}_r$	Geocentric position vector to the reference/marker point of receiver r, described in an inertial coordinate system
$\boldsymbol{r}^s$	Geocentric position vector to the centre of mass of satellite s, described in an inertial coordinate system
$dt_{r,\Xi}$	GNSS receiver clock offset from reference time scale τ_Ξ
dt^s_Ξ	Navigation satellite clock offset from reference time scale τ_Ξ
$dtro^s_r$	Tropospheric delay along the signal path
$dion^s_{r,i}$	Ionospheric delay along the signal path for frequency i
$d_{r,\Sigma ia}$	Receiver code bias for signal Σia
d^s_{ia}	Satellite code bias for signal ia
$\delta_{r,i}$	Receiver phase bias for signal frequency i
δ^s_i	Satellite phase bias for signal frequency i
$N^s_{r,i}$	Carrier phase integer ambiguity for signal frequency i
$M^s_{r,i}$	Carrier phase float ambiguity for signal frequency i, including phase biases

$dm^s_{r,\Sigma ia}$	Pseudorange measurement multipath for signal Σia
$\delta m^s_{r,i}$	Carrier phase measurement multipath for signal frequency i
$\epsilon^s_{r,\Sigma ia}$	Pseudorange observation residual errors and measurement noise
$\eta^s_{r,i}$	Carrier phase observation residual errors and measurement noise
$dr_{r,\Sigma ia}$	Receiver antenna offset range correction for code signal Σia
dr^s_{ia}	Satellite antenna offset range correction for code signal ia
$\delta r_{r,i}$	Receiver antenna offset range correction for signal frequency i
δr^s_i	Satellite antenna offset range correction for signal frequency i
δ_{rel}	Periodic relativistic satellite clock correction
δ_{stc}	Relativistic propagation delay correction due to space-time curvature
pwu^s_r	Phase wind-up effect correction
$disp_r$	Receiver coordinate displacement correction due to tide effects

Parameter Estimation

$\boldsymbol{Y}$	Vector of observations
$\boldsymbol{P}$	Weight matrix of the observations
$\boldsymbol{X}$	Vector of estimated parameters
$\boldsymbol{f}(\boldsymbol{X}, t)$	Functional model relating observations and estimated parameters
$\boldsymbol{X}^*$	Vector of nominal parameter values
$\hat{\boldsymbol{X}}$	Vector of best parameter estimates
$\bar{X}$	A fixed parameter
$\boldsymbol{y}$	Vector of observation deviations from functional model evaluated at nominal parameter values
$\boldsymbol{x}$	Vector of parameter estimate deviations from nominal parameter values
$\boldsymbol{A}$	Design matrix containing the partial derivatives of the functional model $\boldsymbol{f}$ with respect to the estimated parameters $\boldsymbol{X}$
$\boldsymbol{v}$	Vector of residuals of the observations
Ω	Weighted sum of squared residuals
$\boldsymbol{N}$	Normal equation matrix of the observations
$\boldsymbol{X}_c$	Vector of constrained parameter values
$\boldsymbol{z}$	Vector of parameter constraint deviations from nominal parameter values
$\boldsymbol{R}$	Weight matrix of the fictitious observations from parameter constraints
$\boldsymbol{B}$	Design matrix of the parameter constraints, containing only zeros and ones
$\boldsymbol{M}$	Normal equation matrix of the fictitious observations from parameter constraints
$\boldsymbol{\xi}$	Vector of residuals of the fictitious observations from parameter constraints

Integer Ambiguity Resolution

$\boldsymbol{DD}$	Double difference matrix operator
$M^{kl}_{AB,i}$	Double difference float ambiguity for signal frequency i
$N^{kl}_{AB,i}$	Double difference integer ambiguity for signal frequency i
$f^{kl}_{AB,i}$	Fractional part of double difference float ambiguity for signal frequency i

B Constants

G	Gravitational constant, $G = 6.674 \times 10^{-11}\,\mathrm{m^3\,kg^{-1}\,s^{-2}}$
$M_\oplus$	Mass of the Earth, $M_\oplus = 5.9722 \times 10^{24}\,\mathrm{kg}$
$\mu_\oplus$	Gravitational constant of the Earth, $\mu_\oplus = G \cdot M_\oplus = 3.986 \times 10^{14}\,\mathrm{m^3\,s^{-2}}$
$\omega_\oplus$	Nominal rotation rate of the Earth, $\omega_\oplus = 7.292\,115\,124\,7 \times 10^{-5}\,\mathrm{s^{-1}}$
c	Speed of light in vacuum, $c = 299\,792\,458\,\mathrm{m\,s^{-1}}$

C Definitions

Epoch	The clock reading $\tau(t)$ in time scale τ at a certain point in time t
J2000.0	Standard epoch defined as 1 January 2000, 11:58:55.816 UTC
Multipath	Measured non-line of sight signals, which originate from reflections in the receiver's local environment

D Acronyms

ACPC	Antenna Code Phase Center
AltBOC	Alternative BOC
APC	Antenna Phase Center
ARP	Antenna Reference Point
BDT	BeiDou Time
BeiDou	Chinese GNSS
BGD	Broadcast Group Delay
BIH	Bureau International de l'Heure
BIPM	International Bureau of Weights and Measures
BOC	Binary Offset Carrier
BPSK	Binary Phase Shift Keying
CAS	Chinese Academy of Sciences
CBOC	Composite BOC
CC	Common Clock
CDMA	Code Division Multiple Access
CIP	Celestial Intermediate Pole
CIR	Cascading Integer Resolution
DC	Distinct Clocks
DCB	Differential Code Bias
DCM	Decoupled Clock Model
DD	Double Difference

DLL	Delay Lock Loop
DLR	Deutsches Zentrum für Luft- und Raumfahrt
DORIS	Doppler Orbitography and Radiopositioning Integrated by Satellite
DOY	Day Of Year
ECEF	Earth Centred Earth Fixed
ECI	Earth Centred Inertial
EGON	ESA's GNSS Observation Network
EOP	Earth Orientation Parameters
ESA	European Space Agency
ESM	ESOC MGNSS
ESOC	European Space Operations Centre
FCB	Fractional Cycle Bias
FDMA	Frequency Division Multiple Access
FOC	Full Operational Capability
Galileo	European GNSS
GCRS	Geocentric Celestial Reference System
GDV	Group Delay Variation
GEO	Geostationary Orbit
GF	Geometry-Free
GGTO	Galileo-GPS Time Offset
GLONASS	Russian GNSS
GLOT	GLONASS Time
GMF	Global Mapping Function
GNSS	Global Navigation Satellite Systems
GPS	U.S. Global Positioning System
GPST	GPS Time
GPT	Global Pressure Temperature
GST	Galileo System Time
IAR	Integer Ambiguity Resolution
IAU	International Astronomical Union
IB	Integer Bootstrapping
ICD	Interface Control Document
ICRF	International Celestial Reference Frame
ICRS	International Celestial Reference System
IERS	International Earth Rotation and Reference Systems Service
IF	Ionosphere-Free
IGS	International GNSS Service
IGSO	Inclined GeoSynchronous Orbit
ILS	Integer Least Squares
IONEX	Ionosphere Map Exchange
IOV	In-Orbit Validation

IP	Ionospheric Pierce Point
IR	Integer Rounding
IRC	Integer Recovery Clock
IRM	IERS Reference Meridian
IRNSS	Indian Regional Navigation Satellite System
IRP	IERS Reference Pole
IS	Inter-System
ISB	Inter-System Bias
ISTO	Inter-System Time Offset
ITRF	International Terrestrial Reference Frame
ITRS	International Terrestrial Reference System
LAMBDA	Least-Squares AMBiguity Decorrelation Adjustment
LC	Linear Combination
LEO	Low Earth Orbit
LNA	Low Noise Amplifier
LOD	Length Of Day
LOS	Line Of Sight
LSQ	Least Squares
MBOC	Multiplexed BOC
MEO	Medium Earth Orbit
MGEX	Multi-GNSS Experiment
MW	Melbourne-Wuebbena
NAPEOS	NAvigation Package for Earth Observation Satellites
NL	Narrowlane
NMF	Neill Mapping Function
OCB	Observable-specific Code Bias
OPB	Observable-specific Phase Bias
OS	Open Service
P2P	Pass-to-Pass
PCO	Phase Center Offset
PCV	Phase Center Variation
PLL	Phase Lock Loop
PNT	Positioning Navigation Timing
POD	Precise Orbit Determination
POI	Point Of Interest
PPP	Precise Point Positioning
PPP-RTK	PPP Real Time Kinematic
PRN	Pseudo Random Noise
PTB	Physikalisch-Technische Bundesanstalt
PVT	Position Velocity Time

QZSS	Quasi-Zenith Satellite System
RAW	Raw Method
RF	Radio Frequency
RINEX	Receiver Independent Exchange
RMS	Root Mean Square
RNSS	Regional Navigation Satellite Systems
RTK	Real Time Kinematic
SD	Single Difference
SGD	Satellite Group Delay
SI	International System of Units
SLR	Satellite Laser Ranging
SNR	Signal-to-Noise Ratio
SRP	Solar Radiation Pressure
SSV	Space Service Volume
STEC	Slant Total Electron Content
TAI	International Atomic Time
TCAR	Three-Carrier Ambiguity Resolution
TEC	Total Electron Content
TECU	Total Electron Content Unit
TT&C	Telemetry, Tracking and Command
UCD	Uncalibrated Code Delays
UPD	Uncalibrated Phase Delays
USD	Uncalibrated Signal Delays
UT1	Universal Time
UTC	Coordinated Universal Time
UTC(k)	Physical Realisation of UTC
VLBI	Very Long Baseline Interferometry
VMF	Vienna Mapping Function
VTEC	Vertical Total Electron Content
WL	Widelane
ZHD	Zenith Hydrostatic Delay
ZTD	Zenith Tropospheric Delay
ZWD	Zenith Wet Delay

E List of Figures

2.1 Overview of GNSS signal frequencies used in this work with schematically indicated signal bandwidths. . 4

2.2 Signal structure of a GNSS signal carrier wave modulated with PRN code and navigation message. 5

2.3 GNSS code phase (pseudorange) measurement, derived from the signal generation time in the satellite time scale $\tau^s(t^{tog})$ and the measurement time in the receiver time scale $\tau_r(t_{tom})$. 6

2.4 GNSS carrier phase measurement $\phi_r^s(t_{tom})$ of fractional and full cycles, recognised as precise measure of the carrier phase pseudorange by adding the unknown integer ambiguity term N_r^s. 7

3.1 Relationship between TAI, UT1, UTC and GNSS system times (adopted from Ley et al., 2019). 9

3.2 Schematic representation of the relationship between GNSS receiver clock time scale τ_r, reference time scale τ_Ξ and the receiver clock offset $dt_{r,\Xi}$. 10

4.1 Representation of the relationship between the four time arguments: signal generation time t^{tog}, signal transmission time t_{ia}^{tot}, signal reception time $t_{tor,\Sigma ia}$ and time of measurement t_{tom}. 12

4.2 Computed time derivatives of the geometric range between GNSS satellites and receivers for different applications. 18

4.3 Geometric relation between zenith angle z at receiver position and z' at the IP with the radius of the Earth $R_\oplus$ and the single layer height h_i of the ionospheric model. 21

4.4 Antenna offset and variation corrections used for modelling GNSS pseudorange observations. 22

4.5 Antenna offset and variation corrections used for modelling GNSS carrier phase observations. 23

4.6 Dipole vectors D^s and D_r of the transmitting and receiving antennas respectively, used to compute the phase wind-up correction. 24

5.1 Code observation residual RMS daily mean values of individual Galileo signals and the ionosphere-free linear combination IF(E1,E5a) for station CEBR from analyses described in section 7.4. 34

6.1 Flowchart diagram of the iterative integer ambiguity resolution scheme for double difference ambiguities based on multi-GNSS and multi-signal raw observation float ambiguity estimates. 45

6.2 Double difference ambiguity fractional histogram based on raw observation float ambiguity estimates for all Galileo signals. 47

6.3 Widelane double difference ambiguity fractional histogram based on raw observation float ambiguity estimates for Galileo signals relative to E1C. 49

6.4 Inter-system double difference ambiguity fractional histogram based on raw observation float ambiguity estimates for Galileo signals E1C and E5Q and GPS signals G1C and G5Q. 50

7.1 ESA's GNSS Observation Network (EGON) (Navigation Support Office, 2019) 52

7.2 EGON receiver specific differential code biases (DCBs) from simulated multi-signal GNSS raw observations. 53

7.3 EGON receiver specific differential code biases (DCBs) from simulated multi-signal GNSS raw observations. 54

7.4 Future EGON receiver specific differential code biases (DCBs) from simulated multi-signal GNSS raw observations. 54

7.5 Impact of the 4-way GNSS splitter type A output selection on receiver system differential code biases. . . . 55

7.6 Impact of the 4-way GNSS splitter type B output selection on receiver system differential code biases. . . . 56

7.7 Impact of an antenna switch on estimated receiver system differential code biases (DCBs) for different Galileo signals. 57

7.8 Galileo IOV and FOC satellite DCBs $\tilde{d}^s_{E1-E5a}$, derived from broadcast satellite group delays for signals E1/E5a. 59

7.9 Satellite DCBs derived from satellite broadcast group delays. 59

7.10 Galileo IOV and FOC satellite DCBs derived from broadcast satellite group delays for signals E1/E5a. . . . 60

7.11 Galileo satellite $\tilde{d}^s_{E1C-E5Q}$ DCB estimates by DLR (Daily IGS MGEX DCB solutions in Bias-SINEX format) from (CDDIS, Crustal Dynamics Data Information System, 2019a). 61

7.12 Satellite DCB estimates by DLR (Daily IGS MGEX DCB solutions in Bias-SINEX format) from (CDDIS, Crustal Dynamics Data Information System, 2019a). 62

7.13 Galileo satellite $d^s_{E1C-E5Q}$ DCB estimates based on the raw observation processing approach with constrained EGON receiver DCBs and estimated residual ionospheric delays. 63

7.14 Satellite DCB estimates based on the raw observation processing approach with constrained EGON receiver DCBs and estimated residual ionospheric delays. 64

7.15 Ionospheric delay estimates from multi-frequency raw observation processing compared to STEC values derived from IONEX files generated at ESOC. 64

7.16 Ionospheric delay estimates from dual-frequency raw observation processing compared to STEC values derived from IONEX files generated at ESOC. 65

7.17 GNSS system time offset with respect to UTC determined with the raw observation processing approach from multi-GNSS and multi-signal raw observations. 66

7.18 Galileo code observation residual RMS daily mean values for the EGON type timing receiver used to estimate the GNSS system times. 67

7.19 Code observation residual RMS daily mean values for the EGON type timing receiver used to estimate the GNSS system times. 67

7.20 Galileo-GPS time offset (GGTO) comparison between GPGA parameter in mixed broadcast navigation RINEX files, computed GGTO values based on the raw method with absolute or residual ionospheric delay estimates and GGTO values computed from precise multi-GNSS ionosphere-free (IF) satellite clock products. 68

7.21 Global receiver networks used for the analyses of multi-GNSS precise orbit determination with integer ambiguity resolution based on raw phase observations. 69

7.22 Normalized DD ambiguity fractional histogram based on raw observation float ambiguity estimates for Galileo signals tracked by the GE_{100} network in the first iteration of the integer ambiguity resolution (IAR) algorithm. 71

7.23 Normalized DD ambiguity fractional histograms based on raw observation float ambiguity estimates for Galileo signals tracked by the GE_{100} network. 72

7.24 Normalized DD ambiguity fractional histogram based on raw observation float ambiguity estimates for GPS signals tracked by the GE_{100} network in the first iteration of the integer ambiguity resolution (IAR) algorithm. 72

7.25 Normalized DD ambiguity fractional histograms based on raw observation float ambiguity estimates for GPS signals tracked by the GE_{100} network. 73

7.26 Normalized DD ambiguity fractional histogram based on raw observation float ambiguity estimates for BeiDou signals tracked by the GE_{100} network in the first iteration of the integer ambiguity resolution (IAR) algorithm. 73

7.27 Normalized DD ambiguity fractional histograms based on raw observation float ambiguity estimates for BeiDou signals tracked by the GE_{100} network. 74

7.28 Percentage of fixed independent DD integer ambiguities per GNSS for daily solutions of scenario #9. . . . 74

7.29 Percentage of total number of fixed independent DD integer ambiguities (Galileo+GPS) for daily solutions of scenarios #1, #2, #3 and #5. 75

7.30 Percentage of fixed undifferenced ambiguities per GNSS for daily solutions of scenarios #2 and #9. 76

7.31 Percentage of fixed raw observation ambiguities per GNSS signal for daily solutions of scenario #9. 77

7.32 SNR measurements of different satellites tracked simultaneously by a multi-GNSS receiver at ESOC. 77

7.33 Normalized DD ambiguity widelane fractional histogram based on raw observation float ambiguity estimates for Galileo signals tracked by the GE_{100} network relative to E1C. 78

7.34 Normalized DD ambiguity widelane fractional histograms based on raw observation float ambiguity estimates for signals tracked by the GE_{100} network. 78

7.35 Normalized inter-system DD ambiguity fractional histograms based on raw observation float ambiguity estimates for signals tracked by the GE_{100} network. 79

7.36 Comparison of normalized DD ambiguity fractional histograms based on raw observation float ambiguity estimates for GPS signals in the first iteration of the IAR algorithm. . . . 80
7.37 Midnight satellite orbit overlap 1D RMS constellation mean values for the daily float and fixed solutions of scenario #9. . . . 80
7.38 Midnight satellite orbit overlap 1D RMS constellation mean values for the daily float and fixed solutions of scenarios #2 and #5. . . . 81
7.39 Midnight satellite orbit overlap 1D RMS constellation mean values for the daily float and fixed solutions of scenarios #3 and #4. . . . 81
7.40 Midnight satellite orbit overlap 1D RMS constellation mean values for the daily fixed solutions of scenarios #5, #6, #7 and #8. . . . 82
7.41 Orbit comparison 1D RMS constellation mean values for the daily float and fixed solutions of scenario #9 relative to the ESOC multi-GNSS orbits based on the IF processing approach. . . . 82
7.42 Orbit comparison 1D RMS constellation mean values for the daily GPS fixed solutions of scenarios #2, #5, #6 and #8 relative to the IGS final orbits based on the IF processing approach. . . . 83
7.43 Orbit comparison 1D RMS for individual GPS satellites from daily fixed solutions of scenarios #1 and #3 relative to the IGS final orbits. . . . 84
7.44 RMS constellation mean values of the estimated GNSS satellite clock offsets compared to a linear fit clock model. . . . 84
7.45 Difference between phase and code observations for multiple satellites, generated by a multi-GNSS multi-signal simulator and measured by an EGON receiver type (A). . . . 85
7.46 Difference between Galileo signal E8Q phase and code observations for multiple satellites, generated by a multi-GNSS multi-signal simulator. . . . 86
7.47 Difference between Galileo signal E8Q phase and code observations for multiple satellites, generated by a multi-GNSS multi-signal simulator and measured by receiver type C. . . . 86
7.48 Pass-to-pass (P2P) phase bias difference histograms based on fixed raw observation ambiguities. . . . 87
7.49 Between satellite SD phase biases for different pairs of satellites, determined from fixed raw observation ambiguities of multiple receivers, each tracking the respective pair of satellites at the same time. . . . 88
7.50 Between satellite SD phase biases of Galileo satellites E26 and E12 for all signals, determined from fixed raw observation ambiguities of multiple receivers, each tracking both satellites at the same time. . . . 88
7.51 Between satellite SD phase biases of Galileo satellites E26 and E12 for all signals, determined from fixed raw observation ambiguities of multiple receivers, each tracking both satellites at the same time. . . . 89
10.1 Satellite DCB estimates based on the raw observation processing approach with constrained EGON receiver DCBs and estimated residual ionospheric delays. . . . 104
10.2 GPS satellite $d^{s}_{G1C-G5Q}$ DCB estimates based on raw observation processing approach with constrained EGON receiver DCBs and estimated residual ionospheric delays. . . . 104
10.3 Normalized DD ambiguity fractional histogram based on raw observation float ambiguity estimates for Galileo signals tracked by the GE_{60} network in the first iteration of the integer ambiguity resolution (IAR) algorithm. . . . 106
10.4 Normalized DD ambiguity fractional histogram based on raw observation float ambiguity estimates for GPS signals tracked by the GE_{60} network in the first iteration of the integer ambiguity resolution (IAR) algorithm. . . . 106
10.5 Normalized DD ambiguity fractional histogram based on raw observation float ambiguity estimates for Galileo signal E1C tracked by the GE_{100} network in the first iteration of the integer ambiguity resolution (IAR) algorithm. . . . 107
10.6 Normalized DD ambiguity fractional histogram based on raw observation float ambiguity estimates for Galileo signals tracked by the GE_{100} network in the first iteration of the integer ambiguity resolution (IAR) algorithm. . . . 107

10.7 Normalized DD ambiguity fractional histogram based on raw observation float ambiguity estimates for Galileo signals tracked by the GE_{100} network in the first iteration of the integer ambiguity resolution (IAR) algorithm. 108

10.8 Normalized DD ambiguity fractional histogram based on raw observation float ambiguity estimates for GPS signal G1C tracked by the GE_{100} network in the first iteration of the integer ambiguity resolution (IAR) algorithm. 108

10.9 Normalized DD ambiguity fractional histogram based on raw observation float ambiguity estimates for GPS signals tracked by the GE_{100} network in the first iteration of the integer ambiguity resolution (IAR) algorithm. 109

10.10 Normalized DD ambiguity fractional histogram based on raw observation float ambiguity estimates for BeiDou signal C2I tracked by the GE_{100} network in the first iteration of the integer ambiguity resolution (IAR) algorithm. 109

10.11 Normalized DD ambiguity fractional histogram based on raw observation float ambiguity estimates for BeiDou signals tracked by the GE_{100} network in the first iteration of the integer ambiguity resolution (IAR) algorithm. 110

10.12 Between satellite SD phase biases for different pairs of satellites, determined from fixed raw observation ambiguities of multiple receivers, each tracking the respective pair of satellites at the same time. 110

10.13 Between satellite SD phase biases for different pairs of satellites, determined from fixed raw observation ambiguities of multiple receivers, each tracking the respective pair of satellites at the same time. 111

10.14 Between satellite SD phase biases for different pairs of satellites, determined from fixed raw observation ambiguities of multiple receivers, each tracking the respective pair of satellites at the same time. 111

F List of Tables

2.1 Mapping of Galileo, GPS and BeiDou satellite signals to the three-character ID used in this work. 5

4.1 The constant satellite clock frequency offsets due to time delation and gravitationl redshift for different GNSS, applied to the satellite clock hardware prior to launch (Ashby, 2003). 19

4.2 Summary of the components in the raw observation model and observation models of linear combinations of GNSS observables. The symbol ∅ indicates that a component is eliminated by forming the corresponding linear combination. 28

5.1 Observation noise increase factor of the IF linear combination relative to the raw observation noise for different GNSS and signal combinations. 29

5.2 Overview of commonly used PPP-RTK methods. 33

5.3 Galileo IOV satellite group delays (SGD) for the primary and redundant subsystems measured by the spacecraft manufacturer on-ground prior to launch (taken from GSA, European GNSS Agency, 2019a). . . 35

5.4 Perturbing forces acting on GNSS satellites ordered by decreasing acceleration values, computed for GPS satellites (adopted from Flohrer, 2008) 42

7.1 Differential code bias calibration values for the EGON receiver type determined from simulated multi-GNSS and multi-signal raw observations, shown in Figures 7.2 and 7.3a. 53

7.2 Differential code bias calibration values for the future EGON receiver type determined from simulated multi-GNSS and multi-signal raw observations, shown in Figure 7.4. 55

7.3 Receiver system differential code bias dependency on selected splitter and signal output, determined from simulated multi-GNSS and multi-signal raw observations, shown in Figures 7.5 and 7.6. 56

7.4 Multi-GNSS multi-signal absolute code bias calibration values for the ESOC timing receiver used in the time offset analyses in section 7.3. 57

7.5 Galileo satellite BGD realignment values to generate physically meaningful satellite DCBs and remove jumps in the time series of Galileo satellite DCBs derived from broadcast satellite group delays. 61

7.6 Summary of the analysed scenarios for multi-GNSS POD with fixed raw carrier phase ambiguities. 70

7.7 Summary of the parameter setup used in the multi-GNSS POD analyses with fixed raw carrier phase ambiguities. 70

10.7 Mean and standard deviation (in ns) of the Galileo, GPS and BeiDou satellite DCB estimates based on the raw observation processing approach with constrained EGON receiver DCBs and estimated residual ionospheric delays for the processed time interval 2017-001 - 2019-120. 105

G Additional Results

G.1 Satellite Differential Code Bias Estimation

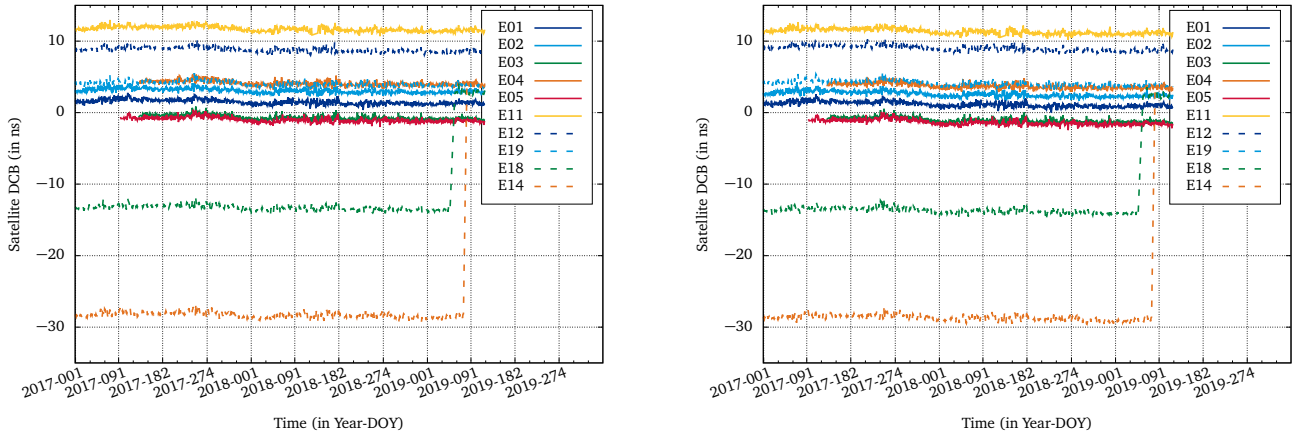

(a) Galileo satellite DCB $d^s_{E1C-E7Q}$

(b) Galileo satellite DCB $d^s_{E1C-E8Q}$

Figure 10.1: Satellite DCB estimates based on the raw observation processing approach with constrained EGON receiver DCBs and estimated residual ionospheric delays.

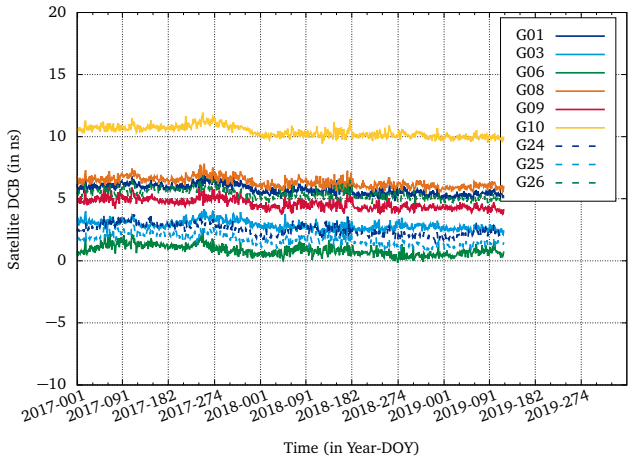

Figure 10.2: GPS satellite $d^s_{G1C-G5Q}$ DCB estimates based on raw observation processing approach with constrained EGON receiver DCBs and estimated residual ionospheric delays.

Table 10.7: Mean and standard deviation (in ns) of the Galileo, GPS and BeiDou satellite DCB estimates based on the raw observation processing approach with constrained EGON receiver DCBs and estimated residual ionospheric delays for the processed time interval 2017-001 - 2019-120.

	$d^s_{E1C-E5Q}$			$d^s_{G1C-G2W}$			$d^s_{C2I-C7I}$	
	mean	std		mean	std		mean	std
E01	0.02	0.45	G01	-3.71	0.3	C06	14.74	0.42
E02	1.32	0.46	G02	16.15	0.34	C07	18.02	0.44
E03	-2.16	0.43	G03	-1.80	0.33	C08	16.3	0.38
E04	2.72	0.44	G04	6.12	0.35	C09	7.90	0.42
E05	-2.43	0.45	G05	7.84	0.34	C10	7.64	0.43
E07	-3.98	0.44	G06	-3.08	0.34	C11	6.67	0.35
E08	3.22	0.46	G07	8.18	0.30	C12	7.52	0.35
E09	-1.04	0.43	G08	-2.02	0.32	C13	-7.44	0.39
E11	10.71	0.44	G09	0.00	0.38	C14	9.28	0.36
E12	8.50	0.45	G10	-0.96	0.33	C16	-2.58	0.44
E13	-0.42	0.23	G11	9.92	0.31			
E14^{+}	-29.86	0.46	G12	8.57	0.35			
E14^{++}	2.37	0.30	G13	8.65	0.31			
E15	-5.12	0.24	G14	8.49	0.33			
E18^{-}	-14.82	0.47	G15	7.81	0.37			
E18^{--}	1.19	0.31	G16	9.70	0.32			
E19	2.90	0.47	G17	8.11	0.3			
E21	-1.69	0.25	G18*	10.33	0.31			
E22	2.20	0.31	G18**	5.12	0.26			
E24	-37.59	0.45	G18***	4.45	0.21			
E25	-2.89	0.29	G19	13.87	0.31			
E26	-4.34	0.46	G20	8.99	0.34			
E27	-1.70	0.29	G21	9.86	0.32			
E30	-1.30	0.44	G22	15.53	0.33			
E31	-3.80	0.28	G23	15.10	0.33			
E33	2.42	0.23	G24	-1.82	0.34			
E36	-4.71	0.23	G25	-2.33	0.32			
			G26	-3.87	0.33			
			G27	0.33	0.34			
			G28	9.91	0.31	G18 (GPS-054)		
$^{+}$ 2017-001 - 2019-076			G29	7.41	0.34	* 2017-001 - 2018-022		
$^{++}$ 2019-083 - 2019-120			G30	-0.88	0.33	G18 (GPS-034)		
$^{-}$ 2017-001 - 2019-048			G31	8.76	0.32	** 2018-070 - 2018-320		
$^{--}$ 2019-058 - 2019-120			G32	-0.94	0.34	*** 2018-333 - 2019-120		

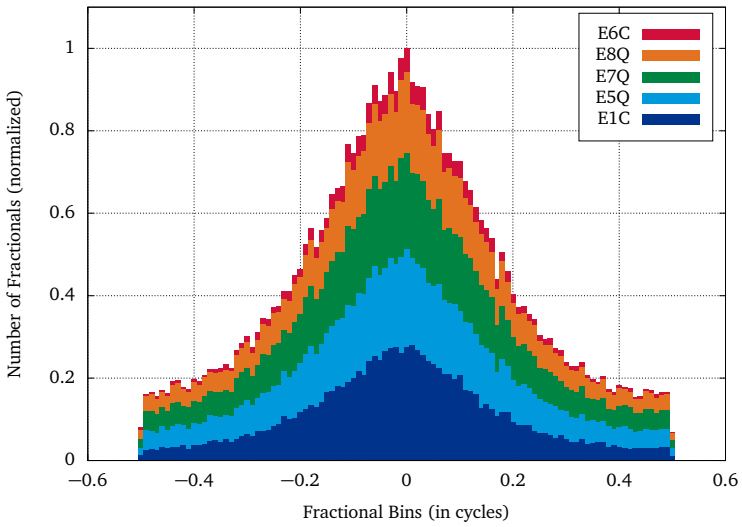

Figure 10.3: Normalized DD ambiguity fractional histogram based on raw observation float ambiguity estimates for Galileo signals tracked by the GE_{60} network in the first iteration of the integer ambiguity resolution (IAR) algorithm.

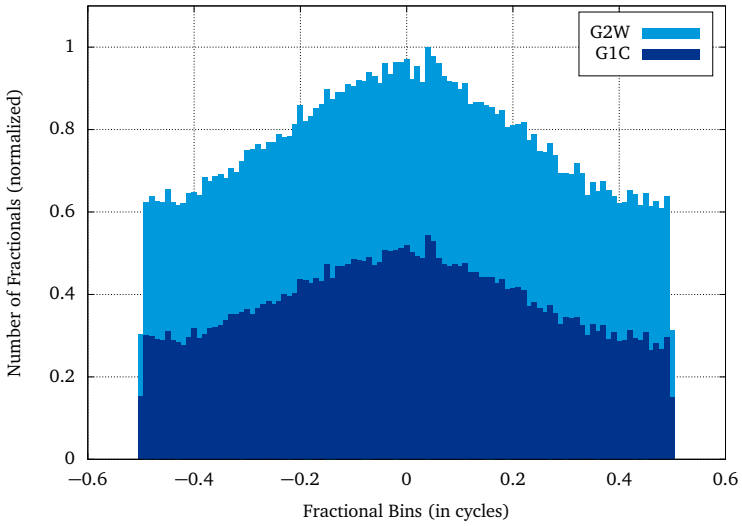

Figure 10.4: Normalized DD ambiguity fractional histogram based on raw observation float ambiguity estimates for GPS signals tracked by the GE_{60} network in the first iteration of the integer ambiguity resolution (IAR) algorithm.

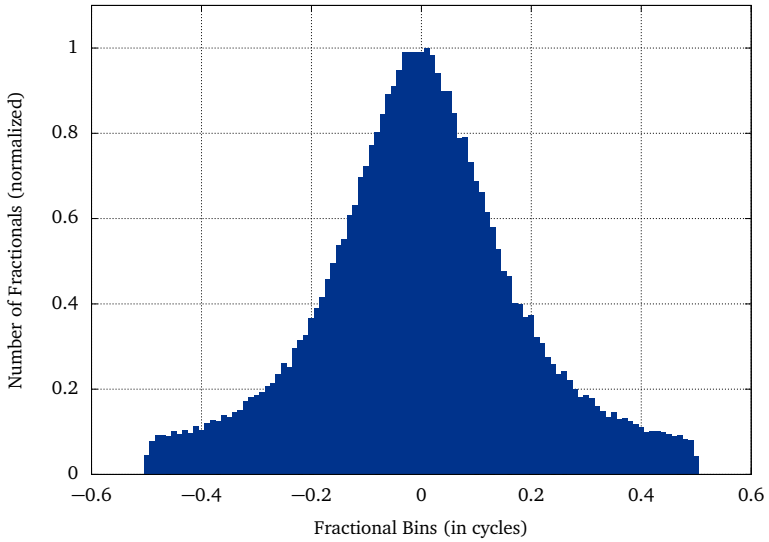

Figure 10.5: Normalized DD ambiguity fractional histogram based on raw observation float ambiguity estimates for Galileo signal E1C tracked by the GE_{100} network in the first iteration of the integer ambiguity resolution (IAR) algorithm.

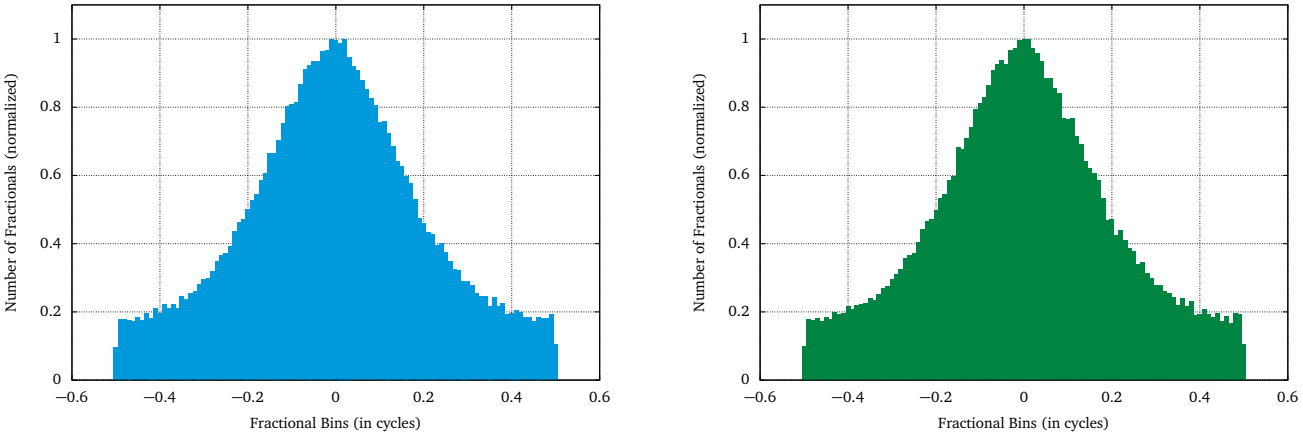

(a) Galileo signal E5Q

(b) Galileo signal E7Q

Figure 10.6: Normalized DD ambiguity fractional histogram based on raw observation float ambiguity estimates for Galileo signals tracked by the GE_{100} network in the first iteration of the integer ambiguity resolution (IAR) algorithm.

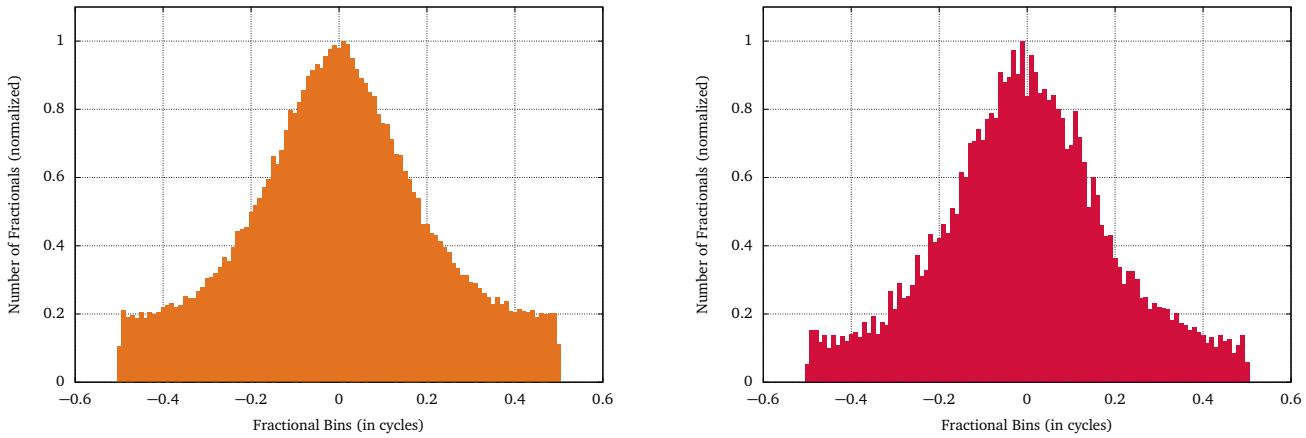

(a) Galileo signal E8Q

(b) Galileo signal E6C

Figure 10.7: Normalized DD ambiguity fractional histogram based on raw observation float ambiguity estimates for Galileo signals tracked by the GE_{100} network in the first iteration of the integer ambiguity resolution (IAR) algorithm.

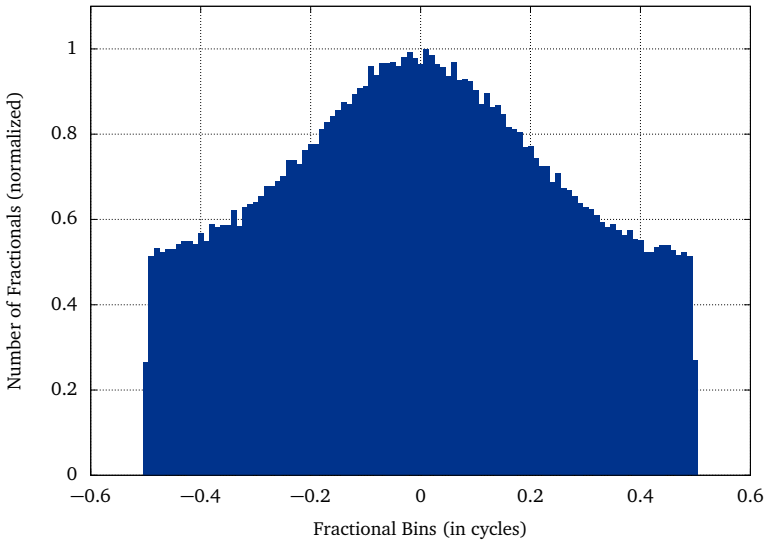

Figure 10.8: Normalized DD ambiguity fractional histogram based on raw observation float ambiguity estimates for GPS signal G1C tracked by the GE_{100} network in the first iteration of the integer ambiguity resolution (IAR) algorithm.

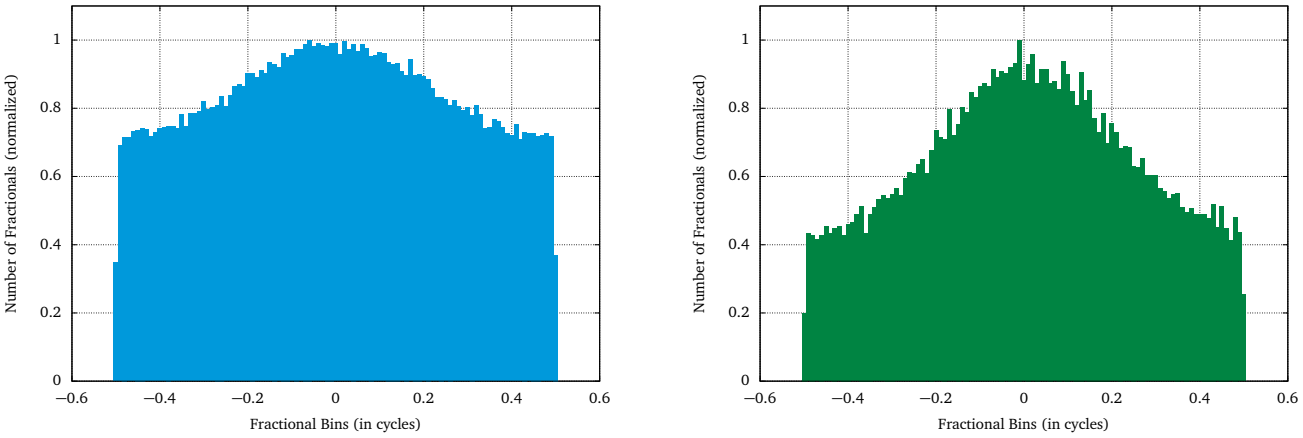

(a) GPS signal G2W

(b) GPS signal G5Q

Figure 10.9: Normalized DD ambiguity fractional histogram based on raw observation float ambiguity estimates for GPS signals tracked by the GE_{100} network in the first iteration of the integer ambiguity resolution (IAR) algorithm.

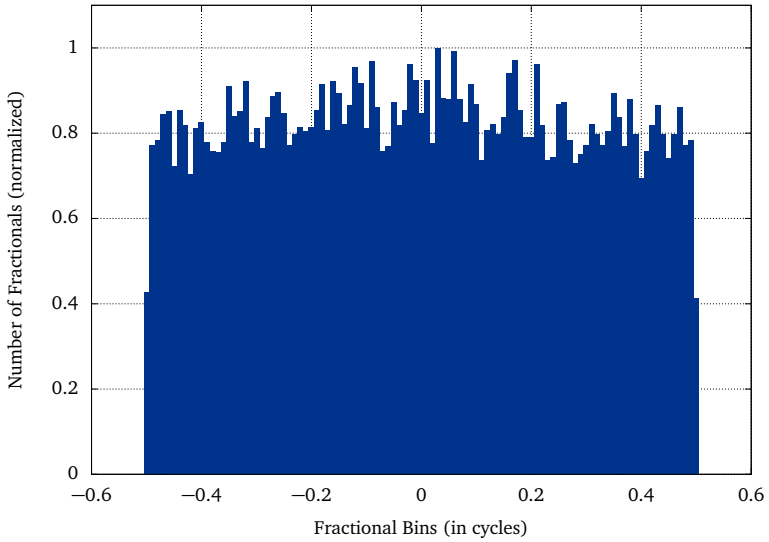

Figure 10.10: Normalized DD ambiguity fractional histogram based on raw observation float ambiguity estimates for BeiDou signal C2I tracked by the GE_{100} network in the first iteration of the integer ambiguity resolution (IAR) algorithm.

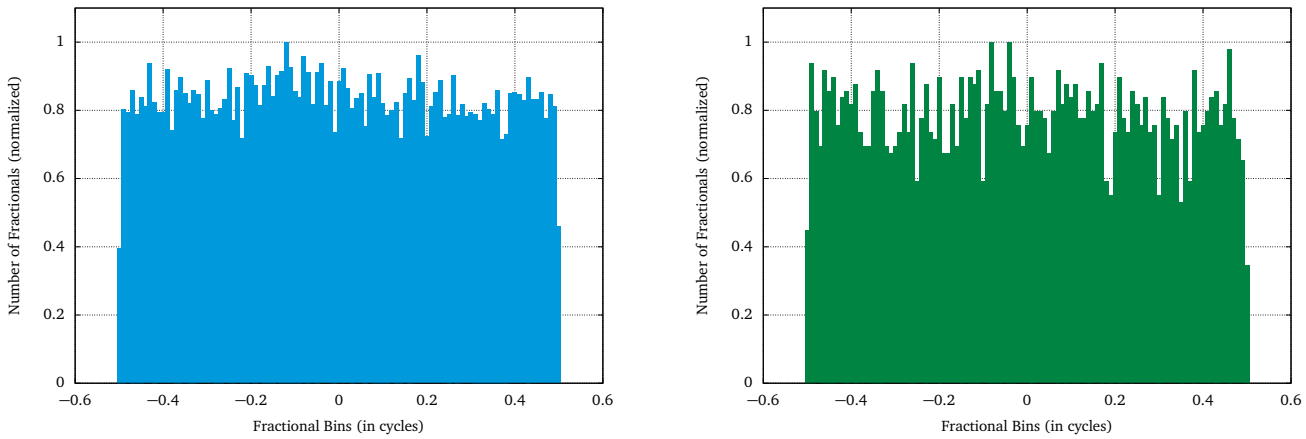

(a) BeiDou signal C7I

(b) BeiDou signal C6I

Figure 10.11: Normalized DD ambiguity fractional histogram based on raw observation float ambiguity estimates for BeiDou signals tracked by the GE_{100} network in the first iteration of the integer ambiguity resolution (IAR) algorithm.

G.3 Satellite SD Phase Biases

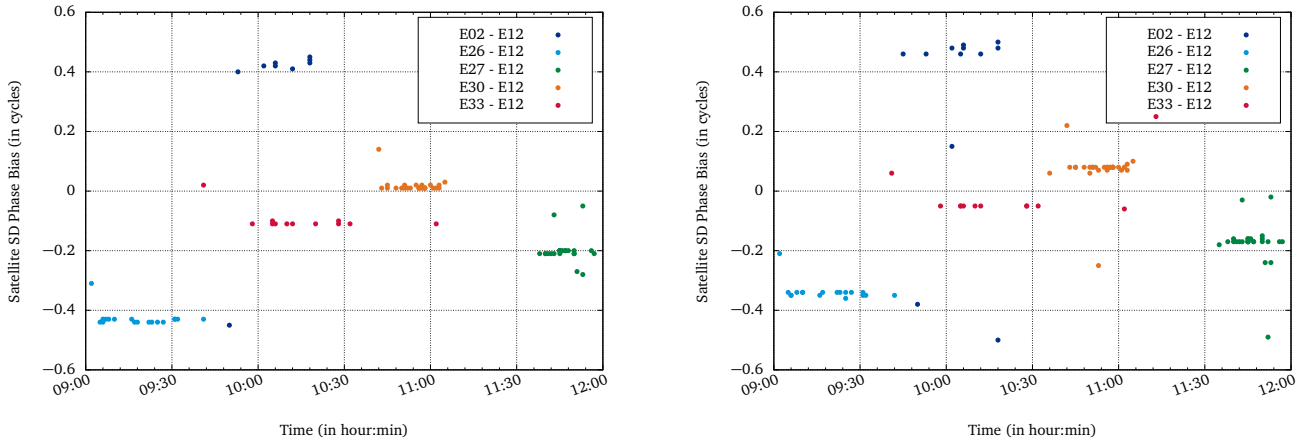

(a) Galileo signal E5Q

(b) Galileo signal E7Q

Figure 10.12: Between satellite SD phase biases for different pairs of satellites, determined from fixed raw observation ambiguities of multiple receivers, each tracking the respective pair of satellites at the same time.

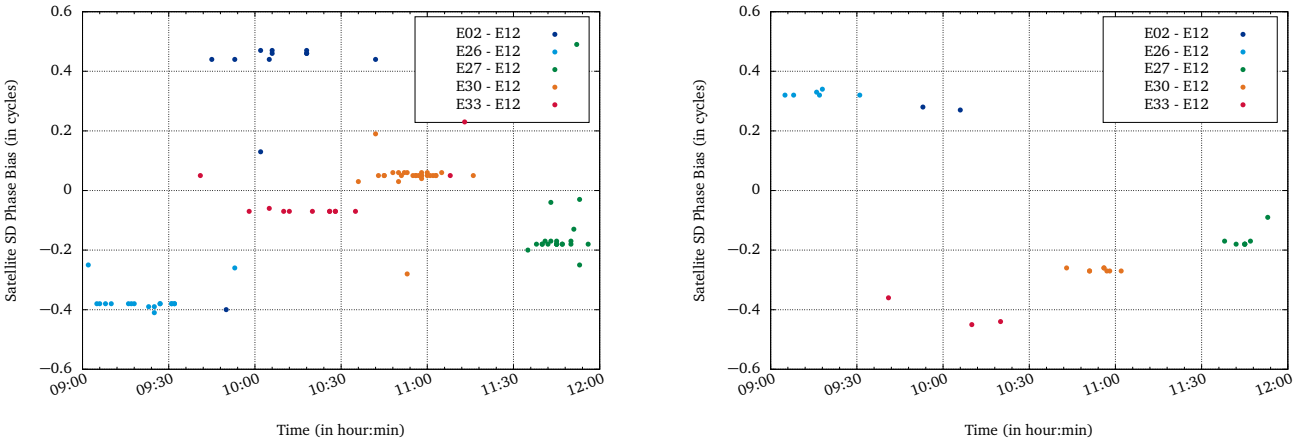

(a) Galileo signal E8Q

(b) Galileo signal E6C

Figure 10.13: Between satellite SD phase biases for different pairs of satellites, determined from fixed raw observation ambiguities of multiple receivers, each tracking the respective pair of satellites at the same time.

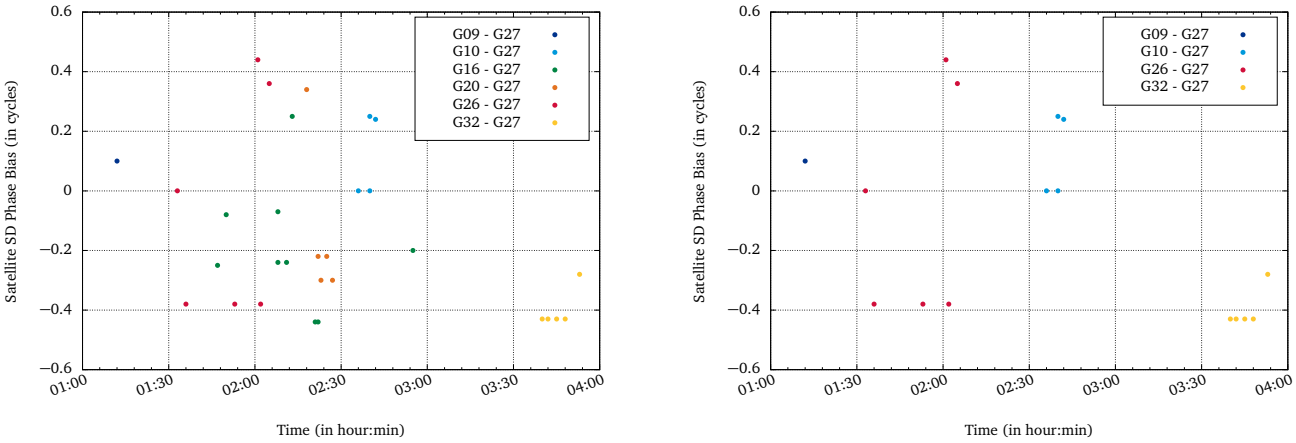

(a) GPS signal G2W

(b) GPS signal G5Q

Figure 10.14: Between satellite SD phase biases for different pairs of satellites, determined from fixed raw observation ambiguities of multiple receivers, each tracking the respective pair of satellites at the same time.

Bibliography

Ashby, N. (2003). Relativity in the global positioning system. *Living Rev. Relativity*, 6(1).

Ashby, N. (2004). *Relativity in Rotating Frames*, chapter The Sagnac Effect In The Global Positioning System. ISBN-13: 978-1402018053.

Bauer, M. (2011). *Vermessung und Ortung mit Satelliten*. Wichmann, 6 edition.

BeiDou OS B1C SIS ICD (2017). *BeiDou Open Service B1C Signal In Space Interface Control Document, Version 1.0*. China Satellite Navigation Office.

BeiDou OS B1I SIS ICD (2019). *BeiDou Open Service B1I Signal In Space Interface Control Document, Version 3.0*. China Satellite Navigation Office.

BeiDou OS B2a SIS ICD (2017). *BeiDou Open Service B2a Signal In Space Interface Control Document, Version 1.0*. China Satellite Navigation Office.

BeiDou OS B3I SIS ICD (2018). *BeiDou Open Service B3I Signal In Space Interface Control Document, Version 1.0*. China Satellite Navigation Office.

BeiDou OS SIS ICD (2016). *BeiDou Open Service Signal In Space Interface Control Document, Version 2.1*. China Satellite Navigation Office.

Beutler, G. (2005). *Methods of Celestial Mechanics*. Springer. ISBN 3-211-82364-6.

BIPM, Bureau International des Poids et Mesures (2019a). *Circular T*. `https://www.bipm.org/en/bipm-services/timescales/time-ftp/Circular-T.html` [Accessed on 2019-04-20].

BIPM, Bureau International des Poids et Mesures (2019b). *International Reference Time Scales*. `https://www.bipm.org/en/bipm-services/timescales/` [Accessed on 2019-07-15].

Blewitt, G. (1989). Carrier Phase Ambiguity Resolution for the Global Positioning System Applied to Geodetic Baselines up to 2000 km. *Journal of Geophysical Research*, 94:10187–10203.

Blewitt, G. (1997). *Geodetic Applications of GPS*, chapter Basics of the GPS Technique: Observation Equations, pages 1–46. Swedish Land Survey.

CDDIS, Crustal Dynamics Data Information System (2019a). *GNSS Bias Products*. `ftp://cddis.gsfc.nasa.gov/gnss/products/bias` [Accessed on 2019-06-20].

CDDIS, Crustal Dynamics Data Information System (2019b). *GNSS Mixed Broadcast Navigation Files*. `ftp://cddis.gsfc.nasa.gov/gnss/data/campaign/mgex` [Accessed on 2019-02-11].

Chang, X., Yang, X., and Zhou, T. (2005). MLAMBDA: A modified LAMBDA method for integer least-squares estimation. *J Geod*, (79(9)):552–565.

Collins, J., Bisnath, S., Lahaye, F., and Heroux, P. (2010). Undifferenced GPS Ambiguity Resolution using the Decoupled Clock Model and Ambiguity Datum Fixing. *Navigation*, 57(2):123–135.

Dach, R., Lutz, S., Walser, P., and Fridez, P. (2015a). Bernese GNSS Software, Version 5.2, Vol. 1. Technical report, Astromincal Institute, University of Bern.

Dach, R., Lutz, S., Walser, P., and Fridez, P. (2015b). Bernese GNSS Software, Version 5.2, Vol. 2. Technical report, Astromincal Institute, University of Bern.

Davis, J., Elgered, G., Niell, A., and Kuehn, C. (1993). Ground-based measurements of gradients in the "wet" radio refractivity of air. *Radio Sci*, 28(6):1003–1018. doi: 10.1029/93RS01917.

De Jonge, P. (1998). A processing strategy for the application of the GPS in networks. *Netherlands Geodetic Commission, Publications on Geodesy, Vol 46*, page 225pp.

De Jonge, P. and Tiberius, C. (1996). The LAMBDA method for integer ambiguity estimation: implementation aspects. *Delft Geodetic Computing Centre, LGR series No.12*, page 49pp.

Defraigne, P., Aerts, W., and et. al. (2013). Advances on the use of Galileo signals in time metrology: calibrated time transfer and estimation of UTC and GGTO using a combined commercial GPS-Galileo receiver. *PTTI*.

Dong, D.-N. and Bock, Y. (1989). Global Positioning System Network Analysis With Phase Ambiguity Resolution Applied to Crustal Deformation Studies in California. *Journal of Geophysical Research*, 94:3949–3966.

Elwischger, B., Thoelert, S., Suess, M., and Furthner, J. (2013). Absolute calibration of dual frequency timing receivers for Galileo. In *Proceedings of ENC 2013, Vienna*.

European Commission (2016). *European GNSS (Galileo) Open Service - Ionospheric Correction Algorithm for Galileo Single Frequency Users, Issue 1.2*. `https://www.gsc-europa.eu/sites/default/files/sites/all/files/Galileo_Ionospheric_Model.pdf` [Accessed on 2019-05-20].

European Space Agency (2019). *Navipedia*. `https://gssc.esa.int/navipedia/index.php` [Accessed on 2019-09-02].

Flohrer, C. (2008). Mutual Validation of Satellite-Geodetich Techniques and its Impact on GNSS Orbit Modelling. Geodätisch-geophysikalische Arbeiten in der Schweiz (Fortsetzung der Publikationsreihe Astronomisch-Geodätische Arbeiten in der Schweiz) 75, Schweizerische Geodätische Kommission, ETH Zürich.

Fonville, B., Powers, A., Ioannides, R., Hahn, J., and Mudrak, A. (2012). Timing Calibration of a GPS/Galileo Combined Receiver. In *Proceedings of 44th PTTI*, pages 167–178.

Galileo OS SIS ICD (2016). *Galileo Open Service Signal-In-Space Interface Control Document, Issue 1.3*. European Union.

Gauss, K. F. (1809). *Theoria Motus Corporum Coelestium*. (Translated into English: Davis, C.H., *Theory of the Motion of the Heavenly Bodies Moving about the Sun in Conic Sections*, Dover, New York, 1963).

Ge, M., Gendt, G., Dick, G., and Zhang, F. (2005). Improving carrier-phase ambiguity resolution in global GPS network solutions. *Journal of Geodesy*, 79:103–110.

Ge, M., Gendt, G., Rothacher, M., Shi, C., and Liu, J. (2008). Resolution of GPS carrier-phase ambiguities in Precise Point Positioning (PPP) with daily observations. *Journal of Geodesy*, 82(7):401.

Geng, J., Shi, C., Ge, M., Dodson, A., Lou, Y., Zhao, Q., and Liu, J. (2012). Improving the estimation of fractional-cycle biases for ambiguity resolution in precise point positioning. *Journal of Geodesy*, 86(8):579–589.

Geng, J., Teferle, F., Meng, X., and Dodson, A. (2011). Towards PPP-RTK: Ambiguity resolution in real-time precise point positioning. *Advances in Space Research*, 47(10):1664–1673.

GLONASS ICD (2008). *GLONASS Interface Control Document L1/L2, Edition 5.1*. Russian Institute of Space Device Engineering.

Golub, G. H. and Van Loan, C. F. (1996). *Matrix Computations*. The Johns Hopkins University Press, 3rd edition. ISBN 978-0-8018-5414-9.

GSA, European GNSS Agency (2019a). *Galileo Satellite Metadata*. `https://www.gsc-europa.eu/support-to-developers/galileo-satellite-metadata#8` [Accessed on 2019-09-08].

GSA, European GNSS Agency (2019b). European GNSS Service Centre. `https://www.gsc-europa.eu` [Accessed on 2019-07-01].

Hauschild, A. and Montenbruck, O. (2016). The Effect of Correlator and Front-End Design on GNSS Pseudorange Biases for Geodetic Receivers. *Journal of the Institute of Navigation*, 63(4).

Hauschild, A., Montenbruck, O., and Steigenberger, P. (2013). Short-term Analysis of GNSS Clocks. *GPS Solutions*, 17(3):295–307.

Hernández-Pajares, M., Juan, J., Sanz, J., Orus, R., Garcia-Rigo, A., Feltens, J., Komjathy, A., Schaer, S., and Krankowski, A. (2009). The IGS VTEC maps: a reliable source of ionospheric information since 1998. *Journal of Geodesy*, 83:263–275. DOI 10.1007/s00190-008-0266-1.

Hernandez-Pajares, M., Juan, J. M., Sanz, J., and Orus, R. (2007). Second-order ionospheric term in GPS: Implementation and impact on geodetic estimates. *Jouranl of Geophysical Research*, (112):1–16. doi:10.1029/2006JB004707.

Hofmann-Wellenhof, B., Lichtenegger, H., and Collins, J. (1992). *GPS: Theory and Practice*. Springer. ISBN 3-211-82364-6.

Hofmann-Wellenhof, B., Lichtenegger, H., and Wasle, E. (2008). *GNSS - Global Navigation Satellite Systems*. Springer. ISBN: 978-3-211-73012-6.

IERS (2010). IERS Conventions (2010). Technical Note 36, International Earth Rotation and Reference Systems Service (IERS), Bundesamt für Kartographie und Geodäsie, Frankfurt am Main. IERS Technical Note No. 36.

IERS (2019a). *ICRF Solutions*. `https://www.iers.org/IERS/EN/DataProducts/ICRS/icrs.html` [Accessed on 2019-07-25].

IERS (2019b). *ITRF Solutions*. `https://www.iers.org/IERS/EN/DataProducts/ITRF/itrf.html` [Accessed on 2019-07-20].

IERS (2019c). *The Earth Orientation Parameters*. `https://www.iers.org/IERS/EN/Science/EarthRotation/EOP.html` [Accessed on 2019-08-10].

IS-GPS-200 (2015). *GPS Interface Specification IS-GPS-200H-003*. Global Positioning Systems Directorate.

Joosten, P. and Verhagen, S. (2003). Analysis of ambiguity resolution algorithms and quality control parameters for Global Navigations Satellite Systems. *ESA publication, contract no. "16793/02/NL/LvH"*.

Kaplan, E. D. and Hegarty, C. J., editors (2017). *Understanding GPS/GNSS - Principles and Applications*. 3rd edition.

Kim, D. and Langley, R. B. (2000). GPS ambiguity resolution and validation: methodologies, trends and issues. In *Proc. of 7th GNSS Workshop, Seoul, Korea*.

Kleusberg, A. and Teunissen, P. J. G., editors (1998). *GPS for Geodesy*. Springer Berlin.

Klobuchar, J. (1987). Ionospheric Time-Delay Algorithms for Single-Frequency GPS Users. . *IEEE Transactions on Aerospace and Electronic Systems*, (3):325–331.

Koch, K. (2004). *Parameterschätzung und Hypothesentests in linearen Modellen*. Dümmler, Bonn, 4., bearbeitete auflage edition.

Kouba, J. (2004). Improved relativistic transformations in gps. *GPS Solutions*, 8(3):170–180.

Laurichesse, D., Mercier, F., Berthias, J.-P., Broca, P., and Cerr, L. (2009). Integer Ambiguity Resolution on Undifferenced GPS Phase Measurements and Its Application to PPP and Satellite Precise Orbit Determination. In *NAVIGATION*, volume 56, pages 135–149.

Ley, W., Wittmann, K., and Hallmann, W., editors (2019). *Handbuch der Raumfahrttechnik*, volume 5. Carl Hanser Verlag München.

Li, Z., Yuan, Y., Li, H., Ou, J., and Huo, X. (2012). Two-step method for the determination of the differential code biases of COMPASS satellites. *Journal of Geodesy*, 86(11):1059–1076.

Mervart, L., Lukes, Z., Rocken, C., and Iwabuchi, T. (2008). Precise point positioning with ambiguity resolution in real-time. In *ION GNSS*, pages 397–405.

Montenbruck, O., Hauschild, A., and Steigenberger, P. (2014). Differential Code Bias Estimation using Multi-GNSS Observations and Global Ionosphere Maps. *Navigation - Journal of the ION*, 61(3):191–201. DOI 10.1002/navi.64.

Montenbruck, O., Hauschild, A., Steigenberger, P., and Langley, R. B. (2010). Three's the challenge: A close look at GPS SVN62 triple-frequency signal combinations finds carrier-phase variations on the new L5. *GPS World*, 21(8):8–19.

Montenbruck, O., Steigenberger, P., Prange, L., Deng, Z., Zhao, Q., Perosanz, F., Romero, I., Noll, C., Stuerze, A., Weber, G., Schmid, R., MacLeod, K., and Schaer, S. (2017). The Multi-GNSS Experiment (MGEX) of the International GNSS Service (IGS) – Achievements, prospects and challenges. *Advances in Space Research*, 59:1671–1697. http://dx.doi.org/10.1016/j.asr.2017.01.011.

Navigation Support Office (2019). http://navigation-office.esa.int/OPS-GN_Navigation_Support_Office.html [Accessed on 2019-08-07].

Newby, S. (1992). An assessment of empirical models for the prediction of the transionospheric propagation delay of radio signals. Technical Report 160, University of New Brunswick, Department of Surveying and Engineering, New Brunswick, Canada.

Niemeier, W. (2008). *Ausgleichungsrechnung*. de Gruyter, 2. edition.

Odijk, D. (2002). *Fast precise GPS positioning in the presence of ionospheric delays*. PhD thesis, Netherlands Geodetic Commission. NCG No. 52 (yellow series).

Peng, Y., Lou, Y., Gong, X., Wang, Y., and Dai, X. (2019). Real-time clock prediction of multi-GNSS satellites and its application in precise point positioning. *Advances in Space Research*, 64(7):1445–1454.

Petit, G. and Luzum, B. (2010). IERS Conventions (2010). Technical Note 36, International Earth Rotation and Reference Systems Service (IERS), Bundesamt für Kartographie und Geodäsie, Frankfurt am Main. IERS Technical Note No. 36.

Reckeweg, F., Schönemann, E., Dilssner, F., Springer, T., Becker, M., and Enderle, W. (2018). Receiver System Calibration for Multi-GNSS Multi-Signal Raw Observation Processing. Navitec 2018, ESTEC, Noordwijk.

Reckeweg, F., Schönemann, E., Springer, T., Becker, M., and Enderle, W. (2016). Multi-GNSS / Multi-Signal code bias determination from RAW GNSS observations. In *Proceedings of Geodätische Woche (InterGEO 2016), Hamburg, Germany*.

Reckeweg, F., Schönemann, E., Springer, T., and Enderle, W. (2017). Galileo FOC Satellite Group Delay Estimation based on Raw Method and published IOV Metadata. EGU General Assembly 2017, Vienna, Austria.

Roskosmos (2019a). *BeiDou Constellation Status*. https://www.glonass-iac.ru/en/BEIDOU/ [Accessed on 2019-09-05].

Roskosmos (2019b). *BeiDou Orbital Constellation*. https://glonass-iac.ru/en/guide/beidou.php [Accessed on 2019-09-07].

Roskosmos (2019c). *GLONASS Constellation Status*. https://www.glonass-iac.ru/en/GLONASS/ [Accessed on 2019-09-05].

Roskosmos (2019d). *GLONASS Orbital Constellation*. https://glonass-iac.ru/en/guide/index.php [Accessed on 2019-09-07].

Saastamoinen, J. (1973). Contributions to the THeory of Atmospheric Refraction, Part II. *Bulletin Géodésique*, 107:13–34.

Schaer, S. (2016). *SINEX for GNSS Biases, Version 1.00*. http://ftp.aiub.unibe.ch/bcwg/format/draft/sinex_bias_100.pdf [Accessed on 2019-07-09].

Schaer, S., Gurtner, W., and Feltens, J. (1998). IONEXThe IONospheric Map EXchange Format Version 1. In *Proceedings of the IGS AC Workshop, Darmstadt, Germany*. Darmstadt, Germany, February 9-11, 1998.

Schönemann, E. (2014). *Analysis of GNSS raw observations in PPP solutions*. PhD thesis, Technische Universität Darmstadt.

Schönemann, E., Becker, M., and Springer, T. (2011). A new Approach for GNSS Analysis in a Multi-GNSS and Multi-Signal Environment. *Journal of Geodetic Science*, 1(3):204–214.

Seeber, G. (1993). *Satellite geodesy: foundations, methods and applications*. Walter deGruyter, Berlin.

Springer, T. (2009). NAPEOS Mathematical Models and Algorithms. Technical Note DOPS-SYS-TN-0100-OPS-GN, European Space Operation Centre / European Space Agency.

Stehlin, X., Wang, Q., Jeanneret, F., and Rochat, P. (2006). GALILEO SYSTEM TIME PHYSICAL GENERATION. *38th Annual Precise Time and Time Interval (PTTI) Meeting*.

Strasser, S., Mayer-Guerr, T., and Zehentner, N. (2018). Processing of GNSS constellations and ground station networks using the raw observation approach. *Journal of Geodesy*.

Tapley, B. D., Schutz, B. E., and Born, G. H. (2004). *Statistical Orbit Determination*. Elsevier Academic Press.

Teunissen, P., Joosten, P., and Tiberius, C. (2002). A Comparison of TCAR, CIR and LAMBDA GNSS Ambiguity Resolution. *ION GPS 2002, Portland, OR*.

Teunissen, P. J. G. (1993). Least squares estimation of the integer GPS ambiguities. *Invited lecture, Section IV Theory and Methodology, IAG General Meeting, Beijing*.

Teunissen, P. J. G. (1995). The least-squares ambiguity decorrelation adjustment: a method for fast GPS integer ambiguity estimation. *Journal of Geodesy*, (70):65–82.

Teunissen, P. J. G. (1998). GPS Carrier Phase Ambiguity Fixing Concepts. In *GPS for Geodesy*. Springer Berlin.

Teunissen, P. J. G. (1999). An optimality property of the integer least-squares estimator. *Journal of Geodesy*, (73):587–593.

Teunissen, P. J. G. (2001). Statistical carrier phase ambiguity resolution: A review. In *Proc IEEE Statistical Signal Processing, Singapore*, pages 4–12.

Teunissen, P. J. G. (2003). Towards a unified theory of GNSS ambiguity resolution. *Journal of Global Positioning Systems*, 2 No 1:1–12.

Teunissen, P. J. G. (2017). Carrier Phase Integer Ambiguity Resolution. In *Springer Handbook of Global Navigation Satellite Systems*. Springer.

Teunissen, P. J. G. and Khodabandeh, A. (2014). Review and principles of PPP-RTK methods. *Journal of Geodesy*. DOI 10.1007/s00190-014-0771-3.

Teunissen, P. J. G. and Kleusberg, A. (1998). GPS Observation Equations and Positiong Concepts. In *GPS for Geodesy*. Springer Berlin.

Teunissen, P. J. G. and Montenbruck, O., editors (2017). *Springer Handbook of Global Navigation Satellite Systems*. Springer.

Teunissen, P. J. G., Odijk, D., and Zhang, B. (2010). PPP-RTK: results of CORS network-based PPP with integer ambiguity resolution. *J Aeronaut, Astronaut Aviat*, 42(4):223–229.

U.S. Government (2019). *GPS Space Segment*. `https://www.gps.gov/systems/gps/space/` [Accessed on 2019-09-04].

Verhagen, S. (2005). *The GNSS integer ambiguities: Estimation and validation*. PhD thesis, NCG, Delft. erschienen in: Publications on Geodesy No. 58, yellow series, Netherlands Geodetic Commission.

Verhagen, S. and Joosten, P. (2004). Analysis of ambiguity resolution algorithms. In *Proc. of the European Navigation Conference GNSS 2004, Rotterdam NL*.

Villiger, A., Schaer, S., Dach, R., Prange, L., Sušnik, A., and Jäggi, A. (2019). Determination of GNSS pseudo-absolute code biases and their long-term combination. *Journal of Geodesy*. https://doi.org/10.1007/s00190-019-01262-w.

Vollath, U., Birnbach, S., Landau, H., Fraile-Ordoñez, J., and Martin-Neira, M. (1998). Analysis of Three-Carrier Ambiguity Resolution (TCAR) Technique for Precise Relative Positioning in GNSS-2. In *Proceedings of the 11th International Technical Meeting of the Satellite Division of the Institute of Navigation, Nashville,*, pages 417–426.

Wang, N., Yuan, Y., Li, Z., Montenbruck, O., and Tan, B. (2016). Determination of differential code biases with multi-GNSS observations. *Journal of Geodesy*, 90(3):209–228.

Wu, J. T., Wu, S. C., Hajj, G. A., Bertiger, W. I., and Lichten, S. M. (1992). Effects of antenna orientation on GPS carrier phase. In P. Blumer, editor, *Astrodynamics 1991*, pages 1647–1660.

Wübbena, G. (1989). The GPS adjustment software package GEONAP - concepts and models. In *Proceedings of the Fifth International Geodetic Symposium on Satellite Positioning, Las Cruces, New Mexico*, volume 2, pages 452–461.

Wübbena, G., Schmitz, M., and Bagge, A. (2005). PPP-RTK: Precise Point Positioning Using State-Space Representation in RTK Networks. In *ION GNSS 2005, September 13-16, Long Beach, California*.

Zhang, B., Teunissen, P. J., and Odijk, D. (2011). A Novel Un-differenced PPP-RTK Concept. *Journal of Navigation*, 64:S180–S191.

Zhu, S. and Groten, E. (1988). Relativistic Effects in GPS. *GPS-Tech. Appl. Geod. Surv. Proc. Int. GPS-Workshop*, pages 41–46.